



HAL
open science

Liquid-liquid mass transfer characterization applied to metallurgical process

Nelson Joubert

► **To cite this version:**

Nelson Joubert. Liquid-liquid mass transfer characterization applied to metallurgical process. Fluid mechanics [physics.class-ph]. Sorbonne Université, 2021. English. NNT : 2021SORUS055 . tel-03227840v2

HAL Id: tel-03227840

<https://hal.science/tel-03227840v2>

Submitted on 17 Nov 2021

HAL is a multi-disciplinary open access archive for the deposit and dissemination of scientific research documents, whether they are published or not. The documents may come from teaching and research institutions in France or abroad, or from public or private research centers.

L'archive ouverte pluridisciplinaire **HAL**, est destinée au dépôt et à la diffusion de documents scientifiques de niveau recherche, publiés ou non, émanant des établissements d'enseignement et de recherche français ou étrangers, des laboratoires publics ou privés.

Thèse de doctorat de Sorbonne Université

Spécialité : Mécanique

Ecole doctorale de *Sciences Mécaniques, Acoustique, Electronique et Robotique de Paris (ED 391)*

présentée par

Nelson Joubert

pour obtenir le grade de

DOCTEUR DE SORBONNE UNIVERSITÉ

Liquid-liquid mass transfer characterization applied to metallurgical process

*Caractérisation du transfert de masse à l'interface liquide-liquide dans les
procédés sidérurgiques*

Directeur de thèse : Stéphane Zaleski

Co-encadrant de thèse : Pascal Gardin, Stéphane Popinet

soutenue le 18 février 2021

devant le jury composé de

M. Stéphane Vincent Prof. UPEM

M. Eric Climent Prof. IMFT

M. Dieter Bothe Prof. TU Darmstadt

Mme. Suzie Protière HDR MC Sorbonne Université

M. Chattopadhyay Kinnor Associate Professor, University of Toronto

Rapporteur

Rapporteur

Examineur

Examineur

Examineur

ACKNOWLEDGEMENTS

First of all, I would like to thank Pascal Gardin who choose me to achieve this PhD and for his encouragement and careful attention to not forget the industrial focus of this PhD during these three years. Then, I want to thank Stéphane Zaleski for the guidance and patience he gave me during the entire length of this PhD. In addition to the ideas and diplomatic skills he brought during the meeting, his eternal enthusiasm whatever the situation has been important for our motivation in the achievement of this PhD. Finally, I want to thank Stéphane Popinet for all the patience he accorded me and also all the good advice and constructive criticisms he could apport during the meeting.

Later on, I want to thank Stéphane Vincent and Eric Climent for their valuable questions and remarks during the first and last year thesis committee, and also for the reviews they made to this work. I also want to thank all the members of the jury for their participation in the PhD defense.

This work was supported by ANRT with convention CIFRE N° 2017/0694 and benefited from access to the HPC resources of CINES under the allocations 2018- A0052B07760 and 2019 - A0072B07760 granted by GENCI, and by the ERC ADV grant TRUFLOW.

Then I will try to thank all the people who assisted me in the achievement of this PhD at ArcelorMittal Maizières Research and at the Institut Jean Le Rond d'Alembert.

I first start with the people of the campus of ArcelorMittal Maizières Research where I want to thank the people of the THEMEF service to have welcomed me in their team and for the interesting discussions we had during my visits at the campus. All the experiments realized during this PhD have been successfully conducted in ArcelorMittal Maizières Research campus thanks to the work on the previous experiment established by Leandro Dijon with the help of Armand Mellinger and Odile Carrier. Then the new version of the experiment has been successfully implemented and tested with the help of Jonathan Nardini, and with the chemical expertise of Odile Carrier and the people of the chemical service. Finally, I want to thank the IT team of the campus and especially Johann Lebard and Franck Vojenis for their precious help to establish all the necessary to be able to run Basilisk simulations at the Maizières campus and for all the interesting discussions we had.

At the Institut Jean Le Rond d'Alembert, I want to thank all the permanents, the administrative, IT team, PhD students, post-docs and ATER people that I had the opportunity to interact with during formal or more frequently informal moments to enable a good research atmosphere at the lab. I want to thank especially the people present during the traditional lunch break at the CROUS restaurant or the other traditional meeting at the Baker.

Last but not least, I would like to thank my parents for the good education they gave me and their continuous and precious support during these three years. This work is dedicated to you and also to the memory of my grand-father chemical engineer of formation who inspired me a scientific path with the numerous anecdotes he told me. I would also like to thank my brother and his family to have welcomed me in their house for precious relaxing time. Then I want to thank all my friends for their support and the fun time we could have in various places and circumstances during these three years.

ABSTRACT

This dissertation aims to characterize the mass transfer between liquid steel and another liquid phase in the case of an industrial argon gas bottom blown ladle used in metallurgical processes. In this study, we consider only the influence of the flow generated by the gas injection on the mass transfer. To do so we use a reduced-scale water experiment of the process developed in ArcelorMittal Maizières Research using air, water and oil at ambient temperature as fluids model. Besides, we use Direct Numerical Simulation with dynamic adaptive mesh to reproduce the water experiment with the Free Software library Basilisk. We first study the hydrodynamics of the experiment by measuring the open-eye area and the fragmentation of the oil layer due to the air injection. Our experimental and numerical results reveal that the open eye area increases following the air flow rate and also show fragmentation of the oil layer at the same critical air flow rate in agreement with the literature.

In the second part of this dissertation, we measure experimentally the mass transfer of thymol between the water and oil phase while the air flow rate varies. Our experimental results show that the mass transfer presents an abrupt increase when the air flow rate is above a critical value in accord with the literature. Moreover, the transition of the different mass transfer regime appears to be correlated with the continuous fragmentation of the oil layer into oil droplets. In order to simulate the complex water experiment mass transfer configuration, several assumptions need to be done. Furthermore, due to the exceedingly thin concentration boundary layer induced by the low experimental diffusion coefficient of thymol in water, we considered a higher diffusion coefficient in the simulation. The numerical results represent qualitatively well the mass transfer configuration of the water experiment with variation of the concentration essentially at the water-oil interface. However, from the limited amount of numerical results, we do not clearly observe an abrupt increase of the mass transfer as observed experimentally. Finally, using a boundary layer theory we established correlations to predict the mass transfer. These correlations give a good prediction of the first mass transfer regime for each specific experimental configuration. On the other hand, using these correlations to extrapolate the numerical results to the low experimental diffusion coefficient leads to an overestimation of the experimental mass transfer results.

Keywords: multiphase flow, reduced-scale experiment, Direct Numerical Simulation, hydrodynamics, mass transfer.

RESUME

L'objectif de cette thèse est de caractériser le transfert de masse entre l'acier liquide et une autre phase liquide dans le cas d'une cuve industrielle agitée avec injection d'argon utilisée dans les procédés sidérurgiques. Lors de cette étude on considère uniquement l'influence de l'écoulement généré par l'injection de gaz sur le transfert de masse. Pour ce faire on utilise une maquette à eau du procédé développée à ArcelorMittal Maizières Research utilisant de l'air, de l'eau et de l'huile à température ambiante. De plus, on utilise une simulation directe avec maillage adaptatif dynamique avec le code Basilisk pour reproduire la configuration de la maquette. Dans un premier temps on étudie l'hydrodynamique de la maquette en mesurant la surface de l'« open eye » et la fragmentation de la couche d'huile sous l'effet de l'injection d'air. Nos résultats expérimentaux et numériques montrent que la surface de l'« open eye » augmente avec le débit d'air en accord avec les résultats de la littérature. On observe aussi que la fragmentation de la couche d'huile a lieu pour des débits similaires dans l'expérience et la simulation.

Dans la deuxième partie de cette thèse, on mesure expérimentalement le transfert de masse du thymol entre l'eau et l'huile lorsque le débit d'air varie. Les résultats expérimentaux montrent que le transfert de masse augmente de manière abrupte lorsque le débit d'air dépasse une valeur critique en accord avec les résultats de la littérature. De plus, la transition entre les différents régimes de transfert de masse est corrélée à la fragmentation en continu de la couche d'huile en gouttes d'huile. Pour simuler cette configuration de transfert de masse complexe plusieurs hypothèses ont dû être effectuées. En raison de la trop faible taille de la couche limite de concentration due à la faible valeur du coefficient de diffusion du thymol dans l'eau on considère un coefficient de diffusion plus élevé dans la simulation. Les résultats numériques représentent qualitativement bien la configuration du transfert de masse de la maquette avec une variation de la concentration principalement le long de l'interface eau huile. Cependant, à partir de la quantité limitée de simulations on n'observe pas d'augmentation abrupte du transfert de masse comme dans les résultats expérimentaux. Enfin, des corrélations pour prédire le transfert de masse ont été établis à partir d'analyse basée sur la théorie de la couche limite. Ces corrélations donnent de relativement bonne prédiction du premier régime de transfert de masse pour chaque expérience. Néanmoins, en utilisant ces corrélations l'extrapolation des résultats numériques vers le faible coefficient de diffusion correspondant au cas expérimental surestime les résultats expérimentaux.

Mots-clefs : écoulement multiphasique, maquette, Direct Numerical Simulation, hydrodynamique, transfert de masse.

CONTENTS

Acknowledgements	ii
Abstract	iii
Résumé.....	iv
Contents	v
1 Introduction.....	1
Part I - Hydrodynamic characterization.....	4
2 Physical model- hydrodynamic characterization	5
2.1 Literature review	5
2.2 Experimental model	10
2.3 Phenomenological analysis	17
2.4 Summary.....	24
3 Numerical model- hydrodynamic characterization.....	26
3.1 Literature review	26
3.2 Two-phase model	27
3.3 Basilisk code	27
3.4 Three-phase model	30
3.5 Numerical validation	31
3.6 Numerical water experiment	42
3.7 Estimation of the mesh size required.....	43
3.8 Summary.....	44
4 Results- hydrodynamic characterization	46
4.1 Experimental results.....	46
4.2 Numerical results.....	54
4.3 Comparison of the results	69
4.4 Summary.....	71
5 Toward industrial application- hydrodynamic characterization	73
5.1 Open-eye experiments in the literature.....	73
5.2 Comparison of the open-eye area.....	75
5.3 Summary.....	81
Part II - Mass transfer characterization	82
6 Physical model- mass transfer characterization.....	83
6.1 Mass transfer theory	83

6.2	Literature review	85
6.3	Experimental model	91
6.4	Phenomenological analysis	94
6.5	Summary.....	107
7	Numerical model- mass transfer characterization	109
7.1	Literature review of numerical mass transfer simulations	109
7.2	Numerical model	110
7.3	Numerical tests.....	113
7.4	Estimation of the mesh size required.....	117
7.5	Summary.....	120
8	Results- mass transfer characterization	122
8.1	Experimental results.....	122
8.2	Numerical results.....	131
8.3	Comparison of the experimental and numerical results.....	141
8.4	Summary.....	144
9	Toward industrial application- mass transfer characterization	146
9.1	Mass transfer measurement	146
9.2	Prediction of the Sherwood number	152
9.3	Summary.....	157
10	Conclusion and perspectives	159
11	Appendices	163
11.1	Assumptions not considered in the phenomenological analysis	163
11.2	Numerical results- mass transfer characterization	165
12	Bibliography.....	173

List of figures

Figure 1.1: Overview of the steelmaking process using a blast furnace from the worldsteel association [5].	1
Figure 1.2: Overview of the steelmaking process using an electric arc furnace from [5].	2
Figure 2.1: Schematic of a metallurgical gas stirred ladle. a): Global view; b) Zoom on the region delimited by a rectangle in the global view.	5
Figure 2.2: Top view of the ladle with the open eye of the top phase delimited for two experiments. a): water/oil model experiments obtained at $Q = 130l/h$ from [26]; b): industrial ladle (170-t) experiments obtained at $Q = 15000lh$ at Standard Temperature and Pressure conditions from [18].	7
Figure 2.3: Example of a thick slag layer fragmentation into droplets due to gas injection for a gas flow rate $Q = 0.4 l/min$ from the water experiment of [27].	9
Figure 2.4: Schematic of the experimental setup of our water experiment.	13
Figure 2.5: Top view of the water experiment used in our experiment at $Q = 0.6l/min$ with $d_{inj} = 7.9 \cdot 10^{-3}m$.	14
Figure 2.6: Face view of the water experiment used in our experiment at $Q = 0.4l/min$ with $d_{inj} = 7.9 \cdot 10^{-3}m$.	14
Figure 2.7: Relative error between the setting point value of the air flow rate and the measured air flow rate as a function of the setting point value of the air flow rate for two different trials.	15
Figure 2.8. Zoom of the face view on the bubble plume from our water experiment with $d_{inj} = 2.35 \cdot 10^{-3}m$ and two different air flow rates. a): $Q = 0.2l/min$; b): $Q = 0.5l/min$.	18
Figure 2.9: Bubble plume basic geometry.	18
Figure 2.10: Open eye model. (a) Face view. Oil surface is situated between the curve zx, y and horizontal line at height $z^\infty + h_0$. (b) Top view. The Ω domain is squared of dimension $Lx \times Lx$ and the open eye is the circle C of radius r_0 . The integration surface is $\Omega S = \Omega - C$.	20
Figure 3.1: Example of quadtree spatial discretisation (left) and the corresponding tree representation (right) from [15].	29
Figure 3.2: Representation of the fluid fractions at the initial state $t = 0$ for the two phase formulation with f_{left} and f_{right} and for the three phase formulation with f_1, f_2 and f_3 .	31
Figure 3.3: Shapes of the interface for $t = 0, t = T/4, t = T/2, t = 3T/4$ and $t = T$ obtained for a maximum mesh number in one direction of $lvl8 = 28$ cells. a): VOF tracer for phase one f_1 ; b): VOF tracer for phase two f_2 .	32
Figure 3.4: Convergence rates for the error shape of the VOF tracer for two-phase and three-phase formulation. a): Left half part of the circle corresponding respectively to f_{left} and f_1 for the two and three-phase formulation with an adaptive grid; b): Right half part of the circle corresponding respectively to f_{right} and f_2 for the two and three-phase formulation with an adaptive grid; c): Outside part of the circle corresponding to phase three f_3 for the three phase formulation with adaptive and uniform grid.	33
Figure 3.5: Time evolution of the error in the conservation of the VOF tracer for different maximum mesh resolutions for three phase formulation. a): VOF tracer for phase one f_1 ; b): VOF tracer for phase two f_2 ; c): VOF tracer for phase three f_3 .	35
Figure 3.6: Comparison of the time evolution of the absolute value of the error in the conservation of the VOF tracer for two-phase and three-phase formulation at a constant maximum mesh resolution of 28 cells. a): Left half part of the circle corresponding respectively to f_{left} and f_1 for the two and three-phase formulation; b): Right half part of the circle corresponding respectively to f_{right} and f_2 for the two and three-phase formulation.	36

Figure 3.7: Schematic of the possible spreading of an oil lens at a solid interface depending on the value of the spreading parameter $S = \sigma_{aw} - (\sigma_{ao} + \sigma_{wo})$.	37
Figure 3.8 : Representation of the fluid fractions at the initial state $t = 0$ with f_1 the air fluid fraction, f_2 the water fluid fraction and f_3 the oil fluid fraction.	37
Figure 3.9: Face view of the oil and water VOF interface for the partial spreading case at different instants. The oil interface is filled in black. a): $t = 0$; b): $t = 10$; c): $t = 20$; d): $t = 30$.	39
Figure 3.10: Zoom on the left part of the oil lens with the reconstructed interface of each VOF tracer and the mesh represented. The air, water and oil interfaces are coloured respectively in red, green and light blue. a): $t = 20$; b): $t = 25$; c): $t = 30$; d): $t = 35$.	39
Figure 3.11: Data for the partial spreading case. a): Time evolution of the maximum horizontal velocity; b): Time evolution of the error in the conservation of the VOF tracer.	40
Figure 3.12: Face view of the oil and water VOF tracer for the total spreading case at different instants. The oil interface is filled in black. a): $t = 0$; b): $t = 10$; c): $t = 20$; d): $t = 30$.	41
Figure 3.13: Zoom on the left part of the oil lens with the reconstructed interface of each VOF tracer and the mesh represented. The air, water and oil interface are coloured respectively in red, green and light blue. a): $t = 20$; b): $t = 25$; c): $t = 30$; d): $t = 35$.	41
Figure 3.14: Data for the total spreading case. a): Time evolution of the maximum horizontal velocity; b): Time evolution of the error in the conservation of VOF tracer quantity.	42
Figure 3.15: Schematic of the numerical setup with the boundary conditions indicated with specific colours.	42
Figure 4.1: Zoom of the face view of our water experiment for different air flow rates. The results are obtained with an oil volume of $V_o = 0.486l$. a): $Q = 1.0l/min$; b): $Q = 4.0l/min$; c): $Q = 5.0l/min$; d): $Q = 6.0l/min$. The white and orange circles show respectively the anti-bubbles and the water-oil emulsion.	48
Figure 4.2: Zoom of the face view of our water experiment for different air flow rates. The results are obtained with an oil volume $V_o = 0.722l$. a): $Q = 1.0l/min$; b): $Q = 4.0l/min$; c): $Q = 5.0l/min$; d): $Q = 6.0l/min$. The white and orange circles show respectively the anti-bubbles and the water-oil emulsion.	49
Figure 4.3: Zoom of the face view of our water experiment at the same air flow rate. The results are obtained with an oil volume $V_o = 0.486l$. a): after the start of air injection; b): after 2 h of air injection. The orange circles show the water-oil emulsion.	50
Figure 4.4: Zoom of the face view of our water experiment for different air flow rates. The results are obtained with an oil volume of $V_o = 0.486l$. a): $Q = 5.0l/min$; b): $Q = 6.0l/min$. The white and orange circles show respectively the anti-bubbles and the water-oil emulsion.	50
Figure 4.5: Schematic of an a) air bubble; b) oil droplet; c) anti-bubble.	50
Figure 4.6: Instantaneous and average open-eye image at $0.6l/min$, colour code: yellow: eye contour; orange: spout zone.	51
Figure 4.7: Open eye area as a function of the injected air flow rate with standard deviation measured from our experiments obtained with the same configuration but measured on two different trials.	52
Figure 4.8: Open-eye area with standard deviation as a function of air flow rate measured from our experiments for two different injection diameters.	52
Figure 4.9: Open-eye area with standard deviation as a function of air flow rate measured from our experiments for two different oil volumes.	53
Figure 4.10: Front view of the simulation where we display the maximum mesh resolution in one direction at the same air flow rate $Q = 0.6l/min$. The minimum and maximum values are coloured respectively with blue and red colour. a): minimum grid size of $\Delta x = 527 \mu m$ at $t = 8.1s$; b): minimum grid size of $\Delta x = 264 \mu m$ at $t = 8.1s$.	55

Figure 4.11: Front view of the simulation where we display instantaneous air and oil interfaces coloured respectively in green and red obtained at the same air flow rate $Q = 0.6l/min$. a): minimum grid size of $\Delta x = 527 \mu m$ at $t = 8.1s$; b): minimum grid size of $\Delta x = 264 \mu m$ at $t = 8.1s$	55
Figure 4.12: Comparison of data obtained at the same air flow rate of $Q = 0.6l/min$. a): Volume of air injected as a function of time for different maximum mesh resolutions in one direction. The setting point value of the air flow rate is $Q = 10 - 5 m^3/s$; b): Histogram of the number of bubbles as a function of their equivalent diameter at $t = 3s$, the solid lines represent the minimum grid size for the lower mesh resolution.....	55
Figure 4.13: Comparison of the phase-specific Kinetic energy obtained at the same air flow rate of $Q = 0.6l/min$ with different mesh resolutions. a): Kinetic energy of the air phase; b): Kinetic energy of the oil phase; c): Kinetic energy of the water phase	56
Figure 4.14: Front view of the instantaneous air and oil interfaces coloured respectively in green and red obtained with a minimum grid size of $\Delta x = 527 \mu m$. a): $Q = 0.6l/min$ at $t = 8.1s$; b): $Q = 2.5l/min$ at $t = 8.1s$;c): $Q = 5.5l/min$ at $t = 8.1s$	57
Figure 4.15: Top view of the instantaneous oil interface coloured in red obtained with a minimum grid size of $\Delta x = 527 \mu m$. a): $Q = 0.6l/min$ at $t = 8.1s$; b): $Q = 2.5l/min$ at $t = 8.1s$; c): $Q = 5.5l/min$ at $t = 8.1s$	58
Figure 4.16: Comparison of the phase-specific Kinetic energy obtained with a minimum grid size of $\Delta x = 527 \mu m$ but with different air flow rates. a): Kinetic energy of the water phase; b): Kinetic energy of the oil phase.....	58
Figure 4.17: Zoom of the face view with the oil interface represented in red at different instants. The images are obtained from a simulation at an air flow rate of $Q = 4.5l/min$ and with a minimum grid size of $\Delta x = 527 \mu m$. a): $t = 9.6s$; b): $t = 9.7s$; c): $t = 9.8s$; d): $t = 9.9s$	60
Figure 4.18: Histogram of the number of oil droplets as a function of their volume for different air flow rates and at different instants. Results obtained from simulations with a minimum grid size of $\Delta x = 527 \mu m$. a): $t = 3.1s$; b): $t = 9.7s$	60
Figure 4.19: Top view of the numerical simulation at $Q = 0.6lmin$ with a minimum grid size of $\Delta x = 527 \mu m$. (a) Oil interface coloured in red before post-processing. (b) Oil interface after the segmentation step of the post-processing with ImageJ.	61
Figure 4.20: Time evolution of the numerical open eye area for two different trials with a minimum grid size of $\Delta x = 527 \mu m$ and at an air flow rate of $Q = 0.6l/min$	61
Figure 4.21: Time evolution of the numerical open eye area with different maximum mesh resolutions in one direction at an air flow rate of $Q = 0.6l/min$	62
Figure 4.22: Time evolution of the open-eye area for different air flow rates with a minimum grid size of $\Delta x = 527 \mu m$	63
Figure 4.23: Time-averaged air fluid fraction in a slice in the middle of the domain. The results are obtained with a minimum grid size of $\Delta x = 527 \mu m$. Maximum and minimum value are represented respectively with red and blue colours. a): $Q = 0.6l/min$; b): $Q = 5.5l/min$	64
Figure 4.24: Time-averaged oil fluid fraction in a slice in the middle of the domain. The results are obtained with a minimum grid size of $\Delta x = 527 \mu m$. Maximum and minimum value are represented respectively with red and blue colours. a): $Q = 0.6l/min$; b): $Q = 5.5l/min$	64
Figure 4.25: Time-averaged horizontal velocity in a slice in the middle of the domain. The results are obtained with a minimum grid size of $\Delta x = 527 \mu m$. Maximum and minimum value are represented respectively with red and blue colours. a): $Q = 0.6l/min$; b): $Q = 5.5l/min$	65
Figure 4.26: Time-averaged vertical velocity in a slice in the middle of the domain. The results are obtained with a minimum grid size of $\Delta x = 527 \mu m$. Maximum and minimum value are represented respectively with red and blue colours. a): $Q = 0.6l/min$; b): $Q = 5.5l/min$	65

Figure 4.27: Schematic of the numerical domain. The blue horizontal lines represent the horizontal profile lines.....	66
Figure 4.28: Time-averaged vertical velocity along the horizontal position for different air flow rates and with a minimum grid size of $\Delta x = 527 \mu m$. The interpolation is done along different lines at a given vertical position. a): $y = 0.05cm$; b): $y = 0.1cm$; c): $y = 0.15cm$; d): $y = 0.2cm$	67
Figure 4.29: Time-averaged horizontal velocity value along the horizontal position for different air flow rates with a minimum grid size of $\Delta x = 527 \mu m$. The interpolation is done along different lines at a given vertical position. a): $y = 0.05cm$; b): $y = 0.1cm$; c): $y = 0.15cm$; d): $y = 0.2cm$	68
Figure 4.30: Comparison of the experimental and numerical average open-eye area with standard deviation. The simulation results are obtained with a minimum grid size of $\Delta x = 527 \mu m$	69
Figure 4.31: Comparison of the experimental and numerical open-eye area with a minimum grid size of $\Delta x = 527 \mu m$. (a) $Q=0.6l/min$; (b) $Q=1.5l/min$; (c) $Q=2.5l/min$; (d) $Q=3.5l/min$; (e) $Q=4.5l/min$; (f) $Q=5.5l/min$	70
Figure 5.1: Dimensionless open-eye area as a function of the slag Froude number for our experiment and the experiments of Krishnapisharody et al. [22], Yonezawa & Schwerdtfeger [17], Thunman et al. [78] and Wu et al. [19].....	77
Figure 5.2: Dimensionless open-eye area as a function of the slag Froude number for our water experiment and the experiments of Krishnapisharody et al. [22]. The solid line represents the fit with the correlation (2.3) of our results.	77
Figure 5.3: Dimensionless open-eye area as a function of the slag Froude number for liquid metals experiments of Yonezawa & Schwerdtfeger [17], Thunman et al. [78] and Wu et al. [19]. The solid line represents the fit with the correlation (2.3) of the results of [17].	78
Figure 5.4: Dimensionless open-eye area as a function of the ratio of Froude number for our experiment and the experiments of Krishnapisharody et al. [22], Yonezawa & Schwerdtfeger [17], Thunman et al. [78] and Wu et al. [19].	79
Figure 5.5: Dimensionless open-eye area as a function of the ratio of Froude number for our water experiment and the experiment of Krishnapisharody et al. [22]. The solid line represents the fit with the correlation (5.4) of our results.	79
Figure 5.6: Dimensionless open-eye area as a function of the ratio of Froude number for liquid metals experiments of Yonezawa & Schwerdtfeger [17], Thunman et al. [78] and Wu et al. [19]. The solid line represents the fit with the correlation (5.4) of the results of [17].	80
Figure 6.1: Sketch of the evolution of the concentration of a chemical species dissolved in fluid one at an interface between two immiscible fluids. The red line corresponds to the interface between the two fluids and the concentration boundary layer are represented with the discontinuity of the concentration at the interface introduced by the difference of solubility of the chemical species. The scale of the sketch is chosen for visual interpretation.....	84
Figure 6.2: Product of the water mass transfer coefficient with interfacial area as a function of the air flow rate for a water/oil model from the experiment of Kim & Fruehan [32].....	89
Figure 6.3: Capacity coefficient as a function of the air flow rate for a water/cyclohexane model with three different ladle diameters from the experiment of Mietz et al. [97].....	89
Figure 6.4: Capacity coefficient or product of the mass transfer coefficient in steel with interfacial area per volume of steel as a function of the gas flow rate for a liquid steel/slag 2.5 ton ladle from the experiment of Ishida et al. [9].	90
Figure 6.5: Variation of the copper mass transfer coefficient as a function of gas flow rates in a high-temperature copper/ slag cylindrical model from the experiment of Hirasawa et al. [99].....	90
Figure 6.6: Top view of the water experiment with thymol dissolved in water at $Q = 5.0l/min$ with $d_{inj} = 7.9mm$, the red cross is approximatively the sample spot.	92

Figure 6.7: Custom scale established from measurements of solutions of known thymol concentration with error bars representing the measurement error.	93
Figure 6.8: Boundary layer structure. (a) Momentum boundary layers. The average velocity on the interface is UIx . In the oil layer $Re_{o,w}$ is low and so a laminar regime of Nusselt type is considered. The water layer has a high $Re_{o,w}$ so a turbulent regime is considered. (b) Concentration boundary layers. The values on the interface are determined by a partition law at equilibrium with $Co' = PCw'$. For easier reading P ratio is not represented scaled on the figure.	96
Figure 6.9: Recirculation in the oi layer. (a) Global view. (b) Details of the oil layer with a parabolic profile.	101
Figure 7.1: a): Schematic of the domain of computation; b): Interfacial cell C where we have represented the advection flux of chemical species with a white arrow and the diffusion flux with blue arrows.....	111
Figure 7.2: Schematic of a stencil of cells where we have represented the fluid fraction by squares of different colours and the white stripes represent the tracer in each phase. The black cross on the cell faces indicates that the diffusion coefficient is zero at these faces. Colour code: White: air phase; blue: water phase; orange: oil phase. a): Without Dirichlet condition; b): With Dirichlet condition.	112
Figure 7.3: a) Schematic of the configuration of the simulation; b) Minimum and maximum values of the concentration of the VOF tracer $T2$ or the diffusive tracer $G2$ at the beginning of the simulation. The blue colour corresponds to the minimum value and the red colour corresponds to the maximum value.	113
Figure 7.4: Comparison of the minimum and maximum values of the concentration of the tracer at the end of the simulation. The blue colour corresponds to the minimum value and the red colour corresponds to the maximum value. a): VOF tracer $T2$; b): Diffusive tracer $G2$	114
Figure 7.5: Comparison of the quantity of VOF tracer $T2$ and diffusive tracer $G2$ in the water phase as a function of time.	114
Figure 7.6: Comparison of the minimum and maximum values of the concentration of the tracer at the end of the simulation. The blue colour corresponds to the minimum value and the red colour corresponds to the maximum value. a): Advection-diffusion of VOF tracer $T2$; b): Advection of VOF tracer $T2$ and diffusion of $c2$; c): Advection-diffusion of diffusive tracer $G2$	115
Figure 7.7: Zoom on the oil droplet interface (in red). Comparison of the minimum and maximum values of the concentration of the tracer at the end of the simulation. The blue colour corresponds to the minimum value and the red colour corresponds to the maximum value. a): Without Dirichlet condition on the value of $T2$; b): With Dirichlet condition on the value of $T2$	116
Figure 7.8: Comparison of the quantity of VOF tracer $T2$ with different assumptions and diffusive tracer $G2$ in the water phase as a function of time.	116
Figure 7.9: Comparison of the quantity of VOF tracer $T2$ with different assumptions and diffusive tracer $G2$ in the oil phase as a function of time.	116
Figure 7.10: Comparison of the quantity of VOF tracer $T2$ with different assumptions and diffusive tracer $G2$ in the air phase as a function of time.	117
Figure 8.1: Front view picture of the water experiment at $Q = 1.1l/min$. (a) just after the start of air injection; (b) after 3h of gas stirring.	123
Figure 8.2: Front view picture of the water experiment at $Q = 3.0l/min$. (a) just after the start of air injection; (b) after 3h of gas stirring.	123
Figure 8.3: Front view picture of the water experiment at $Q = 5.5l/min$. (a) just after the start of air injection; (b) after 3h of gas stirring.	123
Figure 8.4: Front view picture of the water experiment at $Q = 6.1l/min$. (a) just after the start of air injection; (b) after 3h of gas stirring.	124

Figure 8.5: Front view picture of the water experiment at $Q = 7.5l/min$. (a) just after the start of air injection; (b) after 3h of gas stirring.....	124
Figure 8.6: Comparison of the time evolution of the concentration of thymol in water for different air flow rates and $d_{inj} = 7.9mm$	125
Figure 8.7: Comparison of the time evolution of the capacity coefficient $KwAVw$ for different air flow rates and $d_{inj} = 7.9mm$	126
Figure 8.8 : (a) Time evolution of the concentration of thymol in water with error bars corresponding to the measurement error with $Q = 2.5l/min$ and $d_{inj} = 7.9mm$; (b) Time evolution of the capacity coefficient $KwAVw$ with $Q = 2.5l/min$ and $d_{inj} = 7.9mm$	126
Figure 8.9 : (a) Time evolution of the concentration of thymol in water with error bars corresponding to the measurement error with $Q = 6.5l/min$ and $d_{inj} = 7.9mm$; (b) Time evolution of the capacity coefficient $KwAVw$ with $Q = 6.5l/min$ and $d_{inj} = 7.9mm$	126
Figure 8.10: Comparison of the capacity coefficient $KwAVw$ as a function of the air flow rate for our experiment and the one of Kim & Fruehan [32].	128
Figure 8.11: Comparison of the Sherwood number in the water phase as a function of the modified Froude number between our experiment and the experiment of [32]......	129
Figure 8.12: Sherwood number in the water phase as a function of the modified Froude number for our experiment fitted with different correlations.	130
Figure 8.13: Sherwood number in the water phase as a function of the modified Froude number for the results of Kim & Fruehan [32] fitted with different correlations.....	131
Figure 8.14: Face view of the middle plane with min and max values of concentration of tracer in water coloured at $Q = 0.6l/min$. (a) with a maximum mesh resolution in one direction of 29 cells; (b) with a maximum mesh resolution in one direction of 210 cells.....	132
Figure 8.15: Zoom of the face view of the middle plane displayed on the left side border of the open eye at $Q = 0.6l/min$. (a) min and max values of $D\bar{V}cw$ coloured with cells with a maximum mesh resolution in one direction of 29 cells; (b) min and max values of $D\bar{V}cw$ coloured with cells with a maximum mesh resolution in one direction of 210 cells.	132
Figure 8.16: Bottom view with water-oil interface coloured with min and max values of $D\bar{V}cw$ at $Q = 0.6l/min$. (a) min and max values of $D\bar{V}cw$ coloured with a maximum mesh resolution in one direction of 29 cells; (b) min and max values of $D\bar{V}cw$ coloured with a maximum mesh resolution in one direction of 210 cells.....	133
Figure 8.17: Time evolution of the Sherwood number in the water phase at $Q = 0.6l/min$ with $Scw = 1$ with different maximum mesh resolutions in one direction.	134
Figure 8.18: Numerical results obtained at a fixed air flow rate of $Q = 0.6l/min$. (a) Evolution of the concentration of tracer in the water phase with different mesh resolutions with $Scw = 1$; (b) Evolution of the Sherwood number in the water phase with different mesh resolutions with $Scw = 1$; (c) Evolution of the concentration of tracer in the water phase with $Scw = 10$; (d) Evolution of the Sherwood number in the water with $Scw = 10$; (e) Evolution of the concentration of tracer in the water phase with $Scw = 40$; (f) Evolution of the Sherwood number in the water phase with $Scw = 40$	136
Figure 8.19: Numerical results obtained at a fixed air flow rate of $Q = 0.6l/min$.(a) Evolution of the concentration of tracer in the oil phase with different mesh resolutions with $Sco = 10$; (b) Evolution of the Sherwood number in the oil with $Sco = 10$; (c) Evolution of the concentration of tracer in the oil phase with $Sco = 100$; (d) Evolution of the Sherwood number in the oil phase with $Sco = 100$; (e) Evolution of the concentration of tracer in the oil phase with different mesh resolutions with $Sco = 400$; (f) Evolution of the Sherwood number in the oil phase with $Sco = 400$	137
Figure 8.20: Evolution of the Sherwood number in the water phase with different mesh resolutions at a fixed air flow rate of $Q = 5.5l/min$. (a) $Scw = 1$; (b) $Scw = 4$; (c) $Scw = 10$; (d) $Scw = 40$	138

Figure 8.21: Evolution of the Sherwood number in the oil phase with different mesh resolutions at a fixed air flow rate of $Q = 5.5l/min$. (a) $Sc_o = 10$; (b) $Sc_o = 40$; (c) $Sc_o = 100$; (d) $Sc_o = 400$. ..	139
Figure 8.22: Comparison of the Sherwood number in water with standard deviation as a function of the Schmidt number in water with different maximum mesh resolutions at a fixed air flow rate of $0.6l/min$	140
Figure 8.23: Comparison of the Sherwood number in water as a function of the modified Froude number with standard deviation. (a) results obtained with a fixed maximum number of cells in one direction of 210; (b) results obtained with a fixed maximum number of cells in one direction of 211.	140
Figure 8.24: Fit of the numerical Sherwood number in water with standard deviation as a function of the Schmidt number at an air flow rate $Q = 0.6 l/min$ and for different maximum numbers of cells in one direction. The black cross represents our experimental result.	142
Figure 8.25: Fit of the numerical Sherwood number in water with standard deviation as a function of the Schmidt number at an air flow rate $Q = 5.5 l/min$ and for different maximum numbers of cells in one direction. The black cross represents our experimental result.	142
Figure 8.26: Fit of the numerical Sherwood number in water as a function of the Schmidt number and the modified Froude number. The black cross represents our experimental results.....	143
Figure 8.27: Fit of our experimental results of the Sherwood number in water as a function of the modified Froude number with the correlation applied to our numerical results.....	143
Figure 9.1: Comparison of the capacity coefficient in the steel equivalent phase as a function of the air flow rate at operating condition per mass unit of the steel equivalent phase for our experiment and the experiment of Kim & Fruehan [32], Lachmund et al. [8], Ishida et al. [9], Hirasawa et al. [99]. ..	148
Figure 9.2: Comparison of the Sherwood number in the steel equivalent phase as a function of the modified Froude number for our experiment and the experiment of Kim & Fruehan [32], Lachmund et al. [8], Ishida et al. [9], Hirasawa et al. [99].....	149
Figure 9.3: Fit of the critical modified Froude number with the correlation (9.4) for our experiment and the experiment of Kim et al. [40], Lachmund et al. [8], Ishida et al. [9], Hirasawa et al. [99].	151
Figure 9.4: Fit of the critical modified Froude number with the correlation (9.4) (9.5) for our experiment and the experiment of Kim et al. [40], Lachmund et al. [8], Ishida et al. [9], Hirasawa et al. [99].	151
Figure 9.5: Sherwood number in the steel equivalent phase as a function of the modified Froude number for the results of Ishida et al. [9] fitted with correlations (9.11) and (9.12).	153
Figure 9.6: Sherwood number in the steel equivalent phase as a function of the modified Froude number for the results of Hirasawa et al. [99] fitted with correlations (9.11) and (9.12).	153
Figure 9.7: Sherwood number in the steel equivalent phase as a function of the modified Froude number for the results of Ishida et al. [9] fitted with correlation (9.15) corresponding to a Nusselt profile in the slag phase established from our water experiment.....	154
Figure 9.8: Sherwood number in the steel equivalent phase as a function of the modified Froude number for the results of Hirasawa et al. [99] fitted with correlation (9.15) corresponding to a Nusselt profile in the slag phase established from our water experiment.....	155
Figure 9.9: Sherwood number in the steel phase as a function of the modified Froude number for the results of Lachmund et al. [8] fitted with correlations (9.11) and (9.12).....	156
Figure 9.10: Sherwood number in the steel phase as a function of the modified Froude number for the results of Lachmund et al. [8] fitted with correlation (9.15) corresponding to a Nusselt profile in the slag phase established from our water experiment.	156
Figure 11.1: Time evolution of the Sherwood number in water with different mesh resolution at a fixed air flow rate of $Q = 2.5l/min$. (a) $Sc_w = 1$; (b) $Sc_w = 4$; (c) $Sc_w = 10$; (d) $Sc_w = 40$	165
Figure 11.2: Time evolution of the Sherwood number in oil with different mesh resolution at a fixed air flow rate of $Q = 2.5l/min$. (a) $Sc_o = 10$; (b) $Sc_o = 40$; (c) $Sc_o = 100$; (d) $Sc_o = 400$	166

Figure 11.3: Time evolution of the Sherwood number in water with different mesh resolution at a fixed air flow rate of $Q = 3.5\text{ l/min}$. (a) $Sc_w = 1$; (b) $Sc_w = 4$; (c) $Sc_w = 10$; (d) $Sc_w = 40$	167
Figure 11.4: Time evolution of the Sherwood number in oil with different mesh resolution at a fixed air flow rate of $Q = 3.5\text{ l/min}$. (a) $Sc_o = 10$; (b) $Sc_o = 40$; (c) $Sc_o = 100$; (d) $Sc_o = 400$	168
Figure 11.5: Time evolution of the Sherwood number in water with different mesh resolution at a fixed air flow rate of $Q = 4.5\text{ l/min}$. (a) $Sc_w = 1$; (b) $Sc_w = 4$; (c) $Sc_w = 10$; (d) $Sc_w = 40$	169
Figure 11.6: Time evolution of the Sherwood number in oil with different mesh resolution at a fixed air flow rate of $Q = 4.5\text{ l/min}$. (a) $Sc_o = 10$; (b) $Sc_o = 40$; (c) $Sc_o = 100$; (d) $Sc_o = 400$	170
Figure 11.7: Fit of the numerical Sherwood number in water with standard deviation in function of the Schmidt number at an air flow rate $Q = 2.5\text{ l/min}$ and for different maximum number of cells in one direction. The black cross represents our experimental result.....	171
Figure 11.8: Fit of the numerical Sherwood number in water with standard deviation in function of the Schmidt number at an air flow rate $Q = 3.5\text{ l/min}$ and for different maximum number of cells in one direction. The black cross represents our experimental result.....	171
Figure 11.9: Fit of the numerical Sherwood number in water with standard deviation in function of the Schmidt number at an air flow rate $Q = 4.5\text{ l/min}$ and for different maximum number of cells in one direction. The black cross represents our experimental result.....	172

List of Tables

Table 2.1: Geometrical dimensions of an industrial ladle from [8].....	11
Table 2.2 Physical properties of the fluids at 1600 °C in the industrial configuration from [8].....	11
Table 2.3: Order of magnitude of the dimensionless number for the liquid steel phase in the industrial case computed from data in [8].	11
Table 2.4: Main geometrical parameters of our experimental model and the one of [32].....	13
Table 2.5: Physical properties of fluids used in our water experiment and the one for the oil mixture used in [32].	13
Table 2.6: Order of magnitude of the dimensionless number for our experimental model and the one of [32].	13
Table 2.7: Values of the absolute incertitude of the parameters necessary to compute the mass transfer coefficient.....	15
Table 3.1: Physical parameters of the fluids used in the simulation.....	38
Table 3.2: Main geometrical parameters of the numerical simulation.	43
Table 3.3: Physical properties of the fluids used in the numerical simulation.	43
Table 4.1: Measurement of the oil physical properties used in our experiment before and after 3h00 of air agitation.	46
Table 4.2: Main geometrical parameters of our experiment for the reference case.	46
Table 5.1: Main physical and geometrical properties of the steel and the slag equivalent phase for our experiment and the experiment of [17, 19, 22, 78].	74
Table 5.2: Main dimensionless characteristic of the steel and the slag equivalent phase for our experiment and the experiment of [17, 22].	74
Table 6.1: Main chemical properties of Thymol at ambient temperature according to PubChem, [100] [101].	92
Table 6.2: Parameters of the mass transfer of the thymol between water and oil in our model where the diffusion coefficient of thymol in the water phase is taken from Reid et al.[102] and for the oil phase is computed using (6.21).	92
Table 6.3: Parameters of the mass transfer of the sulphur between liquid steel and slag in an industrial ladle where the diffusion coefficients are taken from Gaye [103].	92
Table 6.4: Values of the absolute incertitude of the parameters necessary to compute the mass transfer coefficient.....	93
Table 6.5: Main dimensionless physical properties of the steel equivalent phase and the slag equivalent phase for our experiment and the experiments of [8, 32]. The partition coefficient ratio has been considered as a constant value corresponding to the case of thymol between water and oil as it is not given nor measured in most of the industrial case.	96
Table 6.6: Main global and interfacial velocity characterization of the steel equivalent phase and the slag equivalent phase established from several correlations from the value of the minimum gas flow rate for our experiment and numerical simulation and the experiments of [8, 32].	104
Table 6.7: Main dimensionless numbers for our experiment and the experiments of [8, 32].	104
Table 6.8: Mass transfer properties of the steel and slag equivalent phase in the case of a Nusselt profile in the slag equivalent phase for our experiment and the experiments of [8, 32].	105
Table 6.9: Mass transfer properties of a slag equivalent phase droplet for our experiment and the experiments of [8, 32].	106
Table 7.1: Main parameters necessary to compute the mass transfer coefficient with (7.12) considering a fixed air flow rate $Q = 0.6l/min$ for the experimental and numerical case.....	119

Table 8.1: Measurement of oil physical properties after 3h00 of air agitation with and without thymol dissolved in the water.	122
Table 8.2: Reproducibility test of all the process involved in mass transfer measurement at two distinct gas flow rate value.	127
Table 8.3: Main physical properties and quantities of our water experiment and the experiment of [32].	127
Table 9.1: Main physical properties and quantities of the steel equivalent phase and the slag equivalent phase for our experiment and the experiments of [8, 9, 32, 99].....	147
Table 9.2: Main dimensionless physical properties of the steel equivalent phase and the slag equivalent phase for our experiment and the experiments of [8, 9, 32, 99].....	147

1 INTRODUCTION

Multiphase flows are very common in our surrounding environment either in a natural or industrial context, ranging from the fall of a rain droplet to numerous processes in the metallurgical industry (Guthrie [1]). In these phenomena, the fluids can be seen as the carrier of chemical species or heat between fluids. The phenomena of advection and diffusion of a chemical species can be named as mass transfer. In nature, the mass transfer of carbon dioxide at the ocean interface through the air bubbles and water droplets is an important phenomenon in the global Carbon dioxide exchange (Siegenthaler & Sarmiento [2], Deike *et al.* [3]). In addition to multiphase flow interaction and mass transfer, a chemical reaction can occur at the interface between the fluids. This chemical reaction between fluids can be broken down into three stages: transport by advection of reactive species toward the interface, transport by molecular diffusion through the concentration boundary layer, and finally the chemical reaction at the interface. The global kinetics of the chemical reaction is governed by the kinetics of the slowest stage.

In the steel industry mass transfer can be found in numerous steps of the two different steel production routes. The first one is presented in Figure 1.1 showing a schematic of the overall blast furnace steelmaking process from the raw material on the left to the final product before the continuous casting operation on the right. A schematic of the second process used to produce steel is shown in Figure 1.2. In this process, an electric arc furnace is used to melt recycled steel, and no blast furnace is used anymore. At the end of these two processes, the obtained steel can be differentiated from cast iron by its carbon content which should not overcome a maximum value of 2% by weight. During the process of steelmaking, an important amount of slag is generated. The slag is a by-product of the process and is usually a mixture of metal oxides and silicon dioxide. It can be used in various ways during the different steps of the process of steelmaking. During the secondary metallurgy or refining step, it can be used to promote chemical reactions with the liquid steel to adjust the liquid steel composition or to minimize re-oxidation of the liquid steel (Szekely *et al.* [4]).



Figure 1.1: Overview of the steelmaking process using a blast furnace from the worldsteel association [5].

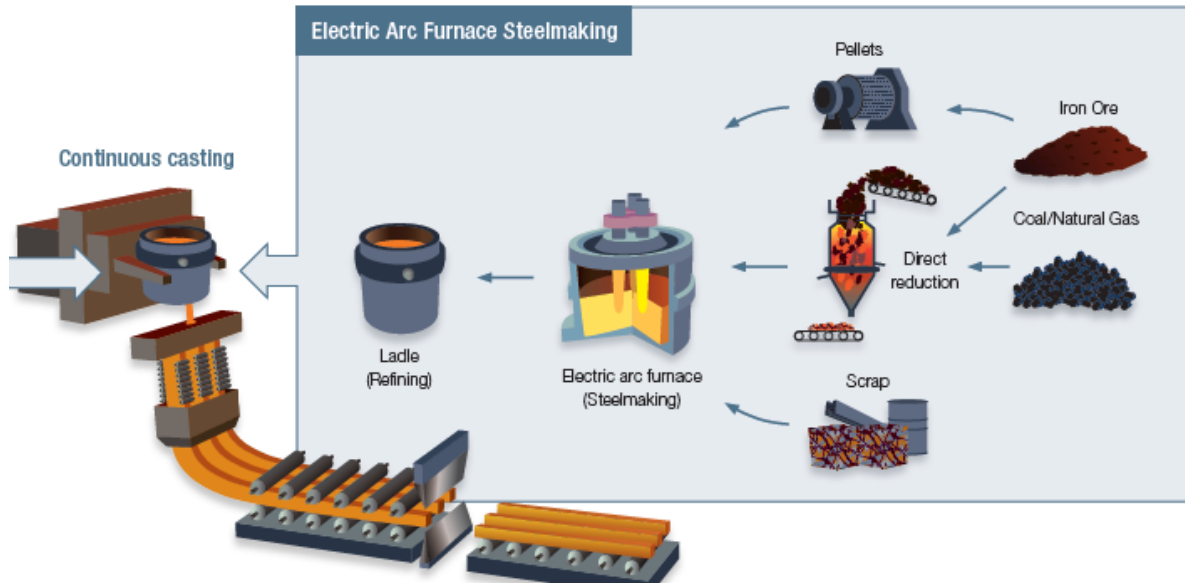


Figure 1.2: Overview of the steelmaking process using an electric arc furnace from [5].

During the refining step, the adjustment of the liquid steel composition at high temperature is done in a cylindrical shape ladle and gas injection is generally used to promote stirring and homogenization of the liquid steel. Then, we are in presence of a multiphase flow (Richardson [6]) and at the liquid-steel-slag interfaces several chemical reactions are occurring (Riboud & Vasse, [7]). In this dissertation, we are particularly interested in the desulfurization of liquid steel by chemical reaction with slag under argon gas bubbling in a ladle (Lachmund *et al.* [8], Ishida *et al.* [9]). The aim is to lower the sulphur concentration in the liquid steel and limit the argon gas stirring time to obtain better mechanical properties for the steel. Because of the high temperature considered in the process, it is generally accepted that the chemical reaction at the interface is not the limiting step. Then, the steps governing the global kinetics of the chemical reaction are the convective and diffusive transport or mass transfer of reactive species. Therefore, to improve the characterization of the global kinetics of the chemical reactions in the refining step, we will focus in this study on the characterization of the mass transfer of reactive species between the liquid steel and slag phase. Ultimately, the obtained mass transfer characterization could be used as input data of a thermodynamic model not considered in this study to predict the evolution of the composition of the different phases of the process.

Due to the complex nature of the industrial process involving multiple phases, multiple physical phenomena and a large variety of time and length scales, it is important to establish representative reduced size experiments of the process. Indeed, it is easier to characterize the various phenomena involved in the process with a reduced scale experiment. It is important to stress that for a large steelmaking ladle, one cannot have simultaneously a similarity in more than one dimensionless number. This is a recipe for failure as there are many more numbers than just the Reynolds number: the numbers involving diffusion (Péclet), gravity (Froude) or surface tension (Weber) are all essential and differ between experimental setups. Thus, only a large-scale trial-and-error approach would remain for development in the absence of global models or simulations of the entire process. This makes the numerical simulation critically important to establish and improve global models of the process.

The existence of small scales such as chemical diffusion boundary layers and small regions where capillarity is of great influence such as near dynamic contact lines limits the progress of numerical simulation of the process. The existence of tiny scales is a formidable barrier to Direct Numerical Simulation (DNS). It operates in discretized space with grids or meshes of typical size Δx .

If ε is the size of the small scales, and L the size of the large scales, then $\Delta x < \varepsilon$ is required and the typical number of grid points is

$$N \sim \left(\frac{L}{\Delta x}\right)^d, \quad (1.1)$$

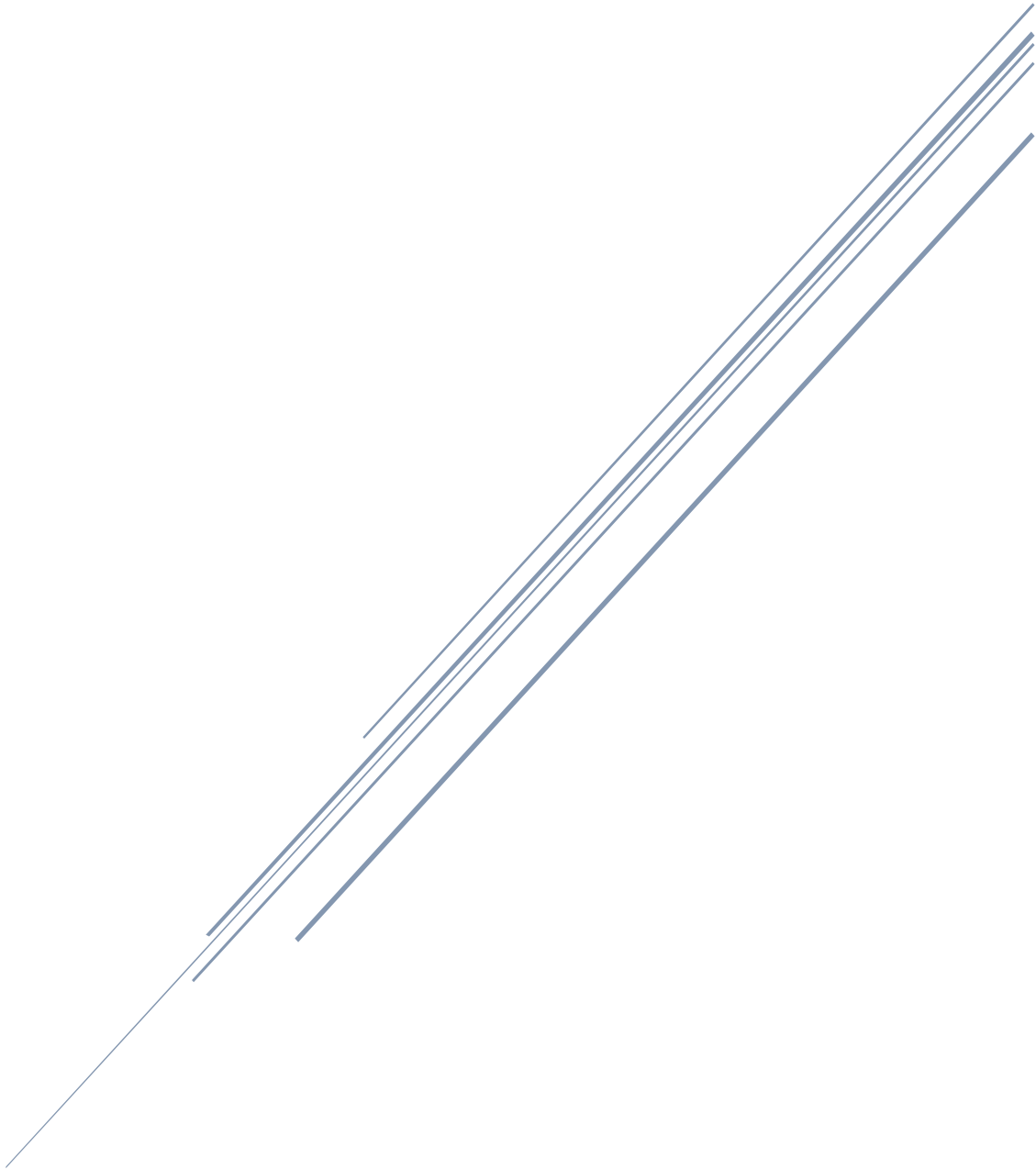
where d is the dimension of the simulation. To some degree this can be mitigated by relatively new, efficient numerical methods such as Lattice Boltzmann, Phase Field, Front Tracking, Level Sets or Volume of Fluid. All of these methods have their successes and all are subject to the constraint in equation (1.1) in terms of the computational work needed (Tryggvason *et al.* [10], Deising *et al.* [11], Gibou *et al.* [12], Karlin *et al.* [13], van der Sman & Van der Graaf [14]). Indeed, we explain below how it is possible to use the asymptotic of thin boundary layers to lower the cost of computation.

To illustrate the difficulty caused by thin boundary layers we consider the example of bubbly flows with chemical diffusion. In that case, thin diffusion boundary layers arise because the Péclet number comparing advection and diffusion, $Pe = Ud/D$ is high, where U is a characteristic scale for the relative velocity of the droplet and the carrier fluid, d is the bubble diameter and D is the diffusivity. The Péclet number can be rewritten $Pe = ReSc$ where the Reynolds number is $Re = Ud/\nu$, $Sc = \nu/D$ with usual notations. Since there are two fluids in this example, boundary layers can arise inside or outside the bubble. It is relatively straightforward to write an equation for the developing boundary layer that leads to the estimate $\delta_c \sim dPe^{-1/2}$ for its thickness. For the fluid flow obeying the Navier-Stokes equation, a similar estimate yields a viscous, momentum boundary layer thickness $\delta_v \sim dRe^{-1/2}$. For $Sc \gg 1$, typical of many systems, we have $\delta_c/\delta_v \sim Sc^{-1/2} \ll 1$. In other words, even when one has enough computer power to resolve the purely fluid dynamics problem of a rising bubble, resolving the mass transfer problem is much harder. Computational grids must not only resolve the small viscous layer thickness δ_v but also the chemical layer thickness δ_c .

In this dissertation, we will then try to characterize the mass transfer of the industrial process with a reduced scale experiment and its DNS. We will limit ourselves to consider only the effect of the flow on the mass transfer of chemical species. To be able to do DNS of this complex process we will use a dynamic adaptive mesh getting refined only on the region where the error on the fluid fraction or the velocity is above specific thresholds. These adaptive methods are implemented in the Basilisk Free Software library (Popinet [15], [16]). Furthermore, the computationally intensive three-dimensional simulations will require to take advantage of the parallelisation implemented in Basilisk to run on large numbers of cores on HPC at low Schmidt numbers $Sc_{m,num} \in [1,40]$. Then, we will extrapolate the results to the experimental Schmidt number $Sc_{m,exp} \sim 1000$ using a boundary layer theory.

We divide this study into two parts, the first part will be addressing the global characterization of the flow behaviour using experimental and numerical methods. The second part will tackle the mass transfer characterization of the process through experimental and numerical experiments. In each part, we will follow the same approach by first describing the physical model, then presenting the numerical model used before presenting both the experimental and numerical results obtained. Finally, we will try to compare our results with results from the literature to check the validity of our scale model results in the case of an industrial ladle.

PART I - HYDRODYNAMIC CHARACTERIZATION



2 PHYSICAL MODEL- HYDRODYNAMIC CHARACTERIZATION

The industrial process that we want to characterize involves multiple physical interactions between the fluids. In addition to the stirring generated by the gas injection, possible effects of the temperature and ferro static pressure at the operating conditions are to be considered. In some regions of the ladle, phase change of the slag layer can occur due to the possible important variations of the flow and temperature condition across the ladle. In this part, we will focus on the effect of the fluid flow induced by the gas injection on the slag layer. The plume region beyond the penetration distance is bounded by conical and parabolic plume profiles. At the free surface, the deformed zone where the gas bubbles reach the free surface is called the spout region and the slag-free region is called the “open-eye” (cf. Figure 2.1-(a)-(b)). In this zone, liquid steel interacts directly with ambient gas. On the edge of the open eye the flow direction is in the opposite direction than in the plume centre and generate shearing of the slag layer as can be seen in Figure 2.1-(b). When the shearing of the slag layer is high enough it is in this particular zone that formation of slag droplets can be observed.

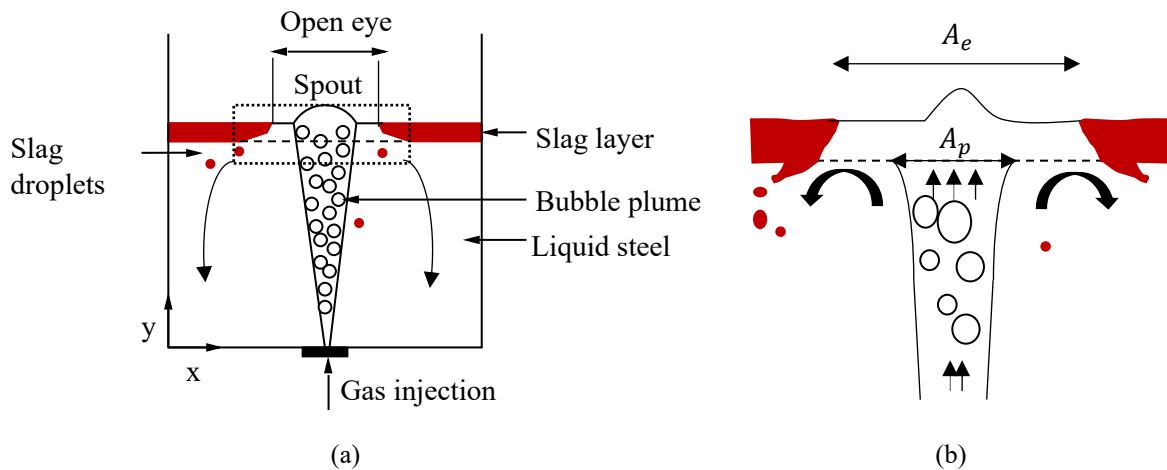


Figure 2.1: Schematic of a metallurgical gas stirred ladle. a): Global view; b) Zoom on the region delimited by a rectangle in the global view.

2.1 LITERATURE REVIEW

In the liquid-metal experiments and especially in the industrial ladle the high temperatures and possible important static pressure effects make experiments complicated and costly. Furthermore, the liquid metals are not transparent and so X-ray methods must be used to be able to measure some flow characteristics. This explains why fewer studies use liquid metals as opposed to water or similar fluids. Because the entire process is still not fully understood with a global theory working both with reduce scale and industrial ladles it is important to characterize its main parameters with reduced-scale models using various fluids. In this part of the dissertation, our main interest is the hydrodynamic characterization of the flow effect on the slag layer and so we will focus on the open eye and slag droplet formation. Indeed, these two phenomena are suspected to act directly on the mass transfer between the liquid steel and slag. In the following, for clarity, we will use the index m for either metal or water and the index s for either slag or the equivalent phase.

2.1.1 Open eye characterization

Open eye characterization is a straightforward way of characterizing the influence of the gas injection on the slag layer. We can see by comparing Figure 2.2-(a) and Figure 2.2-(b) why we have to be cautious when extrapolating the results obtained from water experiment to liquid metal experiments especially for the industrial ladle case. In the water experiment case, the oil layer is not deformed apart from the open eye region (cf. Figure 2.2-(a)). This is not the case for the industrial ladle where we can see that the slag is at a solid-state in some regions (cf. Figure 2.2-(b)).

We will start by mentioning the study of the industrial ladle case in the literature, in Yonezawa & Schwerdtfeger [17] the authors established from their measurement with a mercury-oil experiment and few measurements with an industrial ladle of 350 ton a first try of correlation to predict the open eye area. In the study of Valentin *et al.* [18] the authors measured the open eye area with automated infrared camera measured in the industrial case. Then Wu *et al.* [19] tried to use correlations established with water experiments for the previous industrial results but the authors obtained only a limited agreement. From water experiments, Subagyo *et al.* [20] revised the correlation of [17] by accounting for the conic shape of the bubble plume to give this correlation

$$\frac{A_e}{(h_m + h_s)^2} = a + b \left(\frac{Q}{gh_s^5} \right)^c, \quad (2.1)$$

where a and b are numerical constants, A_e is the open eye area, h_m is the height of the bath of liquid steel equivalent phase, h_s is the height of the bath of slag equivalent phase and Q is the gas flow rate. Then, Iguchi *et al.* [21] established empirical correlations considering the effect of the physical properties of gas and liquids on the open eye area.

Krishnapisharody & Irons [22] measured the slag eye area for a different couple of fluids as a function of the gas flow rate, bath depth and thickness of the slag layer. They used a mechanical model based on the principles of momentum conservation to establish a correlation when $A_e/A_p > 1$, where A_p is the cross sectional bubble plume area at a height equal to h_m and can be computed according to Krishnapisharody & Irons [23] with

$$A_p = 1.41h_m^2 \left(\frac{Q}{gh_s^5} \right)^{0.4}, \quad (2.2)$$

In [22] the authors established the following correlation for the dimensionless open eye area of the general form

$$\frac{A_e}{h_m^2} = \alpha + \beta \left(\frac{\rho_m}{\Delta\rho} \right)^{1/2} (Fr_s)^{1/2}, \quad (2.3)$$

where α and β are numerical constants, ρ_m is the density of the liquid steel equivalent phase and $\Delta\rho = \rho_m - \rho_s$ is the density difference between the liquid steel and slag equivalent phase, U_p is the velocity of the plume and Fr_s is the Froude number in the slag layer defined by

$$Fr_s = \frac{U_p^2}{gh_s} \quad (2.4)$$

Because the plume velocity is not an operating variable, it has to be computed. In [22] the authors computed it from the gas flow rate value with the correlation of Castello-Branco & Schwerdtfeger [24]

$$U_p = 17.4Q^{0.244} d_{inj}^{-0.0288} \left(\frac{\rho_g}{\rho}\right)^{0.0218} h_m^{-0.08}. \quad (2.5)$$

where U_p is expressed in cm/s , Q is the gas flow rate at the Standard Temperature and Pressure conditions expressed in cm^3/s , h_m and d_{inj} are expressed in cm . Later, Peranandhanthan & Mazumdar [25] proposed a revised version of the correlation (2.3) expected to give better results for the industrial ladle case. The authors considered the effect of the Reynolds number on the open eye area giving this correlation

$$\frac{A_e}{h_m^2} = a_2 \left(\frac{\rho_m}{\Delta\rho}\right)^{b_2} (Fr_s)^{c_2} \left(\frac{1}{Re_s}\right)^{d_2}, \quad (2.6)$$

where Re_s is the Reynolds number in the slag layer given by

$$Re_s = \frac{h_s U_p}{\nu_s} \quad (2.7)$$

As the correlation (2.3) was built for the case of a thin slag layer, in Krishnapisharody & Irons [23] the authors established another correlation considering this time the case of a thick slag layer when $A_e/A_p < 1$. More recently, Liu *et al.* [26] have done some measurement of the open eye area with a water experiment with one or two porous plugs. The authors reported an increase in the open eye area when the angle between the two porous plugs is increased.

In order to summarize the study in the literature, we can say that to characterize the open eye phenomena in the slag layer the following parameters are to be considered:

- Gas flow rate;
- Height of the bath of liquid-steel-equivalent phase;
- Thickness of the slag-equivalent phase layer;
- Viscosity and density of the slag-equivalent phase layer.

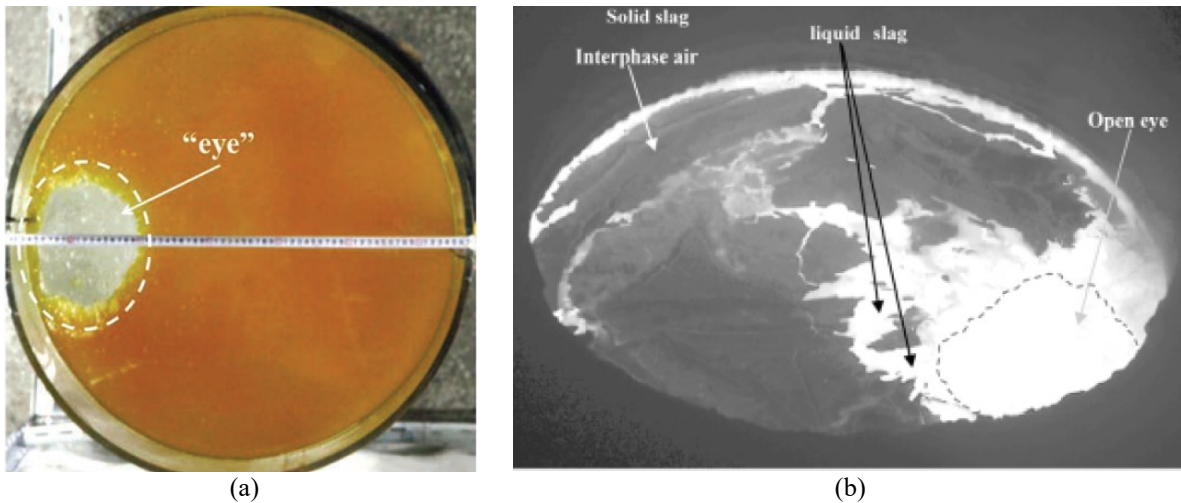


Figure 2.2: Top view of the ladle with the open eye of the top phase delimited for two experiments. a): water/oil model experiments obtained at $Q = 130l/h$ from [26]; b): industrial ladle (170-t) experiments obtained at $Q = 15000l/h$ at Standard Temperature and Pressure conditions from [18].

2.1.2 Slag detachment and entrainment phenomena

At a certain value of steel/slag interfacial velocity, the formation of slag ligaments can occur. Then at a greater or equal steel/slag interfacial velocity, fragmentation of slag ligaments into slag droplets in liquid steel can be observed. This phenomenon can be seen in Figure 2.3 where we can see oil droplets in the water phase in the case of a gas stirred ladle covered with thick oil layer from the experiments of Lin & Guthrie [27]. The phenomena of slag detachment and entrainment at a critical gas flow rate have been reproduced with several experimental setups of water experiments model: with a submerged hose (Feldbauer & Cramb [28]), a submerged cylinder (Hagemann *et al.* [29]), a submerged ramp/weir (Hagemann [30], Savolainen *et al.* [31]) or by gas injection observed in the measurements of Kim & Fruehan [32], Xiao *et al.* [33], Mietz *et al.* [34], Wei & Oeters [35] and Iguchi *et al.* [36], [27]. For the industrial ladle case, Lachmund *et al.* [8] tried to characterize the slag droplet formation by immersing a steel slab with drilled holes into the ladle during gas injection. The solidified steel samples were then analysed with X-ray methods to identify emulsified slag droplets. The authors reported a mean diameter of emulsified droplets of $1mm$.

We detail here the influence of the physical properties of the slag layer in the phenomena of slag droplets formation:

- Influence of slag viscosity on fragmentation:

In reference [32] the authors found that a decrease in oil viscosity does not change the oil droplets formation in the low gas flow rate regime as can. But in the high gas flow rate regime, more droplets are formed for the oil with low viscosity. Calabrese *et al.* [37, 38] and Wang & Calabrese [39] reported from experimental measurements with agitation generated by a Rushton turbine that the equilibrium size of the largest oil droplets and the mean diameter of oil droplets increases when oil viscosity increases.

- Slag thickness influence on fragmentation:

As the oil layer becomes thicker, the rate of formation of oil droplets increases due to the formation of more active and stronger circulation inside the oil layer and increase of interfacial area by giving a smaller diameter for the plume eye. However, [32] reported that the critical gas flow rate for entraining the oil droplets in the water does not change much with oil layer thickness.

-Slag-steel interfacial tension influence on fragmentation:

Interfacial tension is found to be an important parameter for the detachment and entrainment of oil, the greater the interfacial tension is the higher is the critical gas flow rate for oil detachment and entrainment. In reference [39], the authors reported from their measurement that at constant conditions of agitation the relative influence of interfacial tension decreases as the oil viscosity increases.

Now, we focus on studies where the authors tried to characterize the slag droplets detachment with a criterion based on either critical interfacial speed or gas flow rate. In reference [34], [35], the authors proposes from a force balance analysis applied to water experiment that the entrainment should occur for a critical entrainment speed given by

$$u_{i,crit} = \left(\frac{8}{\rho_s}\right)^{1/2} \left[\frac{2}{3} g \sigma_{ms} \Delta \rho \cos(\varphi)\right]^{1/4}, \quad (2.8)$$

where σ_{ms} is the interfacial tension between water and oil and φ is the angle of the liquid interface relative to the direction of gravity.

In reference [33], the authors established with a water-oil model a criterion based on a critical modified Weber number given by

$$We_c = \frac{u_{i,crit}^2 \rho_s}{\sqrt{g \sigma_{ms} \Delta \rho}} \quad (2.9)$$

The authors predict that when $We_c \geq 12.3$ detachment of oil droplets should occur.

In Kim *et al.* [40] the authors made a dimensional analysis with their water experiment using different combination of fluids to find the critical gas flow rate for upper layer entrainment. From their analysis, the authors obtained a relation for the critical gas flow rate following this expression

$$\frac{Q_{crit}}{(gh_m^5)^{1/2}} = c_2 \left(\frac{\sigma_{ms}}{\rho_s g h_m^2} \right)^{a_2} \left(\frac{\Delta \rho}{\rho_s} \right)^{b_2}, \quad (2.10)$$

where a_2 , b_2 and c_2 are numerical constants determined from the experiments. In order to summarize the study in the literature, we can say that to characterize the phenomena of slag entrainment in the open eye region the following parameters need to be considered:

- Critical flow rate for detachment and or entrainment of slag droplet;
- Entrainment rate of slag droplet;
- Residence time of slag droplet in the steel phase;
- Average slag droplet diameter.

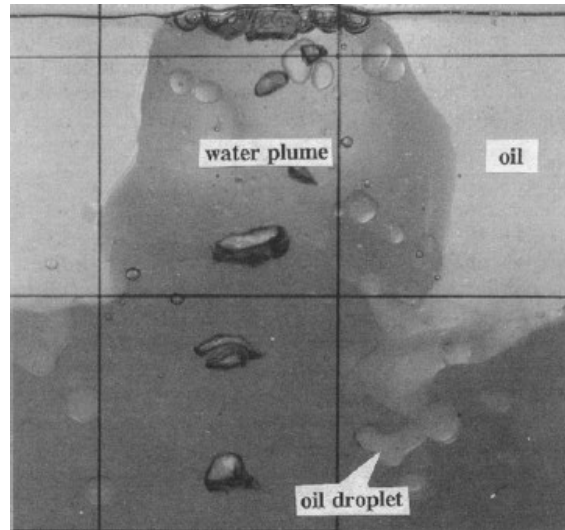


Figure 2.3: Example of a thick slag layer fragmentation into droplets due to gas injection for a gas flow rate $Q = 0.4$ l/min from the water experiment of [27].

2.2 EXPERIMENTAL MODEL

In this study to simplify the problem, we do not consider the influence of the temperature on physical and chemical properties of fluids. So, we will consider that the process is operated at constant temperature and that no phase change is occurring.

2.2.1 Geometrical scaling

In this study, we are interested in reproducing the flow behaviour of an industrial ladle and will consider the data in [8] for 180 tons ladle which is the typical capacity used in an industrial plant. Because in this part we focus only on the hydrodynamic aspect of the process, we do not consider the molar concentration of a chemical species nor diffusion coefficient in the dimensional analysis. We neglect the influence of the viscosity and density of the gas on the process due to the high density and viscosity ratio between steel and argon gas. From the process variables, we can establish with Buckingham π theorem eight non-dimensional parameters.

$$f\left(\frac{\mu_m}{\rho_m UL}, \frac{\mu_s}{\rho_s UL}, \frac{Lg}{U^2}, \frac{\sigma_{gm}}{\rho_m UL^2}, \frac{\sigma_{ms}}{\rho_m UL^2}, \frac{\rho_s}{\rho_m}, \frac{h_m}{L}, \frac{h_s}{L}\right) = 0,$$

where L is a characteristic length, U is a characteristic speed, h_m is the steel height and h_s is the slag height. From the non-dimensional parameters, we can recognize the expression of the Reynolds, Froude and Weber numbers.

$$f(Re_m^{-1}, Re_s^{-1}, Fr^{-2}, We_m^{-1}, We_s^{-1}, r^{-1}, H_m, H_s) = 0, \quad (2.11)$$

where $We_m = \rho_m U^2 L / \sigma_{ms}$ is the Weber number of the steel equivalent phase, $Re_m = \rho_m UL / \mu_m$ is the Reynolds number of the steel equivalent phase, $r = \rho_m / \rho_s$ is the density ratio, $H_m = h_m / L$ is the ratio of the height of the bath of liquid steel equivalent phase and $H_s = h_s / L$ is the ratio of the height of the slag equivalent phase. In the following, we consider as characteristic length the horizontal size of the ladle L_x . If we assume that within the gas flow rate range considered in the industrial case, we are in presence of a bubble plume, the vertical rising velocity due to the bubble plume in the liquid steel can be approximated and as a characteristic velocity scale we can write

$$U = (g^2 Q)^{1/5} \quad (2.12)$$

Further details about this approximation will be given in 2.3.2 equation (2.32). We consider this velocity as the characteristic velocity. Now, considering the expression of (2.12) we can rewrite the Froude number as a function of the gas flow rate to obtain the expression of the modified Froude number N

$$\sqrt{Fr} = \frac{U}{\sqrt{gh_m}},$$

$$N = \left(\frac{Q}{g^{1/2} h_m^{5/2}}\right)^{1/5}. \quad (2.13)$$

We consider the same values for the properties of the fluids and the size of the ladle as in [8]. We gather the parameters of the size in Table 2.1 and the physical properties of the fluids in Table 2.2. and then compute the corresponding dimensionless parameters in Table 2.3. It leads to high Reynolds and Weber numbers meaning that the inertial force is much more important than the viscous one. Also, the surface tension effect can be neglected compared to the fluid inertia in the industrial ladle.

Characteristic parameter	Industrial ladle case
h_m (m)	3.2
h_s (m)	0.08
L_x (m)	3.3
d_{inj} (m)	0.13
Q (m^3s^{-1} (Standard Temperature and Pressure))	$4.2 \cdot 10^{-3} - 4.3 \cdot 10^{-2}$

Table 2.1: Geometrical dimensions of an industrial ladle from [8].

Industrial fluid properties at 1600°C	Argon	Liquid steel	slag
ρ ($kg \cdot m^{-3}$)	0.26	6800	2800
μ (Pa.s)	$7.3 \cdot 10^{-5}$	$5.4 \cdot 10^{-3}$	0.1
σ_{gm} ($N \cdot m^{-1}$)	1.5		
σ_{ms} ($N \cdot m^{-1}$)		1.2	
σ_{gs} ($N \cdot m^{-1}$)			0.5

Table 2.2 Physical properties of the fluids at 1600 °C in the industrial configuration from [8].

Dimensionless number	Expression	Liquid steel
Re_m	$\rho_m U L_x / 4 \mu_m$	10^6
N	$[Q / (g^{1/2} h_m^{5/2})]^{1/5}$	$1.6 \cdot 10^{-1} - 2.9 \cdot 10^{-1}$
We_m	$\rho_m U^2 L_x / 4 \sigma_{ms}$	10^4
r	ρ_m / ρ_s	2.43
H_m	h_m / L_x	0.97
H_s	h_s / L	0.024

Table 2.3: Order of magnitude of the dimensionless number for the liquid steel phase in the industrial case computed from data in [8].

To determine the corresponding value of the gas flow rate for a scaled model of the industrial ladle we could use a similitude based either on the Reynolds, Weber or Froude number. In the case of the gas stirred ladle the turbulent flow behaviour is governed by the large scales of the turbulence. The operating variables that govern the flow are then the gas flow rate and the height of the bath of the steel equivalent phase. So, we can consider that the effects of the viscosity and the surface tension have only a minor influence on global flow behaviour. In that case, we choose to use a similitude based on the modified Froude number

$$N = \left(\frac{Q}{g^{1/2} h_m^{5/2}} \right)^{1/5} \quad (2.14)$$

To determine the industrial gas flow rate, we start from the modified Froude number similitude

$$\begin{aligned} (N)_{il} &= (N)_{rl}, \\ Q_{g,il} &= \left(\frac{h_{m,il}}{h_{m,rl}} \right)^{5/2} Q_{g,rl}, \end{aligned} \quad (2.15)$$

where we denote with the indices il and rl respectively the industrial and the reduced scale ladle. If we take as geometric scale the ratio of the height of the liquid steel bath $\lambda = h_{m,il}/h_{m,rl}$ we can re-express (2.15) to determine the industrial gas flow rate as a function of the model gas flow rate

$$Q_{il} = \lambda^{5/2} Q_{rl} \quad (2.16)$$

In the following, we will use a model with a geometric scale ratio of $\lambda \sim 1/12$ with an industrial ladle with the dimensions of Table 2.1.

2.2.2 Experimental procedure

We want to establish a model that allows reproducing the main flow characteristics that can be observed in an industrial ladle with the easiest experimental setup possible. To achieve this goal, following the geometrical scaling based on the modified Froude number detailed above we use a cubic water experiment at ambient temperature based on the model used by [32]. The choice of a cubic model instead of a cylindrical model is done to simplify the creation of the numerical simulation based on the water experiment (cf. 3.6). This experiment is an improved version of the one established by De Oliveira Campos [41] at the end of his PhD where the author could perform some first measurement of the open eye.

Figure 2.4 displays a sketch of the experimental setup of the water experiment, it is a square section transparent ladle made with acrylic glass, with a single bottom centred circular air injection hole. The ladle is partially filled with water and a layer of oil is floating on top of the water. Air flow is injected from a compressed air network and can be varied through an automate controlling the valve opening. The main geometric parameters of the ladle can be found in Table 2.4.

As in the industrial process, it is a three-phase model where air phase represents the argon gas, water represents the liquid steel, and the oil layer represents the liquid slag. The choice of water can be justified because of its kinematic viscosity $\nu_w = 10^{-6} \text{ m}^2 \cdot \text{s}^{-1}$ which is very close to the liquid steel one $\nu_m = 7 \cdot 10^{-7} \text{ m}^2 \cdot \text{s}^{-1}$. The oil phase is a 50-50% in volume mixture of cottonseed oil and paraffin oil. The fluids follow the ones used in [32] and allow us to study both hydrodynamics and later on mass transfer as will be detailed in 6.3. All the physical parameters of the fluids can be found in Table 2.5. As can be seen in Table 2.5 the physical properties of our oil mixture differ slightly from the one of [32] because of the variations of physical properties between oil producers. Furthermore, if we look at Table 2.6 we can see that we reproduce the same main non-dimensional number relevant in our case than in [32].

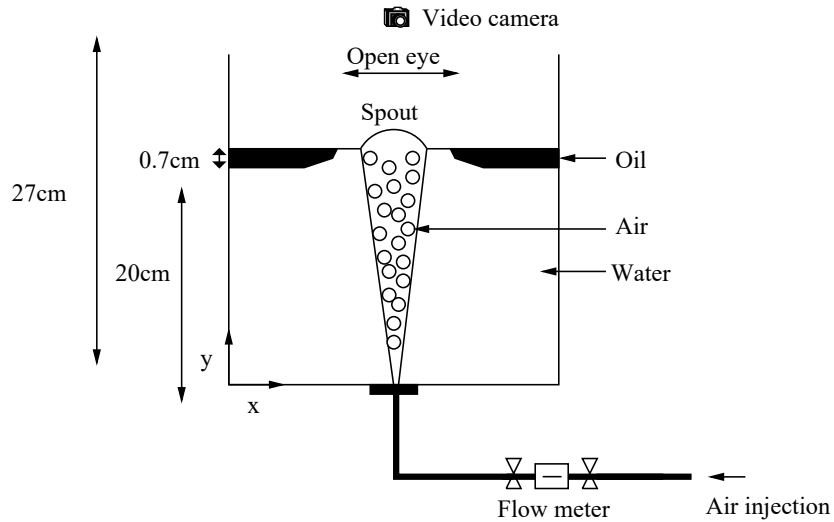


Figure 2.4: Schematic of the experimental setup of our water experiment.

Characteristic parameter	Experimental case	Kim et al. [32]
h_w (m)	0.2	0.445
h_o (m)	0.007	0.015
L_x (m)	0.27	0.456
d_{inj} (m)	$2.35 - 7.9 \cdot 10^{-3}$	$4.76 \cdot 10^{-3}$
Q ($l \cdot min^{-1}$)	0.6 - 7	0.5 - 10
V_w (L)	14.58	75
V_o (L)	0.49	2.5

Table 2.4: Main geometrical parameters of our experimental model and the one of [32].

Fluid properties at 20°C	Air	Water	Oil mixture our experiment	Oil mixture Kim et al. [32]
ρ ($kg \cdot m^{-3}$)	1.225	998	920	886
μ ($Pa \cdot s$)	$1.85 \cdot 10^{-5}$	$1.00 \cdot 10^{-3}$	$7.9 \cdot 10^{-2}$	$3.3 \cdot 10^{-2}$
σ_{aw} ($N \cdot m^{-1}$)	$7.20 \cdot 10^{-2}$			
σ_{wo} ($N \cdot m^{-1}$)		$2.55 \cdot 10^{-2}$		$1.81 \cdot 10^{-2}$
σ_{oa} ($N \cdot m^{-1}$)			$3.17 \cdot 10^{-2}$	

Table 2.5: Physical properties of fluids used in our water experiment and the one for the oil mixture used in [32].

Dimensionless number in Water	Expression	Experimental case	Kim et al. [32]
Re_w	$\rho_w U L_x / 4 \mu_w$	10^4	10^4
N	$[Q / (g^{1/2} h_w^{5/2})]^{1/5}$	10^{-1}	10^{-1}
We_w	$\rho_w U^2 L_x / 4 \sigma_{wo}$	10^2	10^3
r	ρ_w / ρ_o	1.09	1.13
H_w	h_w / L_x	0.74	0.98
H_o	h_o / L	0.035	0.034

Table 2.6: Order of magnitude of the dimensionless number for our experimental model and the one of [32].

To characterize the flow behaviour while varying the air flow rate we use a high-speed camera Motion Blitz EoSens Cube 6 Mikrotron® with a resolution of $1280 * 1024 \text{ pixel}$ and a sensibility of 2500 ISO with an objective AF NIKKOR 1:2.8 Nikon® positioned in front of the ladle. To record the top view of the water experiment, a normal camera Nikon® P200 with a resolution of $1980 * 1080 \text{ pixel}$ and a sensibility of 1600 ISO is used. This allows us to do 2D visualisation characterization of both the face view and the top view at the same time for a given air flow rate. Even though, we do not have synchronisation of the two video recordings because no simple way of automatizing the start of the recording for each device has been found. An example of the top view and the face view obtained with an injection diameter $d_{inj} = 7.9 \cdot 10^{-3} \text{ m}$ and respectively at an air flow rate of $Q = 0.6 \text{ l/min}$ and $Q = 0.4 \text{ l/min}$ can be seen in Figure 2.5 and Figure 2.6.

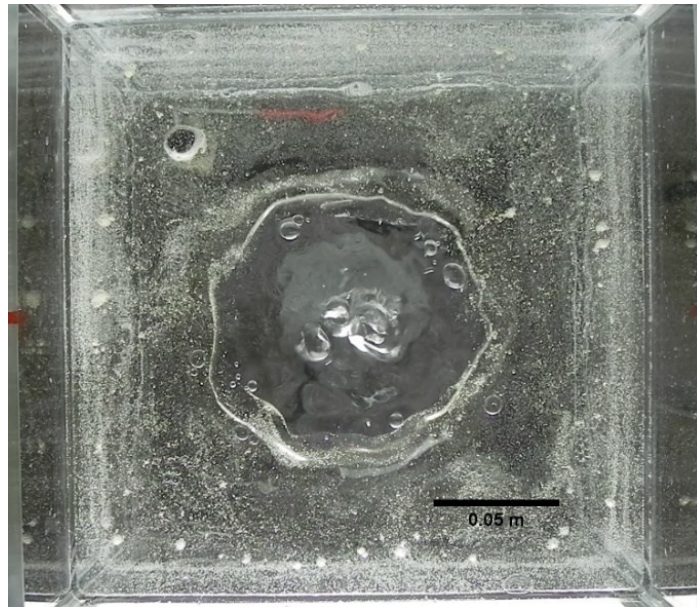


Figure 2.5: Top view of the water experiment used in our experiment at $Q = 0.6 \text{ l/min}$ with $d_{inj} = 7.9 \cdot 10^{-3} \text{ m}$.

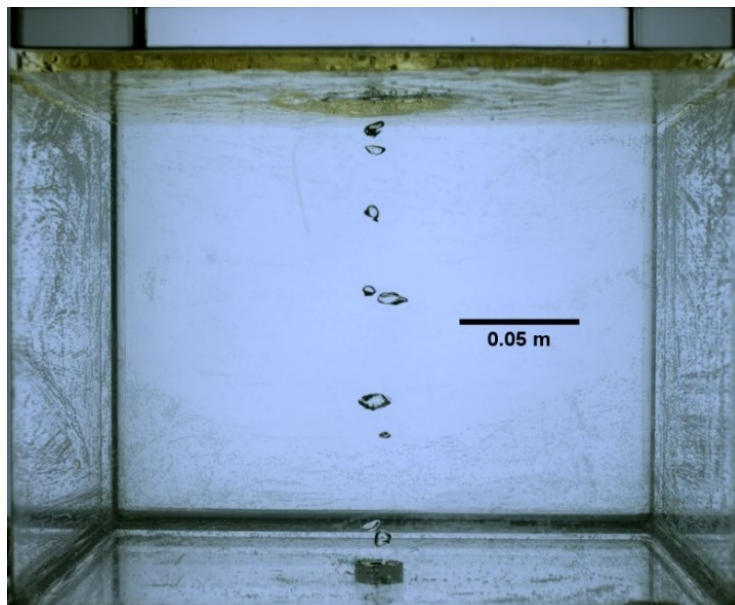


Figure 2.6: Face view of the water experiment used in our experiment at $Q = 0.4 \text{ l/min}$ with $d_{inj} = 7.9 \cdot 10^{-3} \text{ m}$.

2.2.2.1 Uncertainty quantification

As the air flow rate is the main varying parameter in our experiment it is important to quantify the variation from the setting point value to the real value. The constructor of the air regulator gives a difference of $\Delta Q/Q = \pm 0.18\%$ from $Q \in [0,2] \text{ l/min}$ and $\Delta Q/Q = \pm 0.9\%$ from $Q \in [2,10] \text{ l/min}$. But we wanted to check this incertitude within our experimental configuration. As no standard measurement devices were present, we choose to use a rudimentary method and measured the emptying time of a bottle of 1l of water positioned above the injection orifice. Then from the measured emptying time we could calculate the measured gas flow rate and compare it with the setting point value. Of course, this method is subject to measurement errors, but it can give at least a rough estimation of the error between the setting point value and the real value of the air flow rate. From Figure 2.7 we can see that in accord with the constructor, the relative error on the air flow rate appears to be lower between $Q \in [0,2] \text{ l/min}$ than for $Q \in [2,10] \text{ l/min}$. However, there is almost a factor ten of difference from our measurement compared to the error given by the constructor. If we compare the measurement that we have done for two different trials, we can see that globally we get the same relative errors on the gas flow rate with a maximum variation between the two trials of 4% and a minimum of less than 0.5%. If we consider that we might overestimate the relative incertitude due to important incertitude of measurements, and take an error margin of $\pm 40\%$ with our measurements it would lead to a relative error on the gas flow rate around $\Delta Q/Q = \pm 5\%$ in the range considered. The relative difference in the parameters of the water experiment introduced by experimental measurement can be found in Table 2.2.

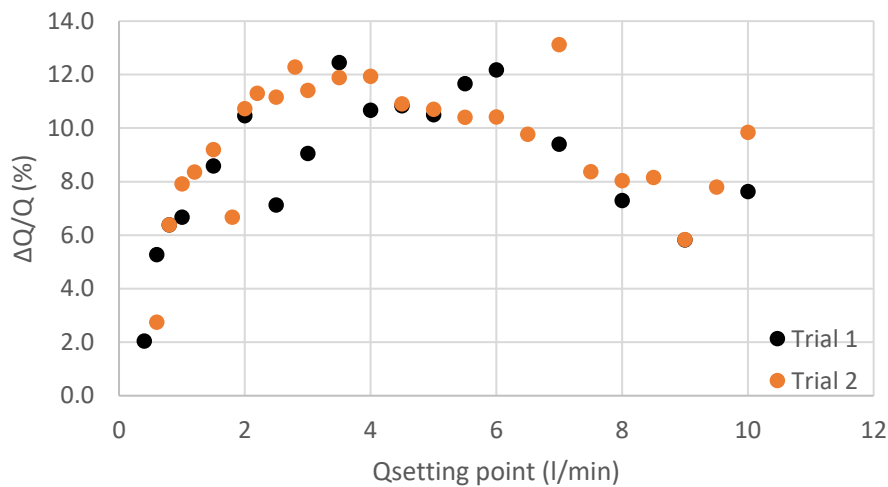


Figure 2.7: Relative error between the setting point value of the air flow rate and the measured air flow rate as a function of the setting point value of the air flow rate for two different trials.

$\Delta V/V_w$ (%)	$\Delta V/V_o$ (%)	$\Delta L/h_w$ (%)	$\Delta L/h_o$ (%)	$\Delta Q/Q$ (%)
0.7	21	0.5	14	8

Table 2.7: Values of the absolute incertitude of the parameters necessary to compute the mass transfer coefficient.

2.2.2.2 Comparison between water and industrial ladle

In this part, we will discuss the possible assumptions that we can do in our water experiment in order to reproduce the flow of the industrial ladle. First, we want to check if we have to consider the compressible effects for the gas injection. To do so we compute the Mach number at the injector given by

$$Ma = \frac{u_0}{c}, \quad (2.17)$$

where u_0 is the velocity in the gas injector given by $u_0 = 4Q/\pi d_{inj}^2$ and c is the sound speed computed with $c = \sqrt{\gamma RT/M}$ where γ is the adiabatic index, $R = 8.31 J/(K.mol)$ is the universal gas constant, T the temperature of the gas and M the molar mass of the gas. Considering an injection diameter for the water experiment and the industrial ladle of respectively $d_{inj,rl} = 0.79 cm$ and $d_{inj,il} = 4 cm$, this gives for the air and argon case at operating conditions respectively $c_{air} = 343 m/s$ and $c_{Ar} = 807 m/s$. We can compute the following Ma range for min and max air flow rates values for each case:

- Air/water experiment case $6.3 \cdot 10^{-3} \leq Ma \leq 3.8 \cdot 10^{-2} \leq 1$;
- Argon/steel industrial case $5.6 \cdot 10^{-3} \leq Ma \leq 1.1 \cdot 10^{-1} \leq 1$.

So, in both cases, the Mach number is too small to have to consider a possible shock wave effect in the injection region.

Now, we are interested to characterize the static pressure and temperature exerted by the liquid steel equivalent phase on the injected gas effect. Indeed, a gas density variation can occur as the bubbles are rising in the ladle. With a simple computation, we will check how this can affect gas density. For both air/water and liquid steel/argon we consider ambient gas at atmospheric pressure and injected gas as a perfect gas so we can write from the perfect gas law

$$\rho = PM/RT \quad (2.18)$$

where P is the absolute value of the static pressure generated by the height of the bath.

- air/water case:

We consider $h_w = 0.2m$ and $h_o = 0.01m$ respectively for the height of water and oil and $T = 20^\circ C$. It will generate a gas density variation of $\Delta\rho_{bubble} = (\rho_{g,top} - \rho_{g,bottom})/\rho_{g,top} \sim 2\%$ from the injection hole to the free surface.

- Argon/steel case:

We consider $h_m = 3.3m$ and $h_s = 0.17m$ respectively for the height of steel and slag. For the industrial case, we can consider that the injected gas is already at the steel temperature of $T = 1600^\circ C$. If we proceed in the same manner than previously for the argon gas, it will cause a gas density change of $\Delta\rho_{bubble} = (\rho_{g,top} - \rho_{g,bottom})/\rho_{g,top} \sim 229\%$ from the injection hole to the free surface.

From this short computation, it appears that we can neglect the density variation of gas due to static pressure for the air/water case but not for the argon/steel industrial configuration.

2.3 PHENOMENOLOGICAL ANALYSIS

In the following, we consider the specific case of the water-oil gas stirred ladle, but all the development can be used with another choice of fluids.

2.3.1 Kinetic energy dissipation

A rising bubble plume can be considered as a thermal plume with an average buoyancy flux given by

$$J(\zeta) = \iint_{z=\zeta} (\rho_w - \rho_a) g w f_a \, dx \, dy ,$$

where f_a is the gas fraction or “void fraction”, w the vertical speed. The gas fraction diffuses not in a molecular way but only through the advection term, so it obeys

$$\partial_t f_a + \mathbf{u} \cdot \nabla f_a = 0$$

As the field \mathbf{u} is incompressible, the quantity f_a is conserved and the flux J is independent of ζ and equal to $J = (\rho_w - \rho_a) g Q$ where Q is the volume flux of injected gas given by

$$Q = \iint_{S_I} w(x, y, 0) \, dx \, dy , \quad (2.19)$$

where S_I is the injector surface. If we consider a cuboid domain of size $L_z \times L_x \times L_y$ with $L_x = L_y$ we can integrate the kinetic energy equation in the Boussinesq approximation

$$L_z L_y L_z \epsilon = \iiint (\rho_w - \rho_a) g w f_a \, dx \, dy \, dz \quad (2.20)$$

Considering that $\rho_a \ll \rho_w$ we get the average kinetic energy dissipation expression

$$\epsilon / \rho_w \simeq \frac{g Q}{L_x^2} \quad (2.21)$$

2.3.2 Bubble plume structure

2.3.2.1 Generalities on the bubble plume

Two theories of the bubble plume are possible: the first one is a bubble column where the bubbles do not interact with each other, the second one is a bubble plume. In our configuration the first theory can be seen at a low air flow rate, the second one at a high air flow rate as can be seen in Figure 2.8- (a) and (b). We assume a Froude number scaling where the quantities used in the dimensionless analyses are the gravity g and the flow rate Q . All the other quantities are established with these two quantities.

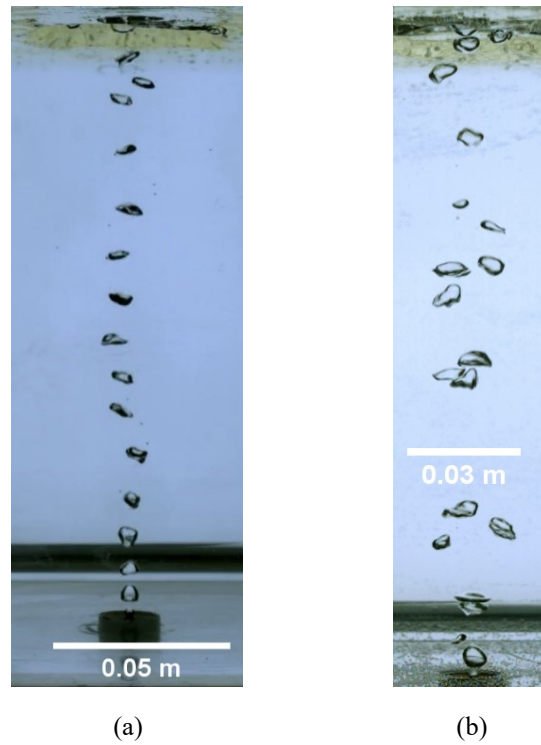


Figure 2.8. Zoom of the face view on the bubble plume from our water experiment with $d_{inj} = 2.35 \cdot 10^{-3}m$ and two different air flow rates. a): $Q = 0.2l/min$; b): $Q = 0.5l/min$.

2.3.2.2 Bubble plume – Boussinesq approximation

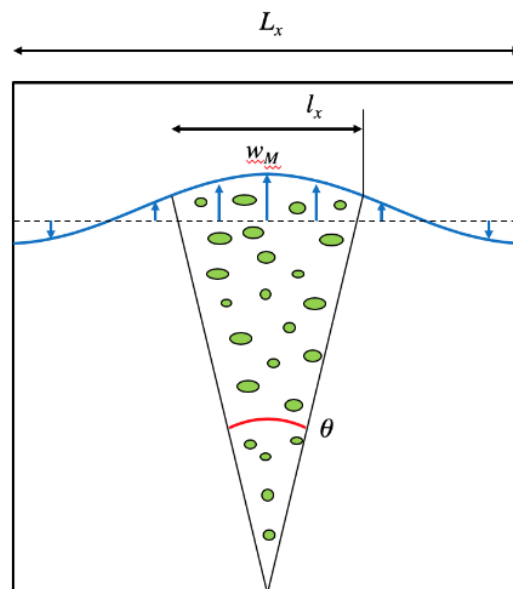


Figure 2.9: Bubble plume basic geometry

Within the Boussinesq approximation the quantity f_a is small and we consider an average density of the water-air bubbles mixture

$$\rho = \rho_w - (\rho_w - \rho_a)f_a \approx \rho_w(1 - f_a) \quad (2.22)$$

This density variation is taken into account only on the gravity term of the equations, this is the Boussinesq approximation (Tritton [42]). The only dimensional quantity is gQ which is reducing one degree of freedom of the dimensional analysis. The dimensional analysis (Monin & Yaglom [43]) based on gQ give a unique solution for the characteristic speed at the height z

$$w'(z) \sim \left(\frac{gQ}{z}\right)^{1/3} \quad (2.23)$$

We can write a scaling for the flow rate

$$Q \sim f_a(z)w'(z)\ell^2(z), \quad (2.24)$$

where ℓ is the plume width, f_a the average void fraction at the height z . We can also write

$$\ell(z) \sim \theta z, \quad (2.25)$$

where θ is the angle from the vertical axis of the plume, [43] give a value of 14° in the case of the thermal plume. Because J should stay constant we can write

$$Q \sim f_a(gQ/z)^{1/3}z^2, \quad (2.26)$$

and get

$$f_a \sim g^{-1/3}Q^{2/3}z^{-5/3}. \quad (2.27)$$

2.3.2.3 Rectilinear bubble column

In this model the bubbles of diameter d_b are considered to not interact with each other and rise in a sort of "tube" of constant width $\ell \sim d_b$. We do not use the Boussinesq approximation anymore. By dimensional analysis at high Re we got

$$w_b \sim (gd_b/C_D)^{1/2}, \quad (2.28)$$

where C_D is a drag coefficient. If the bubbles rise in a line separated by $\ell(z)$ we got $f_a = d_b/\ell(z)$ from (2.24) and (2.28) we can write

$$Q \sim (gd_b)^{1/2}d_b^3/\ell(z) \sim w_b d_b^3/\ell(z). \quad (2.29)$$

Knowing the bubble size, we can deduce

$$\ell(z) \sim (gd_b)^{1/2}d_b^3Q^{-1}, \quad (2.30)$$

valid if $\ell(z) > d_b$ so if $(gd_b)^{1/2}d_b^2Q^{-1} < 1$ the bubbles coalesce to form a larger bubble of size

$$d_b \sim g^{-1/5}Q^{2/5}, \quad (2.31)$$

and thus, we find for the velocity

$$w \sim g^{2/5}Q^{1/5}. \quad (2.32)$$

This assumes that bubbles do not break up and do not get scattered horizontally by turbulence and that the Weber number given by $We_Q \sim \rho_w g^{3/5} Q^{4/5} / \sigma$ stays moderate. In our experiment at an air flow rate $Q = 0.6l/min$ we obtain the following value of the critical Weber number $We_Q = 15.4$.

From Figure 2.8 we can see that in our water experiment, the transition between the plume and column regime occurs between at $Q = 0.3l/min$. When the bubbles start to break up, the bubble plume regime should be dominant.

2.3.2.4 Velocity scaling in the bubble plume

Without gas injection, the water-oil interface is horizontal and situated at a height h_w (cf. Figure 2.10). As already introduced before, we use the expression of the rising velocity of the rectilinear bubble column (2.32) to compute the modified Froude number given by

$$\sqrt{Fr} = \frac{U}{\sqrt{gh_w}},$$

$$N = \left(\frac{Q}{g^{1/2} h_w^{5/2}} \right)^{1/5}. \quad (2.33)$$

The two previous bubble plume models can be summed up with the following expression for the velocity at the height h_w

$$w(h_w) = N^{5\alpha} \sqrt{gh_w}, \quad (2.34)$$

where $\alpha = 1/3$ for the bubble plume and $\alpha = 1/5$ for the rectilinear bubble column. If we do not neglect the air influence, the modified Froude number can be given by

$$N_{aw} = \frac{\rho_w}{(\rho_w - \rho_a)} \left(\frac{Q}{g^{1/2} h_w^{5/2}} \right)^{1/5}. \quad (2.35)$$

2.3.3 Open eye model

2.3.3.1 Basic geometry

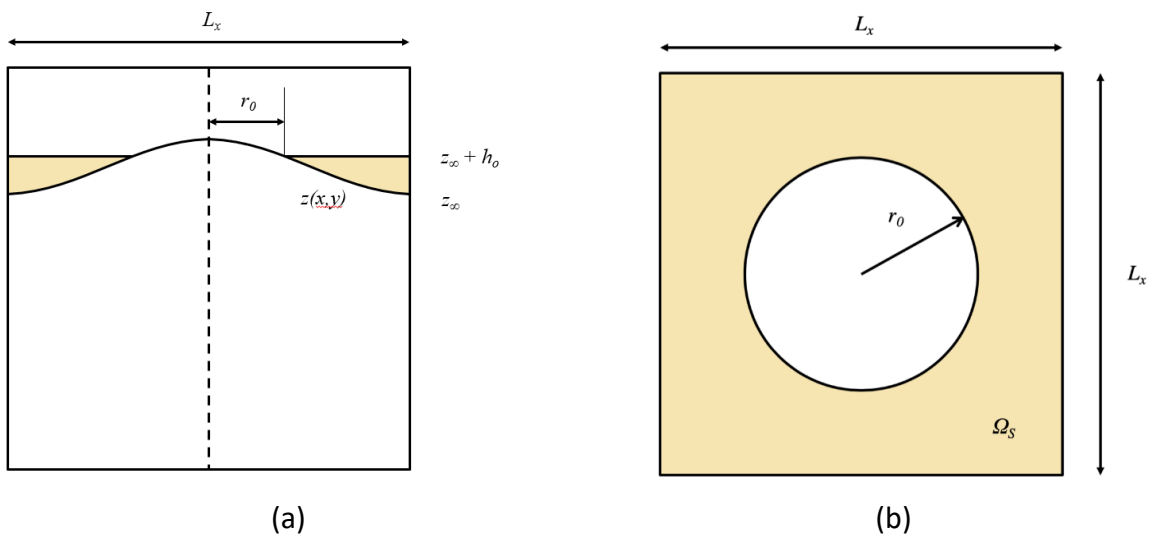


Figure 2.10: Open eye model. (a) Face view. Oil surface is situated between the curve $z(x,y)$ and horizontal line at height $z_\infty + h_o$. (b) Top view. The Ω domain is squared of dimension $L_x \times L_x$ and the open eye is the circle C of radius r_0 . The integration surface is $\Omega_S = \Omega - C$.

2.3.3.2 Water-oil surface geometry

The water-air bubble mixture interface is the height $z(x, y)$ determined by

$$z(x, y) = z_M Z(x, y) + z_\infty, \quad (2.36)$$

$z(x, y)$ is experimentally modeled with a Gaussian function (Schlichting [44]), then we can write

$$Z(x, y) = e^{-r^2/\ell_x^2}, \quad (2.37)$$

with $r^2 = x^2 + y^2$ and $\ell_x = \ell(h_w) = c_\ell h_w$ where c_ℓ is a coefficient to be determined and the relation is valid only for $r > r_0$. We can get the maximum water height with a Bernoulli relation when $r > r_0$

$$(\rho_w - \rho_o)gz(x, y) = \frac{1}{2}\rho_w w^2(x, y, h_w) \quad (2.38)$$

Consequently, the velocity obeys also follows the Gaussian relation

$$w(x, y, z) = w_M e^{-r^2/(2\ell_x^2)}, \quad (2.39)$$

where the maximum of (2.39) $w_M \sim w'(h_w)$ is given by the equations of 2.3.2. The coefficient ℓ_x is related to the coefficient b_w from Ezzamel *et al.* [45] by

$$w(x, y, z) = w_M e^{-r^2/b_w^2} \quad (2.40)$$

Starting from the above equations we get for a rectilinear bubble column

$$z_M = \frac{1}{2} \frac{\rho}{\Delta\rho_o} g^{-1/5} Q^{2/5}, \quad (2.41)$$

using (2.38) and (2.23) for a bubble plume we obtain

$$z_M = \frac{1}{2} \frac{\rho}{\Delta\rho_o} g^{-1/3} Q^{2/3} h_w^{-2/3}. \quad (2.42)$$

We can condense the two previous expressions within a unique expression of the form

$$z_M = \frac{1}{2} \frac{\rho}{\Delta\rho_o} N^\alpha h_w, \quad (2.43)$$

where $\alpha = 1/5$ for the bubble plume and $\alpha = 1/3$ for the rectilinear bubble column.

2.3.3.3 Oil layer shape

We have the dynamic height of the top of the oil layer given by

$$z_o = z_M Z(x_0/\ell_x, y_0/\ell_y), \quad (2.44)$$

and $r_0^2 = x_0^2 + y_0^2$, the height of the oil layer without gas injection is given by

$$h_o = V_o/L_x^2. \quad (2.45)$$

We can compute r_0 with

$$V_o = z_o L_x^2 - \iint_{\Omega_S} z_M Z(x/\ell_x, y/\ell_y) dS \quad (2.46)$$

So, we can write

$$(h_o - z_o) L_x^2 = -z_M I_Z, \quad (2.47)$$

with I_Z the height integral on Ω_S

$$I_Z = \iint_{\Omega} Z dS - \iint_{C(r_o)} Z dS. \quad (2.48)$$

We note

$$I_o = \frac{1}{\ell_x^2} \iint_{\Omega} Z dS \quad (2.49)$$

In the case of a Gaussian function (2.48) can be rewritten

$$\begin{aligned} I_Z &= I_o \ell_x^2 - \int d\theta \int_0^{r_o} e^{-r^2/\ell_x^2} r dr \\ &= I_o \ell_x^2 + \pi \ell_x^2 (e^{-r_o^2/\ell_x^2} - 1) \end{aligned} \quad (2.50)$$

And finally using the above relations we can compute the height

$$z_M = \frac{V_o}{e^{-r_o^2/\ell_x^2} (L_x^2 - \ell_x^2) - I_o \ell_x^2 + \pi \ell_x^2} \quad (2.51)$$

It is easy to recognize the error function

$$I_o = \left(\int_{-\frac{L_x}{2\ell_x}}^{\frac{L_x}{2\ell_x}} e^{-s^2} ds \right)^2 = \pi \operatorname{Erf} \left(\frac{L_x}{2\ell_x} \right)^2 \quad (2.52)$$

I_o is nearly constant for $L_x \gg \ell_x$. Indeed, we have $\lim_{L_x/\ell_x \rightarrow \infty} I_o = \pi$, so in a first-order approximation, we got

$$z_M = \frac{h_o}{e^{-r_o^2/\ell_x^2}} \quad (2.53)$$

2.3.3.4 Open eye correlation

From relations (2.43) and (2.53) we can write from the open eye area $A_o = \pi r_o^2$

$$A_o = \alpha \pi \ell_x^2 \left[\ln(N^{10}) - \ln \left(\frac{\Delta \rho h_o}{\rho_w h_w} \right) \right], \quad (2.54)$$

which can be rewritten

$$A_o = C_A \ln \left(\frac{N}{N_c} \right), \quad (2.55)$$

where $C_A = 10 \alpha \pi c_\rho^2 h_w^2$ and N_c is the critical modified Froude number for the open eye formation given by

$$N_c = \left(\frac{\Delta\rho h_o}{\rho_w h_w} \right)^{1/10}. \quad (2.56)$$

2.3.4 Transition to an oil droplet detachment flow regime

We define the Weber number for the water-oil model with

$$We_{ow} = \frac{\rho_w U^2 d}{\sigma_{ow}}, \quad (2.57)$$

where the horizontal speed U is approximated by $U = w(h_w)$ given by (2.34) and where d is the wavelength used to study the instability of the flow in the horizontal direction. In the following, we consider that $d = L_x/4$, we can then write

$$We_{ow} = N^{10\alpha} Bo_{ow} r_\Delta \frac{d}{h_w}, \quad (2.58)$$

where $r_\Delta \sim \rho_w/(\rho_w - \rho_o)$ and the Bond number at the oil/water interface is given by

$$Bo_{ow} = \frac{(\rho_w - \rho_o) g h_w^2}{\sigma_{ow}}. \quad (2.59)$$

Within the assumption that the transition occurs at a critical Weber number $We_{crit} = 1$ we got the following expression for the critical modified Froude number for the oil droplet detachment flow regime N_{crit}

$$N_{crit} = \left(Bo_{ow} r_\Delta \frac{d}{h_w} \right)^{-1/10\alpha} \quad (2.60)$$

An alternative model for the Weber number gives

$$We_{ow} = \frac{\rho_w U^2 \text{Min}(h_o, d)}{\sigma_{ow}}, \quad (2.61)$$

where h_o is the height of the oil layer. It would lead in the typical case of $h_o < d$

$$N_{crit} = \left(Bo_{ow} r_\Delta \frac{h_o}{h_w} \right)^{-1/10\alpha}. \quad (2.62)$$

2.4 SUMMARY

In this chapter, we have first introduced the open eye and the fragmentation of the slag layer as the main hydrodynamic phenomenon that we are interested to characterize in this dissertation. We then reviewed the studies with water and liquid metal experiments in the literature concerning these two aspects. Because of its ease of use and its low operating cost we choose to use a scaled water experiment to reproduce the flow of the industrial process. Our water experiment follows a modified Froude number similitude with an industrial ladle and, the choice of the fluids followed the one used in [32].

Finally, we have done a phenomenological analysis in order to estimate the kinetic energy dissipation and the rising velocity in the liquid steel phase generated by the gas injection. Finally, we tried to characterize the appearance of a regime of fragmentation of the slag equivalent phase into droplets.

3 NUMERICAL MODEL- HYDRODYNAMIC CHARACTERIZATION

3.1 LITERATURE REVIEW

In the literature, the numerical study of the fluid flow in a gas-stirred ladle with a slag layer can be classified into three main types depending on the approach used to simulate the bubble plume generated by the gas injection.

The first one is the VOF approach using a VOF formulation to characterize all the fluid interfaces in a single-fluid model. In the following studies, only a slice of the steel-slag interface is considered. The gas injection is not modelled, and the problem is thus simplified to a three-phase flow configuration where the gas is only acting on the slag interface. In Sulasalmi *et al.* [46] and Ramasetti *et al.* [47], the authors used the commercial code Fluent with imposed inlet velocity to simulate the configuration previously explained. In Senguttuvan & Irons [48] the authors presented a quite sophisticated assembly of sub-models in order to compute the mass transfer between steel and slag. First, they considered a 2D axisymmetric quasi single-phase RANS simulation to be able to compute the inlet velocity of the thin slice domain. Then the authors used 3D LES simulation with a subgrid-scale model to simulate the fragmentation behaviour of the slag layer. Both simulations were done using the Gerris flow solver (Popinet [15], [16]). Despite the successive assumptions of their sub-models the authors obtained some interesting results about the fragmentation of the slag layer.

More recently, in his PhD thesis, De Oliveira Campos [41] tried to simulate a water scaled experiment of an industrial ladle using the Thetis code (Vincent *et al.* [49], Delteil *et al.* [50]). In his attempt, the author tried this time to simulate the three-phase flow with the bubble plume using an LES approach. His model gave some interesting results for the low air flow rate regime but had more difficulty with the highly deformed interfaces at a high air-flow rate.

A second approach is based on an averaged Euler-Euler description of the flow. This approach has been used in a larger number of studies. In this formulation, a set of coupled equations are solved for each phase. The studies found in the literature are mainly simulations of the whole gas-stirred ladle with a $k-\varepsilon$ turbulence model (Huang *et al.* [51] Lou & Zhu [52], [53], [54], Cao & Nastac [55]).

A third approach is based on a Lagrangian description of the bubble plume in order to further simplify the flow simulation in a water-oil configuration (Li *et al.* [56], [57], [58], Liu *et al.* [59]) or steel slag configuration (Liu *et al.* [60]).

As we have seen, in the literature most of the simulations are done using commercial codes that can be used to simulate the whole industrial process and give an idea of the average flow, provided their limitations in accuracy are kept in mind. To our knowledge, no attempt has been made so far to perform a DNS simulation of the gas-stirred ladle with a slag layer either for a water-oil or steel-slag configuration. As mentioned in Tryggvason *et al.* [10] the improvement of both the efficiency of codes and the increase of the computational power of the computers allow simulating more various industrial-like configuration even encompassing complex phenomena such as fragmentation (Fuster *et al.* [61], Ling *et al.* [62], Aniszewski *et al.* [63]).

3.2 TWO-PHASE MODEL

The Incompressible, variable density, Navier-Stokes equations can be written

$$\rho \left(\frac{\partial \mathbf{u}}{\partial t} + \mathbf{u} \cdot \nabla \mathbf{u} \right) = -\nabla p + \nabla \cdot (2\mu \mathbf{D}) + \sigma \kappa \delta_S \mathbf{n}, \quad (3.1)$$

$$\frac{\partial \rho}{\partial t} + \nabla \cdot (\rho \mathbf{u}) = 0, \quad (3.2)$$

$$\nabla \cdot \mathbf{u} = 0, \quad (3.3)$$

with \mathbf{D} the deformation tensor $\mathbf{D} = (\nabla \mathbf{u} + (\nabla \mathbf{u})^T)/2$.

In the case of a two-phase flow, the volume fraction of the first fluid $\chi(x, t)$ allows to capture the interface between the two fluids. It is defined as

$$\chi(x, t) = \begin{cases} 1 & \text{if } x \in \text{fluid 1} \\ 0 & \text{elsewhere} \end{cases} \quad (3.4)$$

We can note that the volume fraction of the second fluid is defined implicitly by $1 - \chi(x, t)$. With this relation it is possible to use a single-fluid model to describe the variation of density and viscosity in the computational domain with

$$\rho(\chi) \equiv \chi \rho_1 + (1 - \chi) \rho_2, \quad (3.5)$$

$$\mu(\chi) \equiv \chi \mu_1 + (1 - \chi) \mu_2, \quad (3.6)$$

where we denote with the indices 1,2 the fluid one and two. We can then replace the variable density equation (3.2) with an advection equation for the volume fraction given by

$$\frac{\partial \chi}{\partial t} + \nabla \cdot (\chi \mathbf{u}) = 0 \quad (3.7)$$

3.3 BASILISK CODE

Basilisk [64] is a Free Software library designed to solve partial differential equations. It is written with a modified C programming language called Basilisk C which makes it easy to implement code corresponding to the problem modelled from and with the numerous existing modules, scripts, functions existing in the source code. The numerical schemes used in Basilisk are based on its ancestor: the Gerris flow solver ([15], [16]). We will briefly present the details of the Navier-Stokes centred solver [65] of Basilisk used in this study.

3.3.1 Temporal discretisation

The scheme used in the time discretization consists in a time-splitting pressure-correction method. The time-stepping integration procedure is briefly outlined below. The readers can find a more detailed description in [15], [16] and in Lagree *et al.* [66]. First, the volume fraction χ and the concentration of a diffusive tracer C are advanced to a mid-time step, $n + 1/2$

$$\frac{\chi_{n+\frac{1}{2}} - \chi_{n-\frac{1}{2}}}{\Delta t} + \nabla \cdot (\chi_n \mathbf{u}_n) = 0, \quad (3.8)$$

$$\frac{C_{n+\frac{1}{2}} - C_{n-\frac{1}{2}}}{\Delta t} + \nabla \cdot (C_n \mathbf{u}_n) = \nabla \cdot (DC_{n+\frac{1}{2}}), \quad (3.9)$$

where D is the diffusion coefficient. Then the values of the fluid properties are updated

$$\rho_{n+\frac{1}{2}} \equiv \chi_{n+\frac{1}{2}} \rho_1 + (1 - \chi_{n+\frac{1}{2}}) \rho_2 \quad (3.10)$$

$$\mu_{n+\frac{1}{2}} \equiv \chi_{n+\frac{1}{2}} \mu_1 + (1 - \chi_{n+\frac{1}{2}}) \mu_2 \quad (3.11)$$

After updating the fluid properties values, the prediction-diffusion step is done by solving the equation

$$\frac{\rho_{n+\frac{1}{2}}}{\Delta t} \mathbf{u}_* - \nabla \cdot (\mu_{n+\frac{1}{2}} \mathbf{D}_*) = \nabla \cdot (\mu_{n+\frac{1}{2}} \mathbf{D}_n) + (\sigma \kappa n \delta_s)_{n+\frac{1}{2}} + \rho_{n+\frac{1}{2}} \left(\frac{\mathbf{u}_n}{\Delta t} - \mathbf{u}_{n+\frac{1}{2}} \cdot \nabla \mathbf{u}_{n+\frac{1}{2}} \right), \quad (3.12)$$

where \mathbf{u}_* is an auxiliary velocity field and \mathbf{D}_* is an auxiliary deformation tensor. Solving (3.12) allows determining the auxiliary velocity \mathbf{u}_* . In the above expression, the velocity advection term $\mathbf{u}_{n+1/2} \cdot \nabla \mathbf{u}_{n+1/2}$ is estimated through the Bell–Colella–Glaz second-order unsplit upwind scheme ([15]). The projection–correction step is then computed by solving the Poisson equation

$$\nabla \cdot \left(\frac{\Delta t}{\rho_{n+\frac{1}{2}}} \nabla p_{n+\frac{1}{2}} \right) = \nabla \cdot \mathbf{u}_* \quad (3.13)$$

Then the divergence-free velocity field at the new time step $n + 1$ is computed with

$$\mathbf{u}_{n+1} = \mathbf{u}_* - \frac{\Delta t}{\rho_{n+\frac{1}{2}}} \nabla p_{n+\frac{1}{2}} \quad (3.14)$$

As mentioned previously, the surface tension forces are computed using the CSF approach (Brackbill *et al.* [67]). It is well known that the CSF approach can cause parasitic currents when important density or viscosity ratio are considered. However, it is possible to minimise them by using a balanced-force description of the surface tension and pressure gradient together with an accurate curvature estimate (Popinet [68]). The curvature is computed using a generalised height-function technique which allows consistent and accurate estimations. The time integration scheme is explicit with a timestep limited by either capillary, advection or diffusion instability depending on the parameters of the problem. Furthermore, the viscous term is computed implicitly.

3.3.2 Spatial discretisation

We will present briefly the main idea of the spatial discretisation used in Basilisk, for more details the reader is invited to refer to van Hooft *et al.* [69]. The finite-volume method is used to discretise the domain using a Cartesian mesh. In the following, we will denote by cell each finite volume of length Δx . The structure of the mesh in Basilisk can use an unstructured grid based on a tree hierarchy. Depending on error criteria on a scalar field fixed by the user, a cell can be refined or coarsened during the simulation. So, ultimately the mesh can be adaptively refined in the region of the flow where the errors are higher than a threshold chosen by the user. An example of the discretisation for a quadtree in 2D is shown in Figure 3.1 where each cell may be the parent of up to four children cells at each level of refinement of the tree hierarchy. The cell at the base and top of the tree are respectively the root cell which has no parent and the leaf cell which has no children. Considering this unstructured mesh, the length of a cell at each level of refinement starting from zero and incrementing by one for each successive generation of children can be computed by

$$\Delta x = \frac{L_0}{2^{level}}, \quad (3.15)$$

where L_0 is the length of the computational domain and *level* corresponds to the maximum number of cells in one direction of the generation in the tree hierarchy. The minimum mesh size is given using (3.15) for the maximum level of refinement of the mesh with

$$\Delta x_{min} = \frac{L_0}{2^{maxlevel}} \quad (3.16)$$

Some constraints are imposed to simplify the calculation of the gradient and flux calculations:

- The levels of direct neighbouring cells cannot differ by more than one.
- The levels of diagonally neighbouring cells cannot differ by more than one.
- All the cells directly neighbouring a mixed cell must be at the same level.

All the previous explanations concern a two-dimensional grid but can be extended to a three-dimensional grid where all the cells can be refined into height cells following an octree hierarchy.

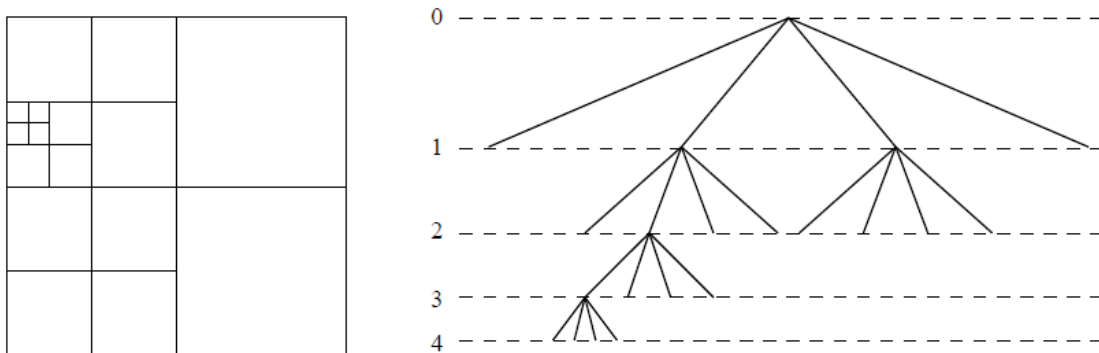


Figure 3.1: Example of quadtree spatial discretisation (left) and the corresponding tree representation (right) from [15].

3.4 THREE-PHASE MODEL

Because in the context of this study we are in presence of a three-phase flow we cannot use the implicit declaration of the second phase. In a two-phase flow, this implicit declaration allows by construction to constrain the sum of fluid fractions equal to one. Instead, we declare explicitly three volume fractions corresponding to each phase. In that case, we want also that the sum of fluid fractions is equal to one

$$\sum_i^n \chi_p(x, t) = 1, \quad (3.17)$$

where p is the fluid phase index. To do so we add a constraint on each fluid fractions at each time-step by normalizing the fluid fraction with the sum of fluid fractions

$$\chi_{p,norm}(x, t) = \frac{\chi_p(x, t)}{\sum_i^n \chi_p(x, t)} \quad (3.18)$$

This way the density and viscosity of each phase follow an equation of the type of (3.7) and the physical properties are determined in the domain using arithmetic means

$$\begin{aligned} \rho(\chi) &\equiv \sum_i^n \chi_p \rho_p \\ \mu(\chi) &\equiv \sum_i^n \chi_p \mu_p \end{aligned} \quad (3.19)$$

The surface tension effect is considered through a force acting on the interface between two fluids, but here we have to consider the possibility that more than one fluid can be the neighbour of a cell. Also, in the code, the surface tension is defined as an attribute of the volume fraction which only works with a specific couple of fluids as in a two-phase flow. For example, the interfacial tension between the water and oil is not the same as the surface tension acting between the water and air phase. That is why we decompose the physical surface tension into phase-specific surface tensions only depending on the volume fraction considered and not the fluid in contact. Based on the work of Smith *et al.* [70], the implementation of surface tension for three fluids has already been done using the Gerris flow solver in Chen *et al.* [71] and Wallmeyer *et al.* [72]. In practical in our case, the physical surface or interfacial tension is decomposed into the sum of two phase-specific surface tensions

$$\sigma_{aw} \equiv \sigma_a + \sigma_w \quad (3.20)$$

$$\sigma_{wo} \equiv \sigma_w + \sigma_o \quad (3.21)$$

$$\sigma_{ao} \equiv \sigma_a + \sigma_o \quad (3.22)$$

In the end, it gives the following expressions of the phase-specific surface tension

$$\sigma_w \equiv (-\sigma_{ao} + \sigma_{aw} + \sigma_{wo})/2, \quad (3.23)$$

$$\sigma_o \equiv (\sigma_{ao} - \sigma_{aw} + \sigma_{wo})/2, \quad (3.24)$$

$$\sigma_a \equiv (\sigma_{ao} + \sigma_{aw} - \sigma_{wo})/2, \quad (3.25)$$

where the indices a, w, o denotes the air, water and oil phases.

Finally, because we have to consider a large density ratio between the air and water phase that can lead to convergence issues, we choose to use a momentum conserving VOF advection of the velocity

components. As in this study, we consider three phases we extended slightly the original momentum-conserving code initially established for the two-phase flow Navier-Stokes solver to adapt it to three-phases. Because within our three-phase formulation each phase has its own fluid fraction the momentum of each phase can be given by

$$q_p = \chi_p \rho_p \mathbf{u}, \quad (3.26)$$

where q is the phase-specific momentum.

3.5 NUMERICAL VALIDATION

In the following, we will test our three-phase implementation formulation introduced previously with some classical numerical tests.

3.5.1 Three-phase formulation

We reproduce here the classical test of the advection of a circular interface in a vortex. It is a periodical reverting flow meaning that after a time equal to the period of the stretching cycle $T = 15$ the interface should be back to its initial position. The flow is non-divergent and during the simulation, the interface is subject to a maximum stretching at $t = T/2$. Here, because we want to test our three-phase formulation, we divide the circular interface into two different VOF tracers f_1 and f_2 (cf. Figure 3.2). The third VOF tracer f_3 is defined as the outer part of the initial circle on the lower left part of the domain. Furthermore, to compare our three-phase formulation with the standard two-phase formulation we will also consider the two-phase simulation of the left and right half of the circle denoted by the respective VOF tracers f_{left} and f_{right} (cf. Figure 3.2). It is a 2D simulation using only the advection solver, with a maximum mesh number in one direction of $lvl8 = 2^8$ cells meaning that there can be a maximum of 102 cells in the circle diameter.

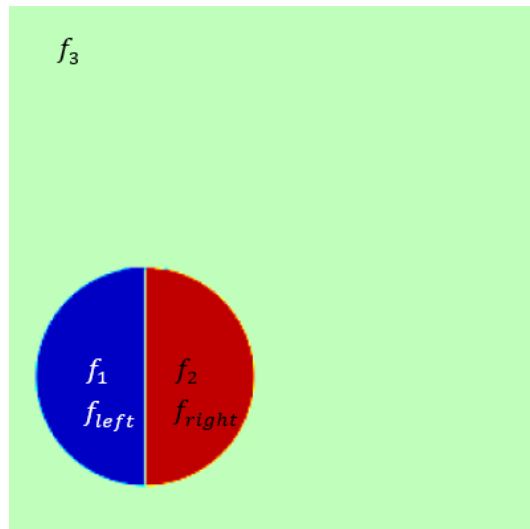


Figure 3.2: Representation of the fluid fractions at the initial state $t = 0$ for the two phase formulation with f_{left} and f_{right} and for the three phase formulation with f_1 , f_2 and f_3 .

In Figure 3.3 we show the shapes of the interface for the two VOF tracers in the three-phase formulation at different times of the periodic stretching. If we look at Figure 3.3-(a) we cannot see any obvious difference in the interface between the initial and final shape. If we look more closely at the tails at $t = T/4$, $t = T/2$ and $t = 3T/4$ we can observe some fragmentation of the VOF tracer for phase one into small droplets. If we compare the initial shape and the final shape, we can see that the interface presents some waves on the bottom of the linear part of the interface. Now if we look at Figure 3.3-(b), we can make the same remark as for the VOF tracer for phase one except that here we see no fragmentation into small droplets at $t = T/4$, $t = T/2$ and $t = 3T/4$. Also, if we compare the initial and final shape, we can observe that the bottom part of the interface of the VOF tracer of phase two is stretched to the top. Of course, the position of the half-circle plays a role in its deformation, and so the apparent higher deformation of the VOF tracer for phase one may be explained by this reason.

We now compare the rate of convergence of the errors between the initial and final shapes of each VOF tracer with the maximum mesh resolution in Figure 3.4. From the results of Figure 3.4-(a) where the convergence rate for the VOF tracer of phase one and its equivalent phase in the two-phase formulation is showed we can see that we have less than an order one of convergence for the norm of the shape error for the VOF tracer with the three-phase formulation. A slightly better convergence of order one is obtained with the two-phase formulation. The maximum of the shape error stays constant at each mesh resolution and for both formulations. Figure 3.4-(b) shows the same behaviour as previously with a slightly poorer convergence rate for both formulation confirming the visual observations made from Figure 3.3-(b). Now, if we look at Figure 3.4-(c), where only the VOF tracer corresponding to the outside part of the circle with the three-phase formulation is shown we can observe a slightly better convergence with uniform grid than with adaptive grid. From this, we can see that we have a slightly poorer convergence rate for all the VOF tracers with the three-phase formulation compare to the two-phase formulation and that the maximum shape error stays constant to a relatively high value.

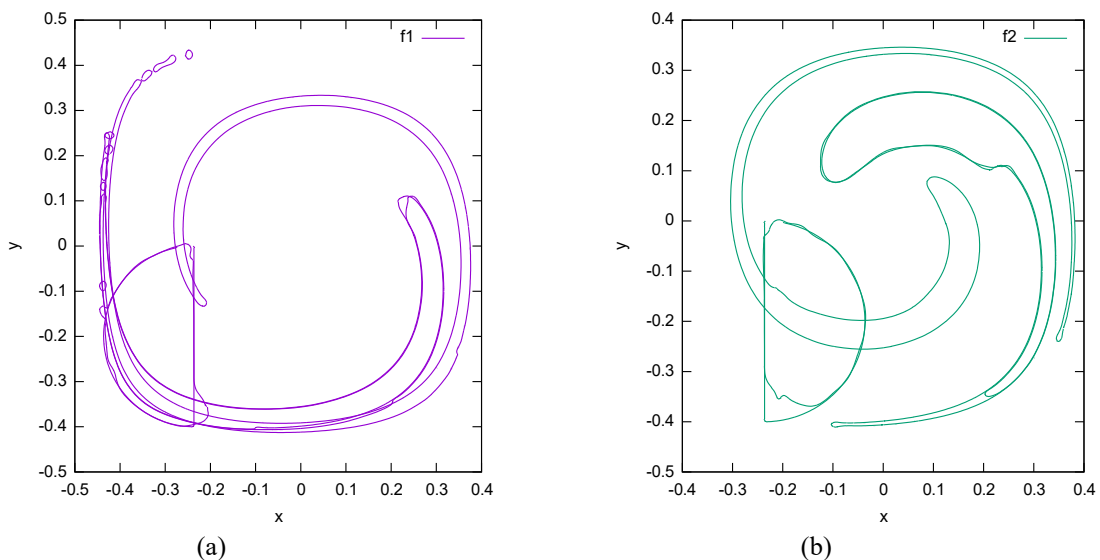


Figure 3.3: Shapes of the interface for $t = 0$, $t = T/4$, $t = T/2$, $t = 3T/4$ and $t = T$ obtained for a maximum mesh number in one direction of $lv18 = 2^8$ cells . a): VOF tracer for phase one f_1 ; b): VOF tracer for phase two f_2 .

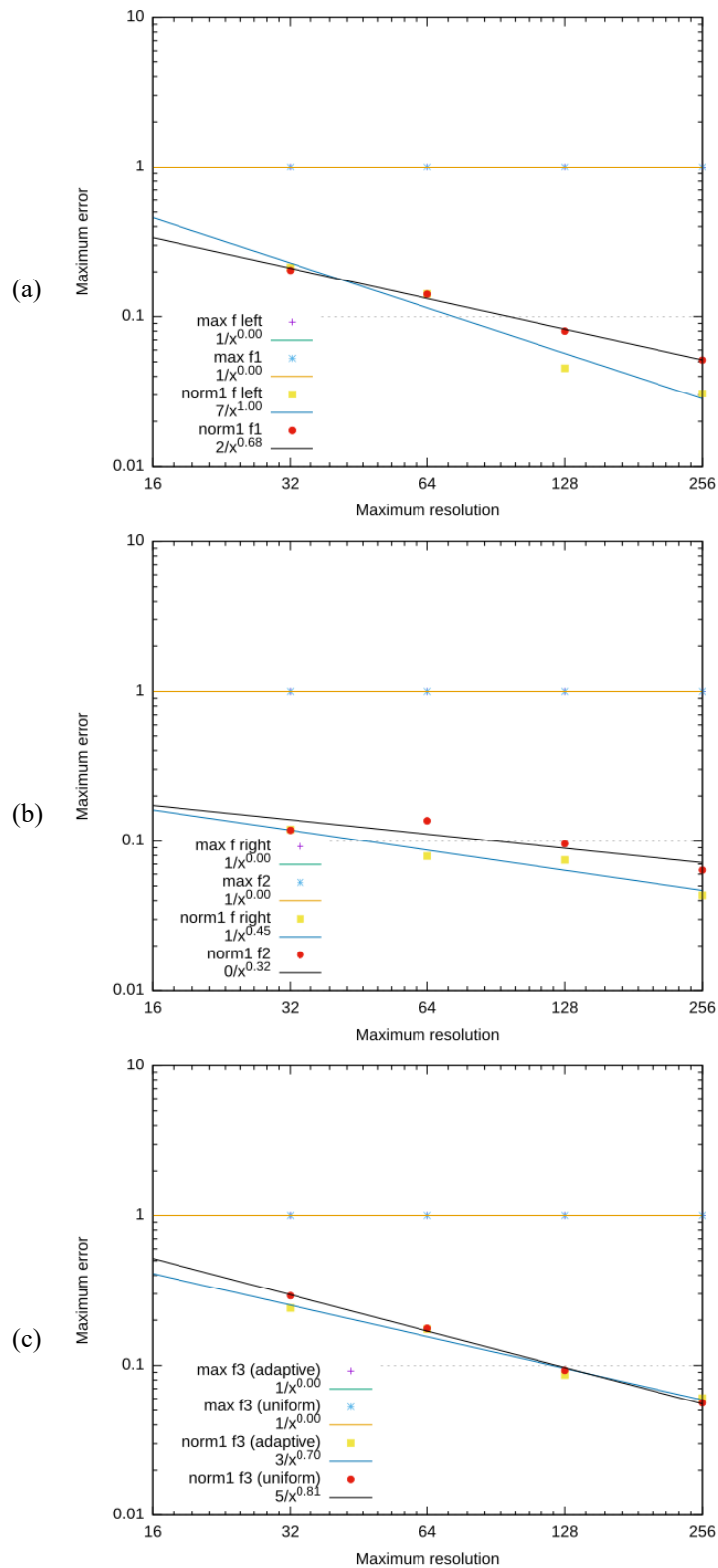


Figure 3.4: Convergence rates for the error shape of the VOF tracer for two-phase and three-phase formulation. a): Left half part of the circle corresponding respectively to f_{left} and f_1 for the two and three-phase formulation with an adaptive grid; b): Right half part of the circle corresponding respectively to f_{right} and f_2 for the two and three-phase formulation with an adaptive grid; c): Outside part of the circle corresponding to phase three f_3 for the three phase formulation with adaptive and uniform grid.

We look now at Figure 3.5, where we show the time evolution of the error on the volume conservation of each VOF tracer for different maximum mesh resolutions. If we look at Figure 3.5-(a) we can see that the maximum error is obtained at the lowest maximum mesh resolution of 2^6 cells in one direction. When the maximum mesh resolution in one direction is increased, the error on the quantity of the VOF tracer of phase one decreases. Now if we look at Figure 3.5-(b) we can observe the same global behaviour than previously. Except, that here at the maximum mesh resolution in one direction of 2^8 the quantity of the VOF tracer two decreases of $\Delta f_2 = 4 \cdot 10^{-3}$ at the end of the simulation. Finally, we look at Figure 3.5-(c) from which we can observe the same global behaviour than previously but a more important decrease of the error when the maximum mesh resolution is increased from 2^6 to 2^8 cells in one direction.

Moreover, from Figure 3.6 where we compare the conservation of the fluid fraction with the two and three-phase formulation, we can see that we have a much more important error with the three-phase formulation than with two-phase formulation.

This test validates the ability of our three-phase formulation to reproduce this classical test within a three-phase flow configuration. Of course, we have to take into account that the error on the shape between the initial and final state has a lower convergence rate with the three-phase formulation than for the two-phase formulation. Also, with the three-phase formulation, a much larger error on the conservation of the VOF tracer than with the two-phase formulation is done. This is partly due to the use of normalization of each fluid fractions by the sum of the fluid fractions.

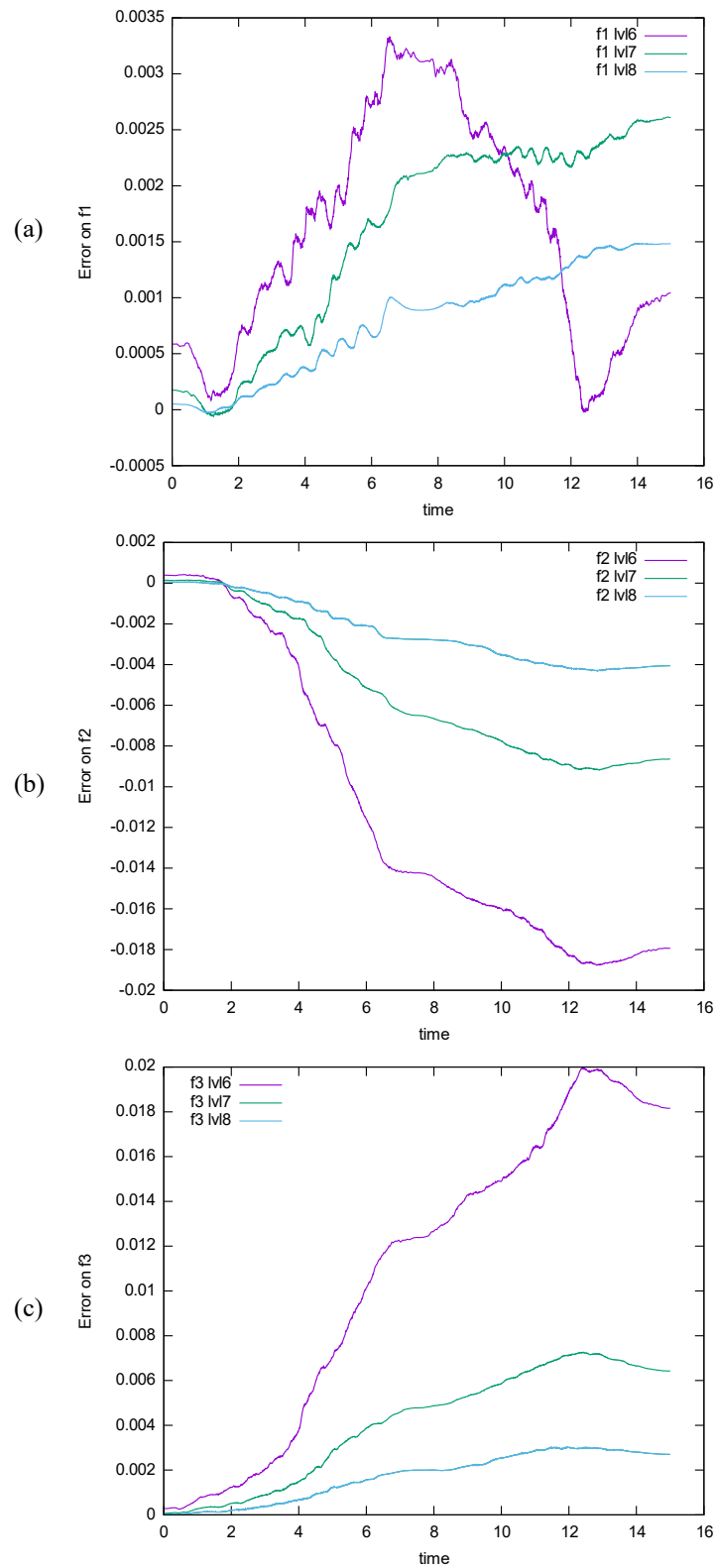


Figure 3.5: Time evolution of the error in the conservation of the VOF tracer for different maximum mesh resolutions for three phase formulation. a): VOF tracer for phase one f_1 ; b): VOF tracer for phase two f_2 ; c): VOF tracer for phase three f_3 .

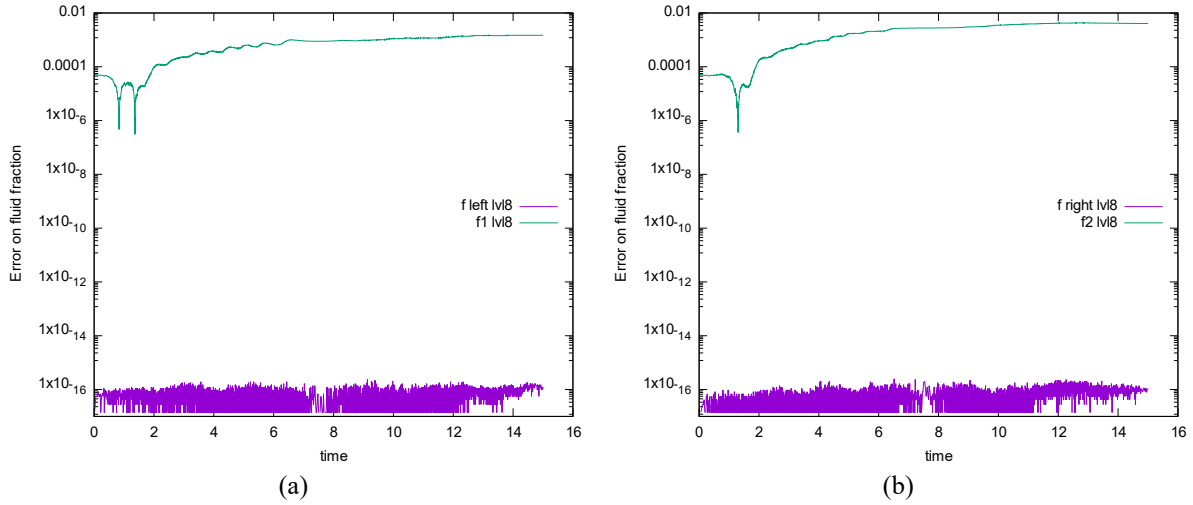


Figure 3.6: Comparison of the time evolution of the absolute value of the error in the conservation of the VOF tracer for two-phase and three-phase formulation at a constant maximum mesh resolution of 2^8 cells. a): Left half part of the circle corresponding respectively to f_{left} and f_1 for the two and three-phase formulation; b): Right half part of the circle corresponding respectively to f_{right} and f_2 for the two and three-phase formulation.

3.5.2 Three-phase surface tension formulation

We now test our three-phase surface tension formulation with the classical test of the spreading of an oil lens at a fluid or solid interface. The spreading of an oil lens can be divided into two different cases depending on the value of the spreading parameter $S = \sigma_{aw} - (\sigma_{ao} + \sigma_{wo})$. As can be seen in Figure 3.7 for the positive value of the spreading parameter a total spreading of the oil lens is expected, and when the spreading parameter is negative a partial spreading of the oil lens will happen. We test here the spreading of an initially spherical oil lens of diameter $D = 0.2m$ at a water-air interface considering that the oil and water phase have the same physical properties and neglecting the effect of gravity (cf. Figure 3.8). The physical properties of all the fluids can be found in Table 3.1.

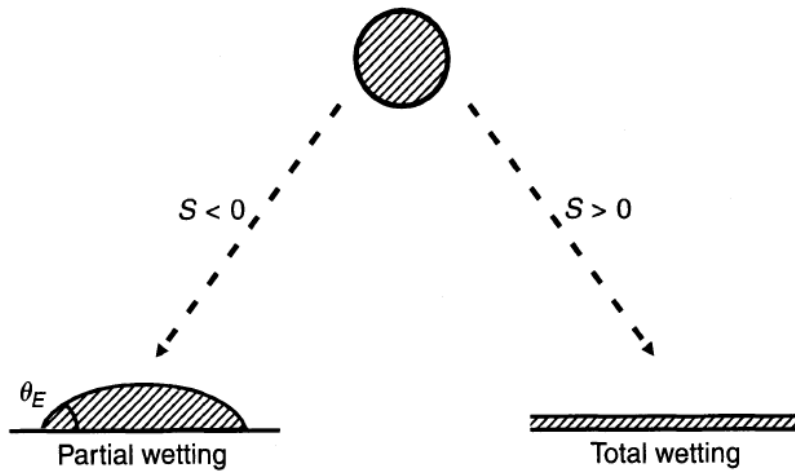


Figure 3.7: Schematic of the possible spreading of an oil lens at a solid interface depending on the value of the spreading parameter $S = \sigma_{aw} - (\sigma_{ao} + \sigma_{wo})$.

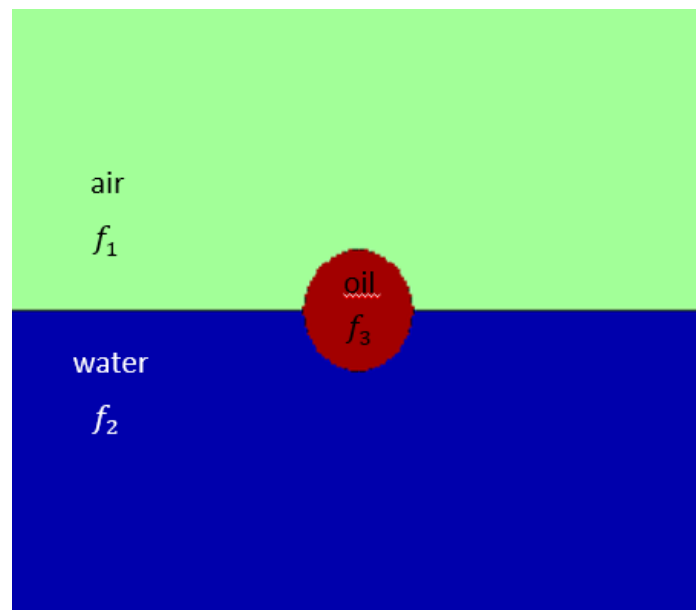


Figure 3.8 : Representation of the fluid fractions at the initial state $t = 0$ with f_1 the air fluid fraction, f_2 the water fluid fraction and f_3 the oil fluid fraction.

Fluid properties		Air	Water	Oil
ρ ($kg.m^{-3}$)		1	1000	1000
μ ($Pa.s$)		10^{-2}	1.0	1.0
Case1 $S < 0$	σ_{aw} ($N.m^{-1}$)	6.10^{-2}		
	σ_{wo} ($N.m^{-1}$)		7.010^{-2}	
	σ_{ao} ($N.m^{-1}$)			$5.0.10^{-2}$
Case2 $S > 0$	σ_{aw} ($N.m^{-1}$)	$8.0.10^{-2}$		
	σ_{wo} ($N.m^{-1}$)		$3.0.10^{-2}$	
	σ_{ao} ($N.m^{-1}$)			$3.0.10^{-2}$

Table 3.1: Physical parameters of the fluids used in the simulation.

This simulation is axisymmetric, and we consider an adaptive grid with a maximum mesh resolution in one direction of 2^8 cells, so there can be a maximum of 51 cells in the diameter of the oil lens. By adjusting the surface tensions and interfacial tension values we will be able to consider the cases of the partial and total spreading of the oil lens. To do so we use the relations (3.23), (3.24) and (3.25) to obtain the phase-specific values required by our numerical model from the physical surface and interfacial tension values of Table 3.1.

3.5.2.1 Partial spreading

We first consider the partial spreading case occurring for a negative value of the spreading parameter. We can see in Figure 3.9 the interface of the oil lens at different instants from the initial spherical shape in Figure 3.9-(a) to a partial equilibrium shape. We can see that globally the shape of the oil lens reaches its equilibrium shape after ten time-units, then its shape does not evolve much. Figure 3.10 shows a zoom on the left part of the oil lens and with the different reconstructed interfaces of each VOF tracer together with the mesh. From Figure 3.10 we can have a confirmation of the previous observation because we can see that the interfaces are not moving too much during the time considered. Also, it appears that the three different interfaces are present only in one cell.

Now, if we look at Figure 3.11-(a) showing the time evolution of the horizontal velocity we can see that despite the important noise observed, the maximum horizontal velocity is of the order of 10^{-2} . We can also note a large peak of the maximum horizontal velocity near the end of the simulation. if we look at Figure 3.11-(b) showing the time evolution of the volume conservation of each VOF tracer we can see that the errors committed for the water and air VOF tracers are symmetric and much larger than the error for the oil phase.

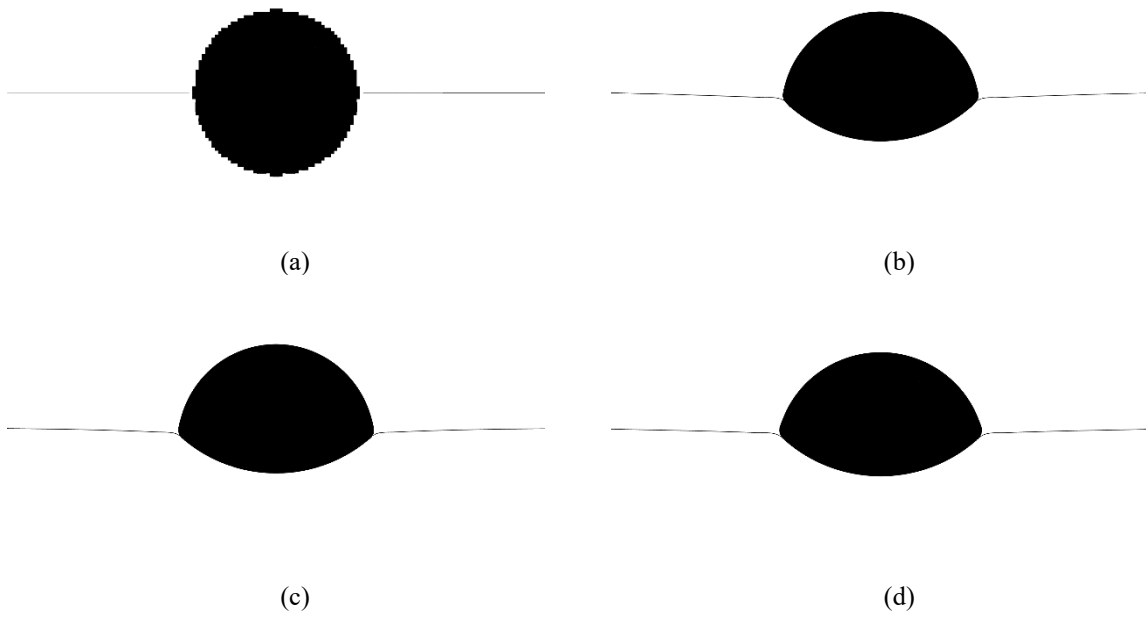


Figure 3.9: Face view of the oil and water VOF interface for the partial spreading case at different instants. The oil interface is filled in black. a): $t = 0$; b): $t = 10$; c): $t = 20$; d): $t = 30$.

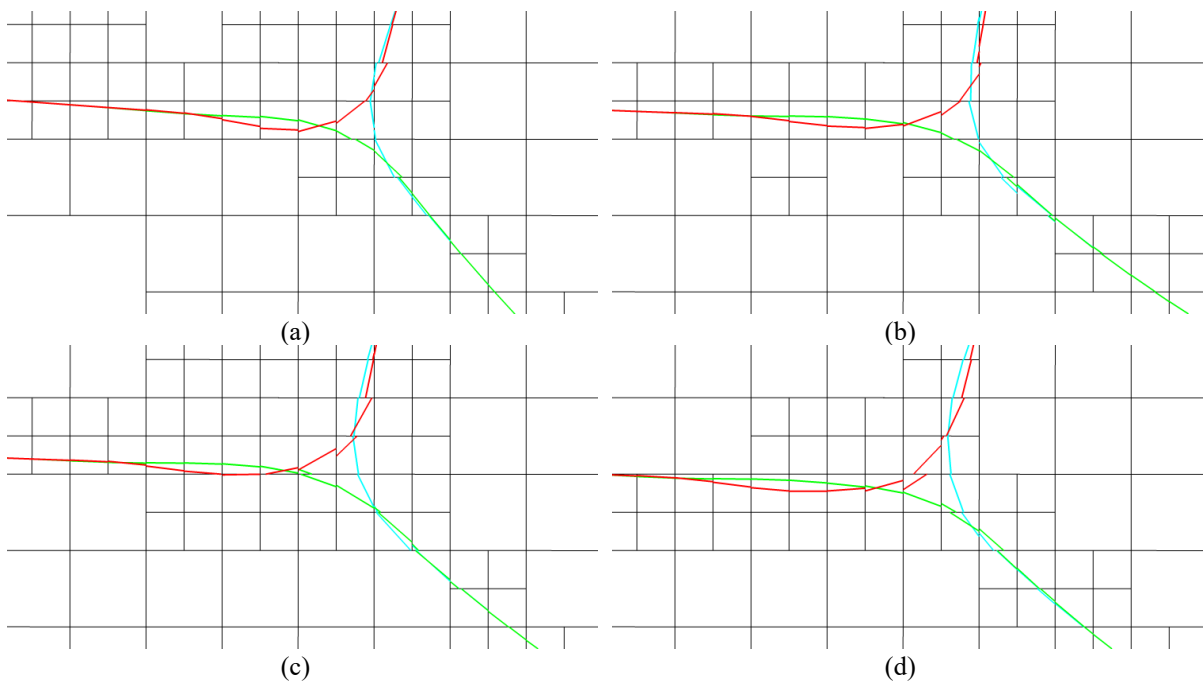


Figure 3.10: Zoom on the left part of the oil lens with the reconstructed interface of each VOF tracer and the mesh represented. The air, water and oil interfaces are coloured respectively in red, green and light blue. a): $t = 20$; b): $t = 25$; c): $t = 30$; d): $t = 35$.

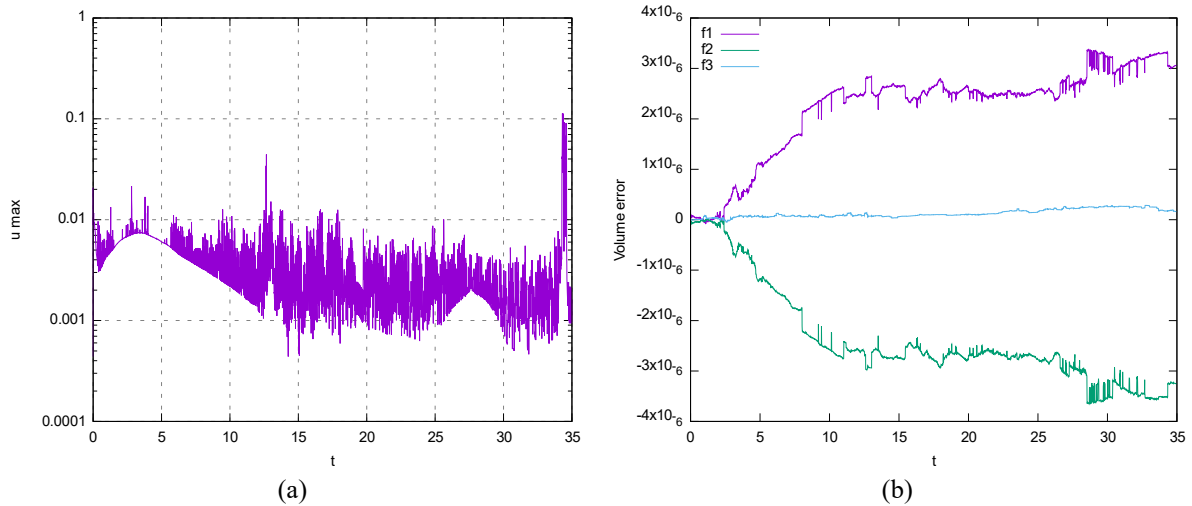


Figure 3.11: Data for the partial spreading case. a): Time evolution of the maximum horizontal velocity; b): Time evolution of the error in the conservation of the VOF tracer.

3.5.2.2 Total spreading

We now consider the case of a positive value of the spreading parameter from which total spreading of the oil lens should occur.

We start by looking at Figure 3.12 where the oil and water interface at different instants is displayed we can see that after ten time-units the initially circular oil lens flattens significantly. It is flattening much more at $t = 20$ but keeps an almost constant height after that time. We do not observe a total spreading of the oil lens over the water-air interface for the simulated time considered. From Figure 3.12 –(c) and (d) we can observe that on the tail of the oil lens, some fragmentation into small droplets is occurring. If we look at Figure 3.13 showing the different reconstructed interfaces corresponding to each VOF tracer we can see that some small blue circles can be identified. These small blue circles correspond to the small oil droplets observed on the tail of the oil lens previously. Furthermore, we can note that in this case, we have more than one cell containing the three different interfaces. Now, if we look at Figure 3.14-(a) showing the time evolution of the maximum horizontal velocity we can see that it presents a large peak after $t = 10$. Also, we can note that before the end of the simulation, the maximum horizontal velocity shows some high values hundred times higher than at the beginning of the simulation. This could reveal the formation of an instability of the horizontal velocity generating a perturbation of the interfaces strong enough to observe oil droplets fragmentation. If we look at Figure 3.14-(b) we can see that the volume conservation of each VOF tracer is nearly of the same order of 10^{-7} .

This test validates the ability of our three-phase surface tension formulation to reproduce the two cases of the spreading of an oil lens considered. Of course, as we have seen, possible issues on the cells containing all the VOF tracers can occur and generate instability leading to an increase of the velocity.

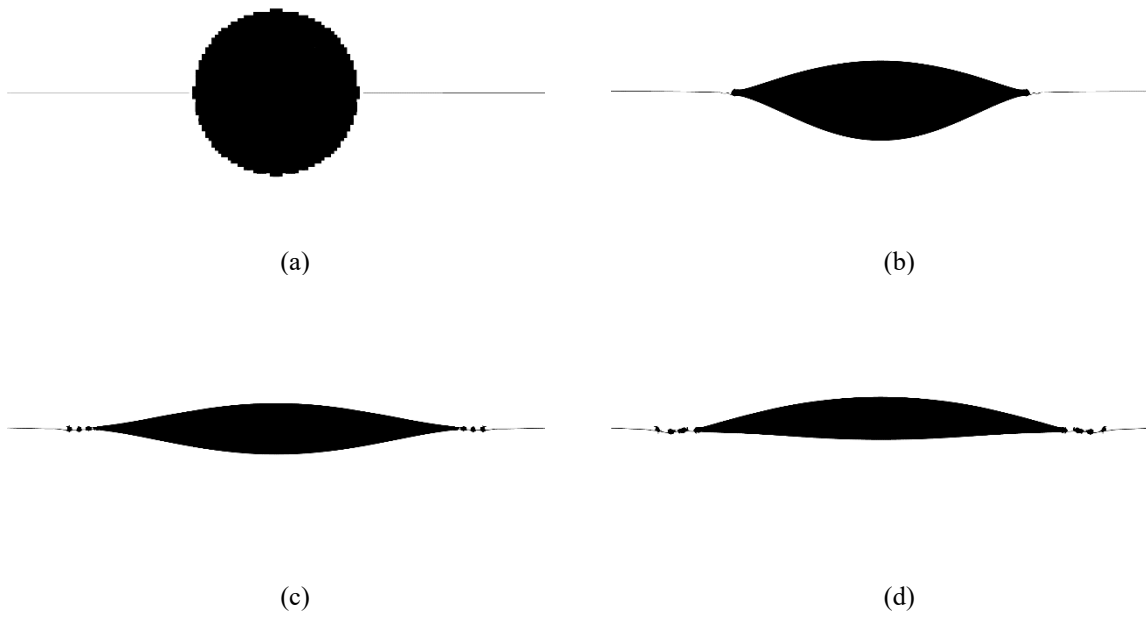


Figure 3.12: Face view of the oil and water VOF tracer for the total spreading case at different instants. The oil interface is filled in black. a): $t = 0$; b): $t = 10$; c): $t = 20$; d): $t = 30$.

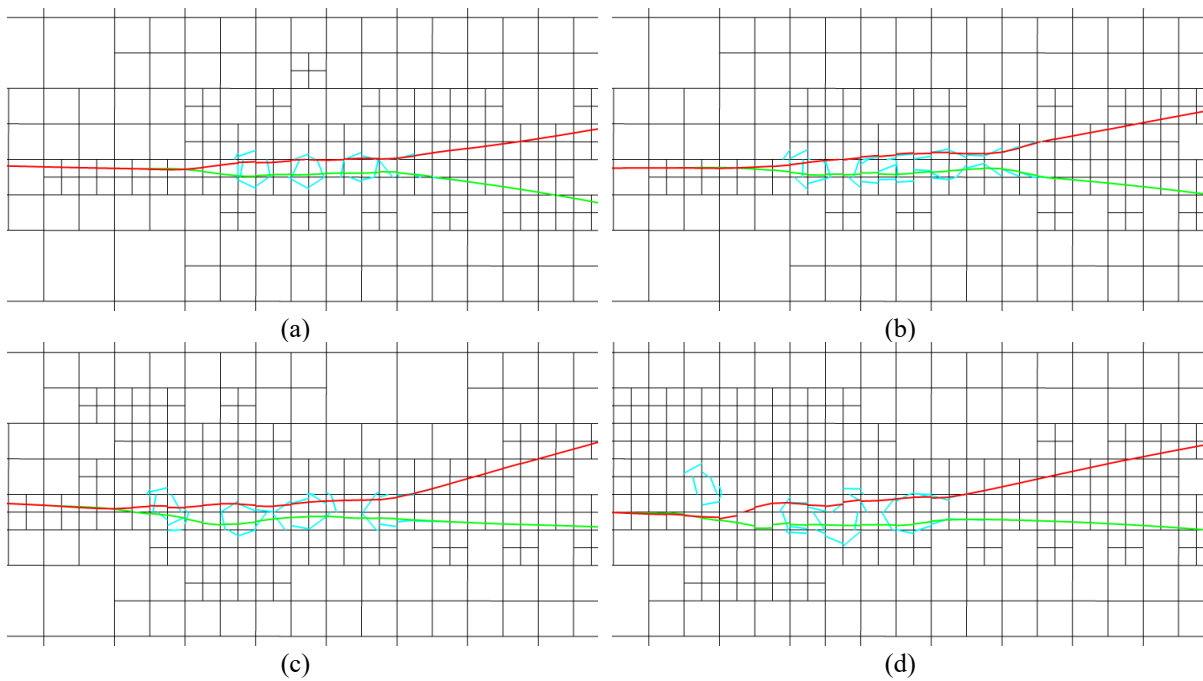


Figure 3.13: Zoom on the left part of the oil lens with the reconstructed interface of each VOF tracer and the mesh represented. The air, water and oil interface are coloured respectively in red, green and light blue. a): $t = 20$; b): $t = 25$; c): $t = 30$; d): $t = 35$.

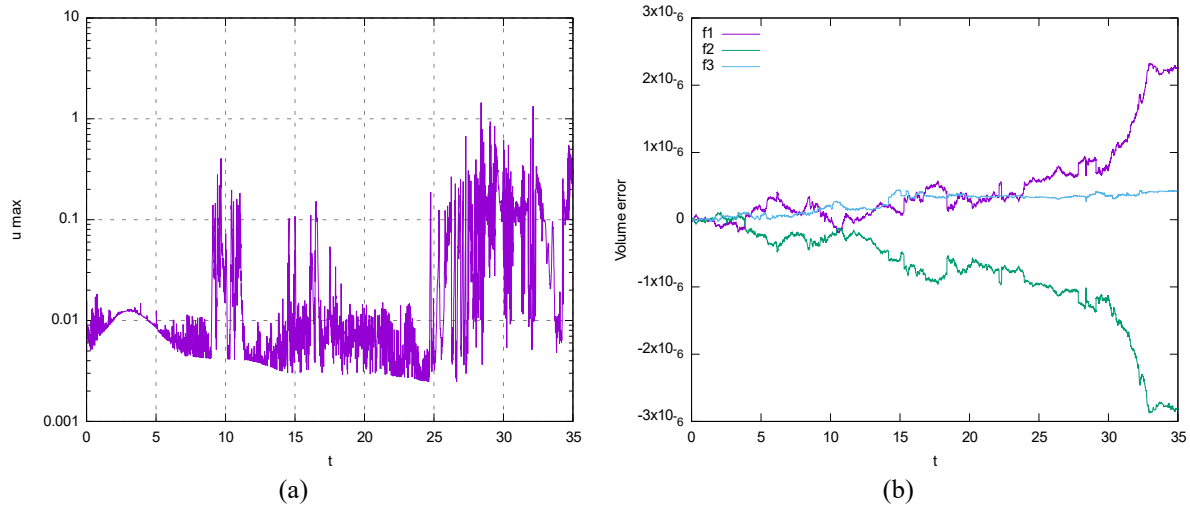


Figure 3.14: Data for the total spreading case. a): Time evolution of the maximum horizontal velocity; b): Time evolution of the error in the conservation of VOF tracer quantity.

3.6 NUMERICAL WATER EXPERIMENT

In the following, we briefly detail the numerical setup used to simulate the water experiment (cf. Figure 3.15). It follows all the dimensions of the water experiment but with only one size of injection diameter (cf. Table 3.2). In Figure 3.15 different colours are used to represent the different boundary conditions used. A no-slip wall boundary condition is set at the bottom face except at the injector where an inflow boundary condition has been set. On the two lateral faces of the ladle, a symmetry boundary condition is considered. At the top face of the numerical domain, we consider an outflow condition with special treatment to avoid backflow. From Table 3.3 showing the physical properties of the fluids in the numerical simulation, the only difference from the water experiment is the value of the air density. In the numerical simulation, we take a value ten times higher than for the water experiment to limit numerical convergence issues due to a high-density ratio between the water and air phase. The influence of the numerical value of the air density has been studied in the work of Esmaeli & Tryggvason [73] and Cano-Lozano *et al.* [74]. The authors reported a small influence of a higher numerical air density on their results. We believe that what is important in our numerical simulation is the density difference between the water and the air phase. This density difference remains high even for a numerical value of the air density ten times higher than in the water experiment.

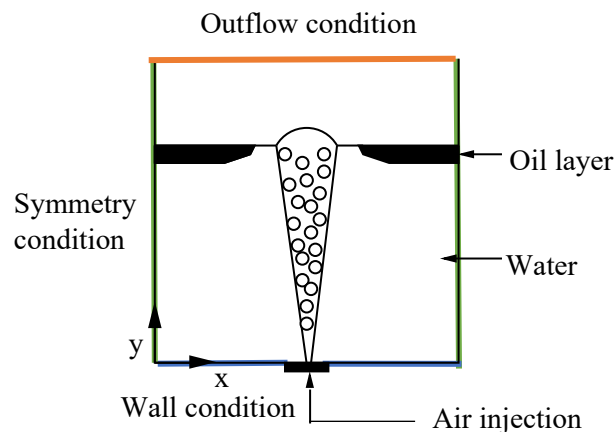


Figure 3.15: Schematic of the numerical setup with the boundary conditions indicated with specific colours.

Characteristic parameter	Numerical case
h_w (m)	0.2
h_o (m)	0.007
L_x (m)	0.27
d_{inj} (m)	$7.9 \cdot 10^{-3}$
Q (l/min)	0.6 – 5.5

Table 3.2: Main geometrical parameters of the numerical simulation.

Numerical fluid properties	Air	Water	Oil mixture
ρ (kg. m ⁻³)	12.25	998	920
μ (Pa.s)	$1.85 \cdot 10^{-5}$	$1.00 \cdot 10^{-3}$	$7.9 \cdot 10^{-2}$
σ_{aw} (N. m ⁻¹)	$7.20 \cdot 10^{-2}$		
σ_{wo} (N. m ⁻¹)		$2.55 \cdot 10^{-2}$	
σ_{ao} (N. m ⁻¹)			$3.17 \cdot 10^{-2}$

Table 3.3: Physical properties of the fluids used in the numerical simulation.

3.7 ESTIMATION OF THE MESH SIZE REQUIRED

In order to have an idea of the smallest scale that has to be considered in our simulation we consider as minimal velocity fluctuation scale the Kolmogorov length scale

$$\eta = \left(\frac{v_w^3}{\epsilon/\rho_w} \right)^{1/4}, \quad (3.27)$$

From the approximation of the kinetic energy dissipation in the configuration of the water experiment established in 2.3 we can directly compute (3.27) from the gas flow rate value

$$\eta = \left(\frac{v_w^3}{gQ/L_x^2} \right)^{1/4}, \quad (3.28)$$

Pope [75] postulated that $\Delta x \leq 2.1\eta$ as a criterion to determine minimum mesh size needed to resolve Kolmogorov length scale in a DNS simulation. The corresponding minimum number of cells can be determined with

$$N_{min} = L_x/(2.1\eta) \quad (3.29)$$

If we apply this with the water model properties it leads at the lowest gas flow rate $Q = 0.6l/min$ to $N_{min} = 7,79 \cdot 10^2$ cells and $\eta = 165 \mu m$. So, a maximum mesh resolution in one direction of 2^{10} cells should be enough to satisfactorily resolve the Kolmogorov length scale. On the other hand, at the highest gas flow rate $Q = 6l/min$ we end up with $N_{min} = 1,38 \cdot 10^3$ cells and $\eta = 92.8 \mu m$. In this case, a maximum mesh resolution in one direction of 2^{11} cells which corresponds to a maxlevel of 11 is necessary.

3.8 SUMMARY

In this chapter we have first briefly presented the library Basilisk and the VOF method in a standard two-phase framework. Then as we are interested in reproducing a three-phase flow we have detailed the adjustment necessary to achieve this goal with Basilisk. In our numerical model each fluid is defined by one fluid fraction. To ensure that the sum of the fluid fractions in one cell remain between zero and one we normalize each fluid fractions by the sum of the fluid fractions. Furthermore, we use a decomposition of the physical surface tension into a phase specific surface tension.

Then, we compared the standard two-phase and our three-phase formulation with the simulation of the revert advection through a vortex of the two halves of a circle. From the obtained results we have observed a slightly better convergence rate for the two-phase formulation than for the three-phase formulation. On the other hand, the error on the conservation of tracer is much higher for the three-phase formulation than for the standard two-phase formulation. However, the high value of the error on the conservation of tracer with the three-phase formulation remain low in comparison to the conservation error of standard level-set method.

Finally, we have tested our decomposition of the physical surface tension into phase specific surface tension by simulating the spreading of an oil droplet at an air water interface. We have seen that we could reproduce the partial spreading of the oil droplet without apparent problem. For the case of the total spreading of the oil droplet we observed at the end of the simulation fragmentation of the oil droplet at its edges. Also, an instability seemed to form in this region at the end of the simulation characterized by much more important velocity.

4 RESULTS- HYDRODYNAMIC CHARACTERIZATION

4.1 EXPERIMENTAL RESULTS

In this chapter, we will mainly measure the effect of the variation of the air flow rate on the flow. We first check the influence of the air injection on the oil physical properties by measuring oil physical properties from samples taken before and after three hours of air injection. From the results of Table 4.1, we can see that there is only a slight difference in the values of the oil physical properties before and after three hours of air stirring. From Table 4.1 the most evident impact of the time of air injection is observed on the interfacial tension between water and oil with a difference around 6% between the two cases. This indicates that the air injection for three hours does not affect too much the physical properties of the oil phase.

	ρ_o ($kg \cdot m^{-3}$)	μ_o ($Pa \cdot s$)	$\sigma_{o/w}$ ($N \cdot m$)
Before air stirring	0.92	$7.91 \cdot 10^{-2}$	$2.73 \cdot 10^{-2}$
After 3h00 air stirring	0.91	$7.85 \cdot 10^{-2}$	$2.57 \cdot 10^{-2}$

Table 4.1: Measurement of the oil physical properties used in our experiment before and after 3h00 of air agitation.

In the following, all the image post-processing has been done using Fiji software (Schindelin *et al.* [76]) which is a distribution of the open-source software ImageJ (Scheider *et al.* [77]). We will consider the parameters of Table 4.2 as the reference parameters for the water experiment and simulation.

Characteristic parameter	Experimental case
h_w (m)	0.2
h_o (m)	0.007
d_{inj} (m)	$7.9 \cdot 10^{-3}$
V_w (L)	14.58
V_o (L)	0.486

Table 4.2: Main geometrical parameters of our experiment for the reference case.

4.1.1 Oil layer fragmentation

In the following, we will try to characterize the oil layer fragmentation phenomena from images of the face view of our water experiment.

We start by looking at Figure 4.1 showing a zoom on the water-oil interface of the face view of our water experiment. The experiment is done with the reference oil volume of $V_o = 0.486l$ for different air flow rates. From the results of Figure 4.1-(a) we can see that the oil layer is almost flat and no oil droplets can be observed in the water at an air flow of $Q = 1l/min$. If the air flow rate is increased to $Q = 4l/min$, the oil layer is not flat anymore and we start to see some oil droplets in the water (cf. Figure 4.1-(b)). Increasing the air flow rate to $Q = 5l/min$ in Figure 4.1-(c) we can see that more oil droplets (cf. white circles in Figure 4.1-(c)) can be identified at various heights in the water. If we look at Figure 4.1-(d) obtained with the maximum air flow rate considered here $Q = 6l/min$, we can see that the oil layer is more deformed and more oil droplets of various size are detached in the water. It seems that more oil droplets are present near the water-oil interface in the regions circled in orange corresponding to water-oil emulsion than deeper into the water. We can also note that the colour of

the oil droplets seems to vary. Some are nearly transparent in the bottom right and other oil droplets have the same colour than the oil layer on the left part near the water-oil interface.

In Figure 4.2 we take images from the same view but this time we increase the oil volume to $V_o = 0.722l$. From Figure 4.2-(a) corresponding to the low air flow rate value we do not observe oil droplets detached and the oil layer is mainly flat. Now, in Figure 4.2-(b) obtained for an air flow rate of $Q = 4l/min$ we can see some almost transparent oil droplets circled in white on the left and right side of the image. Increasing the air flow rate to $Q = 5l/min$ in Figure 4.2-(c) we can see more oil droplets mostly near the water-oil interface in the regions circled in orange corresponding to a water-oil emulsion. Finally in Figure 4.2-(d) obtained at an air flow rate value of $Q = 6l/min$ we can see an important quantity of oil droplets in the entire length. It appears that the oil layer is almost fragmented into oil droplets across its entire length forming a water-oil emulsion with bigger oil fragments compared than in Figure 4.2-(c).

We can note that in Figure 4.1 and Figure 4.2 oil droplet detachment is occurring mainly near the corner and not the faces of the cubic ladle. Also, the colour of the oil layer changes when the air flow rate is increased. In each experiment, there is around thirty minutes of air agitation between the low and high air flow rate value.

In Figure 4.3 we compare the images obtained at $Q = 2l/min$ with a volume of oil $V_o = 0.486l$ after two different times of air injection. We can see from Figure 4.3-(a) obtained few minutes after the start of air injection that the oil layer colour is almost the same as its original colour and presents no sign of oil droplets or water-oil emulsion. If we look at Figure 4.3-(b) obtained after two hours of air injection at various air flow rates we can clearly see that the colour of the oil layer has become darker. We can also identify some oil droplets near the water-oil interface. Also, we can see in the regions circled in orange that a continuous water-oil emulsion with small oil fragments is formed along the water-oil interface.

Now in order to understand why oil droplets of different colours have been identified, we will zoom on the left part of Figure 4.1-(c) and (d) in Figure 4.4. From Figure 4.4-(a) we can see that the oil droplets near the water-oil interface and at the bottom present different colours and shapes. If we look more carefully at the oil droplets circled in white, we can see that they really look like bubbles with a spherical shape but at their top, a darker region can be found. In fact, we think that these oil "droplets" are mainly composed of water encapsulated by the oil phase that is gathering on their top (cf. Figure 4.5) explaining why they have nearly the same colour than the water. We choose to rename these oil "droplets" as anti-bubbles. If we look at Figure 4.4-(b) obtained at an air flow rate of $Q = 6l/min$ this time it is harder to make the distinction between oil droplets and anti-bubbles. If we look at the water-oil interface, we can see that a more important amount of oil droplets is trapped at a water-oil emulsion region at the bottom of the oil layer. By comparing Figure 4.4-(a) and (b) we can see that the height of this water-oil emulsion increases when the air flow rate is increased.

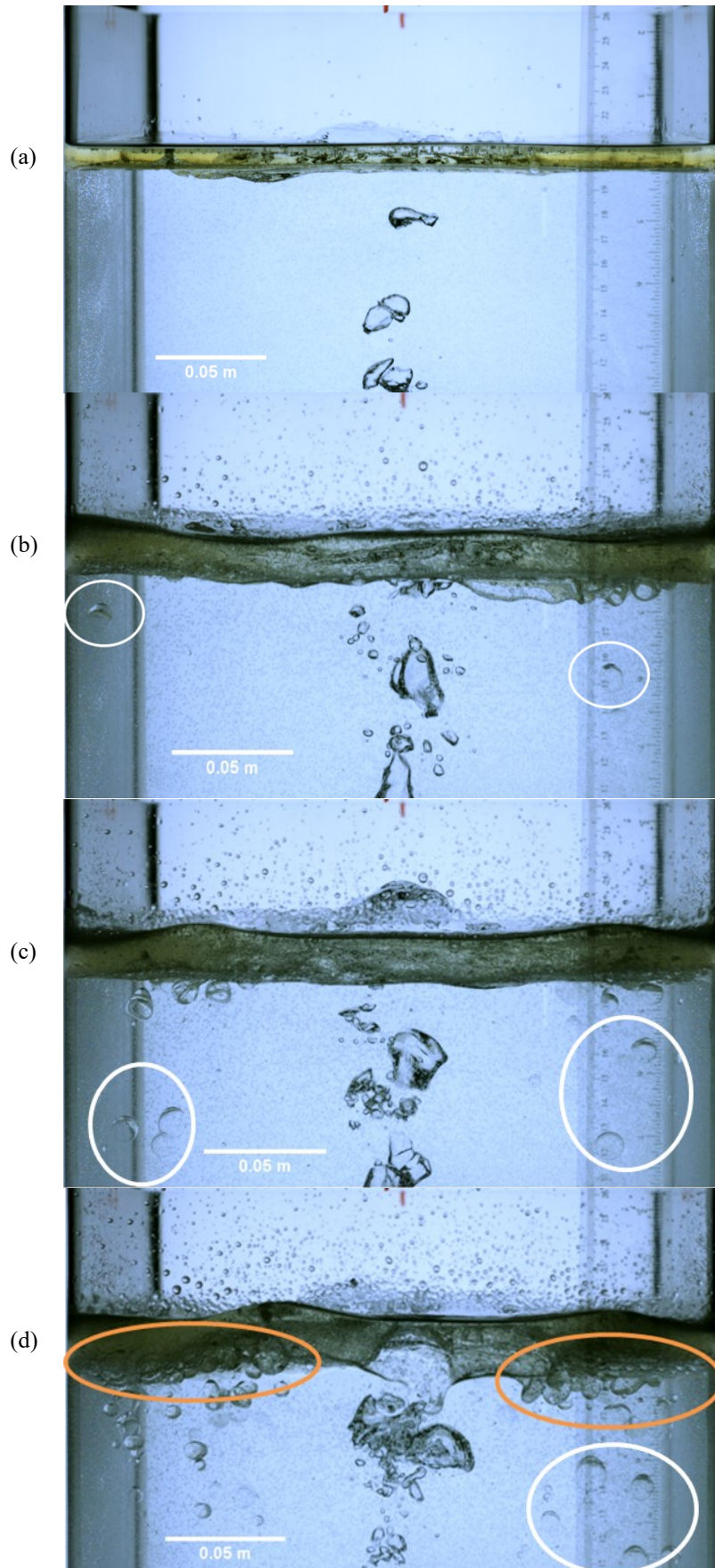


Figure 4.1: Zoom of the face view of our water experiment for different air flow rates. The results are obtained with an oil volume of $V_o = 0.486\text{L}$. a): $Q = 1.0\text{l/min}$; b): $Q = 4.0\text{l/min}$; c): $Q = 5.0\text{l/min}$; d): $Q = 6.0\text{l/min}$. The white and orange circles show respectively the anti-bubbles and the water-oil emulsion.

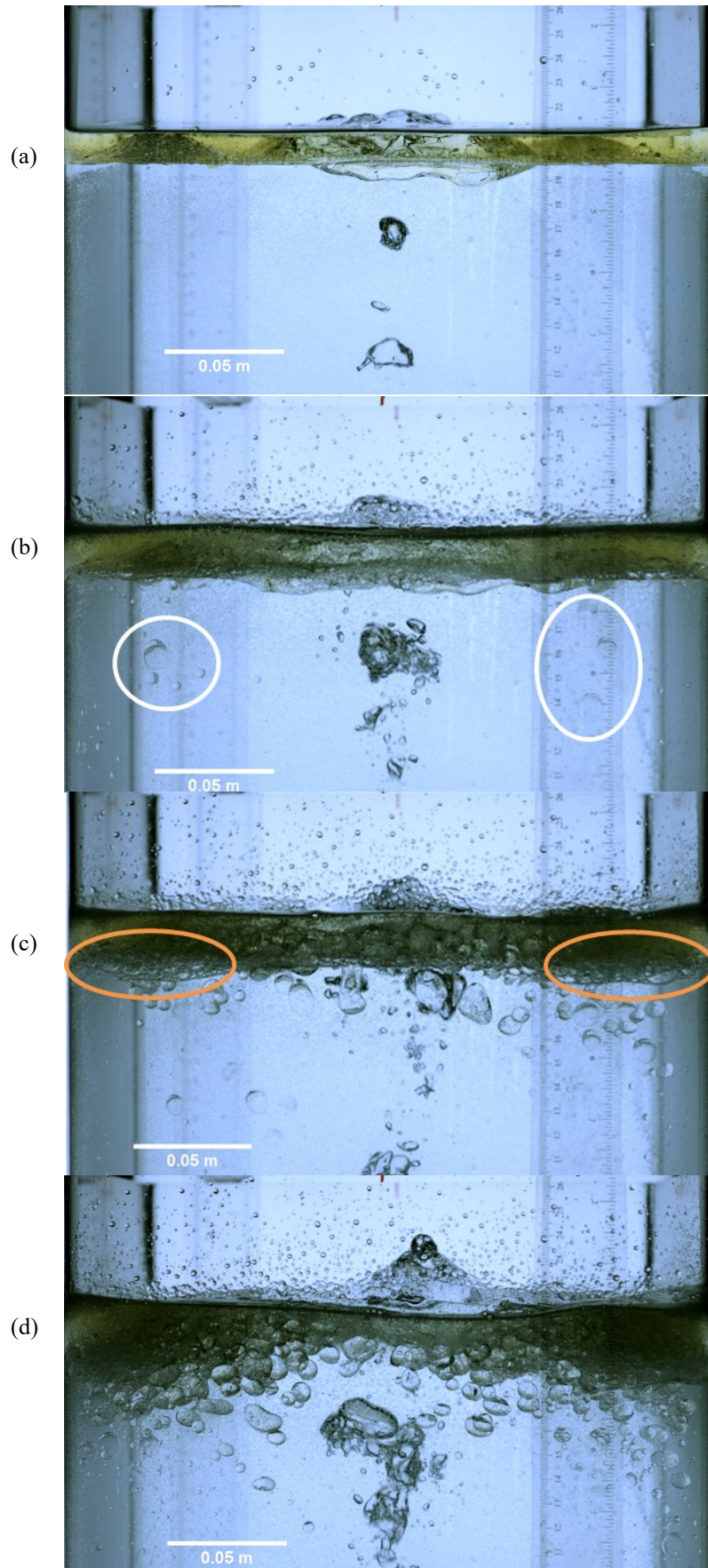


Figure 4.2: Zoom of the face view of our water experiment for different air flow rates. The results are obtained with an oil volume $V_o = 0.722\text{L}$. a): $Q = 1.0\text{l/min}$; b): $Q = 4.0\text{l/min}$; c): $Q = 5.0\text{l/min}$; d): $Q = 6.0\text{l/min}$. The white and orange circles show respectively the anti-bubbles and the water-oil emulsion.

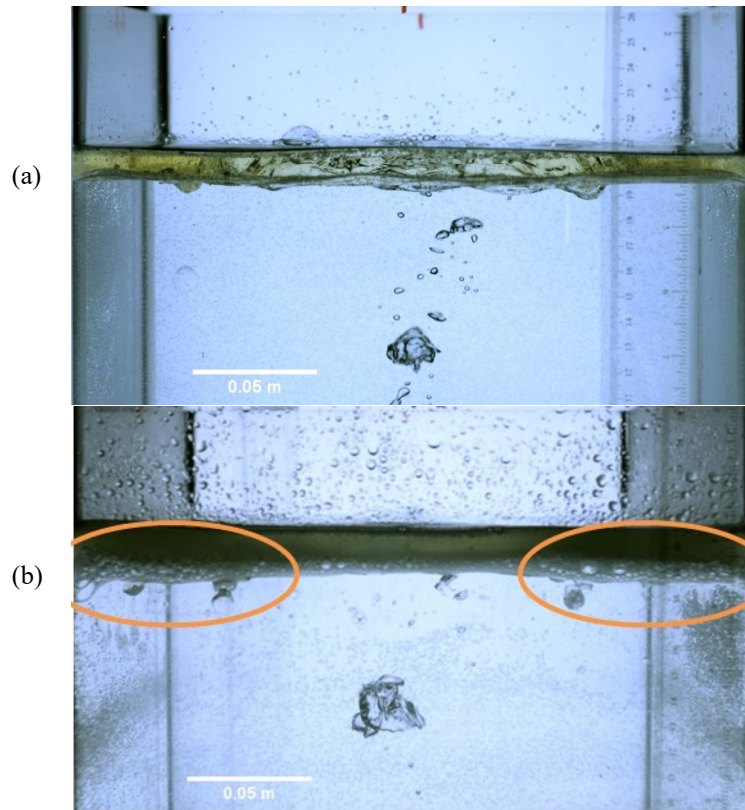


Figure 4.3: Zoom of the face view of our water experiment at the same air flow rate. The results are obtained with an oil volume $V_o = 0.486\text{l}$. a): after the start of air injection; b): after 2 h of air injection. The orange circles show the water-oil emulsion.

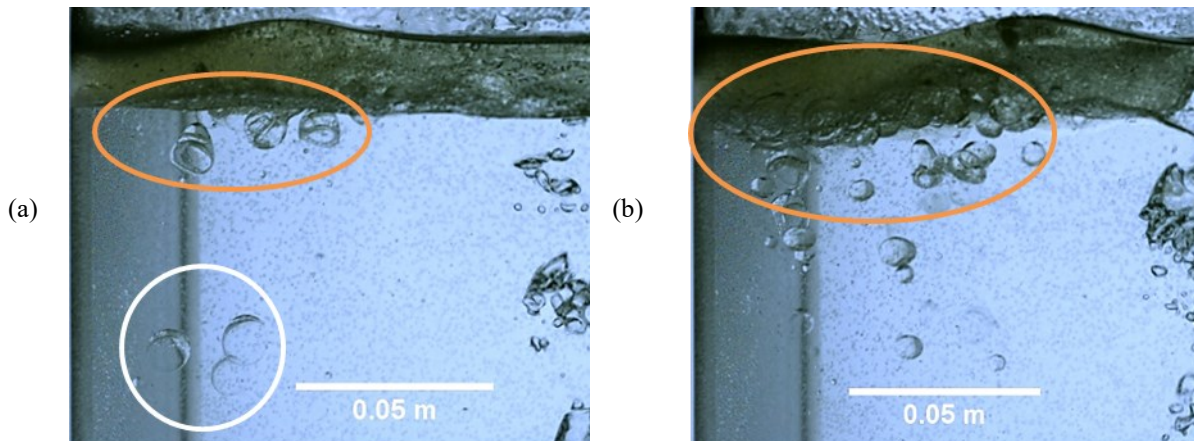


Figure 4.4: Zoom of the face view of our water experiment for different air flow rates. The results are obtained with an oil volume of $V_o = 0.486\text{l}$. a): $Q = 5.0\text{l/min}$; b): $Q = 6.0\text{l/min}$. The white and orange circles show respectively the anti-bubbles and the water-oil emulsion.

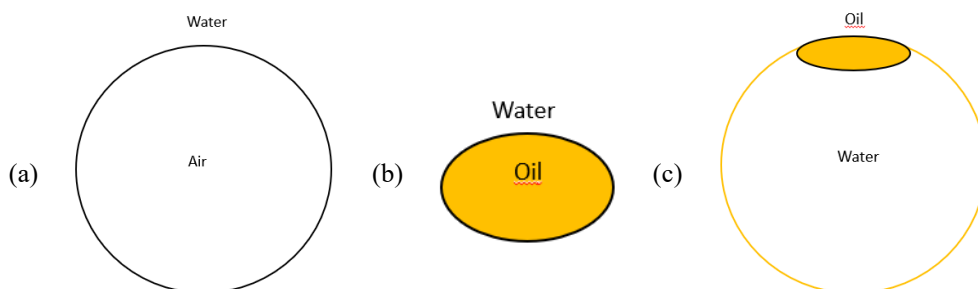


Figure 4.5: Schematic of an a) air bubble; b) oil droplet; c) anti-bubble.

4.1.2 Open eye

We record the images of the top surface of the water experiment with a video camera with an acquisition speed of 30 *fps*. By this mean it is possible to follow the highly dynamical deformation of the oil layer under the influence of gas injection. In the left image of Figure 4.6 showing an instantaneous image of the top view of the ladle, we can clearly identify the open eye of the oil layer contour with a yellow line and the bubbles spout contour in orange. On the other hand in the right picture of Figure 4.6 showing a time-averaged intensity image of the open eye of the oil layer, it is harder to identify the open eye and the bubbles spout contour. This is due to the small colour difference between the oil and the water phase and the presence of trapped bubbles along the oil layer. For these reasons, it has not been possible to extract automatically the open eye contour, so we choose to rather plot manually the open eye contour for four frames separated by approximately 1.8s for each air flow rate.

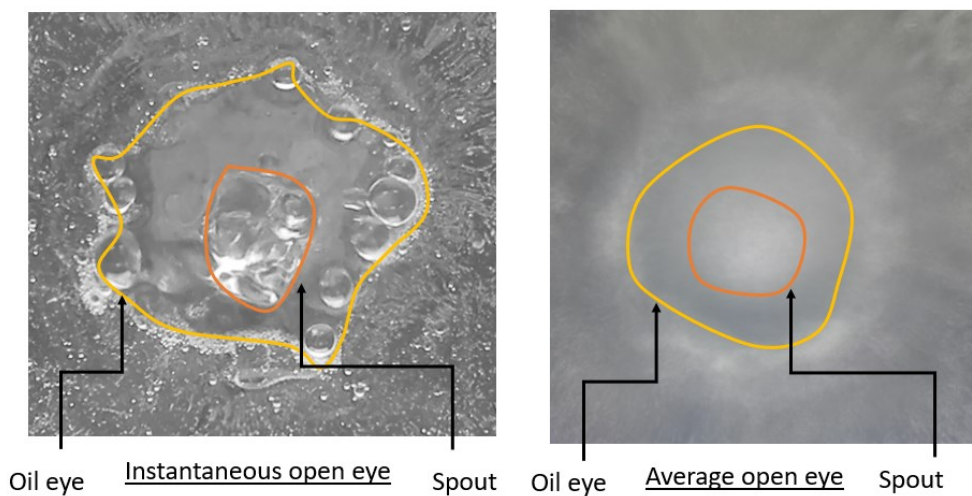


Figure 4.6: Instantaneous and average open-eye image at 0.6l/min, colour code: yellow: eye contour; orange: spout zone

4.1.2.1 Reproducibility test

We first test the reproducibility of our experimental method to capture the open eye area by comparing the results obtained with the same configuration done on different trials. From the results of Figure 4.7, we can observe a good reproducibility with an error between the two trials contained within the error bar. This indicates that both the agitation of the oil layer, image acquisition and post-processing of the images with ImageJ are reasonably reproducible.

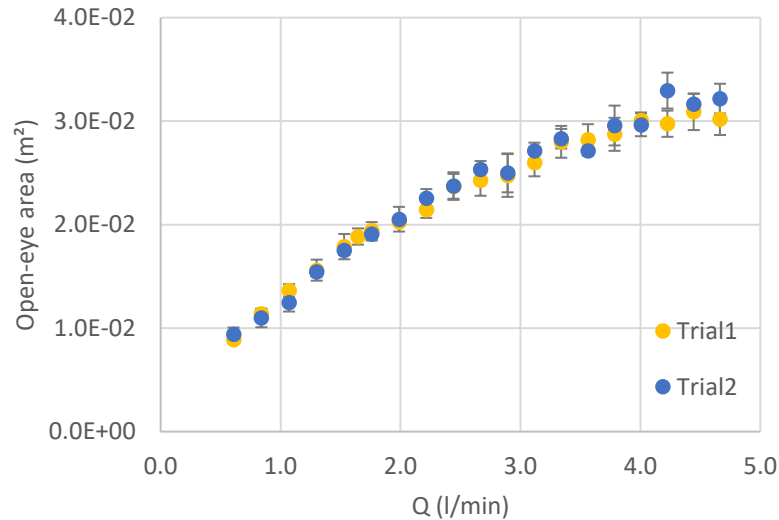


Figure 4.7: Open eye area as a function of the injected air flow rate with standard deviation measured from our experiments obtained with the same configuration but measured on two different trials.

4.1.2.2 Measurement

Now, If we look on Figure 4.7 and Figure 4.8, we can see that for the range of air flow rates considered, the open-eye area is continuously increasing until $Q = 5\text{ l/min}$, then it tends to increase more slowly at a high air flow rate. It appears also from Figure 4.8 that the size of the injection diameter has only a limited influence on the open eye area value. We can also note that the open eye area standard deviation seems to be higher at high air flow rate than at low air flow rate and of comparable magnitude between the two injection diameters.

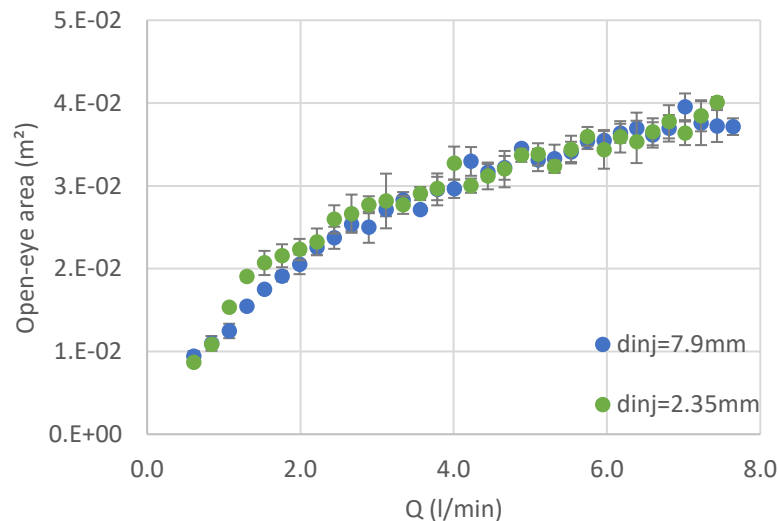


Figure 4.8: Open-eye area with standard deviation as a function of air flow rate measured from our experiments for two different injection diameters.

Now, we fix the injection diameter to the reference size of $d_{inj} = 7.9\text{ mm}$ and we vary the oil volume. We can see from Figure 4.9 that the open eye area value decreases when the oil volume is increased compared to the results obtained with the reference oil volume of $V_o = 0.486\text{ l}$. As one would expect, increasing the oil volume increases the height of the oil layer and thus, increases the resistance to open

eye formation. We can also note that the open eye area evolution as a function of the air flow rate for both oil volume can be perfectly fitted by a logarithmic function. As described by the open-eye model in 2.3 the open-eye area can be given by

$$A_o = C_A \ln\left(\frac{N}{N_c}\right), \quad (4.1)$$

where $C_A = 10\alpha\pi c_\ell^2 h_w^2$ and the critical Froude number for open eye formation is

$$N_c = \left(\frac{\Delta\rho h_o}{\rho_w h_w}\right)^{1/10}. \quad (4.2)$$

From the expression of the modified Froude number we have $C_{A,Q} = 2C_A$ where $C_A \simeq 0,0063m^2$ from our experimental results. Taking $\alpha = 1/3$ within the bubble plume assumption and $c_\ell = 0,081$ we find $C_A \simeq 3.310^{-4}m^2$. We are a bit far from the experimental results, the open eye in the experiment is much wider than the theoretical one. An important discrepancy source comes from the c_ℓ estimation.

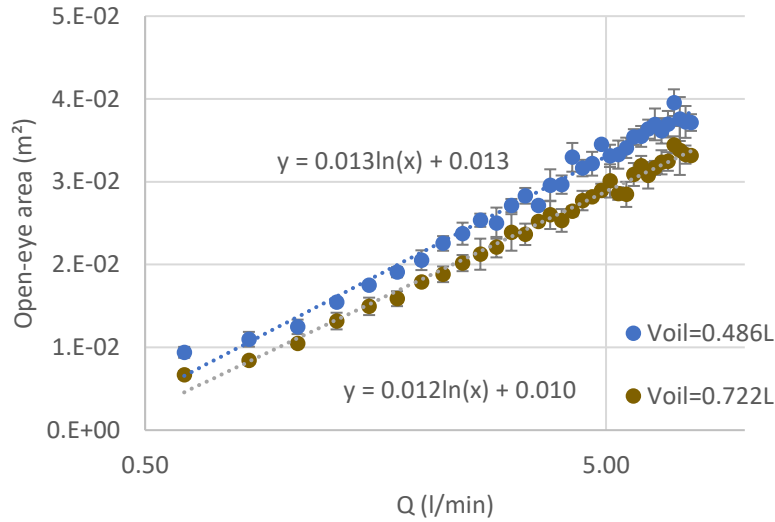


Figure 4.9: Open-eye area with standard deviation as a function of air flow rate measured from our experiments for two different oil volumes.

4.2 NUMERICAL RESULTS

In the following, we will try to characterize the hydrodynamics of the water experiment from the numerical simulation.

4.2.1 Mesh convergence

We will start the study of the numerical results by measuring the effect of the refinement of the mesh on the flow. From Figure 4.10 where we show the maximum mesh resolution in a slice of the domain, we can see that the mesh is much more refined in the bubble plume region and at the water-air interface than in the bottom corner.

If we compare Figure 4.10-(a) and (b) even if the bubble plume region appears to be more refined we do not see a huge difference when increasing the maximum mesh resolution in one direction by a power two from 2^9 to 2^{10} cells. If we look at Figure 4.12-(a) we can see the influence of the maximum mesh resolution in one direction on the injected air flow rate. As the maximum mesh resolution is increased the relative difference with the setting point value of the air flow rate decreases from 10% to 1% with a maximum number of cells in one direction of respectively 2^9 and 2^{11} cells. This can be explained by a better discretization of the circular injector by cubic cells when the mesh resolution is increased.

Now we are interested to visually check the changes in the grid when the mesh resolution is increased. Figure 4.11 shows the air and oil interfaces at the same air flow rates but two different maximum mesh resolutions in one direction. Comparing Figure 4.11-(a) and (b) we can see that globally the bubble plume and the oil layer look the same, but the large amount of air fragments that can be seen in Figure 4.11-(a) seems to have decreased in Figure 4.11-(b). If we look at the histogram of the number of bubbles in Figure 4.12-(b) this observation is not confirmed. When the maximum mesh resolution in one direction is increased the number of bubbles is also increasing but, the equivalent diameter of the bubbles decreases making them harder to identify visually. The bubbles with a smaller equivalent diameter than the minimum grid size are not physical in fact they are air fragments artificially formed by our numerical model.

We will look now to the effect of mesh refinement on the kinetic energy. In Figure 4.13 we have plotted the phase-specific evolution of the kinetic energy as a function of time for three different mesh resolutions. If we look at Figure 4.13-(c) where the water kinetic energy is displayed we do not see a real difference when increasing the maximum mesh resolution in one direction. If we look now at Figure 4.13-(a) we can see a difference in the transient regime between zero and two seconds where the kinetic energy at a mesh resolution of $level = 10$ corresponding to a minimum grid size of $\Delta x = 264 \mu\text{m}$ presents a more abrupt increase than the others. If we look now at Figure 4.13-(b) where the oil kinetic energy is displayed, we can see again some differences during the transient regime especially with the higher mesh resolution of a $level = 11$ corresponding to a minimum grid size of $\Delta x = 132 \mu\text{m}$. The kinetic energy increases seem to be delayed compared to lower mesh resolutions.

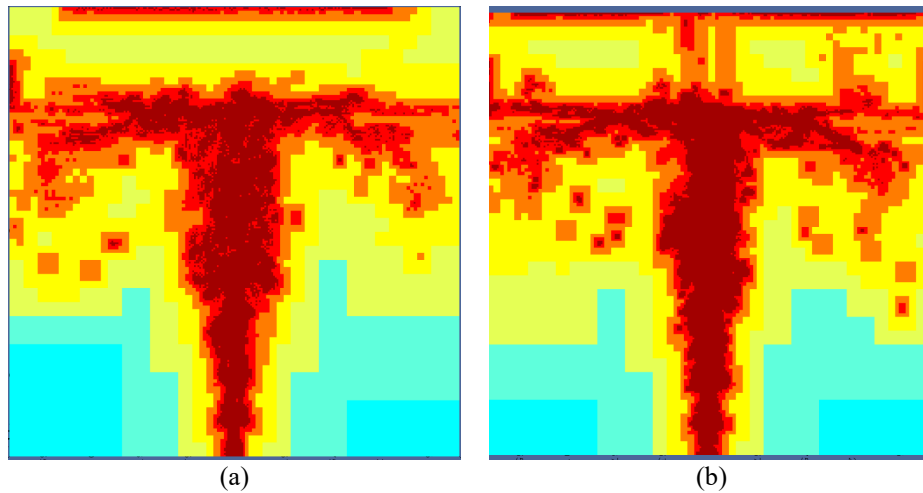


Figure 4.10: Front view of the simulation where we display the maximum mesh resolution in one direction at the same air flow rate $Q = 0.6\text{l/min}$. The minimum and maximum values are coloured respectively with blue and red colour. a): minimum grid size of $\Delta x = 527 \mu\text{m}$ at $t = 8.1\text{s}$; b): minimum grid size of $\Delta x = 264 \mu\text{m}$ at $t = 8.1\text{s}$.

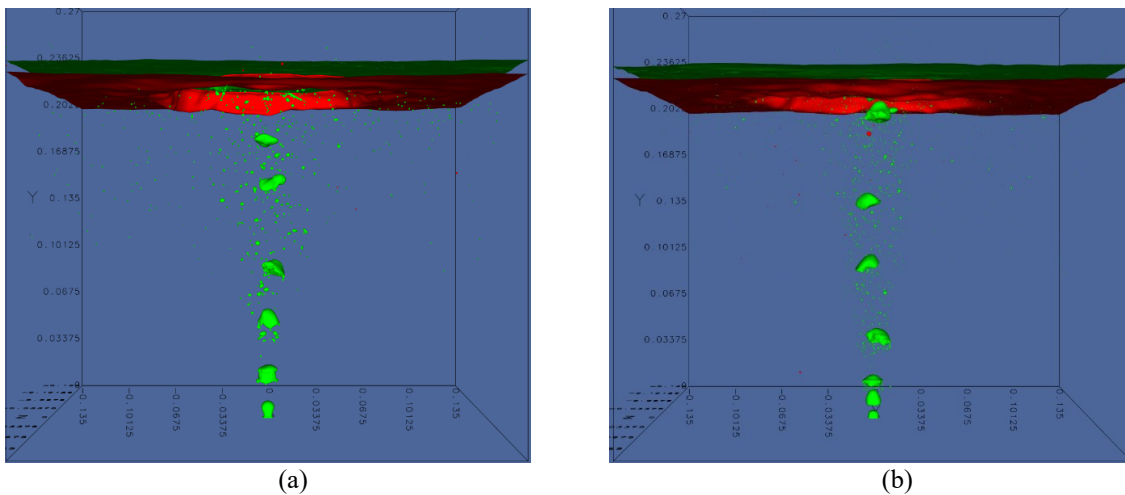


Figure 4.11: Front view of the simulation where we display instantaneous air and oil interfaces coloured respectively in green and red obtained at the same air flow rate $Q = 0.6\text{l/min}$. a): minimum grid size of $\Delta x = 527 \mu\text{m}$ at $t = 8.1\text{s}$; b): minimum grid size of $\Delta x = 264 \mu\text{m}$ at $t = 8.1\text{s}$.

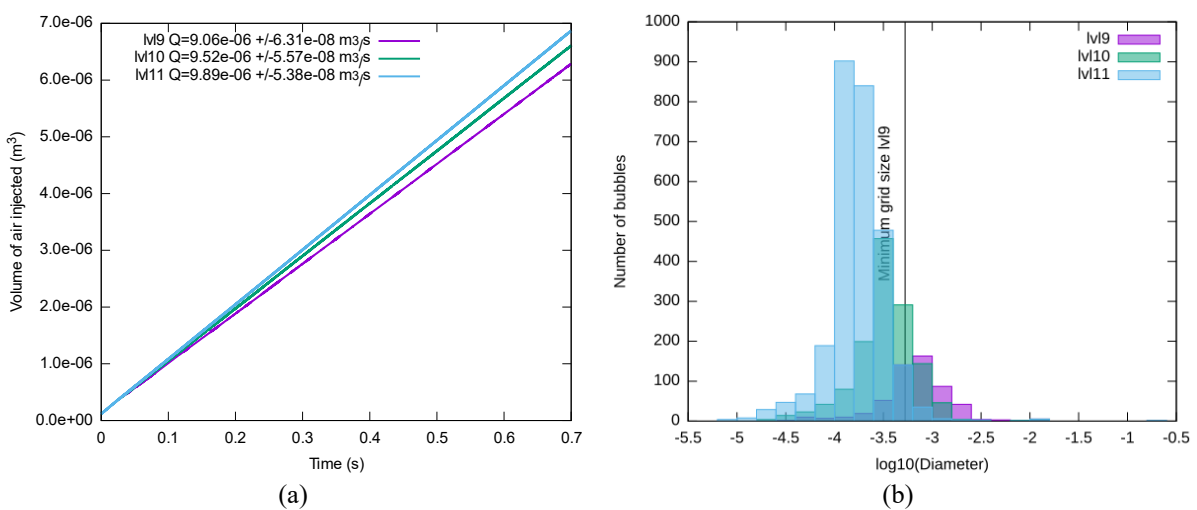


Figure 4.12: Comparison of data obtained at the same air flow rate of $Q = 0.6\text{l/min}$. a): Volume of air injected as a function of time for different maximum mesh resolutions in one direction. The setting point value of the air flow rate is $Q = 10^{-5} \text{m}^3/\text{s}$; b): Histogram of the number of bubbles as a function of their equivalent diameter at $t = 3\text{s}$, the solid lines represent the minimum grid size for the lower mesh resolution.

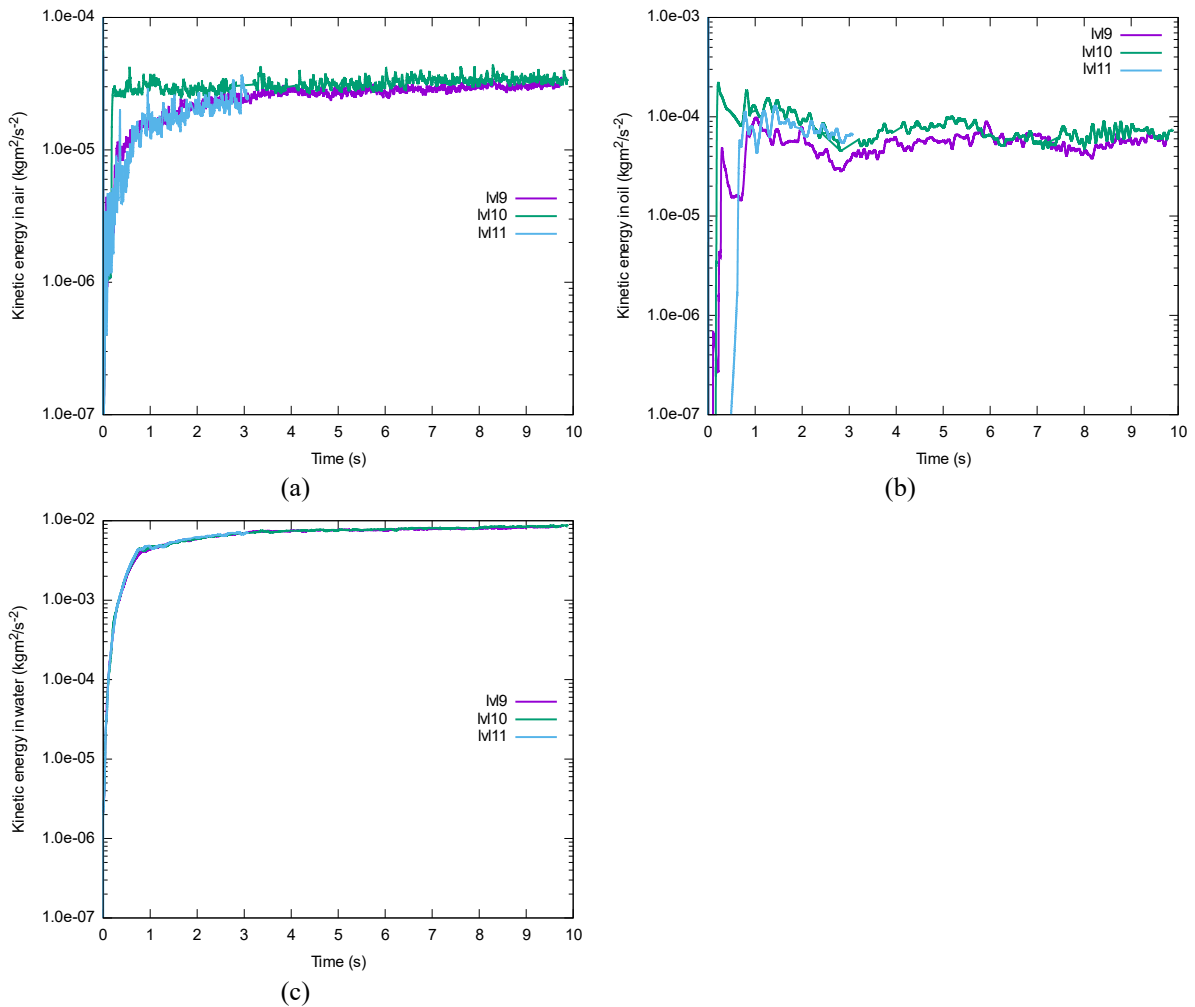


Figure 4.13: Comparison of the phase-specific Kinetic energy obtained at the same air flow rate of $Q = 0.6\text{l}/\text{min}$ with different mesh resolutions. a): Kinetic energy of the air phase; b): Kinetic energy of the oil phase; c): Kinetic energy of the water phase

4.2.2 Instantaneous results

In the following, we will compare visually the effect of the air flow rate value on the fluids by comparing images at three different air flow rates. First, we look at images from the front view of the simulation in Figure 4.14. If we compare Figure 4.14-(a), (b) and (c) we can clearly see a difference in the size and shape of the air bubbles in the plume. As the air flow rate is increased the size of the bubbles is also increasing, the number of air fragments increases drastically, and it is more difficult to distinguish separated bubbles. If we look now at the oil phase we can see that when the air flow rate is increased from Figure 4.14-(a) to Figure 4.14-(c) the oil layer gets more agitated, this can be illustrated by the formation of ligaments in Figure 4.14-(b) or by gravity waves perturbing the oil layer in Figure 4.14-(c). When the agitation is strong enough it will cause a fragmentation of the oil layer into oil droplets of significant size that are transported at various height in the water in Figure 4.14-(c). If we look now to Figure 4.15 where we show a top view of the simulation with the oil interface displayed we can see that the size of the open eye increases when the air flow rate is increased. If we compare Figure 4.15-(b) and Figure 4.15-(c) the difference is less striking between $Q = 2.5\text{l}/\text{min}$ and $Q = 5.5\text{l}/\text{min}$ than when comparing with Figure 4.15-(a) corresponding to the low air flow rate.

If we look at Figure 4.15-(a) and Figure 4.15-(c) we can see that more irregularities on the edge of the open eye can be seen at a high air flow rate and it seems that the edge is not smooth anymore in Figure 4.15-(c).

We look now at Figure 4.16, where we have plotted a comparison of the time evolution of the kinetic energy for different air flow rates. From the results of the kinetic energy of the water in Figure 4.16-(a) we can see that as one would expect, the kinetic energy increases when the air flow rate increases and that the transient regime is much more abrupt at high air flow rate. Also, it seems that the kinetic energy obtained for an air flow rate $Q \geq 2.5l/min$ has not totally converged toward a pseudo permanent regime for the time considered. If we look now at the kinetic energy of the oil phase in Figure 4.16-(b) we can see that the transient regime is appearing and finishing quicker for high air flow rate than low air flow rate. Also, the value of the kinetic energy presents a difference of a factor ten between an air flow rate of $Q = 0.6l/min$ and $Q = 5.5l/min$. We also observe more fluctuations of the kinetic energy at a high air flow rate than at a low air flow rate.

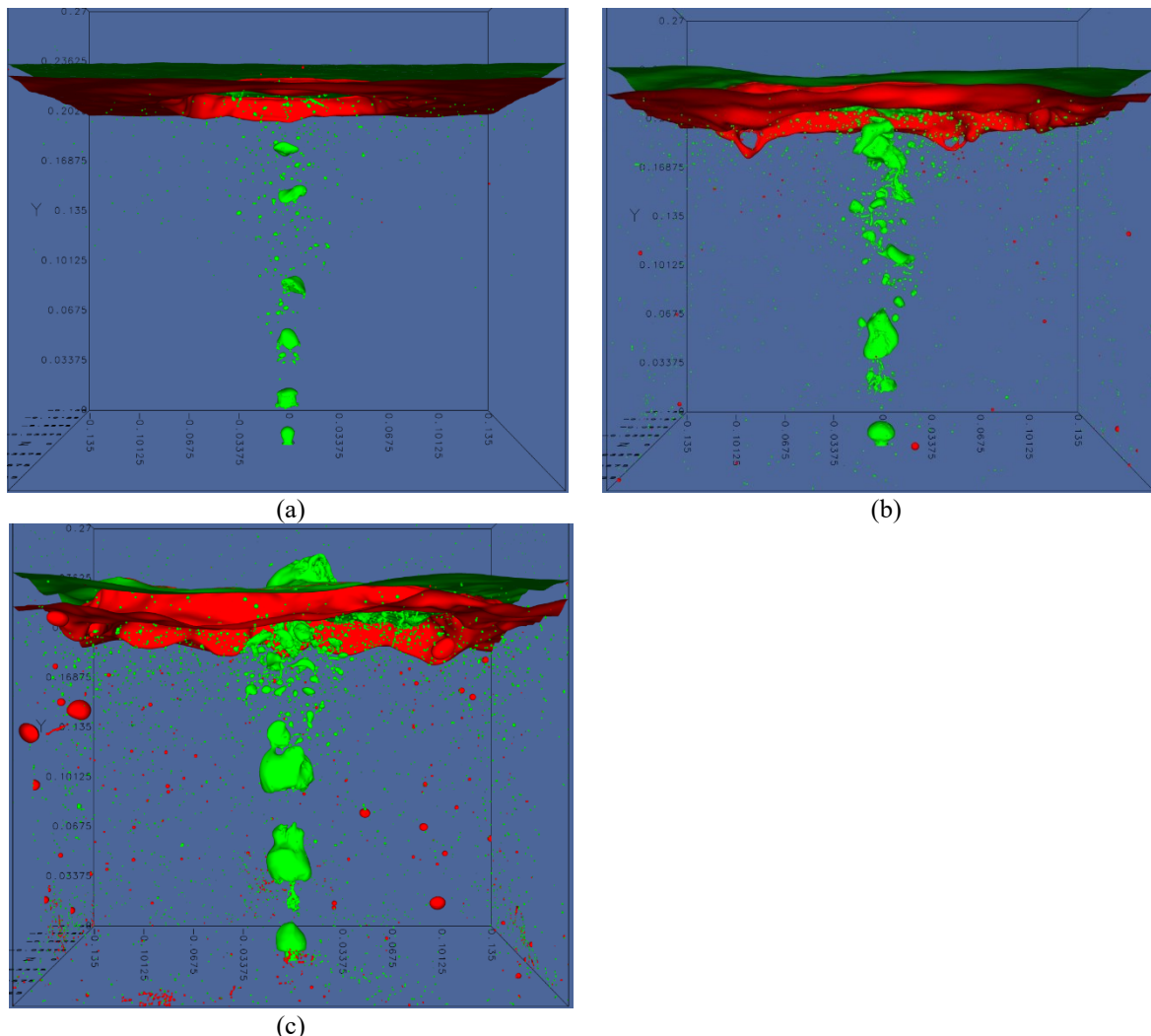


Figure 4.14: Front view of the instantaneous air and oil interfaces coloured respectively in green and red obtained with a minimum grid size of $\Delta x = 527 \mu m$. a): $Q = 0.6l/min$ at $t = 8.1s$; b): $Q = 2.5l/min$ at $t = 8.1s$; c): $Q = 5.5l/min$ at $t = 8.1s$.

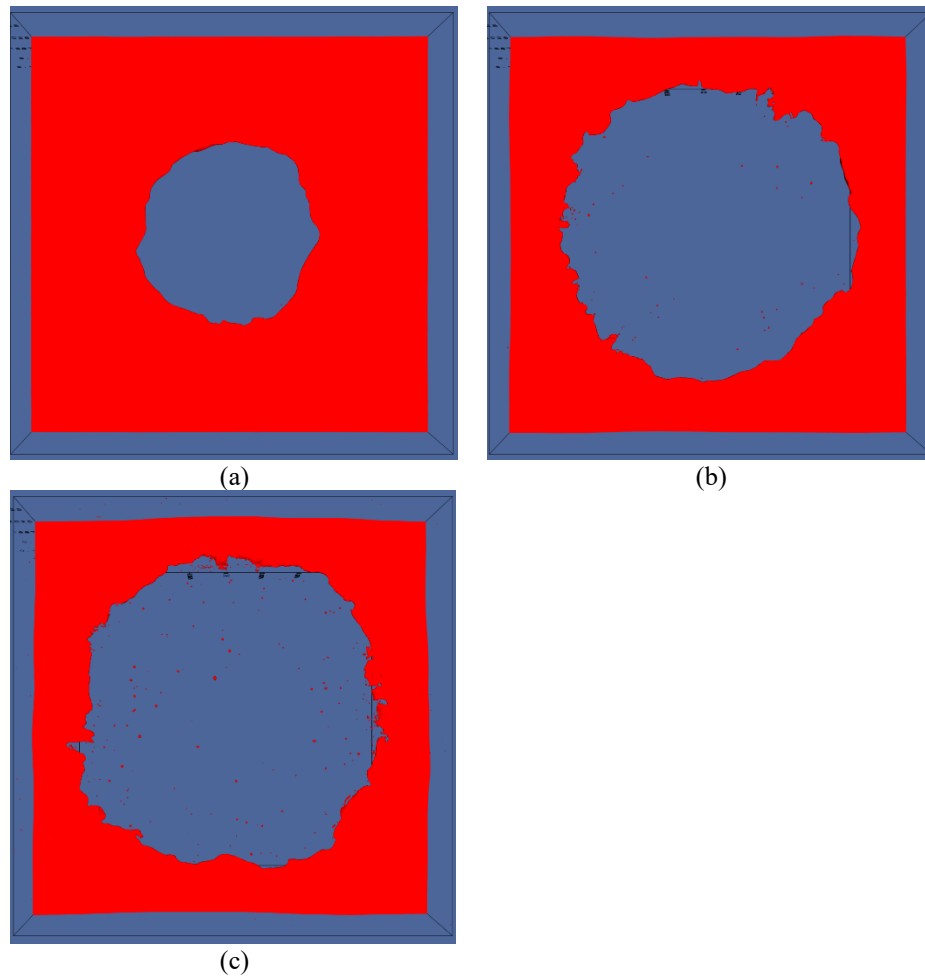


Figure 4.15: Top view of the instantaneous oil interface coloured in red obtained with a minimum grid size of $\Delta x = 527 \mu\text{m}$. a): $Q = 0.6\text{l/min}$ at $t = 8.1\text{s}$; b): $Q = 2.5\text{l/min}$ at $t = 8.1\text{s}$; c): $Q = 5.5\text{l/min}$ at $t = 8.1\text{s}$.

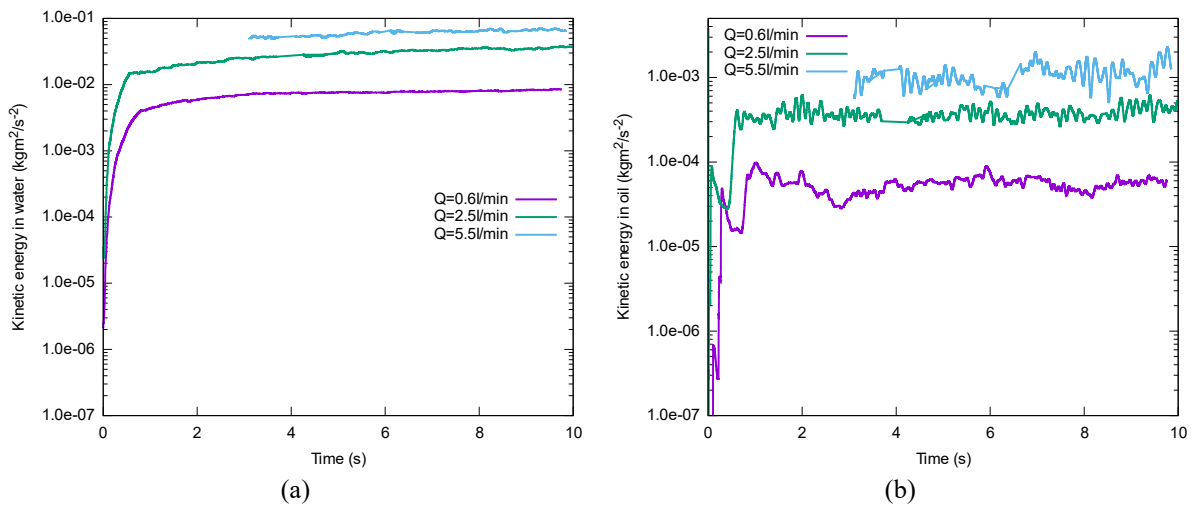


Figure 4.16: Comparison of the phase-specific Kinetic energy obtained with a minimum grid size of $\Delta x = 527 \mu\text{m}$ but with different air flow rates. a): Kinetic energy of the water phase; b): Kinetic energy of the oil phase.

4.2.2.1 Oil layer fragmentation

In the following, we will try to characterize the oil fragmentation from the numerical simulation. As previously seen the phenomenon of fragmentation of the oil layer happen only at a particularly high air flow rate. However, we have to keep in mind that because we start the simulation with a flat oil layer, the formation of the open eye due to the first bubbles reaching the free surface will generate an important fragmentation of the oil layer. As in the real experiment, the oil fragments are expected to merge back to the oil layer after a certain time.

In Figure 4.17 we have represented a zoomed face view of the oil interface at an air flow rate of $Q = 4.5\text{ l/min}$ at different instants. We start by looking at Figure 4.17-(a) where we can see that the oil interface is highly agitated and we can identify an oil droplet detached near the left wall, and two oil sheets. The main oil sheet is located on the front side and a smaller one can be identified in the back of the oil layer. From Figure 4.17-(b) representing the same view but 0.1s later we can see that two ligaments are forming, one in the front and another one in the back of the oil layer. If we look at Figure 4.17-(c) we can see that the ligament at the front of the oil layer is getting thinner and an oil droplet seems to be formed at its end. We can also remark that holes on the oil sheet on the right side of the front of the oil layer are forming. Finally, in Figure 4.17-(d) we can see still see the ligament in the front of the oil layer which has still not yet been fragmented into droplets. Also, oil ligaments have succeeded to the oil sheet previously identified due to the action of the holes formed. A similar phenomenon has been observed in the simulation of the atomisation of a spray in a quasisplanar in the study of Ling *et al.* [62].

Now we will verify the influence of the air flow rate on the oil droplets formation. In Figure 4.18 we have plotted histograms of the number of oil droplets as a function their equivalent diameter for different air flow rates. The results of Figure 4.18-(a) are obtained at $t = 3.1\text{ s}$ that is just after the open eye in the oil layer has been formed. From Figure 4.18-(a) we can see that when the air flow rate is increased the number of oil droplets is also increasing. The oil droplets presenting an equal or smaller equivalent diameter than the minimum grid size can be considered as oil fragments. If we look at the results obtained at an air flow rate of $Q = 4.5\text{ l/min}$ we can also note that the amount of physical oil droplets of equivalent diameter higher than 10^{-3} m increased compared to lower air flow rate. This corresponds to the large oil fragments that are formed during the formation of the open eye (cf. Figure 4.14-(c)). Now, if we look at the results of Figure 4.18-(b) obtained at $t = 9.7\text{ s}$ we can see that the number of oil droplets presents a sharper Gaussian distribution than previously. We can also note that the number of physical oil droplets has decreased except for the high air flow rate of $Q = 4.5\text{ l/min}$ where more small oil droplets can be observed. This illustrates the fact that after that the open eye has been fully formed most of the large oil fragments are merging back the oil layer.

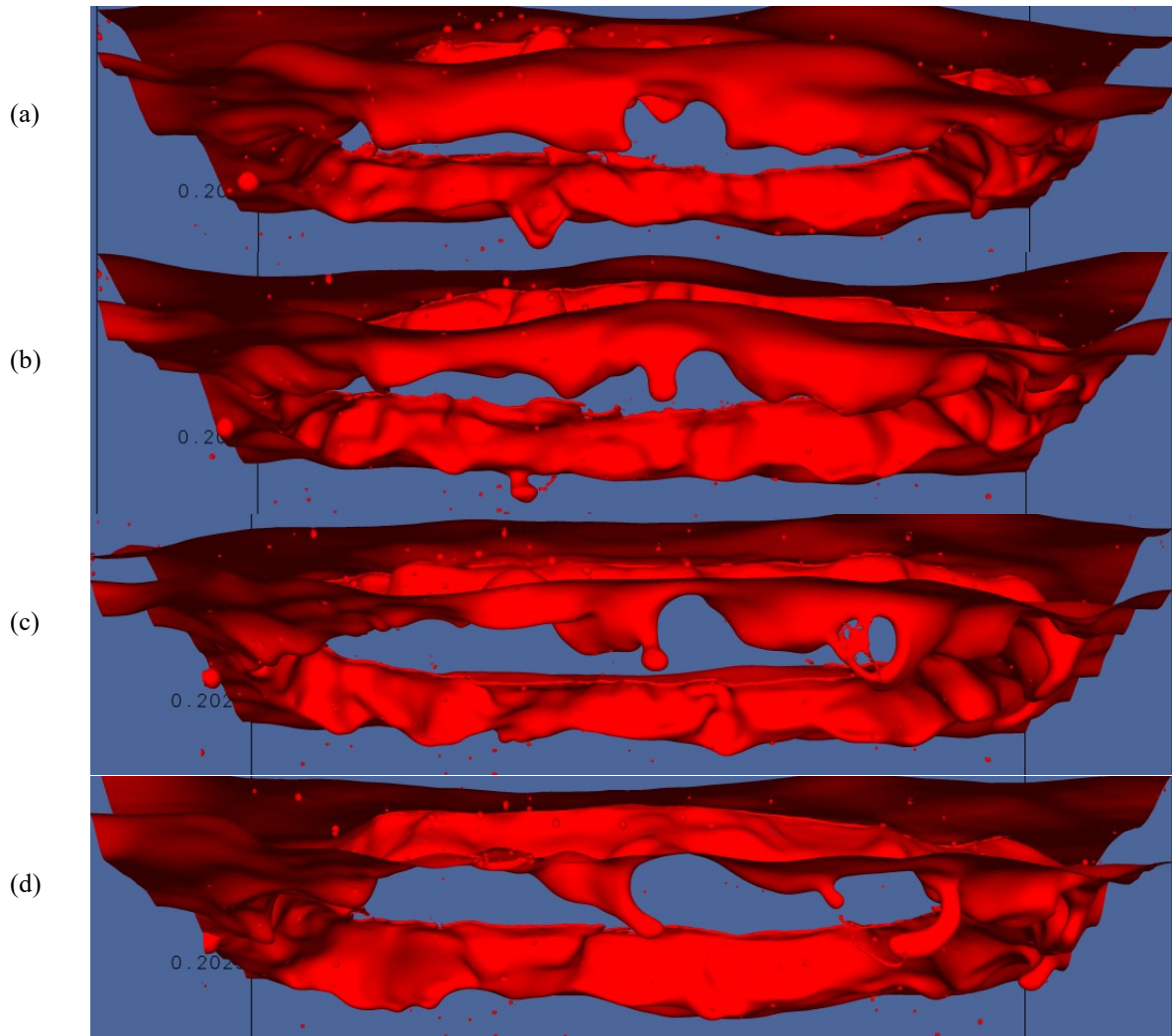


Figure 4.17: Zoom of the face view with the oil interface represented in red at different instants. The images are obtained from a simulation at an air flow rate of $Q = 4.5\text{ l/min}$ and with a minimum grid size of $\Delta x = 527\ \mu\text{m}$. a): $t = 9.6\text{ s}$; b): $t = 9.7\text{ s}$; c): $t = 9.8\text{ s}$; d): $t = 9.9\text{ s}$.

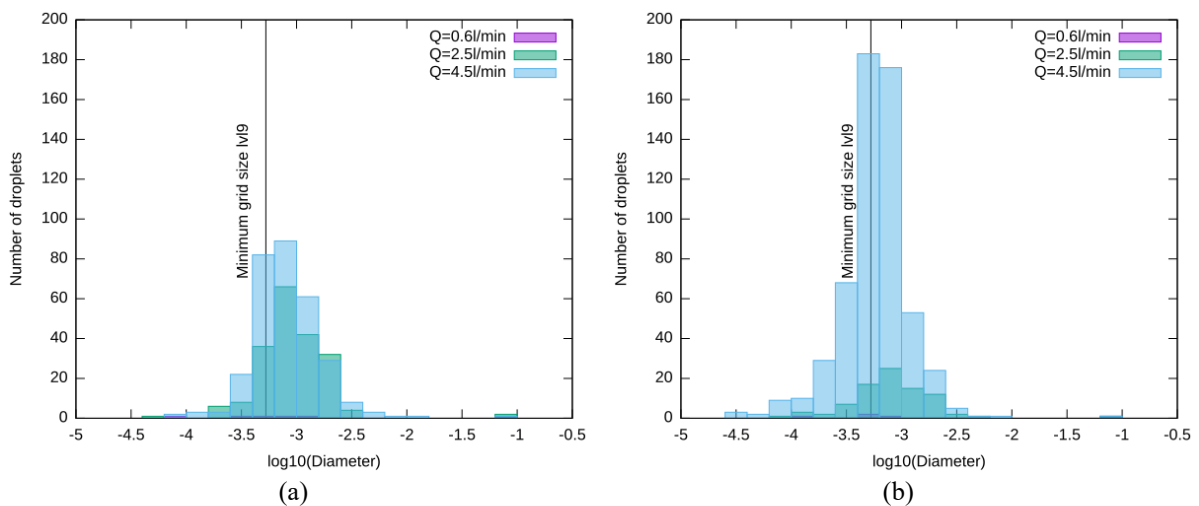


Figure 4.18: Histogram of the number of oil droplets as a function of their volume for different air flow rates and at different instants. Results obtained from simulations with a minimum grid size of $\Delta x = 527\ \mu\text{m}$. a): $t = 3.1\text{ s}$; b): $t = 9.7\text{ s}$.

4.2.2.2 Open eye of the oil layer

To capture the open eye numerically first we do simulations of the water experiment with the same configuration, then we post-process the generated images of the top view of the oil interface with the software ImageJ to get the open eye area. As we can see from Figure 4.19 the oil interface is coloured in red and the other phase in blue making the distinction between the two-phase much more easier compared to the images from the experimental data. Taking advantage of this we can obtain the temporal evolution of the open eye area from the numerical images.

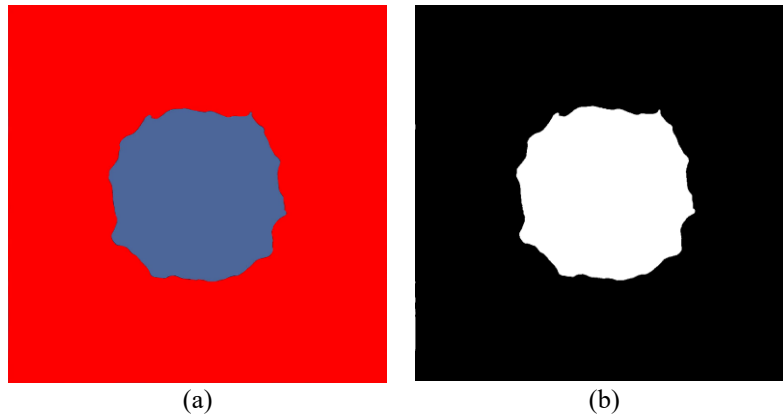


Figure 4.19: Top view of the numerical simulation at $Q = 0.6 \text{ l/min}$ with a minimum grid size of $\Delta x = 527 \mu\text{m}$. (a) Oil interface coloured in red before post-processing. (b) Oil interface after the segmentation step of the post-processing with ImageJ.

4.2.2.2.1 Reproducibility test

We first test the reproducibility of our numerical method to capture the open eye area by comparing the results obtained with the same configuration done on different trials. From the results of Figure 4.20, we can observe a good reproducibility with a small error especially before five seconds. After five seconds of the simulation, the fluctuations of both trials increase and the same for the error between them. This indicates that both the agitation of the numerical simulation and image post-processing of the images with ImageJ are reasonably reproducible.

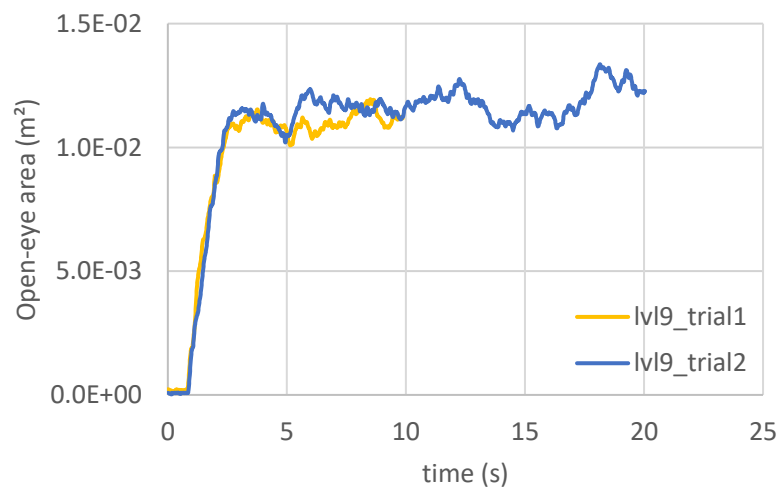


Figure 4.20: Time evolution of the numerical open eye area for two different trials with a minimum grid size of $\Delta x = 527 \mu\text{m}$ and at an air flow rate of $Q = 0.6 \text{ l/min}$.

4.2.2.2.2 Measurement

Figure 4.21 shows the time evolution of the numerical open eye at an air flow rate of $Q = 0.6\text{ l/min}$ for different mesh resolutions. From the results of Figure 4.21, we can see that the convergence of the open eye area value between a mesh resolution of *level9* and *level10* corresponding to a minimum grid size of respectively $\Delta x = 527\ \mu\text{m}$ and $\Delta x = 264\ \mu\text{m}$ is relatively good. We can identify the same fluctuations behaviour between the two mesh resolution even if the fluctuation seems to be more pronounced in *level10* mesh resolution than in the *level9* mesh resolution. Besides, we can see that the transient regime is the same for all the mesh resolution. Unfortunately, as we increase the maximum mesh resolution, the timestep decreases and so the computation becomes more CPU intensive. That is why we do not have more data corresponding to the pseudo permanent regime for the *level11* mesh resolution to compare with the lower mesh resolution cases.

In the following, we show the results obtained with a constant mesh resolution of *level9* corresponding to a minimum grid size of respectively $\Delta x = 527\ \mu\text{m}$. A global comparison of the time evolution of the open eye area for different air flow rates is shown in Figure 4.22. From the results of Figure 4.22 first, it is important to mention that the data gaps observed for $Q = 1.5\ \text{l/min}$ and $Q = 2.5\ \text{l/min}$ are due to a problem of format of the generated images and are left as it is and not interpolated from the non-missing data. We can see that globally the open eye area follows the increase in air flow rate and that ten seconds of simulation seem to be enough to reach a pseudo permanent regime. Furthermore, the convergence toward an asymptotic value is slower for high air flow rate than for low air flow rate and presents more oscillations. If we look at the data for $Q \leq 2.5\ \text{l/min}$ we can see an important change in the slope of the transient regime and on the asymptotic value of the pseudo permanent regime when the air flow rate is increased. For $Q > 2.5\ \text{l/min}$ a small difference between each air flow rate can be observed, for example, it is hard to make the distinction between $Q = 3.5\ \text{l/min}$ and $Q = 4.5\ \text{l/min}$ curves both for the transient regime and the pseudo permanent regime.

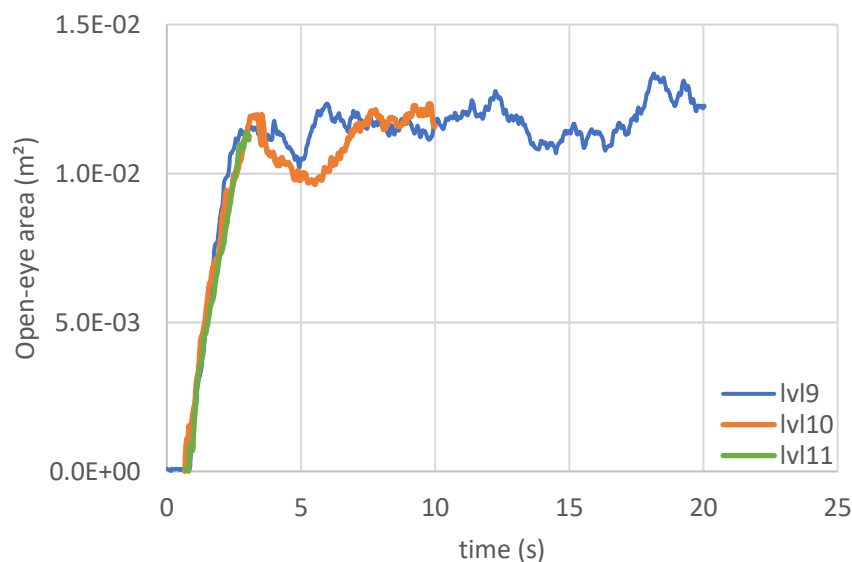


Figure 4.21: Time evolution of the numerical open eye area with different maximum mesh resolutions in one direction at an air flow rate of $Q = 0.6\text{ l/min}$.

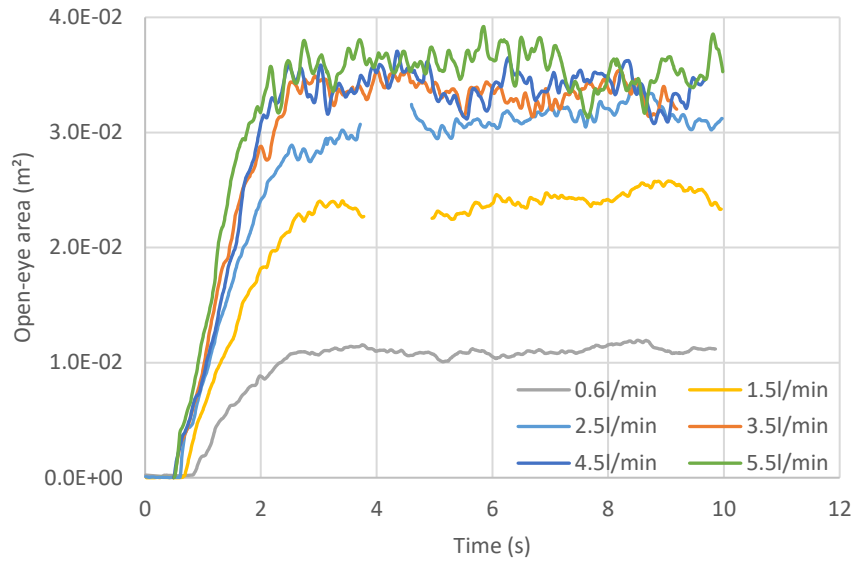


Figure 4.22: Time evolution of the open-eye area for different air flow rates with a minimum grid size of $\Delta x = 527 \mu\text{m}$.

4.2.3 Time-averaged results

In the following, we show the results obtained with a constant mesh resolution of *level9* corresponding to a minimum grid size of $\Delta x = 527 \mu\text{m}$. We will now try to characterize the flow with time-averaged variables. First, we compare images of time-averaged scalar fields. Because from the previous instantaneous images comparison, we did observe an important difference in the open eye size between $Q = 2.5\text{l/min}$ and $Q = 5.5\text{l/min}$ we will only show images corresponding to $Q = 0.6\text{l/min}$ and $Q = 5.5\text{l/min}$.

We first look at the time-averaged fluid-fraction fields. In Figure 4.23 we show the time-averaged air fluid fraction for the minimum and maximum air flow rate. We can see that the maximum values of the air fluid fraction can be found at the injector and at the free surface. Above the injector, in the bubble-plume region, we can see that the time-averaged air fraction has intermediate values. We can then identify the average contour of the bubble plume and the spout at the free surface. If we compare Figure 4.23-(a) and Figure 4.23-(b) we can see that when the air flow rate is increased the average contour of the bubble plume gets wider and the average height of the spout at the free surface gets higher. The fact that the contour of the open eye cannot be clearly identified unlike the free surface is due to the continuous movement of the bubbles inside the bubble plume blurring the contour of the average air fraction. If we look at Figure 4.24 showing the time-averaged oil fluid fraction we can see that as the air flow rate increases the size of the open eye delimited by the oil layer increases. We can also note that its contour gets more blurred showing that the oil layer is more agitated at a high air flow rate (cf. Figure 4.24-(b)).

Now we look at the time-averaged velocity field. In Figure 4.25 we compare the time-averaged horizontal velocity in a slice in the middle of the domain where the minimum and maximum values are coloured in blue and red respectively. We can see from Figure 4.25-(a) and Figure 4.25-(b) that the minimum and maximum values are located at the same height for the two different flow rates. As expected, this height corresponds to the water-oil interface and is generated when the bubble plume reaches the oil layer initiating radial and vertical perturbation on it from the open eye to the wall of

the domain. We look now at Figure 4.26 showing the time-averaged vertical velocity from the same view than before. We can see that the maximum vertical velocity corresponding to an upward velocity is located more or less at the centre of the bubble plume. Away from the bubble-plume centre the vertical velocity slowly decreases to finally reach a downward vertical velocity at the wall (cf. Figure 4.26-(b)). This illustrates the generation of recirculation loops in the water along the wall of the domain due to the bubble plume reaching the oil layer. The vertical velocity decreases abruptly when reaching the water-air interface or free surface.

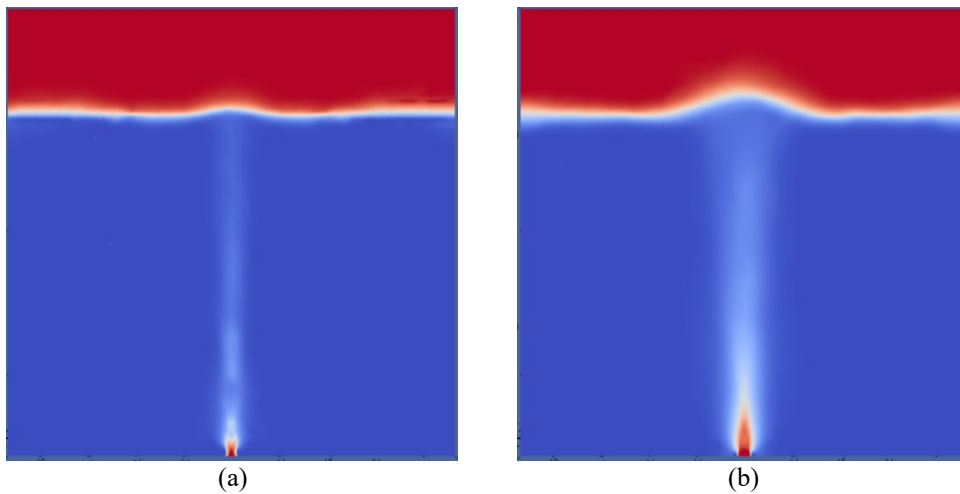


Figure 4.23: Time-averaged air fluid fraction in a slice in the middle of the domain. The results are obtained with a minimum grid size of $\Delta x = 527 \mu\text{m}$. Maximum and minimum value are represented respectively with red and blue colours. a): $Q = 0.6\text{l/min}$; b): $Q = 5.5\text{l/min}$.

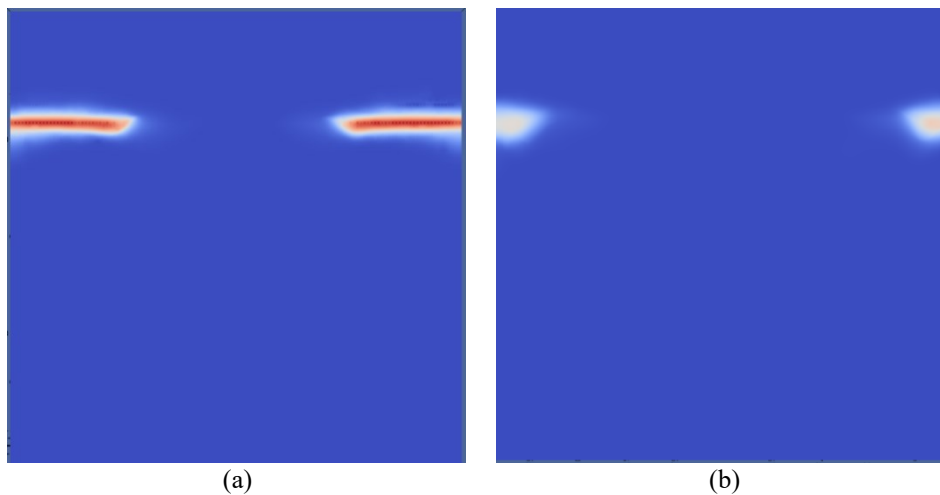


Figure 4.24: Time-averaged oil fluid fraction in a slice in the middle of the domain. The results are obtained with a minimum grid size of $\Delta x = 527 \mu\text{m}$. Maximum and minimum value are represented respectively with red and blue colours. a): $Q = 0.6\text{l/min}$; b): $Q = 5.5\text{l/min}$.

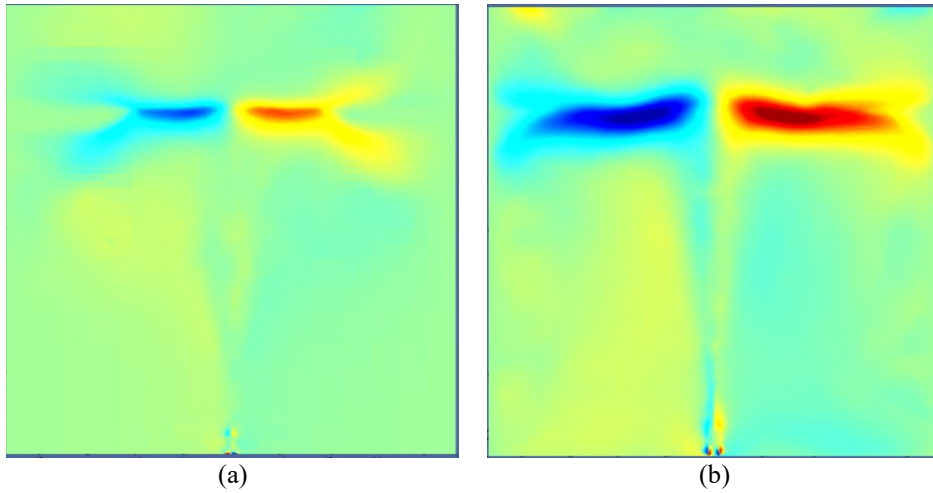


Figure 4.25: Time-averaged horizontal velocity in a slice in the middle of the domain. The results are obtained with a minimum grid size of $\Delta x = 527 \mu\text{m}$. Maximum and minimum value are represented respectively with red and blue colours. a): $Q = 0.6 \text{ l/min}$; b): $Q = 5.5 \text{ l/min}$.

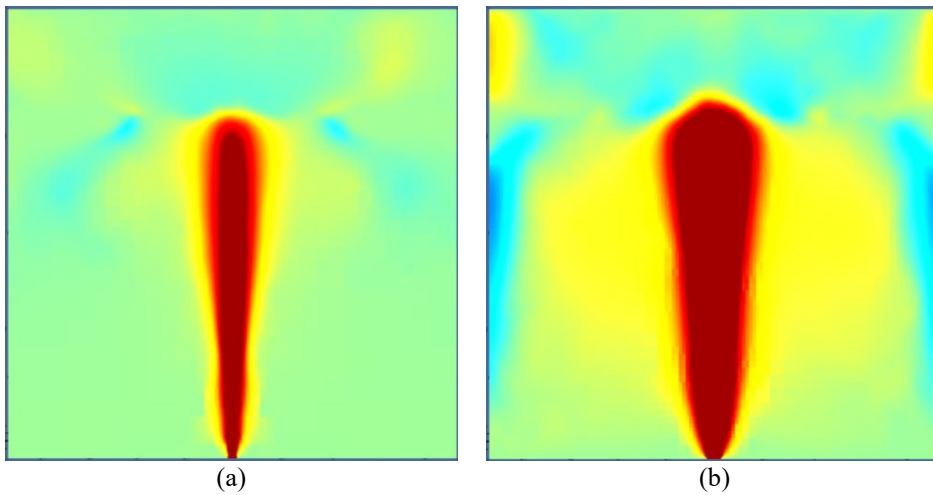


Figure 4.26: Time-averaged vertical velocity in a slice in the middle of the domain. The results are obtained with a minimum grid size of $\Delta x = 527 \mu\text{m}$. Maximum and minimum value are represented respectively with red and blue colours. a): $Q = 0.6 \text{ l/min}$; b): $Q = 5.5 \text{ l/min}$.

In order to characterize the flow with more quantitative data, we selected several positions of the domain where we will interpolate the value of velocity through all the cells (cf. Figure 4.27) along horizontal lines. The origin of the axis is taken as the centre of the injector.

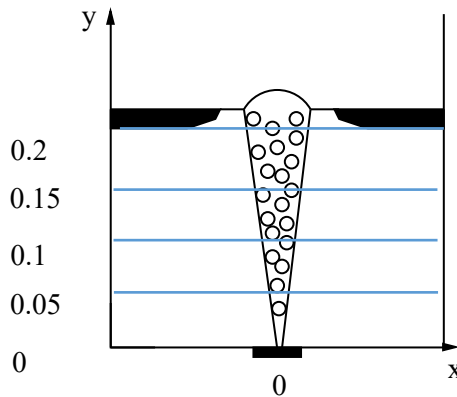


Figure 4.27: Schematic of the numerical domain. The blue horizontal lines represent the horizontal profile lines.

First, we look at Figure 4.28 where we have plotted the evolution of the time-averaged vertical velocity along the horizontal position for different air flow rates and at various heights of the domain (cf. Figure 4.27). We can see that for all the heights considered, the vertical velocity presents globally the same trend with a Gaussian function shape with a maximum value at the centre of the domain. Furthermore, as expected the higher vertical velocity is obtained for the higher gas flow rate $Q = 5.5l/min$ at a height $y = 0.05cm$ that is just above the injector. By comparing Figure 4.28-(a),(b),(c) and (d) we can see that when the height gets closer to the water-oil interface the vertical velocity decreases. If we look closely at Figure 4.28-(c) and Figure 4.28-(d) we can see that near the minimum and maximum horizontal position the average vertical velocity has negative value meaning that the velocity is oriented downward as previously seen in Figure 4.26. From Figure 4.28-(d) and -(b) obtained at the height of the oil layer at the initial state we can remark that as the air flow rate increases the negative peak of the average velocity move further to the extremity of the domain.

Now, we consider the evolution of the horizontal component of the time-averaged velocity along the horizontal position in Figure 4.29. In Figure 4.29-(a),(b) and (c) we can observe similar behaviour of the time-averaged horizontal velocity with globally positive value on the left side of the air injector and negative value on the right side of the air injector. This behaviour illustrates the effect of the recirculation loop forming on both sides of the bubble plume after the revert of the velocity. We can also note that the values of the time-averaged horizontal velocity between each air flow rate are not that much different. If we look now at Figure 4.29-(d) corresponding to the height of the oil layer at the initial state we can see that the time-averaged horizontal velocity follows an opposite trend with positive value on the right side of the air injector and the opposite on the left side. This illustrates the behaviour of the velocity near the water-oil interface. We can also note that there is a factor ten of difference with the value of the horizontal velocity at a lower height.

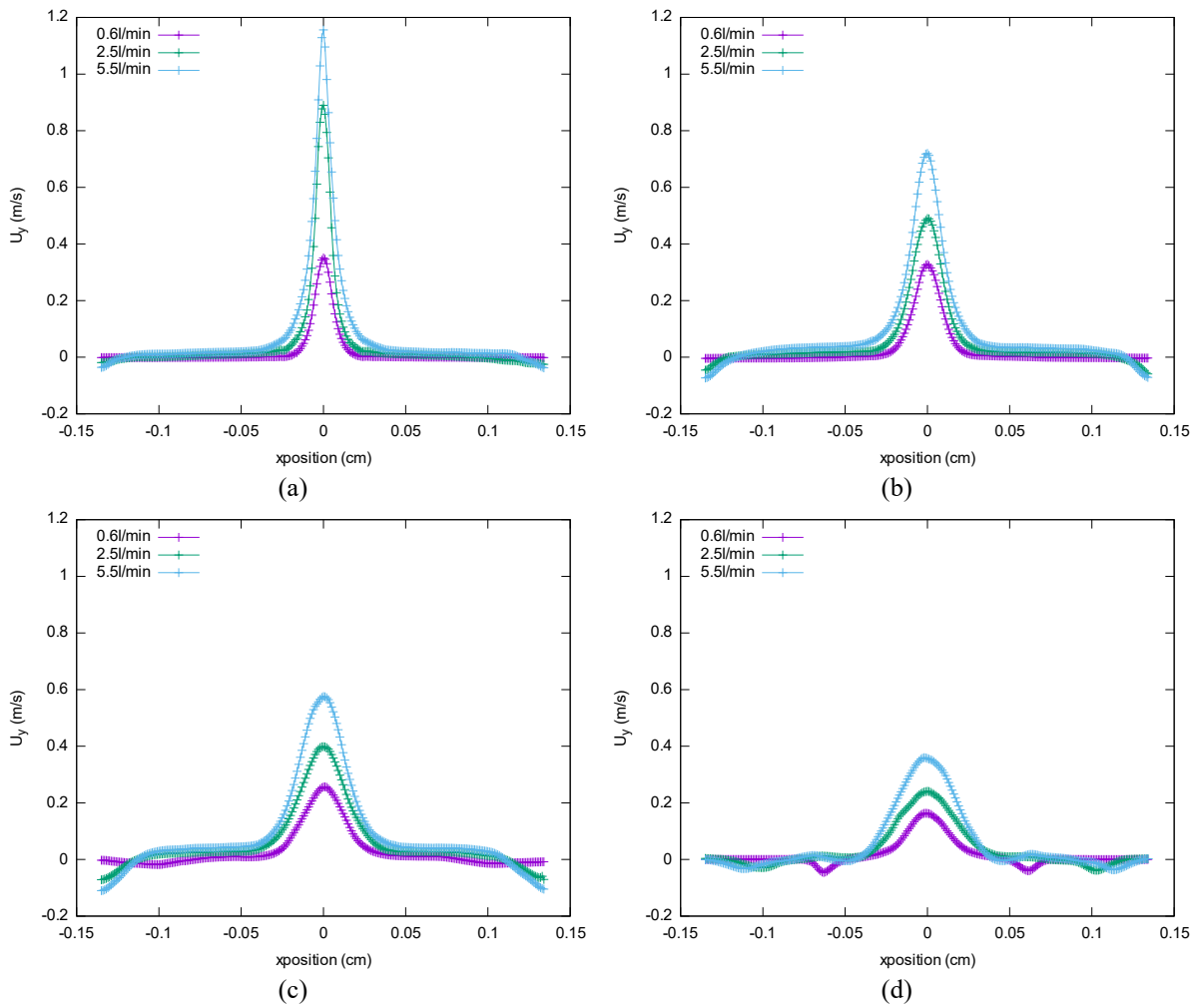


Figure 4.28: Time-averaged vertical velocity along the horizontal position for different air flow rates and with a minimum grid size of $\Delta x = 527\ \mu\text{m}$. The interpolation is done along different lines at a given vertical position. a): $y = 0.05\text{cm}$; b): $y = 0.1\text{cm}$; c): $y = 0.15\text{cm}$; d): $y = 0.2\text{cm}$.

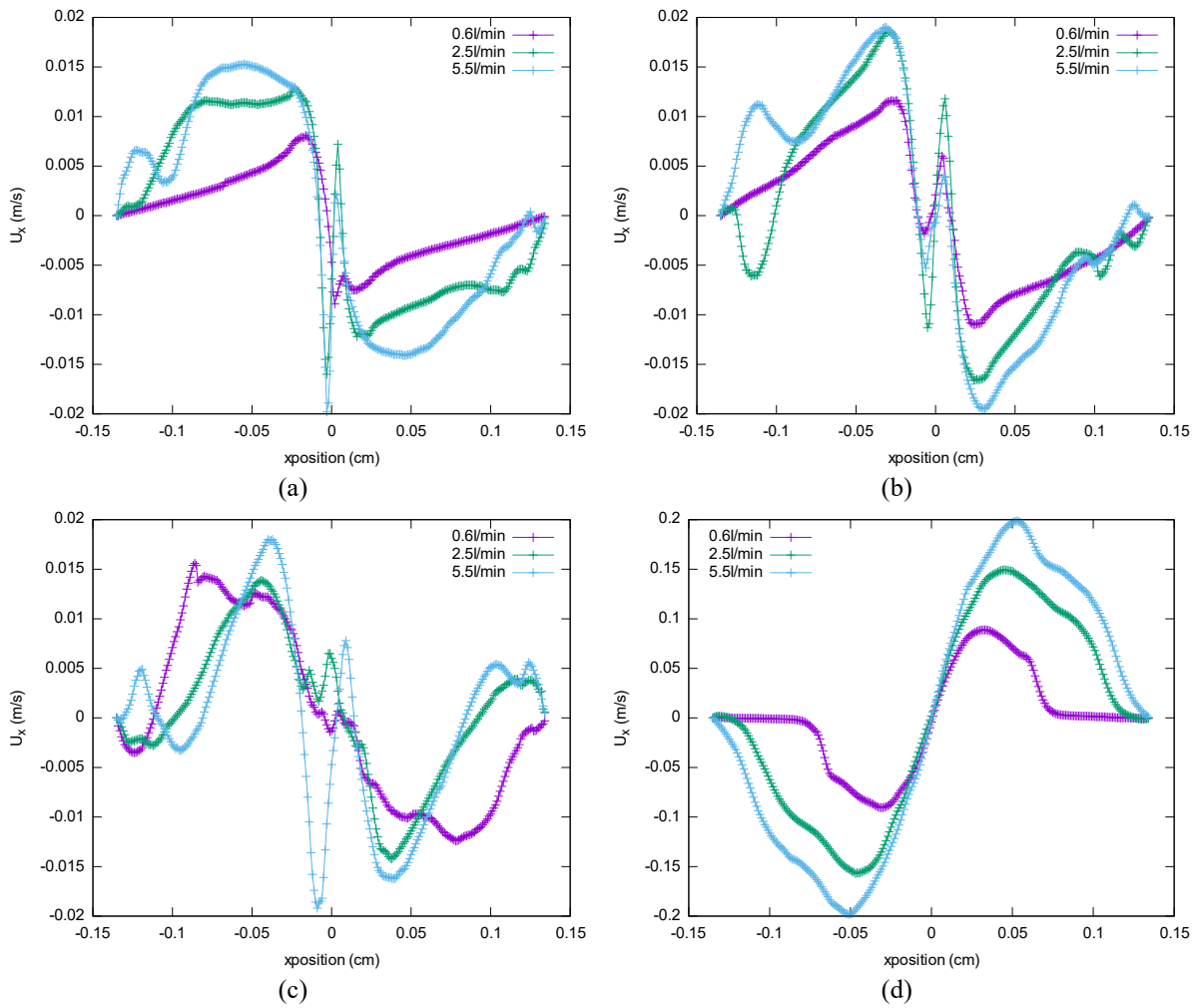


Figure 4.29: Time-averaged horizontal velocity value along the horizontal position for different air flow rates with a minimum grid size of $\Delta x = 527 \mu\text{m}$. The interpolation is done along different lines at a given vertical position. a): $y = 0.05\text{cm}$; b): $y = 0.1\text{cm}$; c): $y = 0.15\text{cm}$; d): $y = 0.2\text{cm}$.

4.3 COMPARISON OF THE RESULTS

In the following, we compare our numerical and experimental results concerning the evolution of the open eye area. Unfortunately, we have obtained only time-averaged results for the water experiments.

4.3.1 Open eye

In Figure 4.31 we plotted the numerical open eye area evolution together with the experimental average open eye area for each air flow rate. From Figure 4.31 we can see that the numerical results are closer to the experimental results at a high air flow rate than at a low air flow rate. Typically starting from $Q = 3.5 \text{ l/min}$ an increasingly good agreement with the experiment is found. For all air flow rate, the transient regime is finished around 5 s after the simulation start. We can then consider a pseudo permanent regime after this time and compute the numerical average open eye and standard deviation from $t = 5\text{s}$ to $t = 10\text{s}$. We can also identify some pseudo periodical fluctuations of the open eye area from $Q = 4.5 \text{ l/min}$. These pseudo periodical fluctuations seem to be correlated with the waves on the oil layer observed at the free surface from the face view of Figure 4.17.

In Figure 4.30 we compare the average numerical open eye area computed when the pseudo permanent regime is attained and the experimental results obtained as described in 4.1.2. We can see that the numerical results globally overestimate the open eye area compared to the experimental results and again that the tendency is more pronounced at low air flow rate than at high air flow rate. The fact that a smaller difference between the numerical and experimental results is observed at high air flow rate could be explained by the longer simulation time required to obtain a more stable open eye at a high air flow rate. Otherwise, several assumptions can be made in order to explain this difference:

- The three-phase formulation for the fluid fractions and surface tensions used in our simulation introduces a systematic error at the cells containing the three phases;
- The fact that we used a value of the air density ten times higher than in the water experiment;
- The choice of a free-slip boundary condition for the left and right faces which reduces the dissipation and thus increases the average kinetic energy.

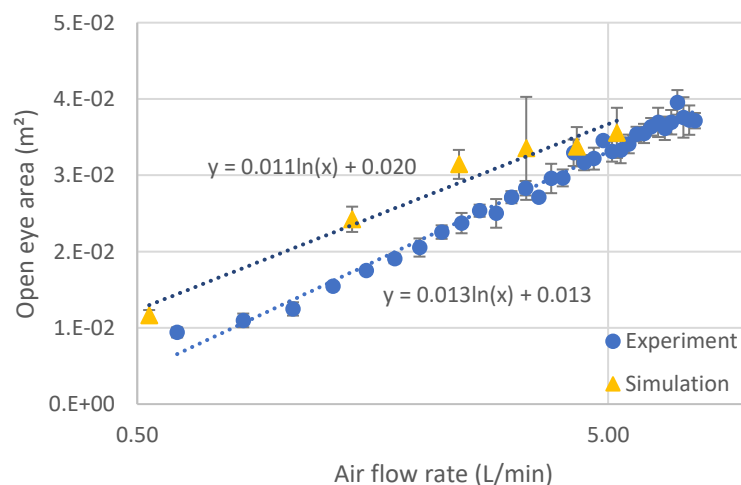


Figure 4.30: Comparison of the experimental and numerical average open-eye area with standard deviation. The simulation results are obtained with a minimum grid size of $\Delta x = 527 \mu\text{m}$.

4-Results- hydrodynamic characterization

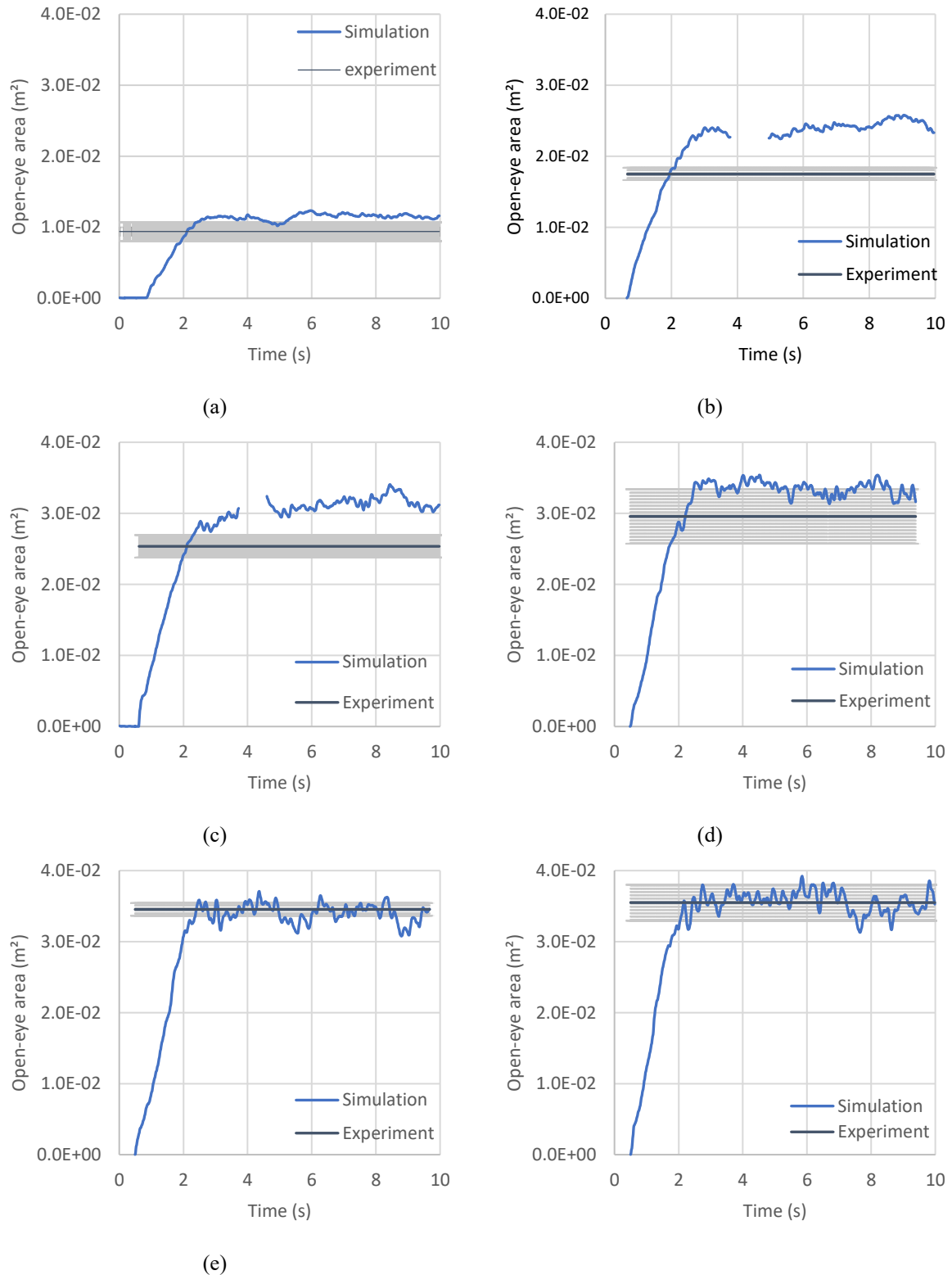


Figure 4.31: Comparison of the experimental and numerical open-eye area with a minimum grid size of $\Delta x = 527 \mu\text{m}$. (a) $Q=0.6\text{ l/min}$; (b) $Q=1.5\text{ l/min}$; (c) $Q=2.5\text{ l/min}$; (d) $Q=3.5\text{ l/min}$; (e) $Q=4.5\text{ l/min}$; (f) $Q=5.5\text{ l/min}$

4.4 SUMMARY

In this chapter, we have first observed visually the phenomenon of oil fragmentation occurring mainly at the corner of our cubic water model. It appears that the value of the specific critical gas flow rate at which this phenomenon can be observed seems to be constant for the two oil volumes considered in our experiments. In addition to the formation of oil droplets, we have also exhibited the formation on the water-oil interface of oil films encapsulating water with a spherical shape to form what we call anti-bubbles. The visual observations showed also that a water-oil emulsion is forming at the water-oil interface. The height of this water-oil emulsion and its aspect depends on the air flow rate and the time of air injection. Despite the measurement of the oil physical properties which showed only a small variation after two hours of air injection further tests should be done in order to confirm the observations made. Then from our measurement of the open eye area at various air flow rate, we have reported no influence of the size of the injection diameter. We have also reported an increase in the open eye area when the air flow rate is increased. Moreover, for a constant air flow rate, an increase of the oil volume leads to a smaller open-eye area.

In a second time, we have observed from our instantaneous numerical results that we reproduced qualitatively well the global flow behaviour with a bigger open eye, more oil droplets and larger air bubbles at high air flow rate than at low air flow rate. Concerning the numerical open eye obtained with the simulation, we observed a mesh convergence that would need to be confirmed for longer simulation time at the maximum mesh resolution which is the more computationally intensive. From the time-averaged numerical results, we have seen that the average vertical velocity in the water presents a Gaussian shape with a maximum aligned with the centre of the injection diameter. The average velocity is decreasing as we get closer to the water-oil interface. On the walls, downward average vertical velocity has been observed confirming the formation of a recirculation loop on the sides of the central bubble plume.

Finally, from the comparison of the numerical and experimental average open eye area, we have seen that the numerical results tend to overestimate the experimental open eye area, especially at a low air flow rate. The main assumptions made to explain this deviation from the experimental results are first the longer simulation time required at a high air flow rate to observe a more stable open eye; a systematic error introduced by our three-phase formulation for the fluid fractions and surface tensions at the cells containing the three phases.

5 TOWARD INDUSTRIAL APPLICATION- HYDRODYNAMIC CHARACTERIZATION

In this chapter, we want to compare our water experimental results of the open eye area presented in 4.1.2 with results from the literature obtained with various fluids and sizes of the ladle. In the following, because we will compare experiments with different fluids for clarity reasons, we will denote the physical properties of the steel and slag equivalent phase for both water and liquid metal experiments with the respective indices m and s .

5.1 OPEN-EYE EXPERIMENTS IN THE LITERATURE

Because of the inherent difficulty of doing measurement in the industrial process, we found only one study in the literature where the open eye area is measured in an industrial ladle configuration. First, we consider the industrial experiment with liquid steel with slag in a 350-ton ladle of Yonezawa & Schwerdtfeger [17]. In the same study, the authors did also some experiments with mercury and silicon oil to reproduce the liquid steel and slag behaviour. In Thunman *et al.* [78] experiments with a rectangular shape ladle using Ga-In-Sn alloy and $MnCl_2$ -glycerol to simulate liquid steel and slag are done. Wu *et al.* [19] used the same alloy to simulate the liquid steel but with a cylindrical ladle and used HCl to represent the slag phase. The other option is to use a water experiment giving a much easier experimental condition but might be less representative of the liquid steel slag behaviour. For the water experiment study of the open eye, we will consider our experimental results and the one of Krishnapisharody & Irons [22]. In the study of [22], the authors measured the open-eye area for different fluids. All the physical properties of the fluids for the aforementioned studies can be found in Table 5.1.

In Table 5.2 we compute the viscosity ratio $m = \mu_m/\mu_s$, the density ratio $r = \rho_m/\rho_s$ together with the bath height ratio h_m/L_x and the slag height ratio h_s/L_x with the horizontal size of the ladle L_x . We can see from Table 5.2 that the viscosity ratio is close to the steel-slag value for almost all the experiments except the water experiment using motor oil of [22] and the experiment of [19]. In the experiment of [19] using Ga-In-Sn alloy, the choice of the HCl to represent the slag layer leads to a much higher viscosity of the Ga-In-Sn alloy than the HCl which should be the opposite in order to reproduce the industrial configuration. Now, if we look at the density ratio, we can see that the water experiments have a lower density ratio than in the industrial configuration. While, for the liquid metal experiments, the density ratio is higher than in the industrial configuration [17]. If we look now at the geometric ratio we can see that in all the experiments the ratio of the height of the bath to the horizontal dimension of the ladle is smaller than in the industrial case especially in the experiments of [22]. For the ratio of the height of the slag layer to the height of the bath we can see that in most of the experiments the value is not far from the industrial configuration corresponding to a thin slag layer. The experiment of [19, 78] presents ten times higher values of this ratio than in the industrial configuration, so it may lead to a difference of behaviour than the other experiments.

	Fluids	T (°C)	ρ_m (kgm^{-3})	ρ_s (kgm^{-3})	μ_m (Pa.s)	μ_s (Pa.s)	L_x (m)	h_m (m)	h_s (m)	d_{inj} (m)
Our experiment	Water-oil	20	998	920	10^{-3}	0.079	0.27	0.20	0.007	$7.9 \cdot 10^{-3}$
Krishnapisharody et al. [22]	Water-paraffin oil	20	$1.0 \cdot 10^3$	870	10^{-3}	0.065	0.42	0.21	0.01	$3.0 \cdot 10^{-3}$
Krishnapisharody et al. [22]	Water-motor oil	20	$1.0 \cdot 10^3$	880	10^{-3}	0.29	0.42	0.21	0.01	$3.0 \cdot 10^{-3}$
Krishnapisharody et al. [22]	CaCl ₂ -motor oil	20	$1.4 \cdot 10^3$	870	$6.2 \cdot 10^{-3}$	0.065	0.42	0.21	0.01	$3.0 \cdot 10^{-3}$
Yonezawa et al. [17]	Hg-paraffin oil	20	1.410^4	960	$1.5 \cdot 10^{-3}$	0.048	0.29	0.225	0.01	$1.5 \cdot 10^{-3}$
Yonezawa et al. [17]	Steel-slag	1600	$6.8 \cdot 10^3$	2800	$5.4 \cdot 10^{-3}$	0.104	4.4	3.5	0.05	$9.0 \cdot 10^{-2}$
Thunman et al. [78]	Ga,In,Sn-glycerol	20	$6.4 \cdot 10^3$	1300	$2.2 \cdot 10^{-3}$	0.055	0.25	0.18	0.018	$5.0 \cdot 10^{-3}$
Wu et al. [19]	Ga,In,Sn-HCl	20	$6.4 \cdot 10^3$	1060	$6.0 \cdot 10^{-3}$	0.001	0.24	0.145	0.015	$6.0 \cdot 10^{-3}$

Table 5.1: Main physical and geometrical properties of the steel and the slag equivalent phase for our experiment and the experiment of [17, 19, 22, 78].

	Fluids	m	r	h_m/L_x	h_s/h_m
Our experiment	Water-oil mixture	$1.3 \cdot 10^{-2}$	1.09	0.74	0.035
Krishnapisharody et al. [22]	Water-paraffin oil	$1.5 \cdot 10^{-2}$	1.15	0.5	0.048
Krishnapisharody et al. [22]	Water-motor oil	$3.4 \cdot 10^{-3}$	1.14	0.5	0.048
Krishnapisharody et al. [22]	CaCl ₂ -motor oil	$9.5 \cdot 10^{-2}$	1.61	0.5	0.048
Yonezawa et al. [17]	Hg- silicon oil	$3.2 \cdot 10^{-2}$	14.2	0.78	0.044
Yonezawa et al. [17]	Steel-slag	$5.3 \cdot 10^{-2}$	2.43	0.80	0.014
Thunman et al. [78]	Ga,In,Sn-glycerol	$4.0 \cdot 10^{-2}$	4.89	0.72	0.100
Wu et al. [19]	Ga,In,Sn-HCl	6	6.04	0.60	0.103

Table 5.2: Main dimensionless characteristic of the steel and the slag equivalent phase for our experiment and the experiment of [17, 22].

5.2 COMPARISON OF THE OPEN-EYE AREA

In the following, we will use two correlations to try to predict the evolution of the open-eye area as a function of the gas flow rate for the water and liquid metal experiments. The first one is the one of [22] who used a mechanical model based on the principles of momentum conservation to establish a correlation valid for a thin slag layer

$$\frac{A_e}{h_m^2} = \alpha + \beta \left(\frac{\rho_m}{\Delta\rho} Fr_s \right)^{1/2}, \quad (5.1)$$

where A_e is the open-eye area, α and β are numerical constants, h_m is the height of the bath of the steel equivalent phase, ρ_m is the density of the liquid steel equivalent phase and $\Delta\rho$ is the difference of density between the steel and slag equivalent phase. Fr_s is the Froude number in the slag layer defined by

$$Fr_s = \frac{U_p^2}{gh_s}, \quad (5.2)$$

where U_p is the plume velocity and h_s is the height of the equivalent slag layer. Because the plume velocity is not an operating variable, we have to compute it from the gas flow rate value with the correlation of Castello-Branco & Schwerdtfeger [24]

$$U_p = 17.4Q^{0.244}d_{inj}^{-0.0288} \left(\frac{\rho_g}{\rho} \right)^{0.0218} h_m^{-0.08}. \quad (5.3)$$

where U_p is expressed in cm/s , Q is the flow rate of gas of density ρ_g at the nozzle exit and taken at the temperature and pressure of the operating conditions and expressed respectively in cm^3/s and kg/m^3 , h_m and d_{inj} are expressed in cm . The other correlation that will be used is the one established in 2.3.3 that can be written in a dimensionless form as

$$\frac{A_e}{h_m^2} = C_A \ln \left(\frac{N}{N_c} \right) + b, \quad (5.4)$$

where $C_A = 10\alpha\pi c_\varphi^2$ and b are constant and N is the modified Froude number given by

$$N = \left(\frac{Q}{g^{1/2}h_m^{5/2}} \right)^{1/5}. \quad (5.5)$$

N_c corresponds to the critical value of the modified Froude number for the open eye formation given by

$$N_c = \left(\frac{\Delta\rho}{\rho_m} \frac{h_s}{h_m} \right)^{1/10}. \quad (5.6)$$

We gather the measurements of the open-eye area for all experiments and plot it in a dimensionless form against a function of the gas flow rate depending on the correlation used.

5.2.1 Formulation of Krishnapisharody et al. [22]

In Figure 5.1 we plot the dimensionless open-eye area as a function of the Froude number. We can see from Figure 5.1 that most of the water experiments with cross symbols show a similar evolution of the open-eye area as a function of the Froude number. On the other hand, the liquid metal experiments with empty symbols present a lower dimensionless open eye area than for the water model and with more dispersion. We can note that the results of the experiments of [78] and [19] using Ga-In-Sn alloy are giving sensibly different results. If we look at the industrial results in plain red symbol, we can see that within this dimensionless formulation, almost no experiments can superpose with the industrial results.

Now in Figure 5.2, we show the same plot than previously but with only the water experiments. From Figure 5.2 we can see that the results of [22] obtained with $CaCl_2$ -paraffin oil deviates the most importantly from all the other results. We try to fit our experimental results with the correlation (2.3) established by [22] to obtain the following relation at the temperature and pressure of the operating conditions

$$\frac{A_e}{h_m^2} = -0.67 + 0.28 \left(\frac{\rho_m}{\Delta\rho} Fr_s \right)^{1/2}. \quad (5.7)$$

We can see in Figure 5.2 that the correlation (5.7) gives a good agreement with our results. It seems that the results of [22] obtained with water-paraffin oil and water-motor oil do not present a linear increase at high value of the Froude number, unlike our results.

In Figure 5.3 we display the same type of plot as previously but with only the liquid metal experiments. We try to fit the industrial results of [17] with the correlation (2.3) established by [22] to obtain at the temperature and pressure of the operating conditions

$$\frac{A_e}{h_m^2} = -0.11 + 0.14 \left(\frac{\rho_m}{\Delta\rho} Fr_s \right)^{1/2}. \quad (5.8)$$

We can see that the fit of the industrial results can give an approximate prediction of the results of [78] obtained with Ga-In-Sn and the one of [17] obtained with mercury. On the other hand, the results of [19] present an important deviation compared to the other results. This deviation could be explained by the combined effect of a much lower viscosity of the slag equivalent phase and a higher density ratio than in the steel-slag configuration. Furthermore, the height of the equivalent slag layer in [19] is ten times higher than in the experiment of [17] and almost the same as the experiment of [78]. But as the results of [78] are similar to the results of [17] we cannot say that the height of the slag layer is the reason for the deviation of the results of [19].

5-Toward industrial application- hydrodynamic characterization

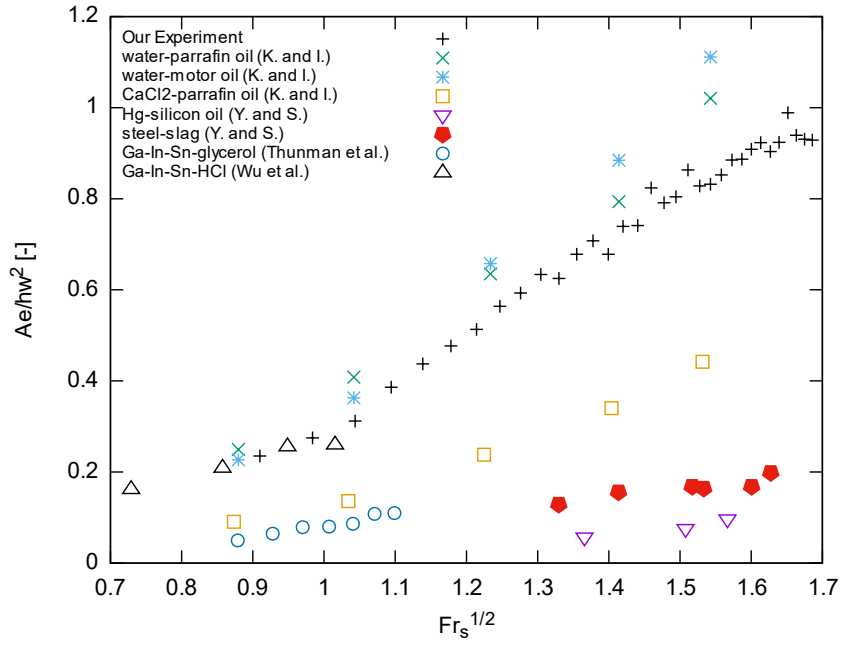


Figure 5.1: Dimensionless open-eye area as a function of the slag Froude number for our experiment and the experiments of Krishnapisharody et al. [22], Yonezawa & Schwerdtfeger [17], Thunman et al. [78] and Wu et al. [19].

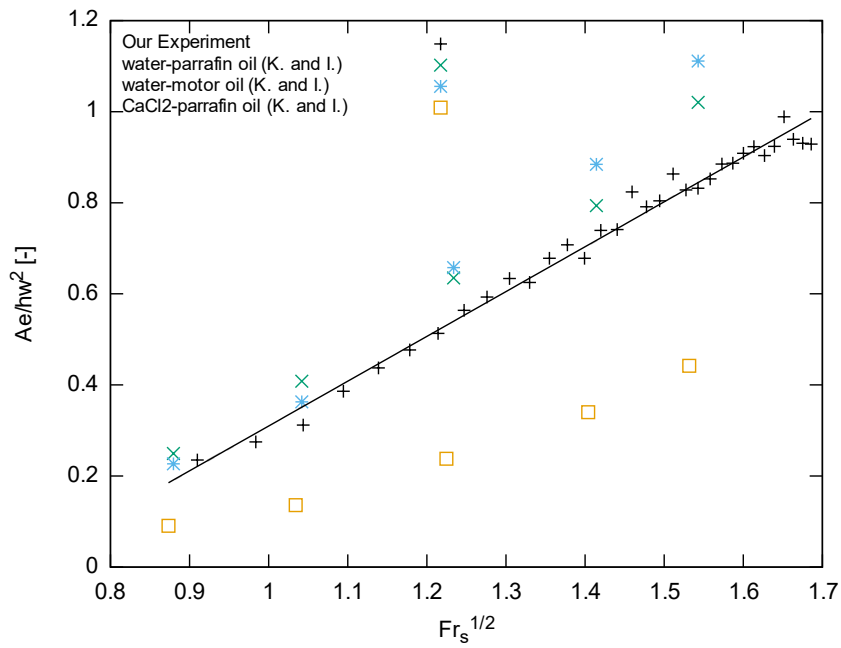


Figure 5.2: Dimensionless open-eye area as a function of the slag Froude number for our water experiment and the experiments of Krishnapisharody et al. [22]. The solid line represents the fit with the correlation (2.3) of our results.

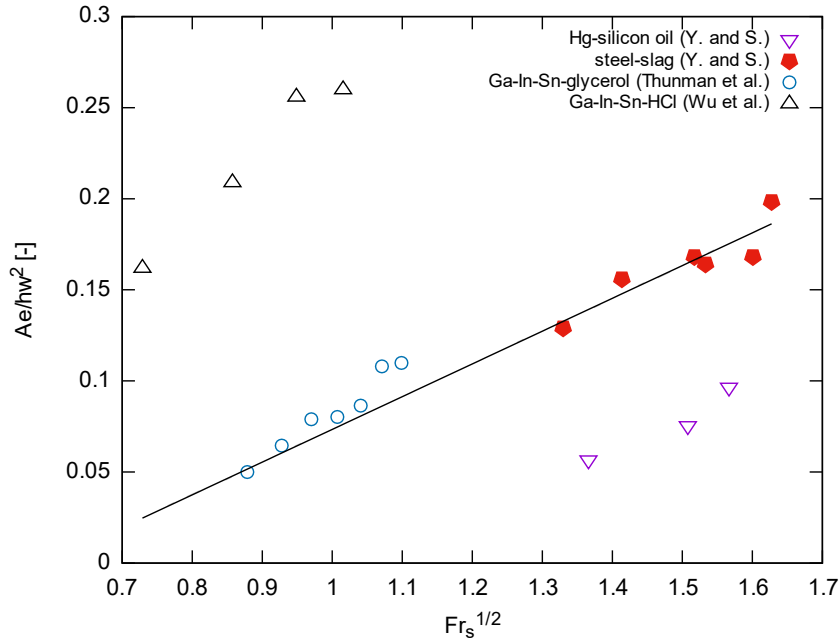


Figure 5.3: Dimensionless open-eye area as a function of the slag Froude number for liquid metals experiments of Yonezawa & Schwerdtfeger [17], Thunman et al. [78] and Wu et al. [19]. The solid line represents the fit with the correlation (2.3) of the results of [17].

5.2.2 Formulation established in 2.3.3

Now we will proceed in the same manner than previously but with the formulation of the correlation established in 2.3.3. We start by looking at Figure 5.4 where we have plotted the evolution of the dimensionless open-eye area as a function of the ratio of the modified Froude number to the critical modified Froude number for the formation of the open eye. We can observe in Figure 5.4 that the water experiments can almost be gathered on the same line while for the liquid metal experiments more dispersion can be observed. We can clearly see that the evolution of the open eye area as a function of the ratio of the modified Froude number to the critical modified Froude number for the liquid metal experiments follows a lower slope than the water experiments.

We replot the data for our water experiment and the one of [22] in Figure 5.5 from which we can remark that except the experiment obtained with $CaCl_2$ -paraffin oil, the results of the experiments can be well predicted by the fit of our results using the correlation (5.4) giving

$$\frac{A_e}{h_m^2} = -1.6 \ln\left(\frac{N}{N_c}\right) + 1.95. \quad (5.9)$$

Now, in Figure 5.6 we replot the data for all the liquid metal experiments. We can note from Figure 5.6 that unlike with the previous formulation of [22] this time the industrial results of [17] are closer to the results of [19] than the other experiments. We try to fit the industrial results of [17] with the correlation (5.4) and obtain the following correlation

$$\frac{A_e}{h_m^2} = 0.3 \ln\left(\frac{N}{N_c}\right) + 0.55. \quad (5.10)$$

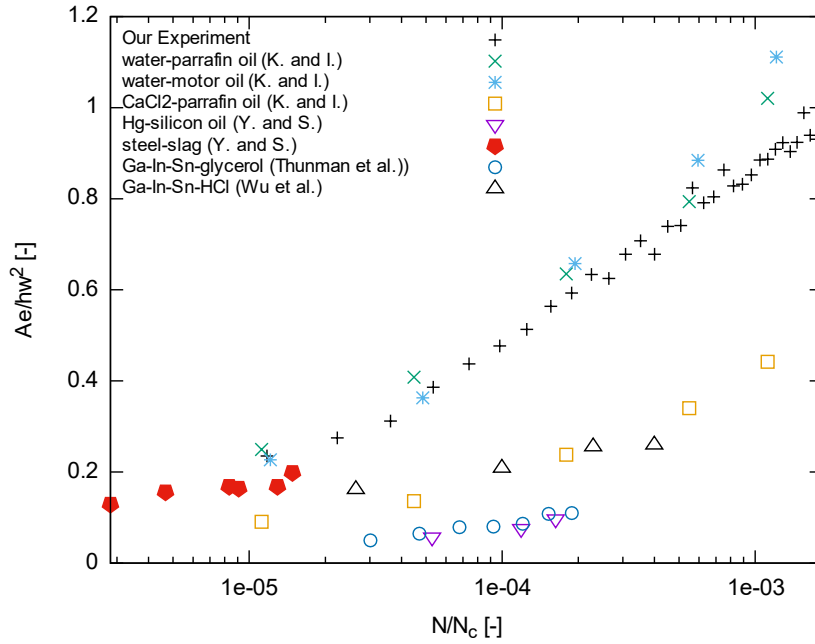


Figure 5.4: Dimensionless open-eye area as a function of the ratio of Froude number for our experiment and the experiments of Krishnapisharody et al. [22], Yonezawa & Schwerdtfeger [17], Thunman et al. [78] and Wu et al. [19].

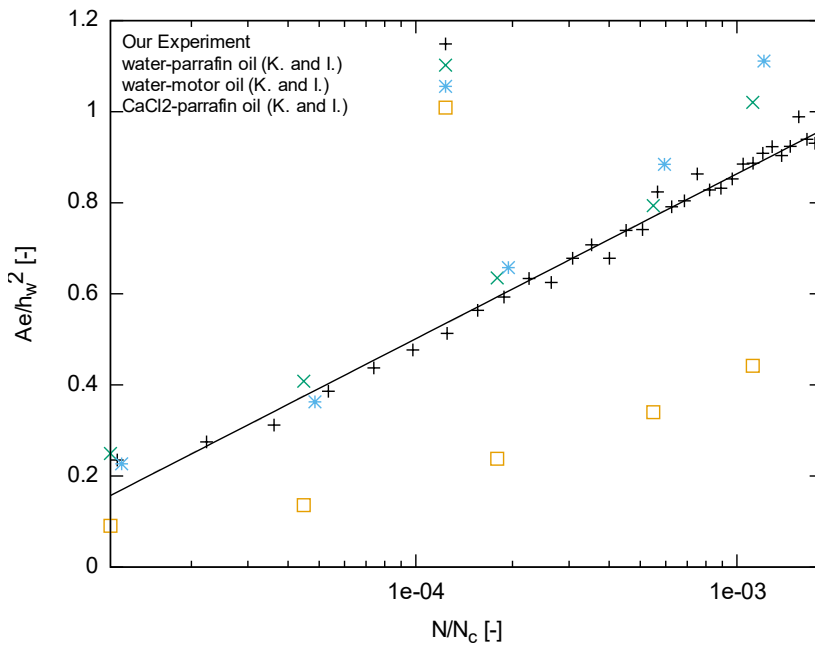


Figure 5.5: Dimensionless open-eye area as a function of the ratio of Froude number for our water experiment and the experiment of Krishnapisharody et al. [22]. The solid line represents the fit with the correlation (5.4) of our results.

5-Toward industrial application- hydrodynamic characterization

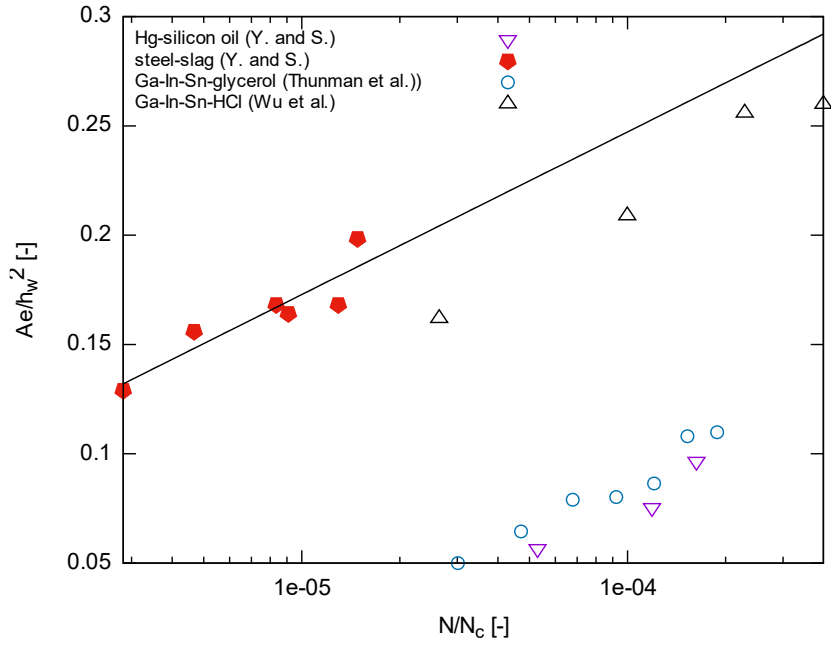


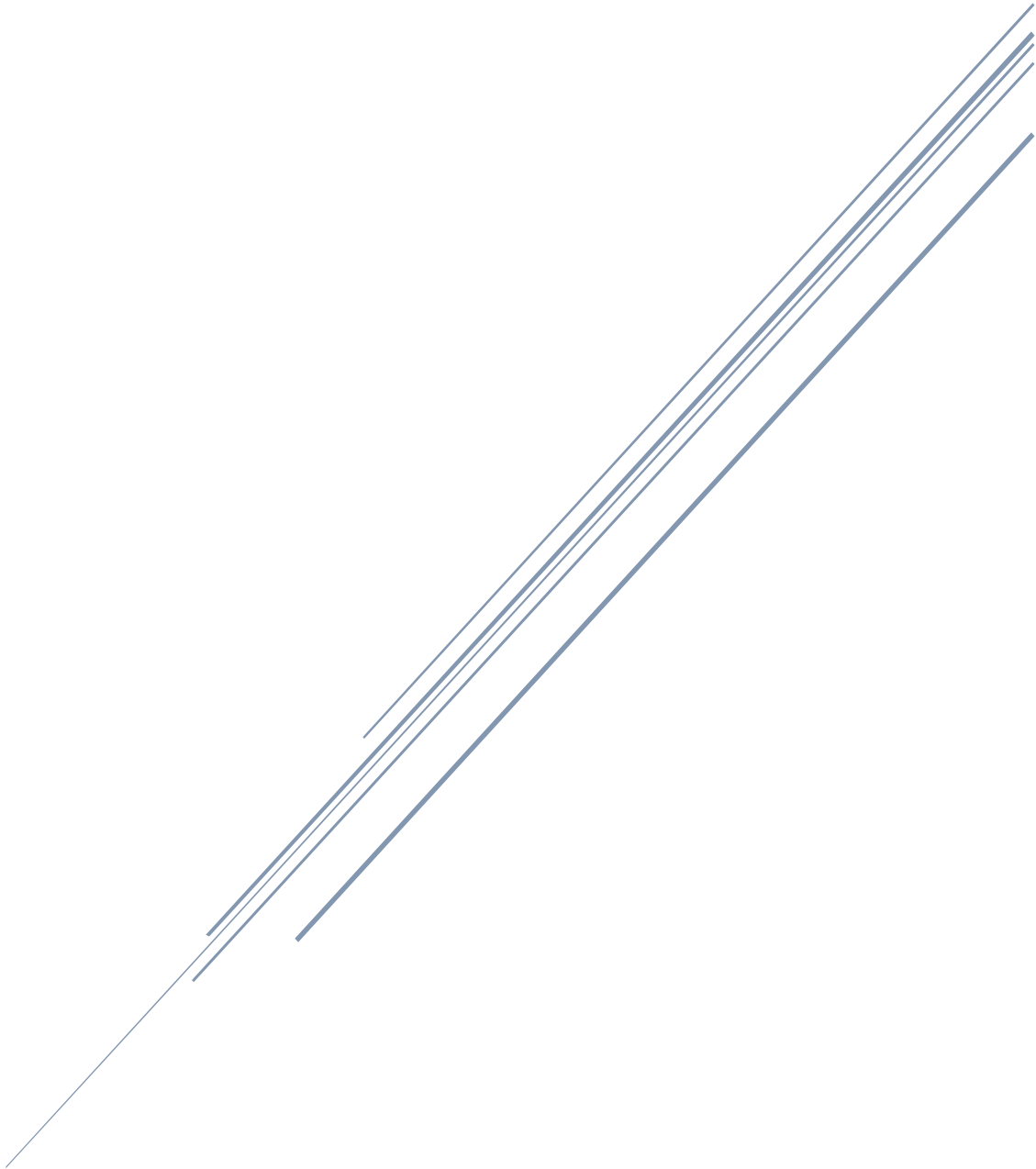
Figure 5.6: Dimensionless open-eye area as a function of the ratio of Froude number for liquid metals experiments of Yonezawa & Schwerdtfeger [17], Thunman et al. [78] and Wu et al. [19]. The solid line represents the fit with the correlation (5.4) of the results of [17].

5.3 SUMMARY

In this chapter first, we have seen the difficulty to find fluids that have approximately the same physical properties at ambient temperature than the liquid steel and slag at high temperature. The experiments with liquid metal with low melting point appears to be a good compromise giving easier experimental procedure than in the industrial case with more similar physical properties than for the water experiments. Then we have seen that is possible to gather the open eye area for the various experiments in a dimensionless form using either the formulation of [22] or the correlation (5.4). However, with these two formulations, an important difference in the value of the dimensionless open eye area between the water and the liquid metal experiments could be observed. No superimposition of the water and liquid metal experiments has been achieved. Compared to the water experiments the liquid metal experiments present a much lower slope for the evolution of the dimensionless open eye area as a function of the gas flow rate.

Finally, from the obtained results we can say that the formulation of [22] appears to give a better estimation of the dimensionless open eye area than with the correlation (5.4) with less dispersion of the results along the x-axis. Comparison with more experimental results especially for liquid metal experiments would allow to further increase the precision of the two formulations and their range of application.

PART II - MASS TRANSFER CHARACTERIZATION



6 PHYSICAL MODEL- MASS TRANSFER CHARACTERIZATION

6.1 MASS TRANSFER THEORY

Without source or sink terms the time variation of the concentration of a chemical species A diluted in a fluid can be described by

$$\begin{aligned}\frac{\partial c}{\partial t} &= -\nabla \cdot \mathbf{F}, \\ \mathbf{F} &= \mathbf{u}c - J, \\ \frac{\partial c}{\partial t} &= \nabla \cdot J - \nabla \cdot (\mathbf{u}c),\end{aligned}\tag{6.1}$$

where c is the concentration, F is the concentration flux by molecular diffusion, \mathbf{u} is the fluid velocity, and J is the concentration flux by molecular diffusion. Because we are considering incompressible fluids in this study, we can rewrite (6.1)

$$\frac{\partial c}{\partial t} = \nabla \cdot J - \mathbf{u} \cdot \nabla c\tag{6.2}$$

In presence of a gradient of concentration, the concentration flux by molecular diffusion can be described by the first law of Fick, which defines the concentration flux by molecular diffusion of a component A in an isothermal, isobaric system

$$\begin{aligned}J &= -D_p \frac{\partial c}{\partial x}, \\ N_m &= JM = -\rho D_p \nabla x,\end{aligned}\tag{6.3}$$

where N_m is the mass flux, D_p is the diffusivity of a chemical species in fluid p and x is the mass fraction. In the case of two immiscible fluids, the chemical species diluted in one fluid present a discontinuity at the interface due to a solubility difference between the two fluids (cf. Figure 6.1). At equilibrium, the discontinuity of the concentration of a chemical species diluted in fluid 1 is described by the partition law

$$P = \frac{C_{2,i}}{C_{1,i}},\tag{6.4}$$

where P is the partition coefficient, $C_{1,i}$ is the concentration at the interface from fluid one side and; $C_{2,i}$ is the concentration at the interface from fluid two side.

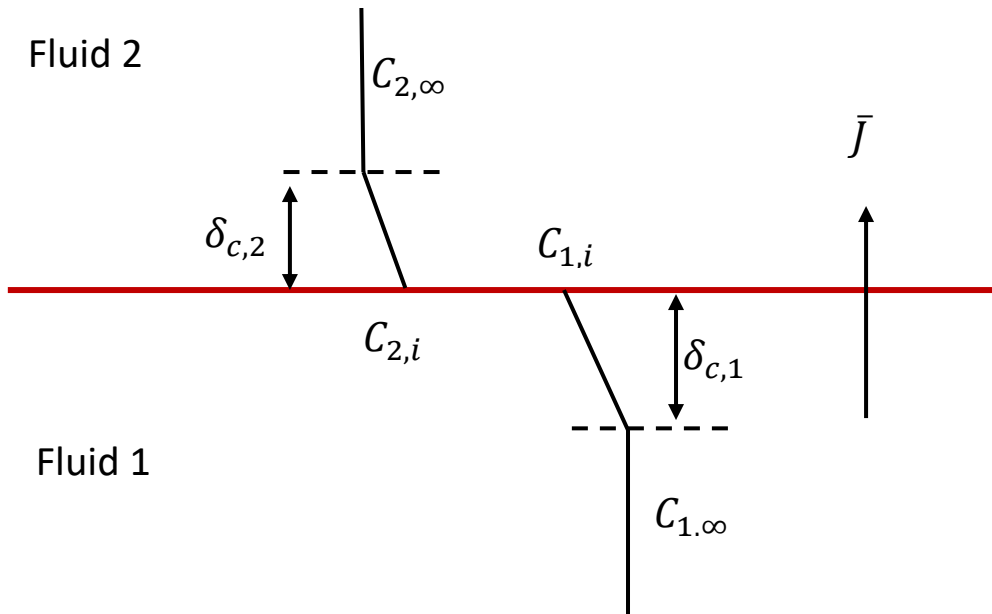


Figure 6.1: Sketch of the evolution of the concentration of a chemical species dissolved in fluid one at an interface between two immiscible fluids. The red line corresponds to the interface between the two fluids and the concentration boundary layer are represented with the discontinuity of the concentration at the interface introduced by the difference of solubility of the chemical species. The scale of the sketch is chosen for visual interpretation.

Since these governing equations are linear with respect to concentration, the time-averaged flux across the interface must be proportional to the concentration difference at the system boundaries for each concentration resistance we can write

$$\bar{J} = \frac{(C_{1,i} - C_{1,\infty})}{R_1} \quad (6.5)$$

$$\bar{J} = \frac{(C_{2,i} - C_{2,\infty})}{R_2}$$

where \bar{J} is the time-averaged concentration flux by molecular diffusion, the proportionality coefficients R_1 and R_2 are respectively the mass transfer resistance in fluid one and in fluid two, $C_{1,\infty}$ is the concentration in the bulk fluid one, $C_{2,\infty}$ is the concentration in the bulk fluid two. Using an analogy of the Ohm law for an electrical circuit we can proceed in the same manner to determine the total resistance to compute the diffusive flux. Combining the above equations (6.4) and (6.5), we can write the following global diffusive flux equation from the fluid one side

$$\bar{J} = \frac{(C_{1,\infty} - C_{2,\infty}/P)}{R_1 + R_2/P} \quad (6.6)$$

The value of the mass transfer resistance R depends on the diffusion coefficient D_p and the fluid motion that affects the concentration boundary layer at the interface $\delta_{c,p}$. The mass transfer coefficient in each fluid can be determined from the mass transfer resistance by $K_p = 1/R_p$. Depending on the value of the mass transfer resistance R_1 , R_i and R_2 , three different cases can be considered:

- 1) Transport regime:

The concentrations at the interface are near equilibrium and depend on the relative values of R_1 and R_2/P . The global mass transfer is then governed by the transport of chemical species to the interface. We can make a distinction between three cases:

- 1-a) Transport regime in fluid 1:

When $R_1 \gg R_i + R_2/P$ the gradient of concentration in the concentration boundary layer of fluid one is dominant, and the expression of the global diffusive flux is given by

$$\bar{J} = \frac{(C_{1,\infty} - C_{2,\infty}/P)}{R_1} \quad (6.7)$$

- 1-b) Transport regime in fluid 2:

When $R_2/P \gg R_1 + R_i$ the gradient of concentration in the concentration boundary layer of fluid two is dominant, and the expression of the global diffusive flux is given by

$$\bar{J} = \frac{(C_{1,\infty} - C_{2,\infty}/P)}{R_2/P} \quad (6.8)$$

- 1-c) Combined transport regime:

When $R_1 \sim R_2/P$ the gradient of concentration in the concentration boundary layer of fluid one and two is of equal importance and the expression of the global diffusive flux is given by

$$\frac{1}{\bar{J}} = \frac{R_1}{(C_{1,\infty} - C_{2,\infty}/P)} + \frac{R_2/P}{(C_{1,\infty} - C_{2,\infty}/P)} \quad (6.9)$$

6.2 LITERATURE REVIEW

6.2.1 Mass transfer models

Rather than being directly computed, the mass transfer coefficient is usually estimated by using macroscopic correlations or simplified models. Most of these models are used for mass-transfer of species across a gas-liquid interface, for example, the CO₂ exchange at the ocean surface in geophysics flow. For the liquid-liquid mass transfer case, no general model exists and depending on the viscosity ratio of the fluids, the limiting case could either be a fluid-solid mass transfer model or fluid-gas model. Because of the lack of liquid-liquid mass transfer model, we will give some details about common gas-liquid mathematical models of mass transfer.

6.2.1.1 Free surface model

6.2.1.1.1 Film model

We start with the simplest mass transfer model described by Lewis and Whitman [79] using the following assumptions: laminar boundary layer, steady-state flow, instantaneous equilibrium condition of the fluid at the interface, mass flux occurs on both sides of the interface. Film theory is

based upon the presence of a conceptual film of fluid that offers the same resistance to mass transfer as exists in the entire flowing fluid, as shown in Figure 6.1.

In other words, all resistance to mass transfer is assumed to exist in a boundary layer fluid film in which the chemical species transport is entirely done by molecular diffusion. The average mass transfer coefficient within this model can be given by

$$K_l = \frac{D_{A,l}}{\delta_{c,l}} = \frac{v_l}{Sc_l \delta_{c,l}} \quad (6.10)$$

where K_l is the time-averaged liquid mass transfer coefficient and $\delta_{c,l}$ is the thickness of the concentration boundary layer on the liquid side, Sc_l the Schmidt number in the liquid phase. The Schmidt number comparing the viscous diffusion rate to the molecular diffusion rate and is given by

$$Sc = \frac{v}{D} \quad (6.11)$$

However, the overly simplistic nature of film theory does not physically explain convective mass transfer in a flowing fluid, and so other theories and models have been postulated to describe this phenomenon.

6.2.1.1.2 Penetration model

Higbie [80] took into consideration the fact that the mass transfer across the interface can be unsteady in his model. Here the fluid in contact with the interface is periodically renewed by fluid coming from the bulk and each new fluid packet remains for the same constant time τ in contact with the interface. This time is a function of the turbulence level of the system. For the mass transfer coefficient at the liquid side we have

$$K_l = \sqrt{\frac{D_{A,l}}{\pi\tau}} = \sqrt{\frac{v_l}{Sc_l\pi\tau}} \quad (6.12)$$

A major weakness of penetration theory is that the exposure time of fluid at the surface τ cannot be theoretically predicted and must be determined experimentally.

6.2.1.1.3 Surface renewal model

The previous penetration model has been reinterpreted by Danckwerts [81], to correct the fact that the time τ should not be a constant but rather follow a normal probability distribution.

$$K_l = \sqrt{\frac{D_{A,l}}{\bar{\tau}}} = \sqrt{\frac{v_l}{Sc_l\bar{\tau}}} \quad (6.13)$$

Various models exist to determine $\bar{\tau}$ the mean time between surface renewals.

Fortescue & Pearson [82] proposed a large eddy model and postulated that $\bar{\tau}$ is the mean turnover time of the largest eddies of a turbulent flow

$$\bar{\tau} \approx \frac{\Lambda}{u'} \quad (6.14)$$

where Λ is a measure of turbulence macroscale in the liquid bulk and u' is the r.m.s. of large scale velocity fluctuation in the liquid bulk.

$$K_l \approx \sqrt{\frac{D_{A,l} u'}{\Lambda}} = cu' Sc_l^{-\frac{1}{2}} Re_t^{-\frac{1}{2}} \text{ where } c = cte \quad (6.15)$$

where $Re_t = u'\Lambda/\nu$ is the turbulent Reynolds number. Suppose Λ is a typical length scale of the large eddies which may be taken equal to the integral length scale defined from a spatial correlation function, analogous to the integral time scale.

Banerjee *et al.* [83] and Lamont & Scott [84] proposed a small eddy model which postulates that the viscous dissipation range small-scale eddies is controlling $\bar{\tau}$

$$\bar{\tau} \approx \sqrt{\frac{\nu}{\varepsilon_i}} \quad (6.16)$$

where ε_i is the turbulent energy dissipation rate close to the interface and can be expressed in terms of large-scale characteristics through Taylor's relationship (Batchelor [85])

$$\varepsilon \propto \frac{u'^3}{\Lambda} \quad (6.17)$$

This yields to

$$K_l \approx \sqrt{\frac{D_{A,l} \varepsilon_i}{\nu_l}} = cu' Sc_l^{-\frac{1}{2}} Re_t^{-\frac{1}{4}} \text{ where } c = cte \quad (6.18)$$

Theofanous *et al.* [86] justified the difference between the two models by explaining that the preponderance of the large eddies is expected at low turbulent Reynolds number while small eddies are preponderant at high turbulent Reynolds number.

6.2.1.1.4 Surface divergence model

The inherent difficulty of measuring $\bar{\tau}$ depending on the experiments and the flow configuration, limit the use the Surface Renewal (S.R.) models. McCready *et al.* [87] proposed another approach using the advection-diffusion equation to suggest that gas/liquid mass transfer is controlled by surface-normal motions. These surface-normal motions have the form of a stagnation flow described similarly than can be found in Chan & Scriven [88]. The important simplification is that at high Schmidt number the interface parallel motions have a negligible effect compared to the interface-normal motions. This means that only near-surface (viscous and concentration boundary layer) motions need consideration. This model is called the Surface Divergence model and the velocity field used in the advection-diffusion equation is the first term in Taylor series expansion

$$v_i = -\left(\frac{\partial u_i}{\partial x} + \frac{\partial w_i}{\partial z}\right)y = -\omega y, \quad (6.19)$$

where u_i , v_i and w_i are the near-surface velocities in the x , y , and z directions, the terms between parenthesis is called the 'surface divergence' strength and is labelled ω . The Surface divergence model has been extensively used for air-water gas transfer predictions (Banerjee & Macintyre [89]; McKenna & McGillis [90]; Magnaudet & Calmet [91]; Jirka [92]; Turney & Banerjee [93]).

6.2.1.2 Solid surface model

Kader & Yaglom [94], Calmet & Magnaudet [95], and Shaw & Hanratty [96] have considered the case of mass transfer in the configuration of a fluid confined with a solid.

6.2.2 Experimental measurement of liquid-liquid mass transfer

Considering the difficulty to make measurements of the mass transfer between liquid steel and slag in the case of an industrial steel ladle, cold models using low melting point metal or water are generally used to characterize the mass transfer.

6.2.2.1 Water experiments

Kim & Fruehan [32] and Mietz *et al.* [97], Asai *et al.* [98] and more recently by De Oliveira Campos [41] performed measurements of the liquid steel equivalent phase mass transfer with a gas stirred water experiment. In [32] the authors studied with a cylindrical ladle at ambient temperature the mass transfer of thymol from the water to the oil phase. The authors measured the influence of the oil properties (viscosity, surface tension, oil volume) as well as diameter and position of the injection orifice on the mass transfer. From their study, the authors concluded that an increase of the water mass transfer coefficient can be obtained for an increase in the air flow rate. They also reported that an increase in the oil viscosity leads at high air flow rate values to a lower value of the water mass transfer coefficient. According to the authors, different mass transfer regimes can be identified depending on the air flow rate value (cf. Figure 6.2). The mass transfer regime change is explained by the authors by the break-up of the oil layer into droplets and the entrainment of these oil droplets into the water causing an increase of the oil/water interfacial area.

Then [97] measured on a cylindrical ladle at ambient temperature the mass transfer of Iodine between water and cyclohexane using a photometer. The authors have done experiments with three different diameters of ladle and kept the aspect ratio of the height of the bath to the ladle diameter to $h_w/L_x = 0.9$ and consider a volume of oil of $V_s = 0.1V_w$. The authors also concluded that the increase of the gas flow rate generates an increase in the mass transfer capacity coefficient for all the size of ladle (cf. Figure 6.3). The authors made the same explanation of the change in the rate of evolution of the capacity coefficient in water than [32] that it is due to slag emulsification.

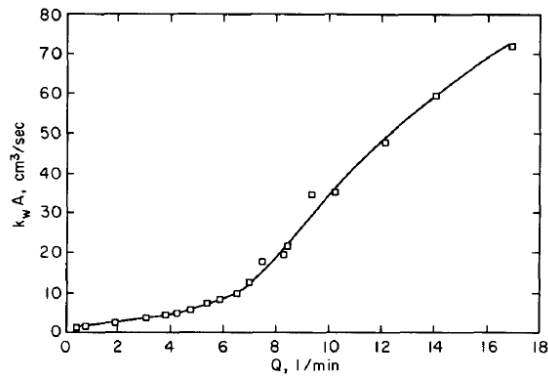


Figure 6.2: Product of the water mass transfer coefficient with interfacial area as a function of the air flow rate for a water/oil model from the experiment of Kim & Fruehan [32].

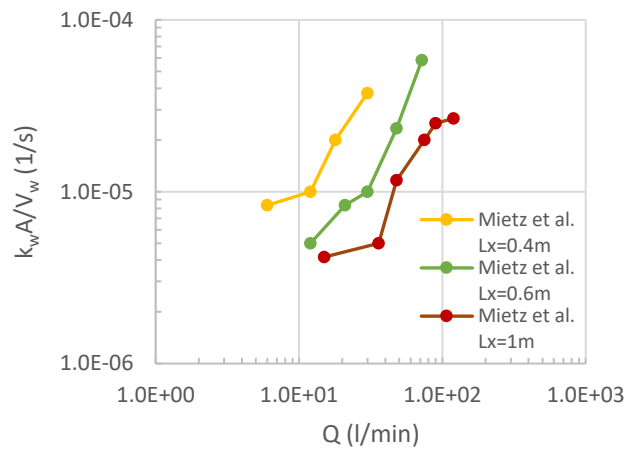


Figure 6.3: Capacity coefficient as a function of the air flow rate for a water/cyclohexane model with three different ladle diameters from the experiment of Mietz et al. [97].

6.2.2.2 Liquid metals experiments

Experiments with liquid metals, unfortunately, are less frequent and only a limited amount of studies are accessible in the literature. Hirasawa *et al.* [99], Ishida *et al.* [9] and performed some measurements with liquid metals at high temperature. First, [9] used a reduced scaled industrial ladle of 2.5 ton using the same fluids as in the industrial process to measure the mass transfer of sulphur between liquid steel and slag. The authors reported also a change in the evolution of the capacity coefficient when the gas flow rate is above a critical value (cf. Figure 6.4).

Then, in [99] the authors studied on a cylindrical copper/slag model at high temperature (1250°C) the influence of the height of the slag layer h_s , the height of the metal bath h_m as well as the crucible diameter on the mass transfer of silicon between liquid copper and slag. According to the authors, different regimes of mass transfer depending on the gas flow rate value have been identified (cf. Figure 6.5). Again, the difference between the different regimes is explained by the break-up of the slag layer into droplets and the entrainment of these droplets in the liquid copper phase. On the other hand, Lachmund *et al.* [8] measured the mass transfer of sulphur between liquid steel and slag but this time with an industrial ladle and reported only one mass transfer regime in the gas flow rate range considered.

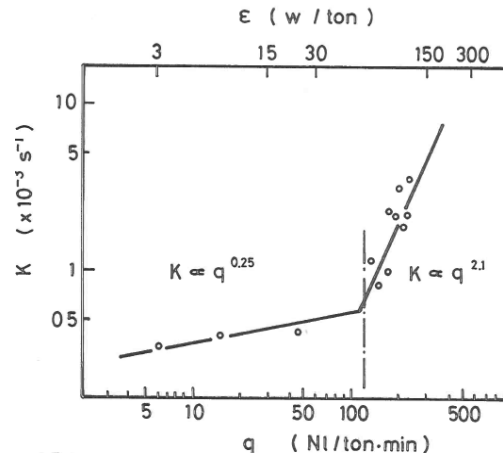


Figure 6.4: Capacity coefficient or product of the mass transfer coefficient in steel with interfacial area per volume of steel as a function of the gas flow rate for a liquid steel/slag 2.5 ton ladle from the experiment of *Ishida et al.* [9].

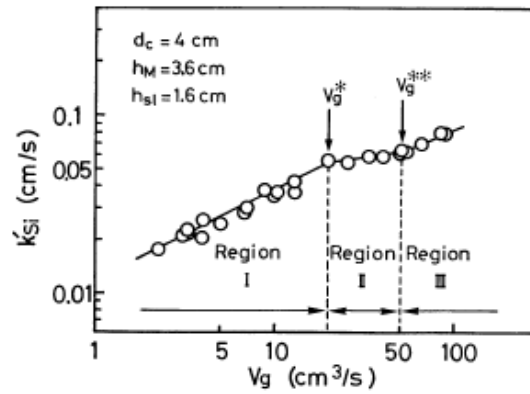


Figure 6.5: Variation of the copper mass transfer coefficient as a function of gas flow rates in a high-temperature copper/ slag cylindrical model from the experiment of *Hirasawa et al.* [99].

To summarize, we can see that from the water and liquid metal experiments different mass transfer regimes are observed when the gas flow rate is increased. On the other hand, in an industrial ladle configuration, the different studies in the literature do not agree on the occurrence of mass transfer regime change.

6.3 EXPERIMENTAL MODEL

We are interested here in the experimental modelling of the mass transfer of sulphur between liquid steel configuration by using a water experiment. We use the same geometrical and physical model of the process as the one presented in section 2.2 except that now we dissolve a chemical tracer in the water phase. This experiment is an improved version of the one established by De Oliveira Campos [41] during the end of his PhD. In this study, the author could perform measurements of the mass transfer of thymol from the water to the oil phase with a slightly smaller water experiment than in our study.

6.3.1 Experimental Procedure

We follow again the work of Kim & Fruehan [32] on the choice of the fluids to reproduce the configuration of the industrial process and use thymol ($C_{10}H_{14}O$) as a chemical tracer dissolved in the water phase. The main reason for the choice of thymol is because it is expected to reproduce the mass transfer of the reaction of the desulfurization process in an industrial ladle. Indeed, thymol has a low diffusion coefficient in water and a high partition coefficient between the oil and water.

To proceed we use thymol powder with a solubility at saturation in the water at ambient temperature of $C_{w,0} = 0.9g/l$ (Karaffa [100]) that we put in a water tank. We heat the solution to get a better dissolution of the thymol around its melting point which is $T^{\circ}_{fusion} = 49.6^{\circ}C$ according to Haynes [101]. All the chemical properties of thymol can be found in Table 6.1. Then we mix the solution to homogenize the thymol in the water and before filling the ladle with the solution we wait that the temperature of the solution returns to ambient temperature. Before pouring the solution in the ladle we roughly filter the solution with a metallic sieve to avoid surfactant of size $d > 2mm$ in the solution. It is important to mention that when the solution is ready it is as transparent as water and no obvious presence of surfactants can be seen. Just before the start of air injection, we add the oil mixture on top of the free surface. When the air injection is started, we record thymol concentration variation in water, by taking two samples of water every ten minutes with a calibrated pipette of $3ml$. The samples are taken on the same spot located on the border of the open eye and around $4cm$ below the free surface which is oil-free (cf. Figure 6.6). As the diffusivity of thymol in water is low, we measure the evolution of the concentration for three hours. The concentration of thymol in the water samples is measured indirectly with a light refractometer (Rudolph J357).

To compute the values of the diffusion coefficient of thymol in fluids we use the Stokes-Einstein law which allows to determine the diffusion coefficient of spherical particles through a liquid at low Reynolds number knowing the temperature, the viscosity of the fluid and the equivalent radius of the particle considered. First, we compute the equivalent radius of the spherical particle knowing the diffusive mass and density of thymol by equalling the volume of this spherical particle to the diffusive volume we can write

$$r_{th} = \left(\frac{3M_{th}}{4\pi\rho_{th}N_A} \right)^{1/3} \quad (6.20)$$

where M_{th} (kg/mol) is the diffusive mass of thymol ρ_{th} (kg/m^3) is the density of thymol and $N_A = 6.022 \cdot 10^{23} mol^{-1}$ is the Avogadro constant.

Then we can use the Stokes-Einstein law in the fluid medium

$$D_{th,k} = \frac{k_B T}{6\pi r_{th} \mu_k} \quad (6.21)$$

where r_{th} (m) is the equivalent radius of the particle μ_k (Pa/s) is the dynamic viscosity of the fluid, T (K) is the temperature of the fluid and $k_B = 1.38 \cdot 10^{-23} \text{ J K}^{-1}$ is the Boltzmann constant. As we can see from Table 6.2, the values in our model are of the same order than in the one in the industrial process for sulphur diffusion from liquid steel to the slag phase as can be seen in Table 6.3. In both cases, the diffusion coefficient value in the slag equivalent phase is lower than the one in the steel equivalent phase. However, we can notice that in the water experiment case the diffusion coefficient of thymol in the oil phase is hundred times lower than in the water phase which is not the case of the diffusion coefficient of sulphur in slag.

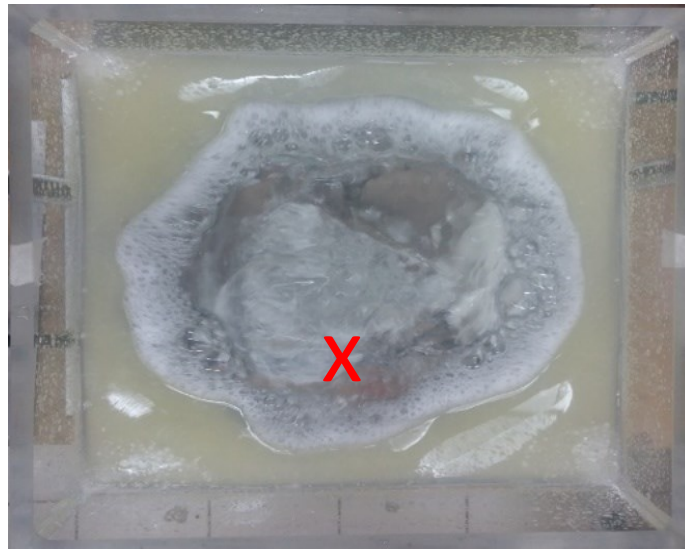


Figure 6.6: Top view of the water experiment with thymol dissolved in water at $Q = 5.0 \text{ l/min}$ with $d_{inj} = 7.9 \text{ mm}$, the red cross is approximatively the sample spot.

$C_{w,0}$ (g/l)	M_{th} (g/mol)	ρ_{th} (g/l)	$S_{th,w}$ (g/l)	T°_{fusion} ($^{\circ}\text{C}$)
0.9	150.2	960	0.9	49.6

Table 6.1: Main chemical properties of Thymol at ambient temperature according to PubChem, [100] [101].

$D_{th,w}$ (m^2/s)	$D_{th,o}$ (m^2/s)	$P_{th,o/w}$	$\beta_{th,w/o}$
$6.8 \cdot 10^{-10}$	$6.8 \cdot 10^{-12}$	350	$8.5 \cdot 10^{-2}$

Table 6.2: Parameters of the mass transfer of the thymol between water and oil in our model where the diffusion coefficient of thymol in the water phase is taken from Reid et al.[102] and for the oil phase is computed using (6.21).

$D_{S,m}$ (m^2/s)	$D_{S,s}$ (m^2/s)	$P_{S,s/m}$	$\beta_{S,m/s}$
$4.4 \cdot 10^{-9}$	$2.8 \cdot 10^{-10}$	350	0.109

Table 6.3: Parameters of the mass transfer of the sulphur between liquid steel and slag in an industrial ladle where the diffusion coefficients are taken from Gaye [103].

6.3.1.1 Uncertainty quantification

The accuracy of the light refractometer (Rudolph J357) for the refraction indices is $n \pm 2 \cdot 10^{-5}$. In order to obtain the thymol concentration with the light refractometer, a custom scale from six solutions of known concentration of thymol using the same water than in the water experiment is made before the measurement. We can see from Figure 6.7 that the light refractometer accuracy induces an error on the measured concentration value of $C \pm 0.1 \text{ g/L}$ considering the error bar on the refractive index value. This is due to the small variation of the refraction indices at the considered thymol concentration range in water. The variation from the maximum and minimum concentration is about $2 \cdot 10^{-4}$, it is only ten times higher than the light refractometer accuracy.

Considering the values of the relative incertitude in Table 6.4 we can see that the limited accuracy of the light refractometer leads to an important relative error on the concentration of thymol especially at low values of the concentration of thymol in water. We can also note the effect of the size difference between the height of the water bath and the height of the oil layer leading to more important relative error for on the geometrical parameters of the oil layer. For the other variables, the relative error is contained to less than fifteen per cent of the value.

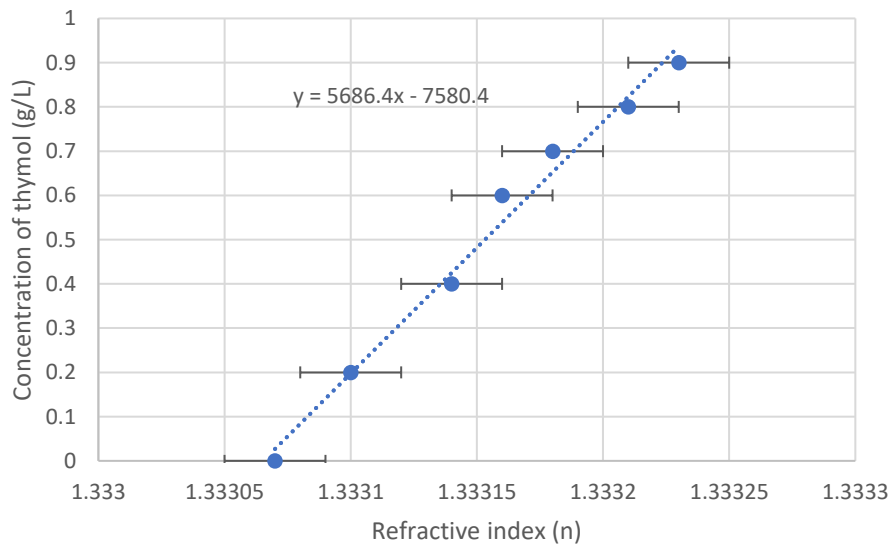


Figure 6.7: Custom scale established from measurements of solutions of known thymol concentration with error bars representing the measurement error.

$\Delta C/C_{w,0}$ (%)	$\Delta C/C_{w,min}$ (%)	$\Delta V/V_w$ (%)	$\Delta V/V_o$ (%)	$\Delta L/h_w$ (%)	$\Delta L/h_o$ (%)	$\Delta t_{sample}/t_{sample}$ (%)
11	50	0.7	21	0.5	14	10

Table 6.4: Values of the absolute incertitude of the parameters necessary to compute the mass transfer coefficient.

6.4 PHENOMENOLOGICAL ANALYSIS

We will now try to characterise the behaviour of the liquid-liquid mass transfer of the water experiment based on the results of the previous hydrodynamic phenomenological analysis in 2.3.

6.4.1 Average concentration evolution model

We detail here the general solution of the evolution of the concentration of thymol in the water experiment without making assumptions of the model used in the study of Kim & Fruehan [32]. The mass transfer equation of thymol in each phase gives

$$\frac{dC_w}{dt} = -\frac{K_w A}{V_w} (C_w - C_w') = J < 0 \quad (6.22)$$

$$\frac{dC_o}{dt} = -\frac{K_o A}{V_o} (C_o - C_o') = -J > 0 \quad (6.23)$$

where C_w (g/L) and C_o (g/l) are respectively the concentration of thymol in water and oil bulk, C_w' (g/l) and C_o' (g/l) are respectively the concentration of thymol at the interface on water and oil side, K_w (m/s) and K_o (m/s) are respectively the mass transfer coefficient of thymol in water and oil, V_w (m³) and V_o (m³) are respectively the water and oil volume and J (g/m³s) is the diffusive flux. The partition coefficient of thymol comparing the solubilities of thymol in water and oil at equilibrium can be given by

$$P = \frac{C_o'}{C_w'} \quad (6.24)$$

Using mass balance for thymol between water and oil from (6.22), (6.23) we can write

$$\frac{V_w dC_w}{dt} + \frac{V_o dC_o}{dt} = 0 \quad (6.25)$$

After time integration we can write

$$V_w C_w + V_o C_o = V_w C_{w,0}, \quad (6.26)$$

where $C_{w,0}$ (g/l) is the initial concentration of thymol in water bulk. Using (6.25) and (6.26) we can rewrite (6.22) and (6.23)

$$\frac{V_o}{V_w} \frac{d}{dt} \left[\frac{C_o}{C_{w,0}} \right] = -\frac{1}{\tau_w} \left(1 - \frac{V_o C_o}{V_w C_{w,0}} \right) + \frac{C_o'}{\tau_w P C_{w,0}}, \quad (6.27)$$

$$\frac{T_o}{T_w P} \frac{d}{dt} \left[\frac{C_o}{C_{w,0}} \right] = \frac{C_o'}{\tau_w P C_{w,0}} - \frac{C_o}{\tau_w P C_{w,0}}, \quad (6.28)$$

with $T_w = V_w/K_w A$ and $T_o = V_o/K_o A$, combining (6.27) and (6.28) we can obtain

$$\frac{d}{dt} \left[\frac{C_o}{C_{w,0}} \right] = -\frac{1}{T_w} \frac{1 + \beta}{1 + \alpha} \frac{C_o}{C_{w,0}} + \frac{1}{T_w} \frac{V_w/V_o}{1 + \alpha}, \quad (6.29)$$

with $\alpha = K_w/PK_o$ a case-specific constant as we do not know a priori K_w and K_o and $\beta = V_w/V_o P$ a constant depending only on the fluid quantity and nature. Equation (6.29) is an ordinary differential equation which has a solution expressed by

$$\frac{C_o}{C_{w,0}} = Ge^{-\lambda t} + \frac{V_w}{V_o} \frac{1}{1 + \beta},$$

with B a constant on \mathbb{R} and $\lambda = \frac{1}{T_w} \frac{1+\beta}{1+\alpha}$. At $t = 0$ we know that $C_{o,0} = 0$ so we can write

$$G = -\frac{V_w}{V_o} \frac{1}{1 + \beta},$$

to obtain the solution for the thymol concentration in the oil phase

$$C_o = \frac{V_w}{V_o} \frac{C_{w,0}}{1 + \beta} (1 - e^{-\lambda t}). \quad (6.30)$$

Using (6.26) and (6.30) we can obtain the time expression of thymol concentration in the water phase

$$C_w = C_{w,0} - \frac{C_{w,0}}{1 + \beta} (1 - e^{-\lambda t}). \quad (6.31)$$

Following (6.31), we can see that the concentration of thymol follow an exponential decay from the initial value $C_{w,0}$ to an equilibrium value of $C_{w,0} - C_{w,0}/(1 + \beta)$. The concentration decay time is given by

$$T_c = 1/\lambda$$

$$T_c = T_w \frac{1 + \alpha}{1 + \beta}$$

α and β need to be small to have a minimum concentration decay time around $T_1 \sim V_w/K_w A$. In the water experiment of [32], the authors consider that the assumption that $\alpha \ll 1$ is suitable to reproduce the mass transfer configuration of the desulfurization process meaning that the steel phase mass transfer is controlled by the steel phase mass transfer resistance. With these assumptions and from their measurement of the mass transfer of thymol from water to the oil phase they determined using (6.24) and (6.26) the following expression to determine the mass transfer coefficient from the water concentration

$$\frac{1}{[C_w(1 + \beta) - C_{w,0}\beta]} \frac{dC_w}{dt} = \frac{K_w A}{V_w},$$

and after integration we obtain

$$\frac{\ln \left[\frac{C_w}{C_{w,0}} (1 + \beta) - \beta \right]}{1 + \beta} = \frac{K_w A}{V_w} t. \quad (6.32)$$

With relation (6.32), it is possible to compute directly the product of the mass transfer coefficient with interfacial area per volume unit as a function of the measured thymol concentration in water. Because of its simplicity, we will use this formulation to determine the mass transfer coefficient in the experimental results.

6.4.1.1 Comparison of three typical cases

In the following comparison, we denote by the indices w both the water and liquid steel phase and use the indices o for both the oil and slag phase.

We gather the main quantities characterizing the mass transfer for three cases corresponding to two water experiments and an industrial ladle experiment in Table 6.5.

Notation	Expression	Our experiment	Kim & Fruehan [32]	Lachmund et al. (Industrial ladle) [8]
m	μ_w/μ_o	$1.3 \cdot 10^{-2}$	$3.0 \cdot 10^{-2}$	$5.4 \cdot 10^{-2}$
r	ρ_w/ρ_o	1.1	1.1	2.4
D_r	D_w/D_o	100	43	16
Sc_m	ν_w/D_w	$1.5 \cdot 10^3$	$1.5 \cdot 10^3$	$1.8 \cdot 10^2$
Sc_s	ν_o/D_o	$1.3 \cdot 10^7$	$2.4 \cdot 10^6$	$1.3 \cdot 10^5$
P	C_o'/C_w'	350	350	350
β	V_w/PV_o	$8.5 \cdot 10^{-3}$	$8.5 \cdot 10^{-3}$	$8.6 \cdot 10^{-2}$

Table 6.5: Main dimensionless physical properties of the steel equivalent phase and the slag equivalent phase for our experiment and the experiments of [8, 32]. The partition coefficient ratio has been considered as a constant value corresponding to the case of thymol between water and oil as it is not given nor measured in most of the industrial case.

6.4.2 Concentration boundary layer structure

We consider the water-oil interface covered by boundary layers, the velocity on the interface is on average $U_I(x)$ where x, y is an orthogonal system of curvilinear coordinates following the surface. Velocity outside the boundary layer is $U_{0,w}$ and we can guess that $U_{0,w}$ is proportional to w_M the vertical velocity of the bubble plume. The surface is located at $y = 0$. The boundary layer structure is described in Figure 6.8.

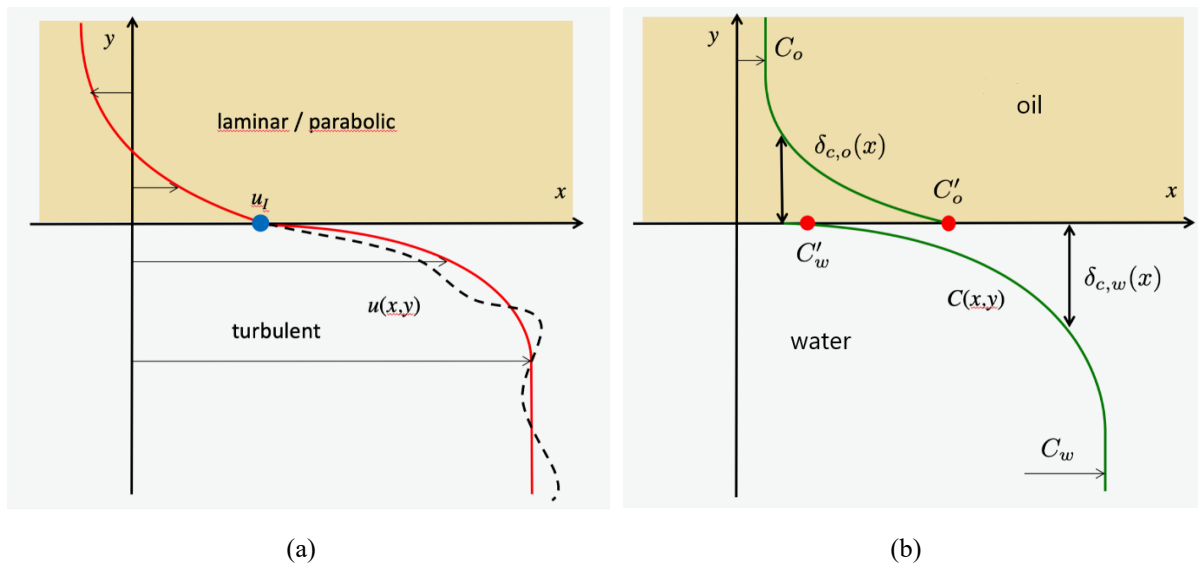


Figure 6.8: Boundary layer structure. (a) Momentum boundary layers. The average velocity on the interface is $U_I(x)$. In the oil layer $Re_{o,w}$ is low and so a laminar regime of Nusselt type is considered. The water layer has a high $Re_{o,w}$ so a turbulent regime is considered. (b) Concentration boundary layers. The values on the interface are determined by a partition law at equilibrium with $C'_o = PC'_w$. For easier reading P ratio is not represented scaled on the figure.

The transport equation of thymol concentration in water or oil is

$$\frac{\partial C}{\partial t} + U \cdot \nabla C = D_p \nabla^2 C \quad (6.33)$$

The partition law at the interface is replaced by a Dirichlet condition

$$C(x, 0) = C'_p, \quad (6.34)$$

where p represents the generic indices of phase which can be w or o and with $C'_w = 0$ and $C'_o = 1$. Far from the interface we have $C(x, y) \rightarrow C_{p,\infty}(t)$. The C quantity is a passive scalar, meaning that the velocity field $U(X, t)$ is given and is not influenced by C . We can modify D_p without affecting the velocity field solution. We suppose that the flow is stationary and that the possible oil droplets do not get deformed too rapidly. This assumption will be verified below. Within a boundary approximation expressed by Schlichting [44] we have

$$U(x, y) \frac{\partial C}{\partial x} = D \frac{\partial^2 C}{\partial y^2} \quad (6.35)$$

We make the following assumption

$$C(x, y) = C_{p,\infty} f[y/\delta_{c,p}(x)], \quad (6.36)$$

where $\delta_{c,p}$ is the concentration boundary layer thickness of the p phase. We simplify the velocity profile

$$U(x, y) = U_I(x) + \omega_p(x)y, \quad (6.37)$$

where

$$\omega_w(x) = \frac{\partial U(x, 0_-)}{\partial y}, \quad \omega_o(x) = \frac{\partial U(x, 0_+)}{\partial y}. \quad (6.38)$$

Then we have

$$\frac{\partial C}{\partial x} = B(x, y) \frac{\partial^2 C}{\partial y^2}, \quad (6.39)$$

and the diffusion coefficient is equal to

$$B(x, y) = \frac{D_p}{U_I(x) + \omega_p(x)y}. \quad (6.40)$$

If we consider x as a time we have a diffusion problem with a diffusion coefficient dependant on y and t . Because U_I is positive, this coefficient is positive for small y but negative for

$$y > y_p(x) = U_I(x)/|\omega_p(x)| \quad (6.41)$$

Moreover, for the water phase D_w changes sign converging toward infinity, meaning that the boundary layer cannot exist for $y > y_p(x)$. Because of this, we find two limits for the water case, the first one is a free surface limit, the other one is a rigid surface. For the oil layer case, we find only one limit which is the free surface one.

6.4.2.1 Free surface limit

In the following, we consider only one fluid delimited by a free surface, this development is valid for the two phases. We take in each phase the self-similar variable applied to the concentration boundary layer

$$\eta = \frac{|y|}{\delta_{c,p}(x)}, \quad f' = \frac{df}{d\eta}, \quad \delta_{c,p}' = \frac{d\delta_{c,p}}{dx} \quad (6.42)$$

We are in the limit of $U_I \gg \omega_p$ and $|y| \sim \delta_{c,p}$. Equation (6.39) can be reduced to a separated variables equation

$$U_I \delta_{c,p}' \delta_{c,p} = \frac{D_p}{\eta} (\ln f')' \quad (6.43)$$

The solution is

$$\delta_{c,p}(x) \sim \left[\int_0^x \frac{D_p}{U_I(s)} ds \right]^{1/2} \quad (6.44)$$

where we are neglecting the multiplying factors 2 and 3. The mass transfer coefficient per surface unit is

$$K_{p,I}(x) \sim \frac{D_p}{\delta_{c,p}(x)} \quad (6.45)$$

Therefore, the following scaling law $K_{p,I} \sim D_p^{1/2} f(Re) \sim Sc^{-1/2} f(Re)$. We can define a characteristic velocity by

$$\frac{1}{u_I} := \frac{1}{L} \int_0^L \frac{1}{U_I(x)} dx, \quad (6.46)$$

where $x = 0$ and $x = L$ are the beginning and end position of the boundary layer. For a droplet of size d or a wave of the same wavelength d we can take $L \sim d$. So, we can write

$$K_{p,I} \sim \left(\frac{D_p u_I}{d} \right)^{1/2}, \quad (6.47)$$

valid for each phase in agreement with the free surface theory of 6.2. To go further we must have an estimation of the interfacial velocity u_I .

6.4.2.2 Rigid surface limit

This development is valid only for the water phase. When $U_I \ll \omega_w$ the Equation (6.39) can be reduced to a separated variable equation

$$\omega_w \delta_{c,w}' \delta_{c,w}^2 = \frac{D_w}{\eta^2} (\ln f')' \quad (6.48)$$

The solution is

$$\delta_{c,w} = \left[\int \frac{D_w}{\omega_w(x)} dx \right]^{1/3}, \quad (6.49)$$

where we are neglecting the multiplying factor 2 and 3. The mass transfer coefficient per surface unit is

$$K_{w,\omega} = \frac{D_w}{\delta_{c,w}}. \quad (6.50)$$

Therefore, the following scaling law can be written $K_{w,\omega} \sim D_w^{2/3} \sim Sc^{-2/3}$. We can define the following characteristic shear stress

$$\frac{1}{\omega} = \frac{1}{L} \int_0^L \frac{1}{\omega_w(x)} dx, \quad (6.51)$$

where $x = 0$ and $x = L$ are the beginning and end position of the boundary layer. For a droplet of size d or a wave of the same wavelength d we can take $L \sim d$. So, we can write

$$K_{w,\omega} \sim \left(\frac{D_w^2 \omega}{d} \right)^{1/3}. \quad (6.52)$$

To go further we must have an estimation of the characteristic shear stress ω .

6.4.3 Momentum boundary layer structure

If we compare the mass transfer coefficients of the two limiting cases for the water phase, we got

$$\frac{K_{w,l}}{K_{w,\omega}} \sim \left(\frac{u_l^3}{D_w d \omega_w^2} \right)^{1/6} \quad (6.53)$$

To go further, we need a relation between u_l and ω by analysing the momentum boundary layers. The tangential viscous shear continuity leads to

$$\mu_w \omega_w = \mu_o \omega_o \quad (6.54)$$

6.4.3.1 Possible cases in oil and water

For each phase we could consider three cases depending on the flow regime: turbulent (T), laminar boundary layer (BL) and Nusselt profile (N). We end up with nine cases, but in the water or liquid steel phase $Re_w \simeq 10^4$, so only the turbulent case is possible. Then, the three cases to be considered are a turbulent flow regime in the oil phase (TO), a laminar boundary layer in the oil phase (BLO) and a Nusselt profile in the oil phase (NO). In the following, we will only consider the Nusselt profile (NO) in the oil layer.

6.4.3.2 Turbulent boundary layer in water

For a turbulent boundary layer in water, the shear stress is

$$\tau_w = \rho u_*^2, \quad (6.55)$$

where u_* is the shear velocity or friction velocity and can be approximated by

$$u_* = \frac{\kappa U_{0,w}}{\ln Re_{0,w}}, \quad (6.56)$$

where κ is the Von Karman constant and

$$Re_{0,w} = \rho_w U_{0,w} h_w / \mu_w. \quad (6.57)$$

From the relation (6.55) we get

$$\omega_w = c_T \frac{U_{0,w}^2}{\nu_w}, \quad (6.58)$$

where the turbulent constant is given by

$$c_T = \frac{\kappa}{\ln Re_{0,w}}. \quad (6.59)$$

From (6.52) we can get

$$K_{w,\omega} = Sc^{-2/3} (Re/c_T)^{-1/3} U_{0,w} \quad (6.60)$$

An alternative to this theory is to consider turbulent fluctuations or eddies in the viscous sub-layer of thickness $\delta_* = \nu/u_*$ where each eddy is associated to a small-scale boundary layer described as above, but with the eddy scale:

- the development length of the small-scale boundary layer is the sublayer scale $d = \delta_*$;
- the shear in the small-scale boundary layer is $\omega = u_*/\delta_*$.

Then we get

$$K_{w,\omega} = Sc^{-2/3} u_* = c_T Sc^{-2/3} U_{0,w} \quad (6.61)$$

This agrees with Kader & Yaglom [94] and Calmet & Magnaudet [95], on the other hand, Shaw & Hanratty [96] find an exponent of $-0,7$ on the Schmidt number.

6.4.3.3 Nusselt profile in the oil layer

The oil layer can be approximated as a thin film if $h_o/d \ll 1$ and a parabolic laminar flow in the oil is considered. In this thin film, the mass rate flowing through a slice is null, the oil flow is recirculating (Figure 6.9).

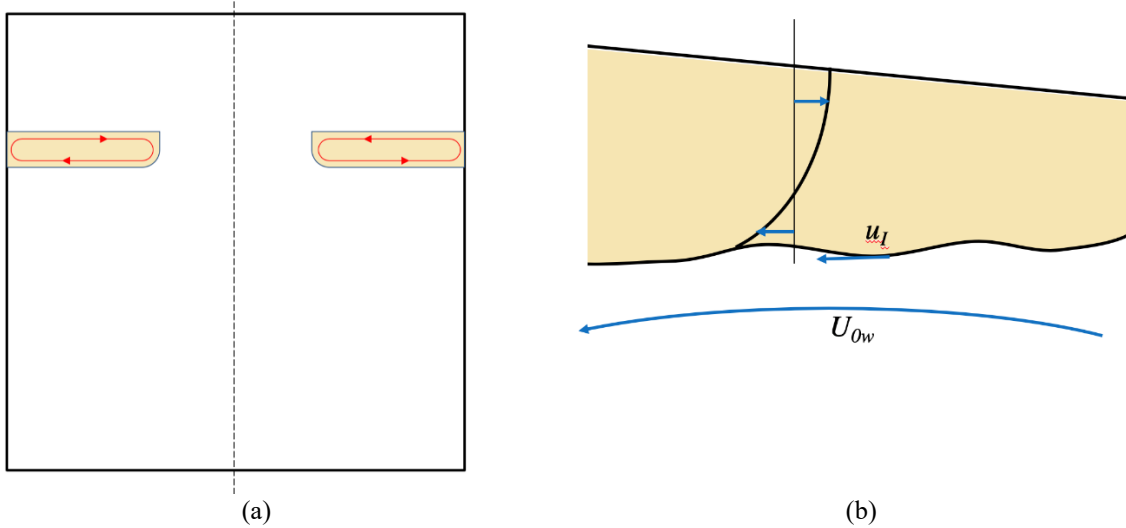


Figure 6.9: Recirculation in the oil layer. (a) Global view. (b) Details of the oil layer with a parabolic profile.

The flow within the oil layer is parabolic and generated by shearing of water flow from below and from a hydrostatic pressure gradient which causes the returning flow in the top part. This case corresponds to a Nusselt profile in the oil phase abbreviated NO. The oil flow is thin and is approximated in each slice by a Poiseuille parabolic profile also called Nusselt profile

$$u(y') = u_I[-1 + (3/2)(y/h_o)(2 - y/h_o)], \quad (6.62)$$

and the shear in the bottom part is $\omega_o = 3u_I/h_o$ which gives

$$y_o = \frac{3h_o}{2}, \quad (6.63)$$

where h_o is the oil thickness. For this Poiseuille flow in the oil layer we have

$$\tau_o = \mu_o \frac{3u_I}{h_o}. \quad (6.64)$$

Combining this with (6.58) we get

$$u_I^{NO} = \frac{c_T}{3} m Re_{0,w} \frac{h_o}{d} U_{0,w}, \quad (6.65)$$

where $m = \mu_w/\mu_o$, we can then get

$$Re_{I,o}^{NO} = \frac{[u(h_o) - u(0)]h_o}{\nu_o} = \frac{c_T h_o^2 m^2}{2 d^2 r} Re_{0,w}^2, \quad (6.66)$$

where $r = \rho_w/\rho_o$.

6.4.4 Transport coefficients

6.4.4.1 In the water phase

From the above assumptions, we can get two possible relations for the transport coefficients depending if we consider a laminar boundary layer in the oil phase case or a Nusselt profile in the oil phase case. In the Nusselt profile in the oil phase case from (6.47) and (6.65) we have

$$K_{w,I} = \left(\frac{mc_T}{3}\right)^{1/2} Sc^{-1/2} \left(\frac{h_o}{d}\right)^{1/2} U_{0,w} \quad (6.67)$$

We also have from (6.60)

$$K_{w,\omega} = Sc^{-2/3} (Re/c_T)^{-1/3} U_{0,w} \quad (6.68)$$

The Reynolds number is given by

$$Re = \frac{w_M z_S}{\nu_w} \quad (6.69)$$

In a general way, we get from (6.53)

$$\frac{K_{w,I}}{K_{w,\omega}} \sim \left(\frac{u_i^3}{D_w d \omega_w^2}\right)^{1/6}, \quad (6.70)$$

and get

$$\frac{K_{w,I}}{K_{w,\omega}} \sim (8c_T)^{-1/6} m^{1/2} \left(\frac{h_o}{d}\right)^{1/2} Sc^{1/6} Re^{1/3}. \quad (6.71)$$

The transition between the two behaviours in the Nusselt profile in the oil phase case, if it is additive, can be expressed by $K_w = K_{w,I} + K_{w,\omega}$ and so

$$K_w^{NO}/w_M = a m^{1/2} Sc^{-1/2} \left(\frac{h_o}{z_S}\right)^{1/2} + b Sc^{-2/3} Re^{-1/3}, \quad (6.72)$$

where we have considered $w_M/U_{0,w}$, d/z_S as constant factors and where all the other factors have reduced to a and b . Finally, the Sherwood number which can be written using the Schmidt and the Reynolds number is given by

$$Sh_w = \frac{K_w Re Sc_w}{w_M} \quad (6.73)$$

Then we can rewrite (6.72) to obtain

$$Sh_w^{NO} = a m^{1/2} Sc^{1/2} Re \left(\frac{h_o}{z_S}\right)^{1/2} + b Sc^{1/3} Re^{2/3} \quad (6.74)$$

If we consider a classical turbulent boundary layer theory of [94] with a relation of (6.61) type, we get

$$Sh_w^{NO-KY} = a m^{1/2} Sc^{1/2} Re \left(\frac{h_o}{z_S}\right)^{1/2} + b Sc^{1/3} Re \quad (6.75)$$

The correlations give $Sh = f(Re, Sc)$ but the control parameter is the injected gas flow rate from which we can be computed the modified Froude number. In order to re-express the correlations with the modified Froude number $Sh = f(N, Sc)$ we consider that the vertical velocity in the water is

described as in 2.3.2 with the rectilinear bubble plume description $U = (g^2 Q)^{1/5}$. Then we can rewrite the Reynolds number as a function of the modified Froude number

$$Re = \frac{UL_x}{4\nu_w},$$

$$Re = \left(\frac{L_x^2 g h_w}{16\nu_w^2} \right)^{1/2} N. \quad (6.76)$$

If we consider the Archimedes number given by

$$Ar = \frac{gL_c^3 \rho_w (\rho_w - \rho_g)}{\mu_w^2}, \quad (6.77)$$

and that $L_x \sim h_w$ and neglect the air density compared to the water one $\rho_g \ll \rho_w$ we can rewrite (6.76) using (6.77) to obtain

$$Re = \left(\frac{Ar}{16} \right)^{1/2} N \quad (6.78)$$

Finally we can re-express the correlations (6.74) and (6.75) with the modified Froude number and the Archimedes number

$$Sh_w^{NO} = a_2 \left(\frac{h_o m Ar}{h_w 16} \right)^{1/2} Sc_w^{1/2} N + b_2 \left(\frac{Ar}{16} \right)^{1/3} Sc_w^{1/3} N^{2/3} \quad (6.79)$$

$$Sh_w^{NO-KY} = a_3 \left(\frac{h_o m Ar}{h_w 16} \right)^{1/2} Sc_w^{1/2} N + b_3 \left(\frac{Ar}{16} \right)^{1/2} Sc_w^{1/3} N \quad (6.80)$$

6.4.4.2 In the oil phase

In the oil layer, the boundary layer theory in the free surface limit can be applied. Applying (6.47) we have in that case $K_o = K_{o,I}$ and

$$K_o \sim \left(\frac{D_o u_I}{d} \right)^{1/2}, \quad (6.81)$$

combined with (6.65) it gives

$$K_o = \left(\frac{c_T r h_o}{3d} \right)^{1/2} Sc_o^{-1/2} U_{0,w}. \quad (6.82)$$

The theory is still applicable if the boundary layer thickness is smaller than the thickness given in (6.41), (6.64). We get

$$\frac{\delta}{h_o} = \frac{D_o}{K_o h_o} \sim Sc_o^{-1/2} Re_o^{-1} \left(\frac{c_T m}{3} \right)^{-1/2} \left(\frac{h_o}{d} \right)^{-1/2}, \quad (6.83)$$

which is equal to the inverse of the Sherwood number for the oil. For our experimental configuration, we get

$$\frac{\delta}{h_o} = Sh_o^{-1} \simeq 2 \cdot 10^{-4} \quad (6.84)$$

6.4.4.3 Comparison of three typical cases

For a simulation of a given water experiment, where only the Sc varies it would allow to do an extrapolation. It means that we could try to fit a and b from the simulations at “doable” Sc values with DNS and then extrapolate the results toward the experimental Sc value.

In the following comparison, we denote by the indices w both the water and liquid steel phase and use the indices o for both the oil and slag phase. We gather the main quantities characterizing the flow at a minimum gas flow rate for two water experiments and an industrial ladle experiment in Table 6.6. Table 6.7 gives a comparison of the values of the dimensionless number of interest and Table 6.8 gives the values of the mass transfer computations for three different experiments.

Notation	Expression	Unit	Our experiment	Our simulation	Kim & Fruehan [32]	Lachmund et al. (Industrial ladle) [8]
Q_{min}		m^3/s	$1.0 \cdot 10^{-5}$	$1.0 \cdot 10^{-5}$	$8.3 \cdot 10^{-6}$	$5.2 \cdot 10^{-3}$
$U_{0,w,plume}$	$(g^2 Q/h_w)^{1/3}$	m/s	$7.9 \cdot 10^{-2}$		$5.7 \cdot 10^{-2}$	$2.5 \cdot 10^{-1}$
$U_{0,w,rectilinear}$	$(g^2 Q)^{1/5}$	m/s	$2.5 \cdot 10^{-1}$		$2.4 \cdot 10^{-1}$	$8.7 \cdot 10^{-1}$
$U_{w,max}(y = h_w)$		m/s		$1.8 \cdot 10^{-1}$		
$Re_{0,w}$	$U_{0,w} L_x \rho_w / 4 \mu_w$		$1.7 \cdot 10^4$	$1.2 \cdot 10^4$	$2.7 \cdot 10^4$	$9.0 \cdot 10^5$
c_T	$0.4 / \ln(Re_{0,w})$		$4.1 \cdot 10^{-2}$	$4.3 \cdot 10^{-2}$	$3.9 \cdot 10^{-2}$	$2.9 \cdot 10^{-2}$
u_i^{NO}	$\frac{c_T}{3} m Re_{0,w} \frac{h_o}{d} U_{0,w}$	m/s	$7.2 \cdot 10^{-2}$	$3.9 \cdot 10^{-2}$	$3.5 \cdot 10^{-2}$	$4.0 \cdot 10^1$
Re_o^{NO}	$u_i^{NO} h_o \rho_o / \mu_o$		13	3	1	$9.0 \cdot 10^4$

Table 6.6: Main global and interfacial velocity characterization of the steel equivalent phase and the slag equivalent phase established from several correlations from the value of the minimum gas flow rate for our experiment and numerical simulation and the experiments of [8, 32].

Notation	Expression	Our experiment	Kim & Fruehan [32]	Lachmund et al. (Industrial ladle) [8]
$Bo_{w,o}$	$\Delta \rho g h_o^2 / \sigma_{wo}$	$1.2 \cdot 10^3$	$1.1 \cdot 10^4$	$8.0 \cdot 10^5$
	$\Delta \rho g h_w / (\sigma_{wo} / h_o)$	$4.1 \cdot 10^1$	$3.8 \cdot 10^2$	$2.0 \cdot 10^4$
Ga	$\rho_w \Delta \rho g h_w^3 / \mu_w^2$	$6.3 \cdot 10^9$	$9.9 \cdot 10^{10}$	$3.0 \cdot 10^{14}$
Fr_o	$u_i / \sqrt{g h_o}$	$8.8 \cdot 10^{-2}$	$3.3 \cdot 10^{-2}$	$1.4 \cdot 10^1$

Table 6.7: Main dimensionless numbers for our experiment and the experiments of [8, 32].

Notation	Expression	Unit	Our experiment	Kim & Fruehan [32]	Lachmund et al. [8]
$K_{w,I}/K_{w,\omega}$	$(8c_T)^{-1/6} m^{1/2} (h_o/d)^{1/2} Sc_w^{1/6} Re^{1/3}$		1.8	1.2	$1.1 \cdot 10^1$
K_w	$m^{1/2} Sc_w^{-1/2} (h_o/h_w)^{1/2} + Sc_w^{-2/3} Re^{-1/3}$	m/s	$8.4 \cdot 10^{-5}$	$6.6 \cdot 10^{-5}$	$3.3 \cdot 10^{-4}$
$\delta_{c,w}/L_x$	$D_w/(K_w L_x)$		$3.00 \cdot 10^{-5}$	$2.3 \cdot 10^{-5}$	$4.0 \cdot 10^{-6}$
$K_{w,exp}$		m/s	$2.9 \cdot 10^{-3}$	$1.6 \cdot 10^{-3}$	$2.3 \cdot 10^{-1}$
$\delta_{c,o,exp}/L_x$	$D_w/(K_{w,exp} L_x)$		$8.8 \cdot 10^{-7}$	$9.5 \cdot 10^{-7}$	$5.9 \cdot 10^{-9}$
K_o	$(c_T r h_o / 3d^2)^{1/2} Sc_o^{-1/2} U_{0,w}$	m/s	$2.7 \cdot 10^{-6}$	$1.4 \cdot 10^{-6}$	$1.2 \cdot 10^{-4}$
	$(D_o u_I / L_x)^{1/2}$		$2.7 \cdot 10^{-6}$	$1.4 \cdot 10^{-6}$	$1.2 \cdot 10^{-4}$
α	K_w / PK_o		$8.9 \cdot 10^{-2}$	$1.3 \cdot 10^{-1}$	$8.1 \cdot 10^{-3}$
T_c	$V_w / (K_w L_x^2)$	s	$2.4 \cdot 10^2$	$5.5 \cdot 10^3$	$7.6 \cdot 10^3$

Table 6.8: Mass transfer properties of the steel and slag equivalent phase in the case of a Nusselt profile in the slag equivalent phase for our experiment and the experiments of [8, 32].

6.4.5 Mass transfer coefficient in oil droplets

We are considering a small spherical droplet of diameter d_d detaching from the oil layer and migrating back to the oil layer. Meaning that it is rising toward the oil at a velocity u_d . The Archimede number for a rising droplet is

$$Ar_{w,o} = \frac{\rho_w (\rho_w - \rho_o) g d_d^3}{\mu_w^2} \quad (6.85)$$

Considering a typical droplet of diameter $d_d = 1mm$ size we find $Ar_{w,o} = 1640$ which is small enough to make the viscous approximation of Stokes drag for the sedimentation velocity given by

$$u_d = \frac{(\rho_w - \rho_o) g d_d^2}{18\mu_w} \quad (6.86)$$

Considering that $u_d \simeq 0,04 m/s$ which is of the same order than $U_{0,w}$ and could explain why the droplet has difficulty to rise the “downward current”. Of course, the bigger the droplet is the easier it will rise. The transports coefficients are computed from the flow structure inside the droplet. The flow inside is very viscous, the droplet surface velocity is $u_{I,d}$. To compute it we estimate $\omega_{o,d} = u_{I,d}/d_d$, $\omega_{o,d} = (u_d - u_{I,d})/d_d$ and use (6.54) because $m \ll 1 u_{I,d} \simeq m u_d$ we can get $K_{o,d} = (D_o u_{I,d}/d_d)^{1/2}$. We can write

$$K_{w,d} \simeq a \left(\frac{D_w^2 \omega_w}{d_d} \right)^{1/3} + b m^{1/2} \left(\frac{D_w u_d}{d_d} \right)^{1/2}, \quad (6.87)$$

which can be written as

$$K_{w,d}/u_d \sim a Pe^{-2/3} + b m^{1/2} Pe^{-1/2}. \quad (6.88)$$

We find $Pe := Sc_w Re_d \simeq 6 \cdot 10^4$. The concentration decrease time is given with the following expression

$$T_c = \frac{V_w}{K_{w,d}A_d} \frac{1 + \alpha_d}{1 + \beta_d}, \quad (6.89)$$

where $A_d = \pi d_d^2$ is the droplet surface, α_d and β_d are defined as previously but with the parameters of the oil droplet. For our experimental configuration, we consider a droplet of 1mm of diameter and we find $\beta_d \gg 1$ which is expected for a relatively small droplet. β_d is a capacity ratio, meaning that the ability of the droplet to store thymol is much lower than the water one. On the other hand, still within our experimental configuration, we find $\alpha_d \approx 6.9 \cdot 10^{-2}$ meaning that the transport coefficient depends principally on m , r and Sc , so, it is independent of the length scale. We can then do the following approximation

$$T_{c,d} \approx \frac{V_d P}{K_{w,d} A_d} \quad (6.90)$$

For an oil droplet of 1mm size, it gives in our case $T_{c,d} \approx 510$ s! Meaning that the droplet is saturated with thymol concentration and do not contribute to thymol absorption after this time. We should add the droplet contribution to mass transfer but only for time $t \ll T_{c,d}$. This time has to be compared to the rising time. For a droplet at a depth $h_w/2$ the rising time is $T_d = h_w/(2u_d)$. For our experimental configuration, it is $T_d \approx 2.3$ s. Therefore, the droplet rises before getting thymol saturated.

6.4.5.1 Comparison of three typical cases

In the following comparison, we denote by the indices w both the water and liquid steel phase and use the indices o for both the oil and slag phase. We gather the main quantities characterizing the mass transfer of a slag equivalent droplet for three cases corresponding to two water experiments and an industrial ladle experiment in Table 6.9.

Notation	Expression	Unit	Our experiment	Kim & Fruehan [32]	Lachmund et al. (Industrial ladle) [8]
d_d		m	$1.0 \cdot 10^{-3}$	$1.0 \cdot 10^{-3}$	$1.0 \cdot 10^{-3}$
V_d	$\pi d_d^3/6$	m^3	$5.2 \cdot 10^{-10}$	$5.2 \cdot 10^{-10}$	$5.2 \cdot 10^{-10}$
β_d	V_w/PV_d		$7.9 \cdot 10^3$	$4.1 \cdot 10^5$	$1.5 \cdot 10^8$
$Ar_{w,o}$	$\rho_w \Delta \rho g d_d^3 / \mu_w^2$		$4.1 \cdot 10^2$	$5.9 \cdot 10^2$	$4.8 \cdot 10^3$
u_d	$(\rho_w - \rho_o) g d_d^2 / 18 \mu_w$	m/s	$4.4 \cdot 10^{-2}$	$6.2 \cdot 10^{-2}$	$4.0 \cdot 10^{-1}$
$u_{I,d}$	$u_d \mu_w / \mu_o$	m/s	$5.5 \cdot 10^{-4}$	$1.9 \cdot 10^{-4}$	$2.2 \cdot 10^{-2}$
$T_{c,d}$	$V_d P / (K_w 2 \pi d_d^2)$	s	$5.1 \cdot 10^2$	$8.9 \cdot 10^2$	$1.8 \cdot 10^2$
ω_o	$u_{I,d} / d_d$	$1/s$	$5.5 \cdot 10^{-1}$	$1.9 \cdot 10^{-1}$	$2.2 \cdot 10^1$
ω_w	u_d / d_d	$1/s$	$4.4 \cdot 10^1$	$6.2 \cdot 10^1$	$4.0 \cdot 10^2$
$K_{w,d}$	$(D_w^2 \omega_w / d_d)^{1/3} + m^{1/2} (D_w u_d / d_d)^{1/2}$	m/s	$4.7 \cdot 10^{-5}$	$4.2 \cdot 10^{-5}$	$5.1 \cdot 10^{-4}$
$K_{o,d}$	$(D_o u_{I,d} / d_d)^{1/2}$	m/s	$1.9 \cdot 10^{-6}$	$1.1 \cdot 10^{-6}$	$7.8 \cdot 10^{-5}$
α_d	$K_w / (PK_o)$		$6.9 \cdot 10^{-2}$	$1.1 \cdot 10^{-1}$	$1.9 \cdot 10^{-2}$
Pe	$Sc_w Re_d$		$6.4 \cdot 10^4$	$9.1 \cdot 10^4$	$9.2 \cdot 10^4$
T_d	$h_w / 2 u_d$	s	2.3	3.6	4.0

Table 6.9: Mass transfer properties of a slag equivalent phase droplet for our experiment and the experiments of [8, 32].

6.5 SUMMARY

In this chapter, we have first presented the existing mass transfer models in the literature established mainly for gas-liquid configuration from the simple film theory to more elaborated model as the surface divergence model. Later, we have seen that in most of the experimental studies measuring the mass transfer with water or liquid metal experiments different mass transfer regimes were observed when the gas flow rate is above a critical value.

To perform our experimental measurement, we add thymol in the water phase as a chemical tracer. According to Kim & Fruehan [32], the use of thymol as a chemical tracer is expected to reproduce the mass transfer configuration of the desulfurization process in an industrial ladle. In [32] the authors assumed that the ratio of the mass transfer coefficient in the water and oil phase are small. We also follow this assumption to determine the mass transfer coefficient of thymol in water from the evolution of its concentration in our experiment.

Finally, we have tried to characterize the various mass transfer configurations through a phenomenological analysis. In this analysis, we established correlations to determine the Sherwood number as a function of the Reynolds and Schmidt number. These correlations are built from a hydrodynamic analysis considering the free surface and rigid surface as the two limiting cases. From the liquid steel equivalent phase side only, a turbulent regime is considered while for the slag equivalent phase, a laminar boundary layer, parabolic profile or a turbulent flow regime are possible. We only treated the case of a parabolic or Nusselt profile in the slag equivalent phase in this dissertation.

7 NUMERICAL MODEL- MASS TRANSFER CHARACTERIZATION

The mass transfer numerical model can be thought of as an additional layer to the model used for the hydrodynamic characterization. The numerical model used to resolve the flow (cf. 3) is reused here to obtain the velocity field. So in the following, we will only give the details necessary to simulate the diffusion and advection of a tracer with a velocity field computed following the numerical model of chapter 3. The reader is invited to read the chapter 3 for general details of the Basilisk code and the numerical model used for the hydrodynamic characterization.

7.1 LITERATURE REVIEW OF NUMERICAL MASS TRANSFER SIMULATIONS

In the following, we will briefly present different simulations from studies of the literature on DNS of mass transfer of chemical species.

Davidson and Rudman [104] have done VOF-based simulations of mass transfer a deformable interface for 2D planar axisymmetric flow. Koynov *et al.* [105] performed 2D simulations using front tracking/front capturing hybrid methods to model reactive mass transfer in bubble swarms. Onea *et al.* [106] developed a VOF model where the authors transformed the physical discontinuous concentration field into a continuous numerical field. Marschall *et al.* [107] build a single field model for mass transfer in multiphase flow using a conditional volume-averaging technique and concentration jump with the OpenFoam® code. Fleckenstein & Bothe [108] describe a conservative VOF method to simulate mass transfer allowing for local volume change. López-Herrera *et al.* [109] used the code Gerris, the ancestor of Basilisk in a different configuration than the other studies to simulate advection-diffusion of ionic species with a VOF method for the breakup of a charged liquid column. Weiner & Bothe [110] established a subgrid-scale model to be able to predict the mass transfer, even for poorly-resolved concentration boundary layers, in the case of convection-dominated species transport. More recently, Balcazar *et al.* [111] proposed a multiple marker level-set model for capturing the reactive mass transfer in bubble swarms.

Globally, we can see that most of the studies mentioned are using VOF methods and are tested with the mass transfer from rising bubble.

7.2 NUMERICAL MODEL

The time variation of a scalar can be described by the generic scalar transport equation. The concentration of a chemical species c (mass per unit volume) evolves according to

$$\frac{\partial c}{\partial t} = \nabla \cdot (D\nabla c) - \nabla \cdot (\mathbf{u}c) + R,$$

where R describes the source or sink of chemical species. As we consider the flow as incompressible and that no source or sink of chemical species is present in the domain, we can rewrite the previous equation as

$$\frac{\partial c}{\partial t} = \nabla \cdot (D\nabla c) - \mathbf{u} \cdot \nabla c \quad (7.1)$$

Equation (7.1) combines both parabolic and hyperbolic partial differential equations and cannot be solved analytically with complex geometry and flow conditions. We can see that the global transport of tracer can be split into two parts:

- $\nabla \cdot (D\nabla c)$ describe the concentration flux, measuring the influence of molecular diffusion on c value;
- $\mathbf{u} \cdot \nabla c$ describe the advection flux, measuring the influence of the flow velocity on c .

c has no influence on the global flow behaviour and is only advected by the flow, therefore, we call it a passive scalar. In Basilisk there are two ways to define such a scalar:

- Diffusive tracer: is a tracer which is not confined to a specific phase and is transported with the flow without taking into account the interface between each phase;
- VOF tracer: is a tracer attached to a VOF phase and transported with the VOF phase, it cannot cross an interface.

As we want to simulate the mass transfer of thymol dissolved in the water phase to the oil phase, we choose to use the VOF tracer formulation to be able to attach the tracer to the water phase. Following the formulation of Basilisk described in [109], the concentration of a chemical species in a multiphase case can be written

$$T_p = cf_p, \quad (7.2)$$

where c is the amount of chemical species per unit of volume in the cell and f_p is the fluid fraction of the phase p in the cell. We can see that from this expression we cannot have a concentration of tracer of a particular phase in another phase. We can use (7.2) to re-express (7.1) in a multiphase case

$$\frac{\partial (cf_p)}{\partial t} = \nabla \cdot (D\nabla c) - \nabla \cdot (cf_p \mathbf{u}) \quad (7.3)$$

We can note from (7.3) that the fluid fraction is not considered in the molar flux part as will be explained below. In Figure 7.1 (a) we show the domain Ω where we have only represented the water phase f_2 and the oil phase f_3 . In Figure 7.1 (b) we consider as a volume of control an interfacial cell C of Ω of size h with an average concentration value at its centre of c . The dark grey part on the right of the cell shows the amount of fluid that will be advected through the face ∂C . The face velocity u^f and the diffusion coefficient D are defined at the face ∂C . The advection flux of chemical species (white arrow in Figure 7.1 (b)) is computed in the same manner as the advection of the fluid fractions (Popinet

[16]). The average molar flux added or extracted by molecular diffusion in the cell C (blue arrow in Figure 7.1 (b)) can be computed as

$$h \int_C \nabla \cdot (D \nabla c) = \int_{\partial C} D \nabla c \cdot \mathbf{n} = \sum_f D \nabla^f c, \quad (7.4)$$

where $\nabla^f c$ is the slope-limited normal gradient at the cell faces computed using the centre value of the neighbouring cells (Popinet [15]). (7.3) is discretized using a time-implicit backward Euler scheme and solved using a multigrid solver.

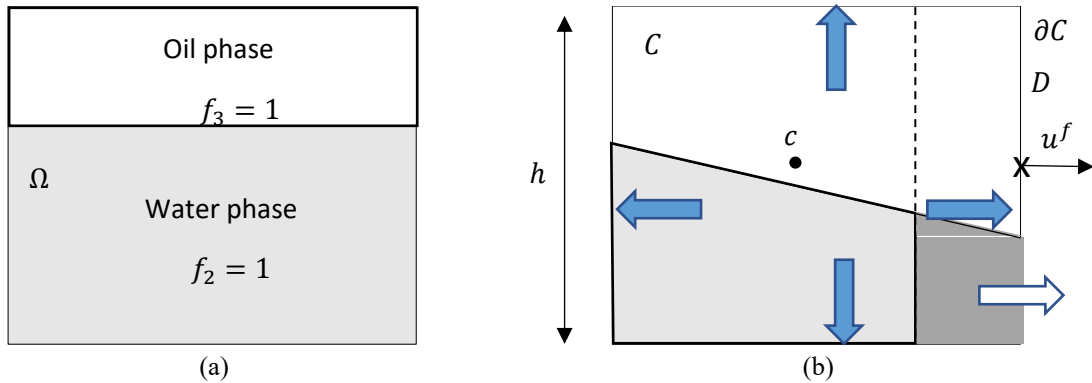


Figure 7.1: a): Schematic of the domain of computation; b): Interfacial cell C where we have represented the advection flux of chemical species with a white arrow and the diffusion flux with blue arrows.

The following pseudocode where we split the advection and diffusion of chemical species can be established as a global framework of the resolution of (7.3) within Basilisk:

Pseudocode:

```

1)-Advection of the VOF tracer  $T_p$ 
If ( $f_p > 10^{-12}$ )
  Set  $c_p := T_p / f_p$ 
else
  Set  $c_p := 0$ 
endif
2)-Diffusion of the concentration of VOF tracer  $c_p$ 
3)-Update the VOF tracer value with the value of the concentration of VOF tracer after diffusion
set  $T_p := c_p f_p$ 

```

7.2.1 Diffusion coefficient

For commodity reasons and because of the low value of the diffusion coefficient of the thymol in the air phase we set the diffusion coefficient value to $D_a = 0 \text{ m}^2/\text{s}$ in the air phase. We also simplify the model by considering a constant phase-specific diffusion coefficient with the value determined by the Schmidt number. The following pseudocode is used to determine the value of the diffusion coefficient:

Pseudocode:

```

If air fraction is greater than  $10^{-12}$  in the central cell or left cell
  if water or oil fraction is bigger than 0.95 in the central cell and left cell
    set  $D \neq 0$ 
  else
    set  $D = 0$ 
endif
else
  set  $D \neq 0$ 
endif

```

We can see in Figure 7.2 (a) that in all the faces with a black cross the cell is containing a large air phase value and the diffusion coefficient is then set to zero. On all the faces where there is no black cross, the diffusion of the tracer from the water phase to the oil phase can occur with a constant value of the diffusion coefficient.

7.2.2 Partition law at the interface

We could not add easily the equivalent of the concentration jump at the VOF interface between the water phase and the oil phase in Basilisk because it was not implemented. Instead of that, we use a Dirichlet condition imposed on the p phase side when the fluid fraction value is above a threshold value

$$\text{if } f_p > 0.5, \quad c'_p = 0 \quad (7.5)$$

This is an approximation of the large variation of concentration due to the high value of the partition coefficient in our configuration. Figure 7.2 (a) and (b) represent a schematic of a stencil of cells before and after applying the Dirichlet condition. We can note by comparing Figure 7.2 (a) and (b) that the Dirichlet condition is activated in six cells where the oil or water fluid fraction is validating the criteria $f_p > 0.5$. Only the lower left cell containing both water and oil in the same quantity is not affected by the Dirichlet condition.

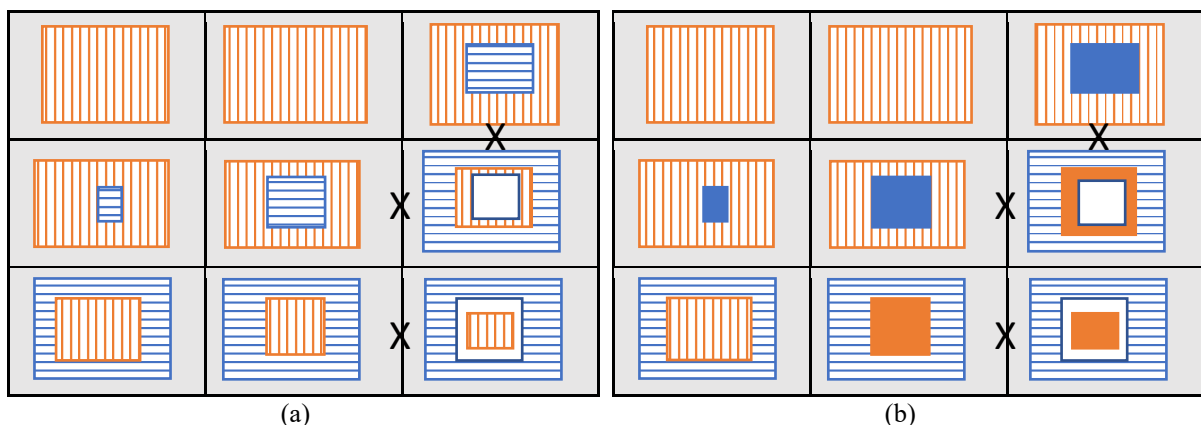


Figure 7.2: Schematic of a stencil of cells where we have represented the fluid fraction by squares of different colours and the white stripes represent the tracer in each phase. The black cross on the cell faces indicates that the diffusion coefficient is zero at these faces. Colour code: White: air phase; blue: water phase; orange: oil phase. a): Without Dirichlet condition; b): With Dirichlet condition.

7.3 NUMERICAL TESTS

In the following, we will illustrate the previous assumptions of our numerical model through a simple example of a three-phase flow.

It is a 2D simulation with a uniform grid of 128 *cells* per direction, we impose a constant velocity as a boundary condition at the left face, and we are only solving advection-diffusion equation for fluid fractions and tracers. Neither the Navier-Stokes equations nor the surface tension are considered here. In the simulation, we implement three fluid fractions f_1 , f_2 and f_3 corresponding respectively to the air, water and oil phase with one diffusive tracer and a VOF tracer initialized in the water phase (f_2) by

$$T_2 = f_2, G_2 = f_2$$

So, by definition, the concentration of the two tracers in the water phase at the beginning of the simulation is strictly equal to one as can be seen in Figure 7.3.

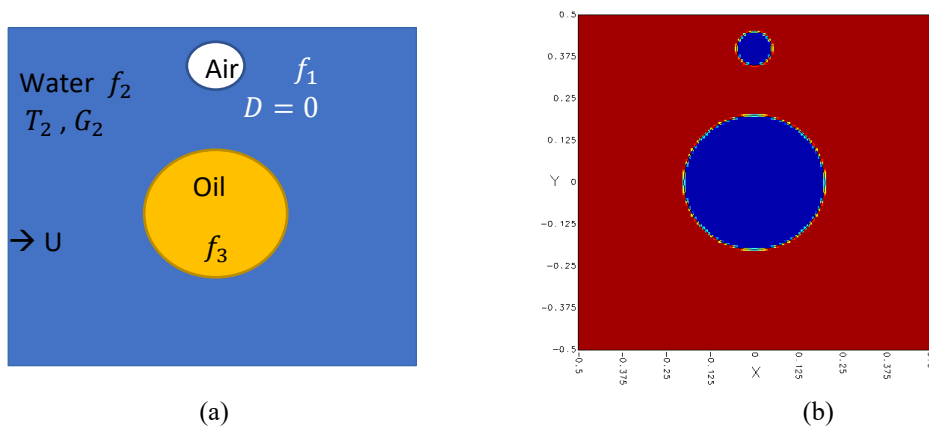


Figure 7.3: a) Schematic of the configuration of the simulation; b) Minimum and maximum values of the concentration of the VOF tracer T_2 or the diffusive tracer G_2 at the beginning of the simulation. The blue colour corresponds to the minimum value and the red colour corresponds to the maximum value.

7.3.1 Advection of the tracers

We first test only the advection of the two tracers with the fluid fractions and do not consider the effect of diffusion. If we compare Figure 7.3 and Figure 7.4 (a) we cannot see a possible erroneous numerical diffusion of the VOF tracer T_2 in the oil droplet or the air bubble. On the other hand, comparing Figure 7.3 and Figure 7.4 (b) we can see on the contour of the oil droplet and the air bubble some variation of the concentration of the diffusive tracer G_2 . Figure 7.5 confirm the visual observation by confirming that the quantity of VOF tracer T_2 in the water phase is constant unlike the quantity of diffusive tracer G_2 in the water phase. This justifies using a VOF tracer instead of a diffusive tracer which is too diffusive for our configuration.

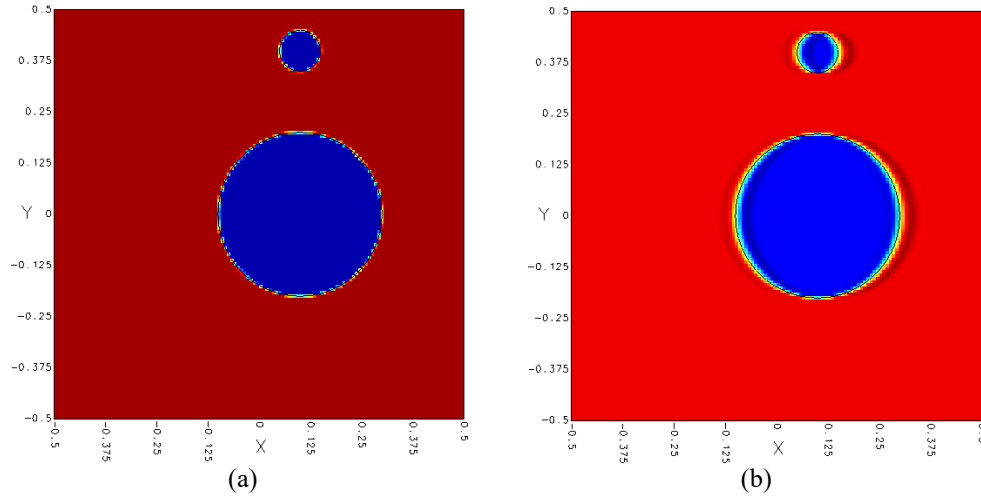


Figure 7.4: Comparison of the minimum and maximum values of the concentration of the tracer at the end of the simulation. The blue colour corresponds to the minimum value and the red colour corresponds to the maximum value. a): VOF tracer T_2 ; b): Diffusive tracer G_2 .

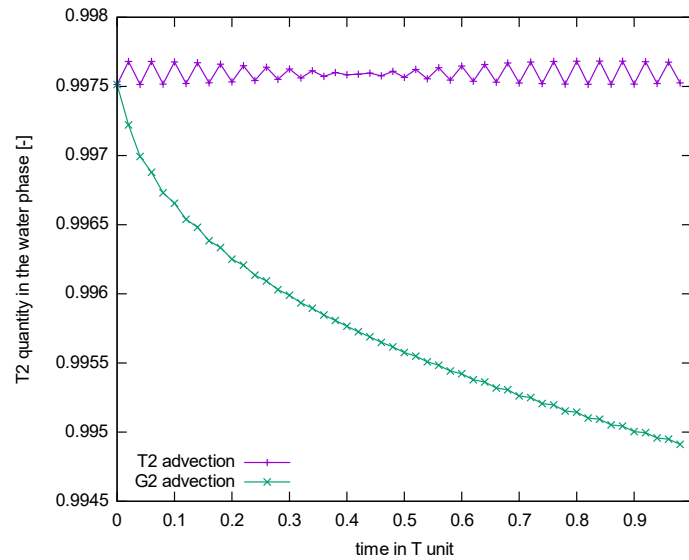


Figure 7.5: Comparison of the quantity of VOF tracer T_2 and diffusive tracer G_2 in the water phase as a function of time.

7.3.2 Advection-diffusion of the tracers

We will now consider the diffusion of the tracers in addition to the advection. In Figure 7.6 we have represented the concentration of the tracer in the water phase at the end of the simulation for different cases. From Figure 7.6 (a) corresponding to a naïve advection-diffusion of the VOF tracer, we can see that the tracer is not uniformly distributed around the oil droplet. The non-constant value of f_2 on the oil droplet border causes erroneous variations of the concentration of tracer when doing the advection-diffusion directly on T_2 . In the results of Figure 7.6 (b) we are still doing the advection of the VOF tracer T_2 , but now we consider only the tracer concentration c_2 for the diffusion

$$\text{if } (f_2 > 10^{-12}) \\ c_2 := T_2/f_2 \quad (7.6)$$

After the diffusion of concentration, we update the VOF tracer with the new value of the concentration following the pseudocode describing the general framework of the advection-diffusion in 7.2. We can see from Figure 7.6 (b) that the concentration of tracer is now uniformly distributed around the oil droplet, but because of the threshold on the fluid fraction, no tracer can be found inside the oil droplet. If we look now at Figure 7.6 (c) where we show the advection-diffusion of the diffusive tracer G_2 we can see that the tracer is uniformly distributed around and inside the oil droplet.

Looking at Figure 7.8 we can see that the quantity of tracer in the water phase decreases more abruptly for the VOF tracer than for the diffusive tracer. This can be explained by the threshold on the fluid fraction $f_2 < 10^{-12}$ which causes large variations of the concentration of the tracer at the border of the oil droplet.

If we look at Figure 7.9 we can see that the quantity of tracer inside the oil droplet is increasing only in the case of the diffusive tracer G_2 or when we consider only diffusion of the VOF tracer T_2 . If we now look at the air bubble at the top of the domain we can see that no tracer diffuses toward the air bubble in Figure 7.6 (a)-(b) unlike in Figure 7.6 (c). This is confirmed by Figure 7.10. If we omit the erroneous value due to the interfacial cells, we can see that the quantity of the diffusive tracer G_2 is increasing much more than for the other case where the value stays around zero.

Finally, from Figure 7.8, we can see that the variation of the quantity of the VOF tracer in the water phase is a bit more abrupt when we impose a Dirichlet condition on its value on the interfacial cells. Comparing Figure 7.7 (a) and Figure 7.7 (b) we can observe the interfacial cells where the value of the VOF tracer T_2 is set to zero.

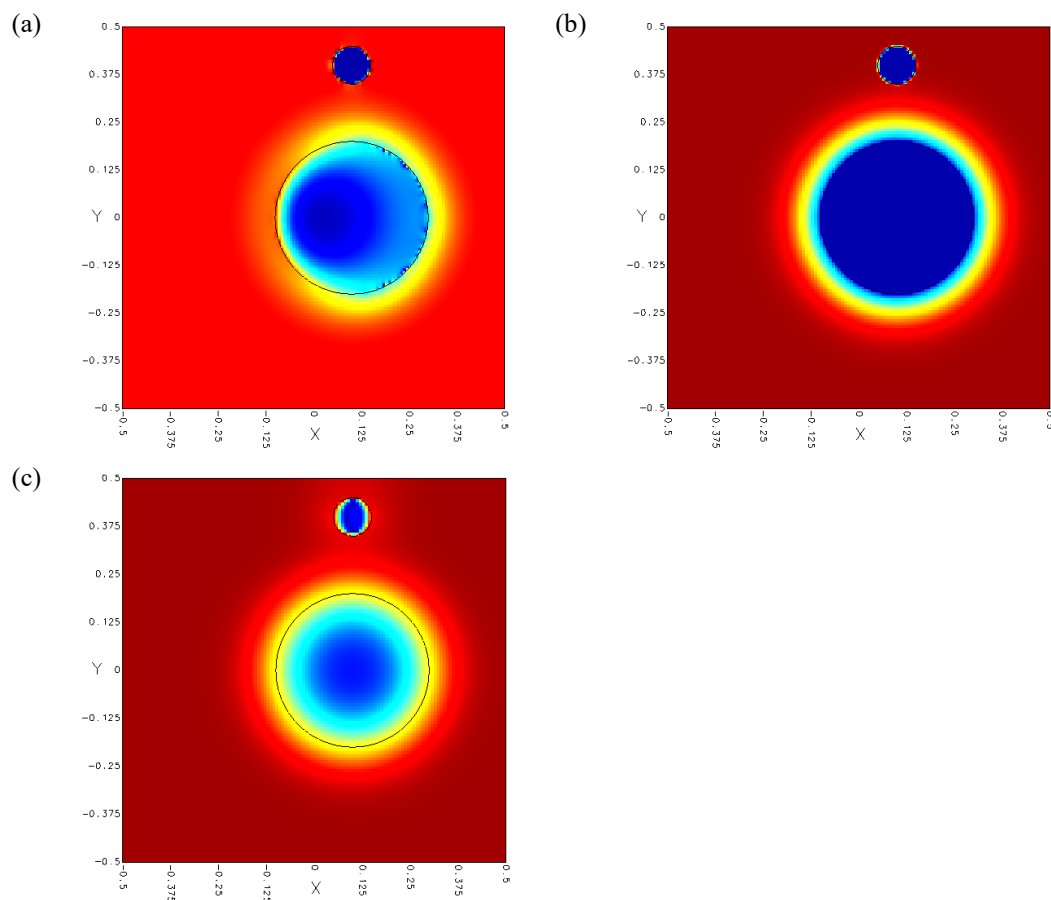


Figure 7.6: Comparison of the minimum and maximum values of the concentration of the tracer at the end of the simulation. The blue colour corresponds to the minimum value and the red colour corresponds to the maximum value. a): Advection-diffusion of VOF tracer T_2 ; b): Advection of VOF tracer T_2 and diffusion of c_2 ; c): Advection-diffusion of diffusive tracer G_2 .

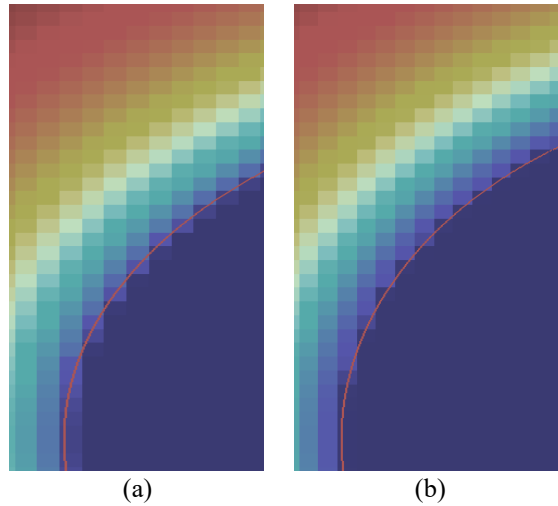


Figure 7.7: Zoom on the oil droplet interface (in red). Comparison of the minimum and maximum values of the concentration of the tracer at the end of the simulation. The blue colour corresponds to the minimum value and the red colour corresponds to the maximum value. a): Without Dirichlet condition on the value of T_2 ; b): With Dirichlet condition on the value of T_2 .

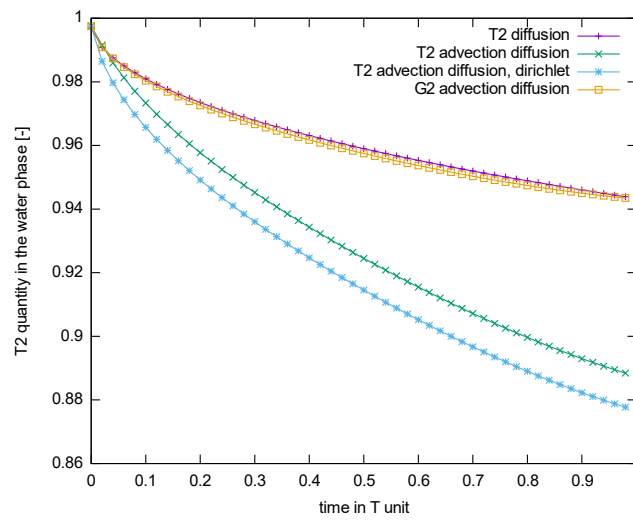


Figure 7.8: Comparison of the quantity of VOF tracer T_2 with different assumptions and diffusive tracer G_2 in the water phase as a function of time.

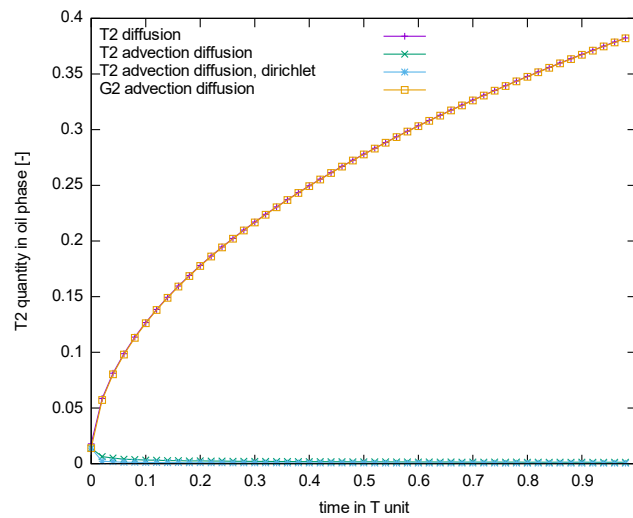


Figure 7.9: Comparison of the quantity of VOF tracer T_2 with different assumptions and diffusive tracer G_2 in the oil phase as a function of time.

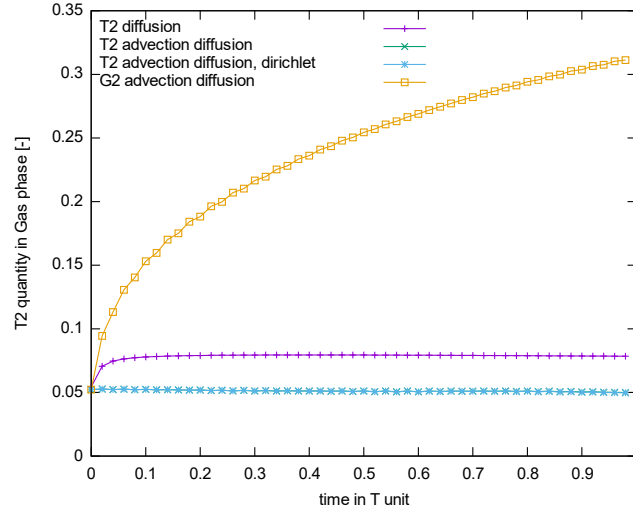


Figure 7.10: Comparison of the quantity of VOF tracer T_2 with different assumptions and diffusive tracer G_2 in the air phase as a function of time.

7.4 ESTIMATION OF THE MESH SIZE REQUIRED

As in this part, we are interested to do a simulation of the diffusion of a tracer by solving (7.3), we need to know the minimal mesh resolution needed to sufficiently resolve the concentration boundary layer. In the following, we will compare two ways of estimating the mesh resolution necessary to resolve the concentration boundary layer.

In the case of homogenous turbulence, the smallest scale of concentration fluctuation is defined as the Batchelor length scale (Batchelor [85]) and is given by

$$\lambda_B = \frac{\eta}{Sc^{1/2}}, \quad (7.7)$$

where $Sc = \mu/\rho D$ is the Schmidt number and $\eta = [v_w^3/(\epsilon/\rho_w)]^{1/4}$ is the Kolmogorov length scale. If we use the criteria of Pope (Pope [75]) for a well-resolved DNS but this time with the Batchelor length scale, we can write

$$\Delta \leq 2.1\lambda_B \quad (7.8)$$

We can then determine the minimum number of grid points in one direction required to resolve λ_B using (7.8) with

$$N_{min,B} \geq Sc^{1/2} L_x / (2.1\eta) \quad (7.9)$$

Applying (7.9) in the water experiment configuration i.e. a Schmidt number of thymol in the water of $Sc_{th,w} = 1.48 \cdot 10^3$ and for the lowest gas flow rate of $Q = 0.6l/min$ leads to $N_{min,B} = 3.0 \cdot 10^4$ cells. So, to resolve sufficiently the boundary layer in this case, a maximum mesh resolution of $lvl15 = 2^{15}$ cells in one direction would be necessary.

This estimation of mesh resolution might be too strict but gives a worst-case scenario for the simulation. As we can see this estimation of mesh resolution leads to a mesh resolution which is too high to reasonably do a DNS. Instead of that, we choose to do a simulation at smaller Schmidt numbers than the experimental value and choose values in the range of $Sc_w \in \{1,4,10,40\}$ by adjusting the value of the diffusion coefficient for each tracer. In the case of a Schmidt number of $Sc_w = 1$ and

$Sc_w = 40$ and applying (7.9) the maximum mesh resolution in one direction necessary to resolve the concentration boundary layer is respectively $lvl10 = 2^{10}$ and $lvl13 = 2^{13}$ cells in one direction.

The second way to estimate the concentration boundary layer thickness is to use the expression of the mass transfer coefficient of the film model of Lewis and Whitman [79]. With this model, we can write the following expression of the concentration boundary layer thickness

$$\delta_{c,w} = \frac{D_w}{K_w} \quad (7.10)$$

The only unknown in (7.10) is the mass transfer coefficient. To obtain the mass transfer coefficient value we use the correlation corresponding to a Nusselt profile in the oil phase, given by

$$K_w = m^{1/2} Sc_w^{-1/2} (h_o/h_w)^{1/2} + Sc_w^{-2/3} Re^{-1/3} \quad (7.11)$$

It is then possible to compute the minimum number of cells in one direction necessary to resolve the concentration boundary layer following the Pope criteria (7.8) with

$$N > N_{min,deltac} = \frac{L_x}{2.1\delta_{c,w}} \quad (7.12)$$

We gather all the parameters necessary to compute the mass transfer coefficient of thymol in the water from (7.11) in Table 7.1 for the experimental case and the simulation case considering a constant air flow rate $Q = 0.6l/min$. We can see from the results of Table 7.1 that it would require a minimum number of cells in one direction $N_{min} = 1.59 \cdot 10^4$ cells to sufficiently resolve the concentration boundary layer for the experimental Schmidt number. This could be sufficiently resolved using a maximum mesh number in one direction of $lvl14 = 2^{14}$ cells. If we look now to the numerical case with $Sc_w = 1$ and $Sc_w = 40$ the maximum number of cells in one direction necessary to resolve the concentration boundary layer is respectively $N_{min} = 1.29 \cdot 10^3$ and $N_{min} = 2.83 \cdot 10^3$ cells. This corresponds to a maximum mesh number in one direction of $lvl11 = 2^{11}$ and $lvl12 = 2^{12}$ cells.

If we compare these two estimates, we can see that the minimum mesh resolution in one direction necessary to resolve the concentration boundary layer given by (7.12) is twice lower than when using the estimation obtained with (7.8). Because in our experimental and numerical configuration we do not expect to have homogenous turbulence we choose to follow the estimation of the maximum mesh resolution in one direction given by (7.12).

Notation	Expression	Unit	Our experiment	Numerical simulation	
h_w		m	0.27	0.27	0.27
h_o		m	0.007	0.007	0.007
m	μ_w/μ_o		$1.27 \cdot 10^{-2}$	$1.27 \cdot 10^{-2}$	$1.27 \cdot 10^{-2}$
Re_w	$UL_x/4\nu_w$		$1.68 \cdot 10^4$	$1.68 \cdot 10^4$	$1.68 \cdot 10^4$
Sc_w	ν_w/D_w		$1.48 \cdot 10^3$	1	40
K_w	$m^{1/2}Sc_w^{-1/2}(h_o/h_w)^{1/2} + Sc_w^{-2/3}Re^{-1/3}$	m/s	$8.42 \cdot 10^{-5}$	$1.01 \cdot 10^{-2}$	$2.2 \cdot 10^{-3}$
$\delta_{c,w}/L_x$	$D_w/(K_wL_x)$		$2.99 \cdot 10^{-5}$	$3.68 \cdot 10^{-4}$	$1.68 \cdot 10^{-4}$
N_{min}	$L_x/2.1\delta_{c,w}$		$1.59 \cdot 10^4$	$1.29 \cdot 10^3$	$2.83 \cdot 10^3$

Table 7.1: Main parameters necessary to compute the mass transfer coefficient with (7.12) considering a fixed air flow rate $Q = 0.6l/min$ for the experimental and numerical case.

7.5 SUMMARY

In this chapter, we have first detailed the numerical procedure to advect and diffuse a tracer attached to a VOF phase. Several assumptions are made in order to be as close as possible to the mass transfer configuration in the water experiment. First, we choose to not track the evolution of the concentration of the tracer in another phase than the one it is attached. Secondly, to neglect the influence of the air on the mass transfer, we set the value of the diffusion coefficient to zero when the air-fluid fraction is above a certain threshold. Finally, instead of a concentration jump at the water-oil interface cells, we impose a concentration equal to zero with a Dirichlet condition when the oil fluid fraction is larger than 0.5.

From the numerical tests, we have seen that the tracer attached to a VOF phase allows to limit the numerical diffusion compared to the standard diffusive tracer. On the other hand, when the tracer is attached to a VOF phase, special treatment must be taken in order to diffuse the tracer because of the discontinuous value of the fluid fraction across the interface.

Finally, we have seen that the mesh required to resolve the concentration boundary layer with the high Schmidt number of the water experiment would require too important computational power. Indeed, it would require a too large number of cores to reasonably do a DNS. To circumvent this issue, we choose to do DNS at low Schmidt numbers and then do a scaling of the obtained results toward the experimental Schmidt number.

8 RESULTS- MASS TRANSFER CHARACTERIZATION

In the following, we will describe the evolution of the mass transfer as a function of the air flow rate based on our results obtained either with the water experiment or the numerical simulation. Both models are based on the model used for the hydrodynamic characterization in part one with slight change described in chapters 6 and 7.

8.1 EXPERIMENTAL RESULTS

We first check the influence of the thymol dissolved in the water on the oil physical properties. We measure oil physical properties from samples taken after 3h00 of air agitation. From the results of Table 8.1, we can see that there is only a slight difference in the values of the oil physical properties when thymol is dissolved in water. The higher impact of thymol is on the oil dynamic viscosity with a difference of 6% between the two cases. This indicates that the thymol does not affect too much the physical properties of the oil phase.

	ρ_o ($kg \cdot m^{-3}$)	μ_o ($Pa \cdot s$)	$\sigma_{o/w}$ ($N \cdot m$)
Without thymol	0.91	$7.85 \cdot 10^{-2}$	$2.57 \cdot 10^{-2}$
With thymol	0.92	$8.06 \cdot 10^{-2}$	$2.48 \cdot 10^{-2}$

Table 8.1: Measurement of oil physical properties after 3h00 of air agitation with and without thymol dissolved in the water.

8.1.1 Visual observation

As presented in chapter 6 the continuous formation of oil droplets of various sizes at high air flow rate is suspected to be the major explanation of the observed different mass transfer regimes. In order to check this assumption, we record images of the face view of the water experiment with thymol solution every 10 minutes from the start to the end of the air stirring. It can be seen in Figure 8.1 that no oil droplet is visible in water for $Q = 1l/min$. As the air flow rate increases, we start to see oil droplets in the water phase just below the oil layer but only until roughly thirty minutes after air injection has started (cf. Figure 8.2 (a), Figure 8.3 (a)). After this time, we can observe the formation of foam at the water-oil interface and almost no formation of oil droplets (cf. Figure 8.2 (b), Figure 8.3 (b)). Increasing the air flow rate further, a lot of dark spots corresponding to oil droplets can be identified particularly on both sides of the central bubble plume on Figure 8.4 and Figure 8.5 respectively for $Q = 6.1l/min$ and $Q = 7.5l/min$. At these high flow rate values, oil droplets of various sizes and shapes are present in water both at the start of air injection and after three hours of air stirring. These oil droplets can change the interfacial area and the mass transfer mechanism around oil droplets and then be the cause of the different mass transfer regimes.



Figure 8.1: Front view picture of the water experiment at $Q = 1.1\text{l/min}$. (a) just after the start of air injection; (b) after 3h of gas stirring.

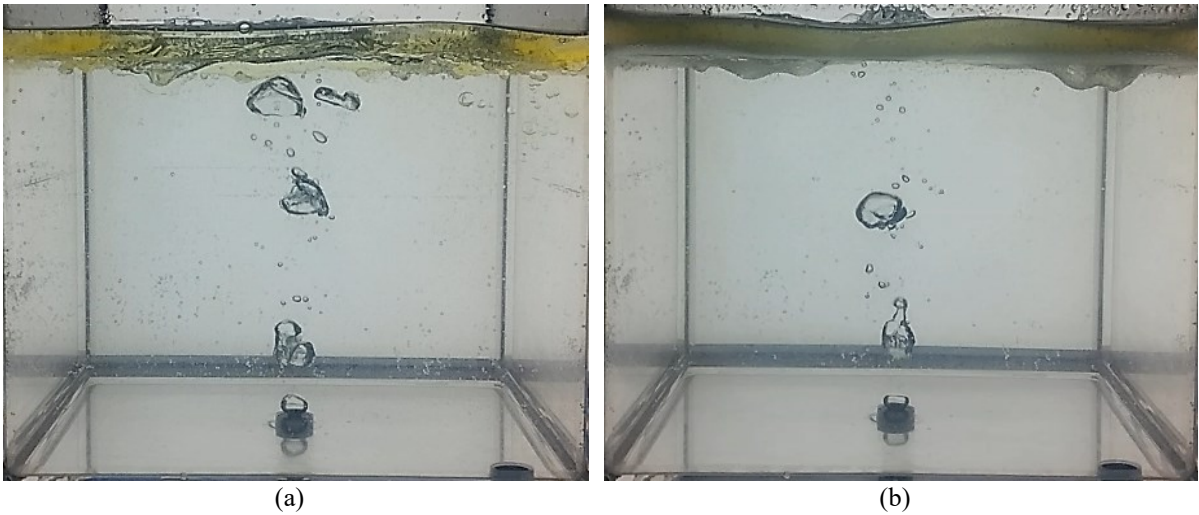


Figure 8.2: Front view picture of the water experiment at $Q = 3.0\text{l/min}$. (a) just after the start of air injection; (b) after 3h of gas stirring.

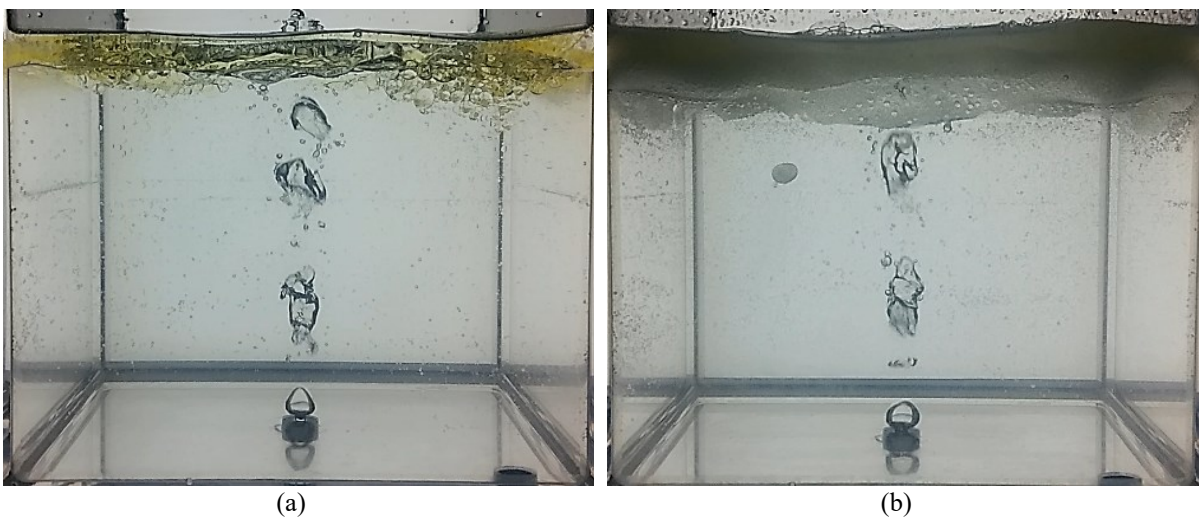


Figure 8.3: Front view picture of the water experiment at $Q = 5.5\text{l/min}$. (a) just after the start of air injection; (b) after 3h of gas stirring.

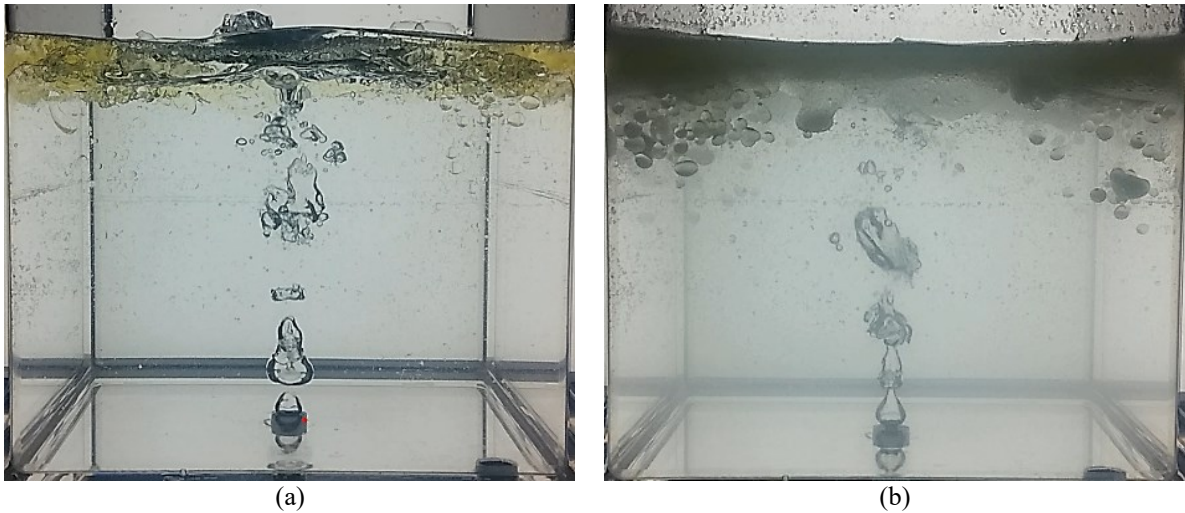


Figure 8.4: Front view picture of the water experiment at $Q = 6.1\text{ l/min}$. (a) just after the start of air injection; (b) after 3h of gas stirring.

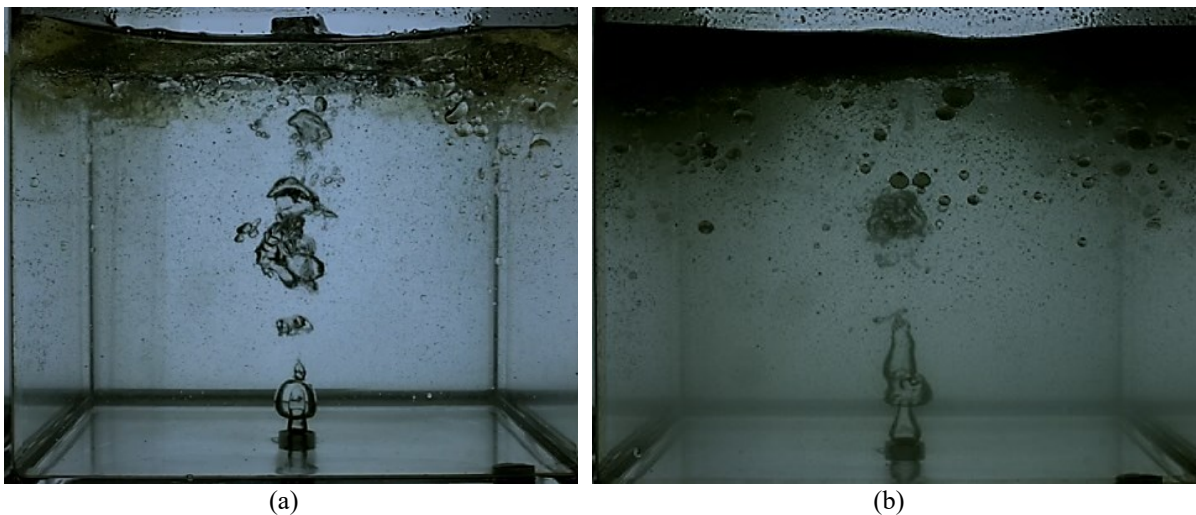


Figure 8.5: Front view picture of the water experiment at $Q = 7.5\text{ l/min}$. (a) just after the start of air injection; (b) after 3h of gas stirring.

8.1.2 Concentration measurement

8.1.2.1 Instantaneous values

From the measurements of the concentration of thymol in the water phase we can plot its time evolution in Figure 8.6. First, it is important to note that the error on the concentration measurement of thymol in water made is $\Delta C_w \pm 0.1\text{ g/l}$. We can see from the results that before $t = 2000\text{ s}$ that the influence of the air flow rate on the evolution of the concentration of thymol in water is small. The difference between the points for all the air flow rates are within the measurement error. After $t = 2500\text{ s}$ we can clearly see that starting from $Q = 5.5\text{ l/min}$ the evolution of the concentration of thymol in water decreases more abruptly than for the lower values of air flow rate. Starting from $Q = 6.5\text{ l/min}$ the evolution of concentration of thymol in water seems to follow the same trend with the one obtained at $Q = 7.5\text{ l/min}$. Figure 8.7 shows the evolution of the capacity coefficient or product of the mass transfer coefficient with the interfacial area per volume of water given by

$$\frac{K_w A}{V_w} t = \frac{\ln \left[\frac{C_w}{C_{w,0}} (1 + \beta) - \beta \right]}{1 + \beta}, \quad (8.1)$$

where K_w is the mass transfer coefficient in the water phase, V_w is the volume of water, A is the water-oil interfacial area, C_w is the concentration of thymol in the water, $C_{w,0}$ is the initial concentration of thymol in the water and $\beta = V_w/(V_o P)$ is a constant depending on the experiment. We observe an important change in the slope of the capacity coefficient starting from $Q = 5.5l/min$ compared to lower air flow rate values. These two observations indicate that a transition between two different evolutions of the concentration of thymol in water occurs at an air flow rate value between $5.5l/min \leq Q \leq 6.5l/min$.

We will now look more closely at the results obtained in the two different regimes of the evolution of the concentration of thymol in water. In Figure 8.8-(a) and Figure 8.9-(a) the evolution of the concentration of thymol in water at a gas flow rate of respectively $Q = 2.5l/min$ and $Q = 6.5l/min$ shows that we can perfectly fit our experimental data with an exponential decay of the form $C_w = C_{w,0} e^{-\lambda t}$. It confirms the relation (6.31) with $\lambda = 5.8 \cdot 10^{-5} s^{-1}$ at $Q = 2.5l/min$ and $\lambda = 1.7 \cdot 10^{-4} s^{-1}$ at $Q = 6.5l/min$. From Figure 8.8-(b) and Figure 8.9-(b) showing the time evolution of the capacity coefficient we obtain a capacity coefficient of $K_w A/V_w = 6.2 \cdot 10^{-5} s^{-1}$ at $Q = 2.5l/min$ and $K_w A/V_w = 2 \cdot 10^{-4} s^{-1}$ at $Q = 6.5l/min$. From the results we can remark that $\lambda \sim K_w A/V_w$, from the expression of $\lambda = (1 + \beta)/T_w(1 + \alpha)$ with $T_w = V_w/K_w A$ it means that $\lambda \sim 1/T_w$. This illustrates the fact that in our mass transfer model, we know that $\beta \ll 1$ but the fact that $\alpha \ll 1$ is coming from the assumption on the mass transfer resistance relation made in this model that is $1/K_w \gg 1/PK_o$.

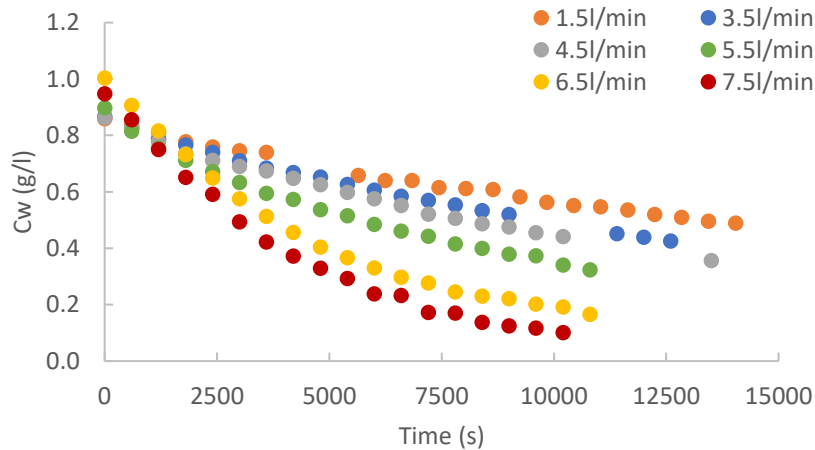


Figure 8.6: Comparison of the time evolution of the concentration of thymol in water for different air flow rates and $d_{inj} = 7.9mm$.

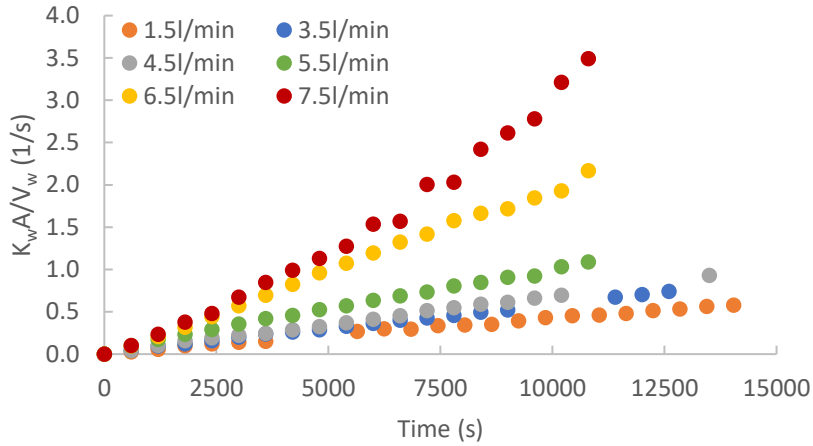


Figure 8.7: Comparison of the time evolution of the capacity coefficient $K_w A/V_w$ for different air flow rates and $d_{inj} = 7.9\text{mm}$.

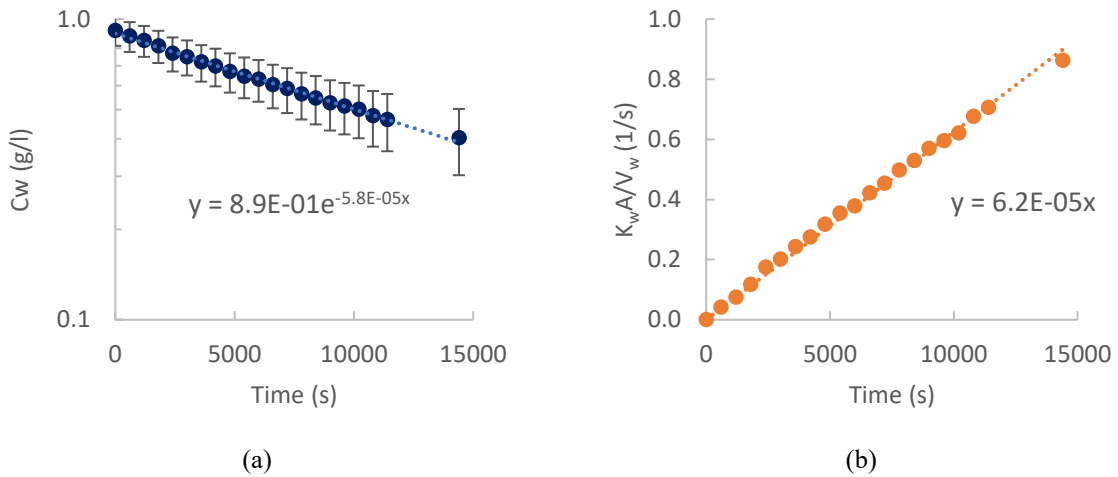


Figure 8.8 : (a) Time evolution of the concentration of thymol in water with error bars corresponding to the measurement error with $Q = 2.5\text{l/min}$ and $d_{inj} = 7.9\text{mm}$; (b) Time evolution of the capacity coefficient $K_w A/V_w$ with $Q = 2.5\text{l/min}$ and $d_{inj} = 7.9\text{mm}$.

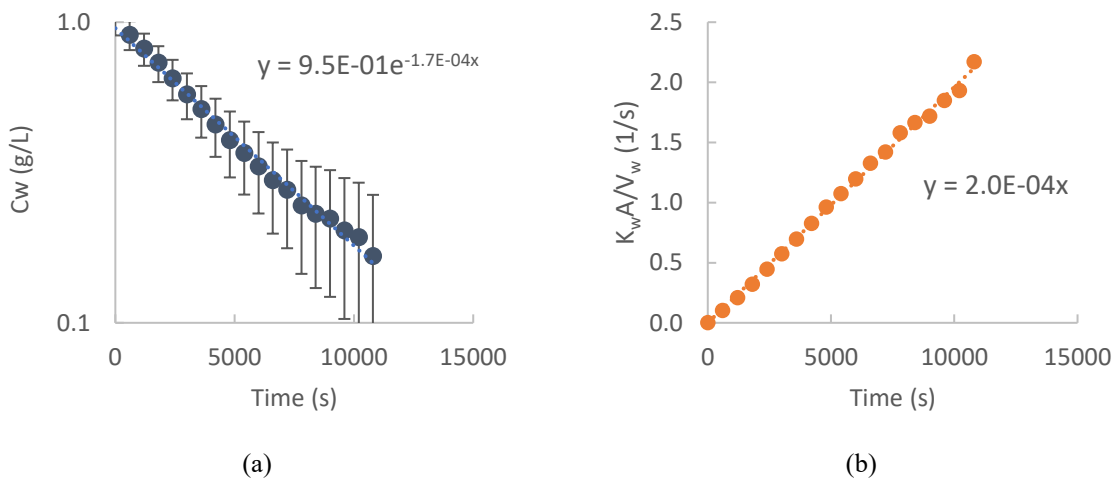


Figure 8.9 : (a) Time evolution of the concentration of thymol in water with error bars corresponding to the measurement error with $Q = 6.5\text{l/min}$ and $d_{inj} = 7.9\text{mm}$; (b) Time evolution of the capacity coefficient $K_w A/V_w$ with $Q = 6.5\text{l/min}$ and $d_{inj} = 7.9\text{mm}$.

8.1.2.2 Reproducibility test

We test the reproducibility of our mass transfer measurement by repeating during several trials the same experiment at a low and high gas flow rate. From the results in Table 8.2 we observe a similar maximum variation of the product of the mass transfer coefficient with the interfacial area. These two values are nearly the same and so we can consider a maximum deviation value at a given flow rate of $K_w A \pm 0.31$.

Trial number	1	2	3
$K_w A$ (cm ³ /s) at $Q = 1.1$ l/min	0.69	0.84	0.91
$K_w A$ (cm ³ /s) at $Q = 4.1$ l/min	0.75	0.86	1.06

Table 8.2: Reproducibility test of all the process involved in mass transfer measurement at two distinct gas flow rate value.

8.1.2.3 Time-averaged values

Gathering all the values of the capacity coefficient or product of the water mass transfer coefficient with interfacial area per volume of water for different air flow rates we can plot the evolution of the average capacity coefficient as a function of the air flow rate in a log/log scale (Figure 8.10). From our experimental results in Figure 8.10 we can first observe that the capacity coefficient increases when the air flow rate is increased for both injection diameters. Even if we have less data for the $d_{inj} = 2.35$ mm case it appears that the capacity coefficient varies only a little compared to the results obtained with $d_{inj} = 7.9$ mm. So, in the following we will only consider the results obtained with $d_{inj} = 7.9$ mm. We can also identify two different mass transfer regimes below and above a critical air flow rate $Q \sim 4.6$ l/min for both injection diameters.

If we now compare our results with the ones of Kim & Fruehan [32] obtained with a bigger ladle (cf. Table 8.3) we observe a critical air flow rate nearly the same as the one we measured with $d_{inj} = 7.9$ mm. Our values of the capacity coefficient are approximately the same at a high air flow rate with almost the same slope of the power-law fit. On the other hand, there is a difference of a factor three between the slope of the power-law fit of our results and the results of [32] at low air flow rate. This significative difference observed mainly at low air flow rate is difficult to explain because, in this regime, almost no oil droplets are formed in the water phase. So, one explanation could be that the size difference between the two water experiments would be an important parameter in the first mass transfer regime compared to the second one.

	ρ_w (kgm ⁻³)	μ_w (Pa.s)	μ_o (Pa.s)	D_w (m.s ⁻²)	Sc_w	L_x (m)	h_w (m)	h_o (m)
Our experiment	998	10 ⁻³	0.079	6.8 10 ⁻¹⁰	1480	0.27	0.20	0.007
Kim et al. [32]	886	10 ⁻³	0.033	6.8 10 ⁻¹⁰	1480	0.46	0.445	0.015

Table 8.3: Main physical properties and quantities of our water experiment and the experiment of [32].

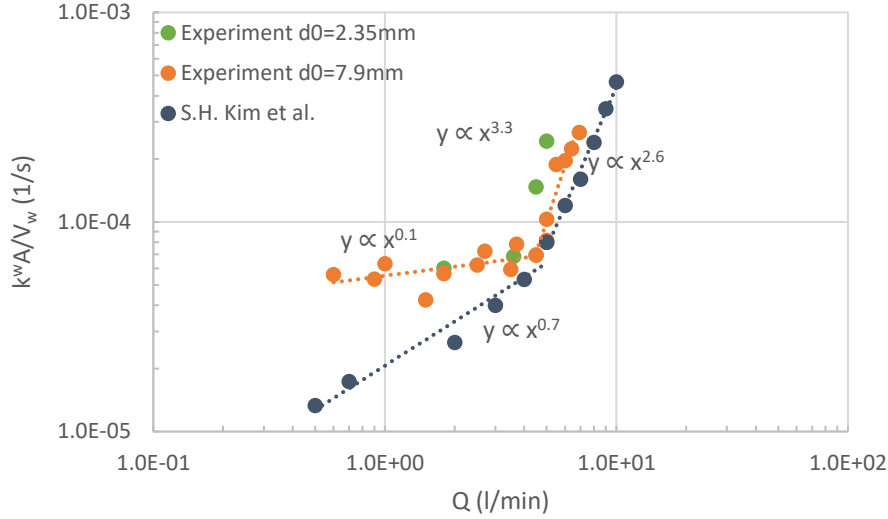


Figure 8.10: Comparison of the capacity coefficient $K_w A/V_w$ as a function of the air flow rate for our experiment and the one of Kim & Fruehan [32].

If we now consider the oil area without air injection as a reference area and the specific volume in each experiment, we can compute the global Sherwood number for the water phase from the results of Figure 8.10 with

$$Sh_w = \frac{K_w L_x}{4D_w}, \quad (8.2)$$

where L_x is the horizontal size of the ladle and D_w is the diffusion coefficient of thymol in the water. We can re-express the expression of the Sherwood number as a function of dimensionless numbers with this relation

$$Sh_w = \frac{K_w L_x Re Sc}{4\nu_w}, \quad (8.3)$$

where $\nu_w = \mu_w/\rho_w$ is the kinematic viscosity of water. If we assume that for all experiments, we are in presence of a bubble column, the vertical rising velocity in the water can be approximated with

$$U = (g^2 Q)^{1/5} \quad (8.4)$$

Using the previous expression, we can rewrite the Froude number as a function of the gas flow rate to obtain the expression of the modified Froude number N

$$\sqrt{Fr} = \frac{U}{\sqrt{gh_w}},$$

$$N = \left(\frac{Q}{g^{1/2} h_w^{5/2}} \right)^{1/5}, \quad (8.5)$$

where h_w is the height of the water bath. In Figure 8.11 we replot the data of Figure 8.10 using the Sherwood number in the steel equivalent phase as a function of the modified Froude number for our experiment and the one of [32]. First, we can note that the difference in the range of the modified Froude number between the two experiments is mainly due to the difference in the height of the bath between the experiments. From Figure 8.11 comparing our results with the one of [32] which uses the same chemical reaction and the same fluids but a different size and ladle shapes (cf. Table 8.3), we can see that the Sherwood number value is close to our results for the first mass transfer regime.

On the other hand, it shows a different slope of the power-law fit for the first mass transfer regime. For the second mass transfer regime, the results of [32] show nearly an order of magnitude of difference with our results but with a more similar slope of the power-law fit $Sh_{w,Kim2} \propto N^{13}$ than our results $Sh_{w,2} \propto N^{14.5}$. From (8.3) we can anticipate that for approximately the same Reynolds number if the Schmidt number is kept constant the only explanation in the difference of the Sherwood number is the value of the product $K_w L_x/4$.

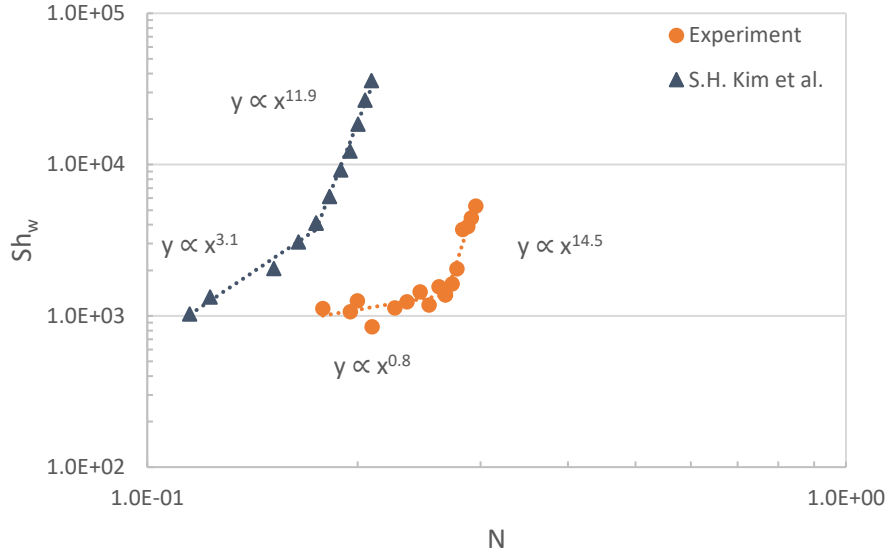


Figure 8.11: Comparison of the Sherwood number in the water phase as a function of the modified Froude number between our experiment and the experiment of [32].

We will now try to fit the water experiment results with the correlations of the Sherwood number in the steel equivalent phase established in chapter 6. The fit of the results of each experiment is done with two different Sherwood correlations considering a Nusselt or parabolic profile in the slag equivalent phase. The correlations give $Sh = f(Re, Sc)$ but in each experiment, the control parameter is the injected gas flow rate from which we can compute the modified Froude number. In order to re-express the correlations $Sh = f(N, Sc)$ as previously we consider that the vertical velocity in water is described as in the rectilinear bubble plume description $U = (g^2 Q)^{1/5}$. Then we can rewrite the Reynolds number

$$Re = \frac{UL_x}{4\nu_w},$$

$$Re = \left(\frac{L_x^2 g h_w}{16\nu_w^2} \right)^{1/2} N. \quad (8.6)$$

If we consider the Archimedes number given by

$$Ar = \frac{gL_c^3 \rho_w (\rho_w - \rho_g)}{\mu_w^2}, \quad (8.7)$$

and that $L_x \sim h_w$ and we can neglect the air density compared to the water one $\rho_g \ll \rho_w$ we can rewrite (8.6) using (8.7) to obtain

$$Re = \left(\frac{Ar}{16} \right)^{1/2} N \quad (8.8)$$

We can then re-express the correlations of chapter 6 with the modified Froude number instead of the Reynolds number

$$Sh_w^{NO} = a_2 \left(\frac{h_o m Ar}{h_w 16} \right)^{1/2} Sc_w^{1/2} N + b_2 \left(\frac{Ar}{16} \right)^{1/3} Sc_w^{1/3} N^{2/3} \quad (8.9)$$

$$Sh_w^{NO-KY} = a_3 \left(\frac{h_o m Ar}{h_w 16} \right)^{1/2} Sc_w^{1/2} N + b_3 \left(\frac{Ar}{16} \right)^{1/2} Sc_w^{1/3} N \quad (8.10)$$

In the following we will try to fit the water experiment results corresponding to the first mass transfer regime with the correlations (8.9) and (8.10). From the results of Figure 8.12, the correlation (8.9) shows a better agreement with our experimental results than the correlation (1.10). On the other hand the correlation (8.10) for a Nusselt profile in the oil phase and a turbulent boundary layer in the water phase following Kader & Yaglom [94] formulation give overestimated results. Using the correlation (8.9) for a Nusselt profile in the oil phase to fit our experimental results it is possible to write

$$Sh_{w,exp1}^{NO} = 6.8 \cdot 10^{-2} \left(\frac{h_o m Ar}{h_w 16} \right)^{1/2} Sc^{1/2} N + 7.1 \cdot 10^{-3} \left(\frac{Ar}{16} \right)^{1/3} Sc^{1/3} N^{2/3} \quad (8.11)$$

From the results of Figure 8.13, we can now see that it is nearly impossible to distinguish the estimated Sherwood number from the different correlations. All the correlations overestimate the results of [32] especially at low modified Froude number. If we consider the correlation (8.9) for a Nusselt profile in the oil phase, we can fit the results of [32] with the following correlation

$$Sh_{w,exp2}^{NO} = 7.1 \cdot 10^{-2} \left(\frac{h_o m Ar}{h_w 16} \right)^{1/2} Sc^{1/2} N + 4.9 \cdot 10^{-6} \left(\frac{Ar}{16} \right)^{1/3} Sc^{1/3} N^{2/3} \quad (8.12)$$

From all the results we can say that globally the correlation (8.9) is more suitable to predict the evolution of the Sherwood number as a function of the Schmidt and modified Froude number for the first mass transfer regime.

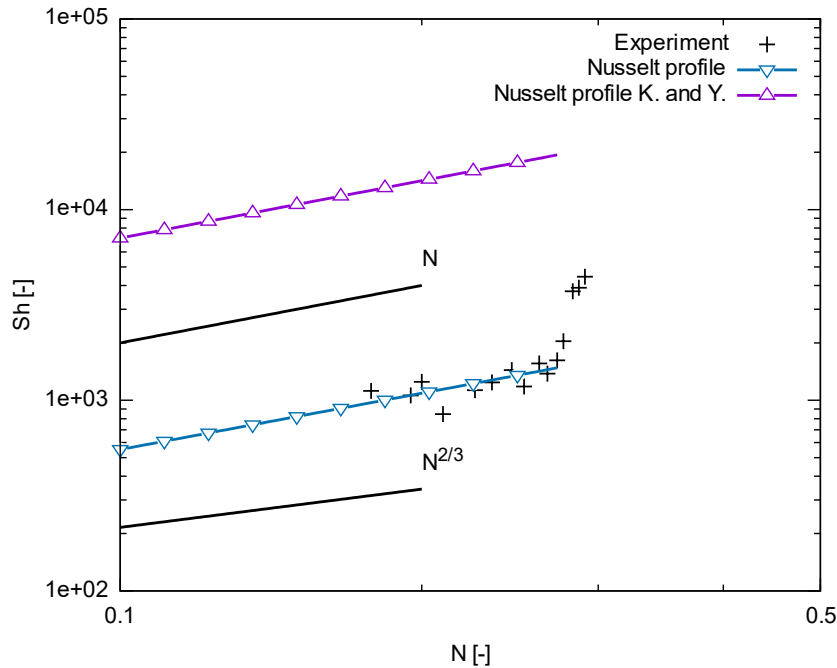


Figure 8.12: Sherwood number in the water phase as a function of the modified Froude number for our experiment fitted with different correlations.

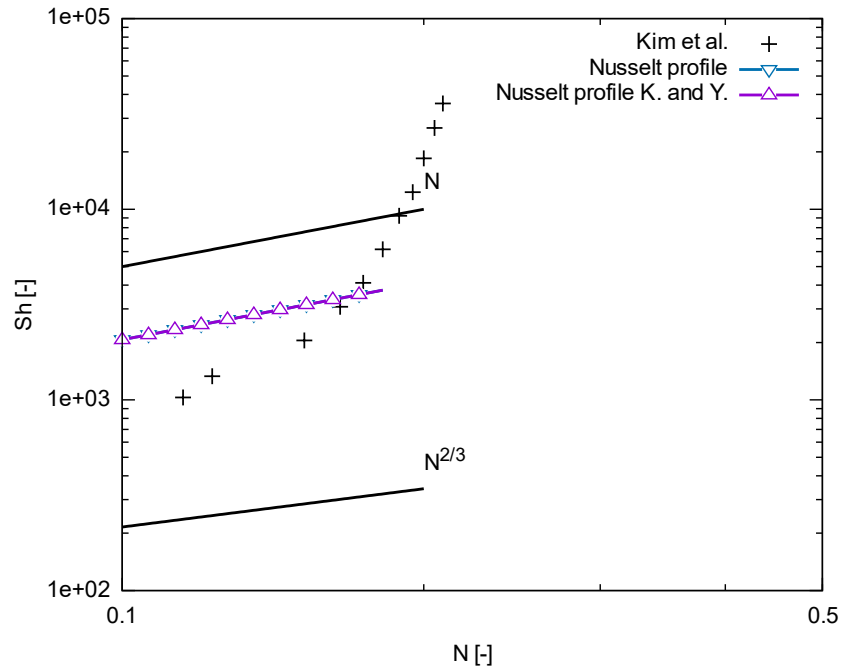


Figure 8.13: Sherwood number in the water phase as a function of the modified Froude number for the results of Kim & Fruehan [32] fitted with different correlations.

8.2 NUMERICAL RESULTS

The mass transfer simulations are performed with a constant injection diameter $d_{inj} = 7.9 \text{ mm}$ for five distinct flow rates below and around the mass transfer transition observed experimentally. Simulations are done with four tracers in water with $Sc_w \in \{1, 4, 10, 40\}$ and four tracers in oil with $Sc_o \in \{10, 40, 100, 400\}$ which are lower values than in the real experiment for both phases. Unlike the experiment, it is easy to track the tracer concentration in both phases without affecting the mass transfer conditions. We start the simulation with a maximum mesh resolution in one direction of 2^9 cells. Then when the mass transfer transient regime is finished, we use the obtained results to restart the simulation with a maximum mesh resolution in one direction increased by a power two. This allows us to save computational time by not recomputing the mass transfer and hydrodynamic transient regime for each maximum mesh resolution.

8.2.1 Visual observation

Here, we first want to visualize the behaviour of the concentration of tracer in the numerical domain when increasing the mesh resolution for the same air flow rate. In Figure 8.14 where the water phase is in red and the oil phase is in blue, we can see that the region where the variation of concentration of tracer is the more important is along the water-oil interface and especially on the open eye border from the oil layer side. If we now look more precisely at the left part of the oil layer represented in grey in Figure 8.15 we can confirm the observations made previously by clearly identifying the zone of important variation of $\|D\nabla c_w\|$ corresponding to the concentration boundary layer at the water-oil interface.

If we compare Figure 8.15-(a) and Figure 8.15-(b) we can see that globally the concentration boundary layer has the same shape, as we increase the number of cells by a power 2 from a maximum mesh resolution in one direction of 2^9 to 2^{10} we capture more details of fluctuations of concentration in the water. In Figure 8.16 we show the oil interface coloured with the values of $\|D\nabla c_w\|$. It confirms that the region where the more important value of $\|D\nabla c_w\|$ is observed is on the border of the open eye, then if we move radially away from the centre of the open eye the value of $\|D\nabla c_w\|$ reached a minimum before increasing again.

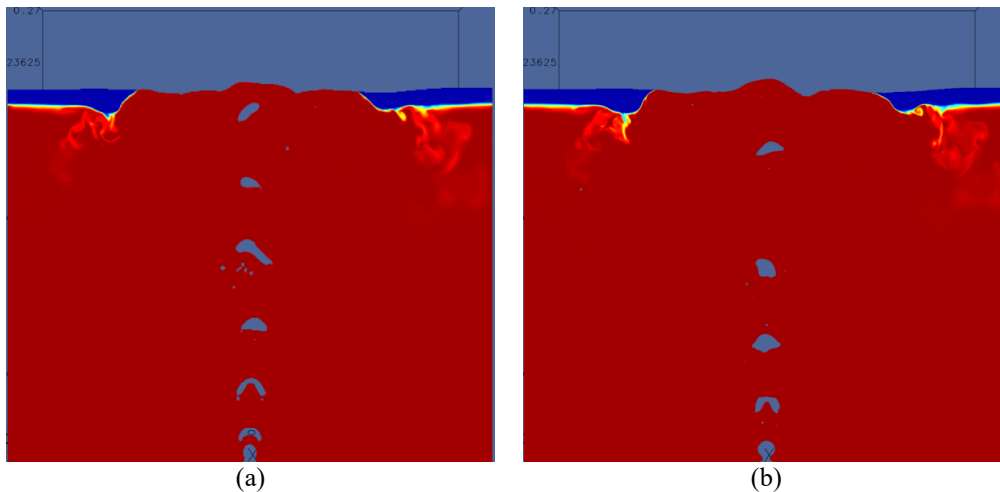


Figure 8.14: Face view of the middle plane with min and max values of concentration of tracer in water coloured at $Q = 0.6l/min$. (a) with a maximum mesh resolution in one direction of 2^9 cells; (b) with a maximum mesh resolution in one direction of 2^{10} cells.

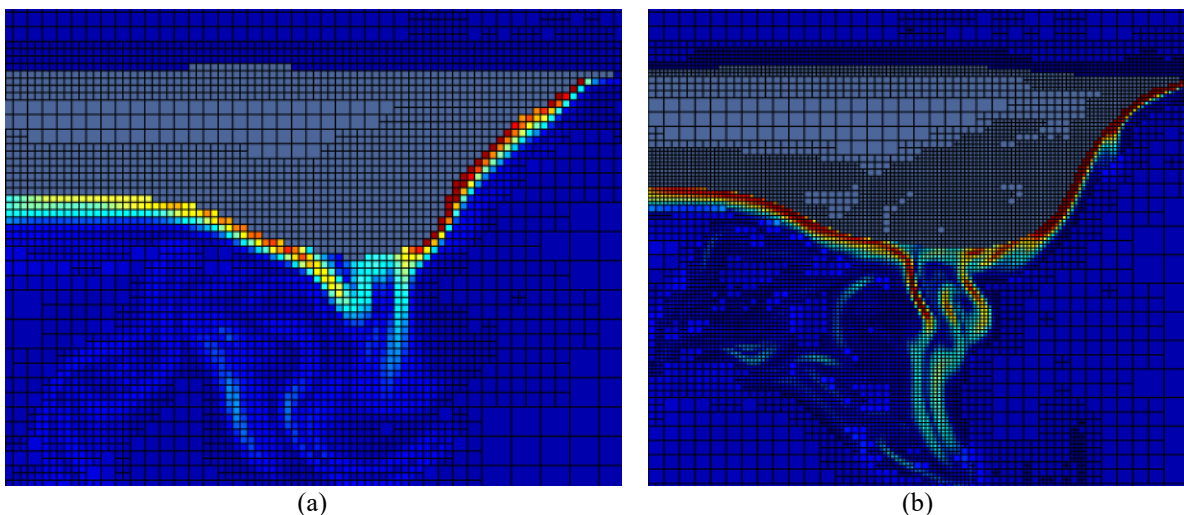


Figure 8.15: Zoom of the face view of the middle plane displayed on the left side border of the open eye at $Q = 0.6l/min$. (a) min and max values of $\|D\nabla c_w\|$ coloured with cells with a maximum mesh resolution in one direction of 2^9 cells; (b) min and max values of $\|D\nabla c_w\|$ coloured with cells with a maximum mesh resolution in one direction of 2^{10} cells.

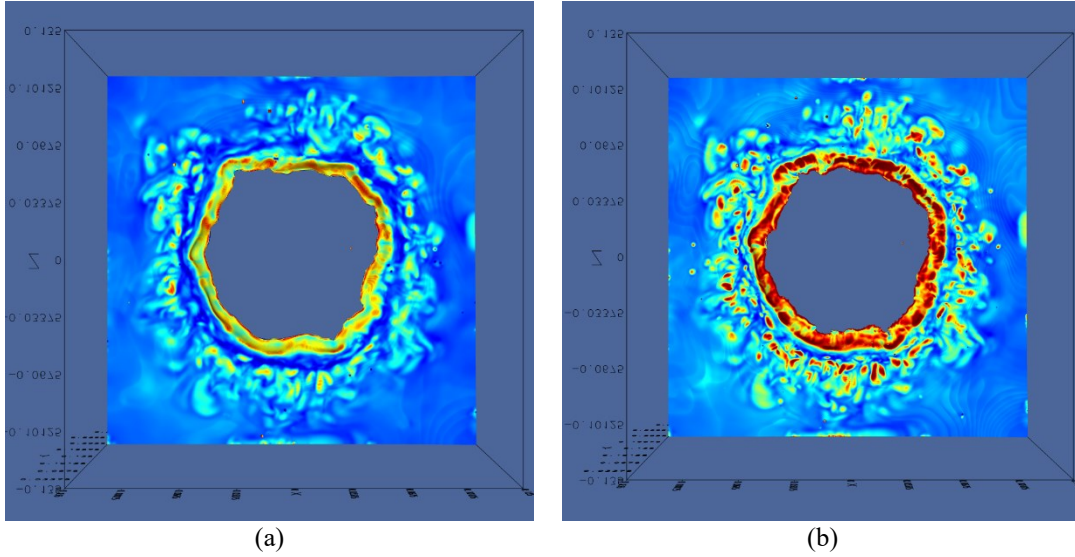


Figure 8.16: Bottom view with water-oil interface coloured with min and max values of $\|D\nabla c_w\|$ at $Q = 0.6l/min$. (a) min and max values of $\|D\nabla c_w\|$ coloured with a maximum mesh resolution in one direction of 2^9 cells; (b) min and max values of $\|D\nabla c_w\|$ coloured with a maximum mesh resolution in one direction of 2^{10} cells.

8.2.2 Concentration measurement

8.2.2.1 Instantaneous values

8.2.2.1.1 $Q = 0.6l/min$ case

First, we plot the time evolution of the concentration of tracer in water for different maximum mesh resolutions and different Schmidt numbers at $Q = 0.6l/min$ in Figure 8.18 (a),(c),(e),(g). We can see that even for the low Schmidt number value, the concentration variation is small for the physical time simulated. For $Sc_w = 1$ the difference in the slope of the concentration curve when increasing the maximum mesh resolution is small, but from $Sc_w = 4$ we clearly see change in the slope between the low maximum mesh resolution and the other mesh resolutions. There is almost no difference when increasing the mesh resolution from 2^{10} to 2^{11} at $Sc_w = 1$ but more visible difference from $Sc_w = 10$.

Then, from the evolution of the concentration of tracer in water, we can compute the phase-specific mass transfer coefficient. Considering that because of the imposed Dirichlet condition on the water-oil interface the tracer concentration on the interface is zero we can write for both the water and oil phase

$$K_k(t)A = \frac{V_k}{C_{k,\infty}} \frac{dC_k}{dt} \quad (8.13)$$

Then we can compute the phase-specific global Sherwood number

$$Sh_k = \frac{K_k L_x}{4D_k} \quad (8.14)$$

In Figure 8.17 we plot the raw data of the time evolution of the Sherwood number in the water phase at an air flow rate $Q = 0.6l/min$ and a Schmidt number $Sc_w = 1$. We can note that the first points are obtained at $t = 7.6s$ when we restart the simulation considering mass transfer with a maximum mesh

resolution in one direction of $lvl9 = 2^9$ cells from previous hydrodynamic simulation at the same mesh resolution. We can see that at the beginning of the simulation that the Sherwood number shows an abrupt decrease in its value from one thousand to one hundred in one second. This corresponds to a transient regime at the start of the simulation when there is a sharp discontinuity of the concentration at the water-oil interface and the boundary layer is not formed.

So, the mass transfer coefficient has a large value during the transient regime and one second is enough to reach the pseudo permanent regime. At this time, we use the simulation files to restart the simulation with an increased mesh resolution by a power of two from a $lvl9 = 2^9$ to a $lvl10 = 2^{10}$ maximum number of cells in one direction. Later, we restart a second time the simulation and increase the mesh resolution by a power of two from a $lvl10 = 2^{10}$ to a $lvl11 = 2^{11}$ maximum number of cells in one direction. We can see that the Sherwood number at each restart is almost constant and has a really low value. Then the Sherwood number increases following a transient regime faster than the one at the start of the mass transfer simulation to finally reach a pseudo permanent regime.

An explanation for this second type of transient regime is that when we restart the simulation from files already considering mass transfer and increase the maximum mesh resolution the mesh is progressively refined along the concentration boundary layer.

The low value of the Sherwood number at the start of the simulation might be due to an erroneous value of the concentration of tracer in the water derivative at the first-time step. In the following for more concision, we have chosen to display only the pseudo-permanent regime and filter the erroneous low Sherwood number at each restart.

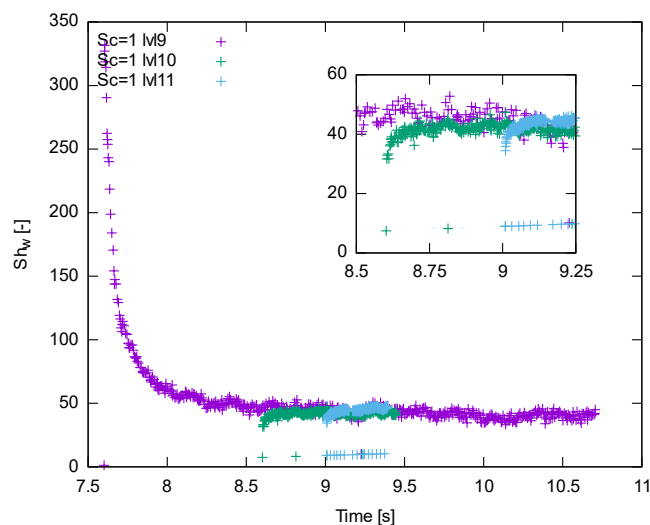


Figure 8.17: Time evolution of the Sherwood number in the water phase at $Q = 0.6l/min$ with $Sc_w = 1$ with different maximum mesh resolutions in one direction.

In Figure 8.18-(b),(d),(f) we can observe the time evolution of the Sherwood number in water for different Schmidt numbers and different maximum mesh resolutions. If we look at Figure 8.18-(b), as observed in Figure 8.18-(a) all Sh_w values superpose to nearly the same asymptotic value without important deviation when increasing the maximum mesh resolution from 2^9 to 2^{10} cells. If we now look at Figure 8.18-(b) the results are a bit noisier, but we clearly see a gap between Sh_w values with the lower maximum mesh resolution in one direction of 2^9 and higher mesh resolutions.

The results between the two mesh resolutions of 2^{10} and 2^{11} seem to converge toward the same asymptotic value. From these results, we can reasonably say that the variation of the concentration of tracer in the water phase at $Q = 0.6l/min$ show convergence from a maximum number of cells in one direction of 2^{10} .

In Figure 8.19-(a), (c), (e), (g) we plot the time evolution of the concentration of tracer in the oil phase with different maximum mesh resolutions and for different Schmidt numbers. We can see from Figure 8.19-(a) and (b) that the concentration of tracer in the oil phase respectively at $Sc_o = 10$ and $Sc_o = 40$ shows an important decrease during the time of the simulation and that no change in the slope of the concentration in the oil phase is observed when the maximum mesh is increased. From Figure 8.19-(e) and Figure 8.19-(g) we can see that as we increase the Schmidt number the decrease of the concentration of tracer in oil takes more time and that we observe a small change in the slope when increasing the maximum mesh resolution.

If we now look at Figure 8.19-(b) showing the time evolution of the Sherwood number in the oil phase we see that the Sherwood number for all the mesh resolutions seems to continuously decrease and not converge toward an asymptotic value. In that case, the concentration of tracer in the oil phase decreases too rapidly to reach a pseudo-periodic regime for the Sherwood number.

Our mass transfer model is based on the assumption of a high Péclet number $Pe = ReSc$. So, this means that for $Sc_o = 10$ the value of the Reynolds number in the oil layer is not high enough to have a high Péclet number. If we look at Figure 8.19-(d), (f) obtained respectively for $Sc_o = 100$ and $Sc_o = 400$ we can now see that the Sherwood number reach a pseudo permanent regime by converging toward an asymptotic value. We cannot really see a difference in the Sherwood number when increasing the maximum mesh resolution.

If we compare globally the time evolution of the Sherwood number in the water and the oil phase, we observe that the results of the Sherwood number in the oil phase present higher standard deviation than in the water phase. Also, for $Sc_o > 10$ we can remark that the Sherwood number is roughly ten times higher in the water than in the oil phase with ten-time lower value of the Schmidt number.

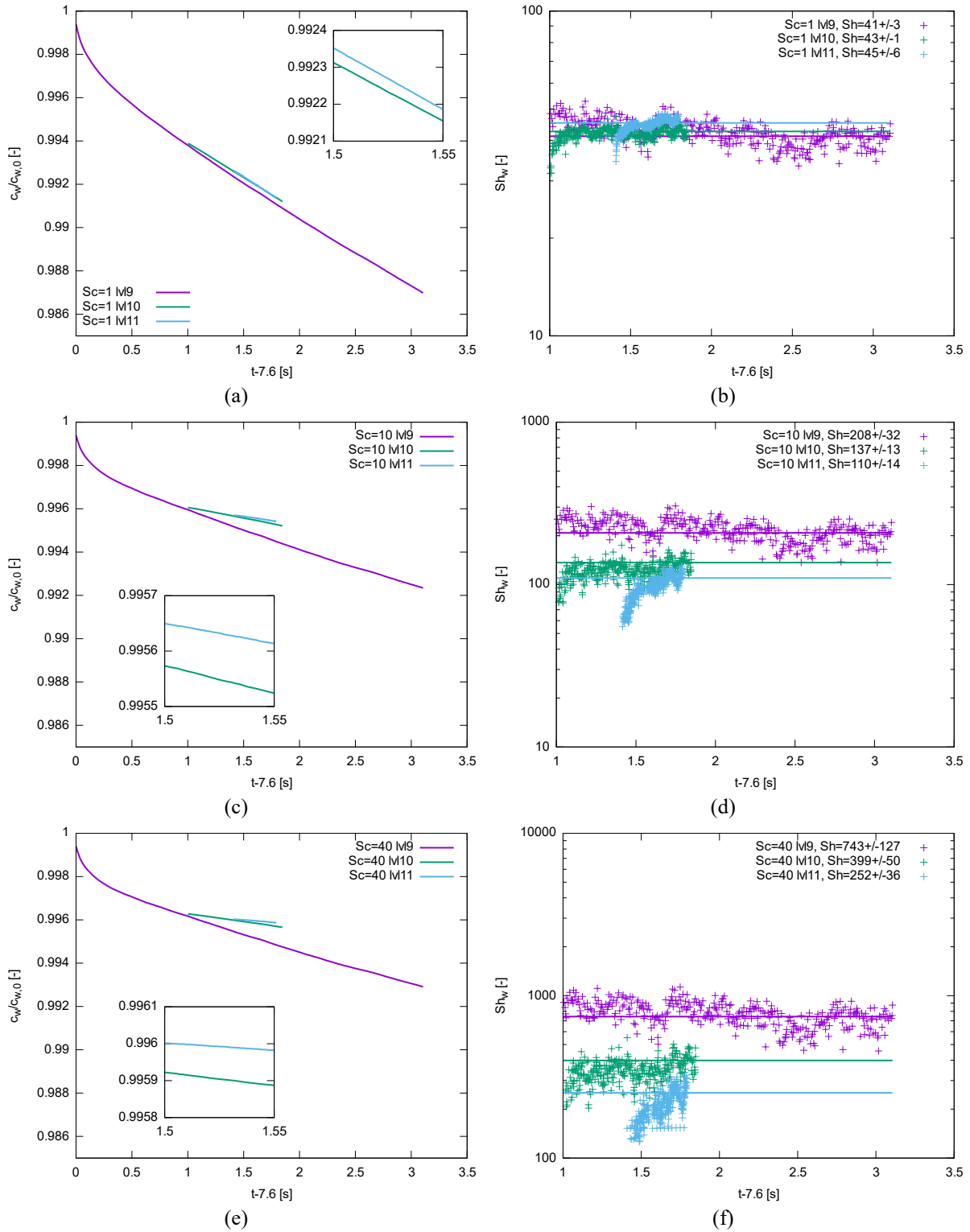


Figure 8.18: Numerical results obtained at a fixed air flow rate of $Q = 0.6l/min$. (a) Evolution of the concentration of tracer in the water phase with different mesh resolutions with $Sc_w = 1$; (b) Evolution of the Sherwood number in the water phase with different mesh resolutions with $Sc_w = 1$; (c) Evolution of the concentration of tracer in the water phase with $Sc_w = 10$; (d) Evolution of the Sherwood number in the water phase with $Sc_w = 10$; (e) Evolution of the concentration of tracer in the water phase with $Sc_w = 40$; (f) Evolution of the Sherwood number in the water phase with $Sc_w = 40$.

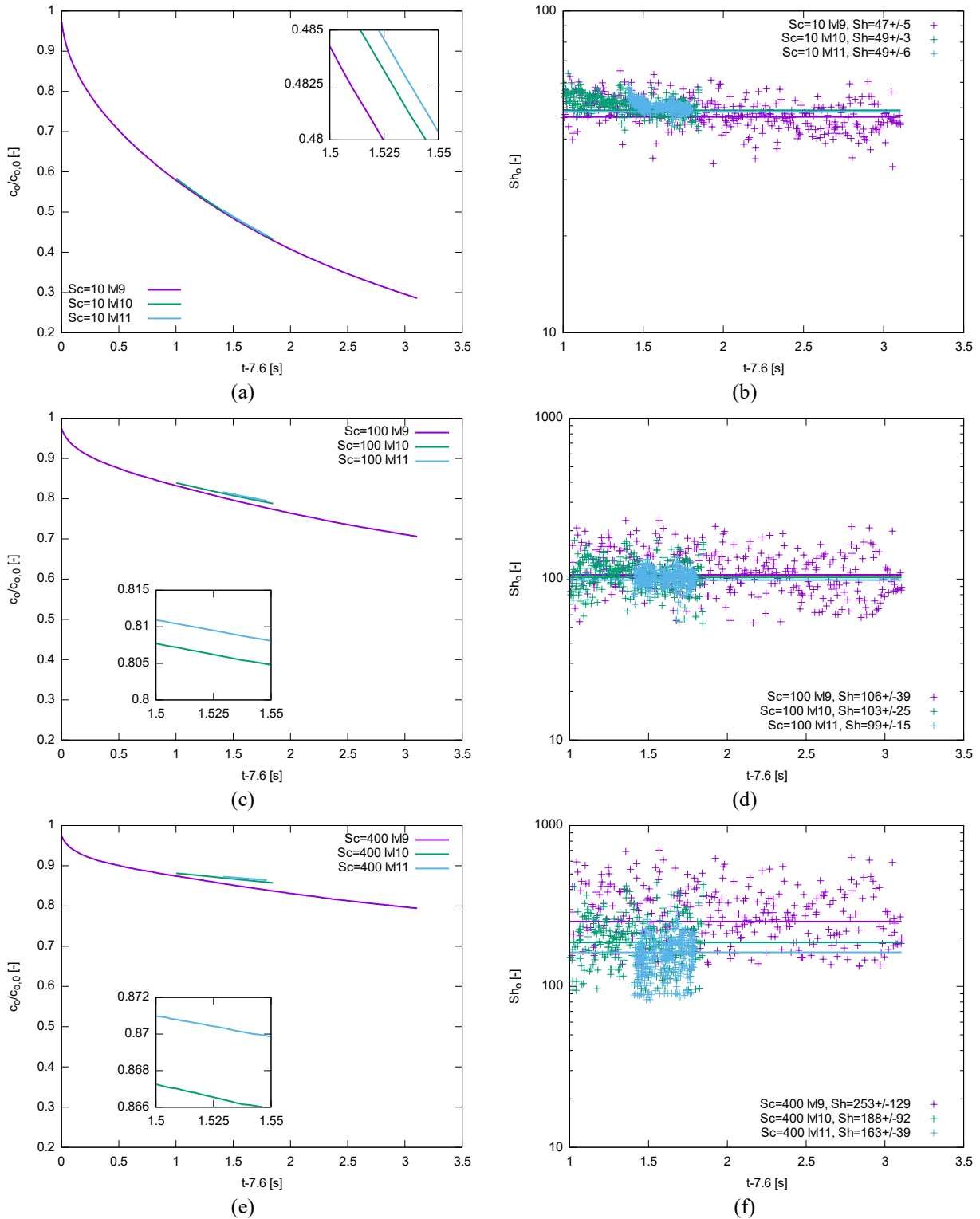


Figure 8.19: Numerical results obtained at a fixed air flow rate of $Q = 0.6\text{ l/min}$. (a) Evolution of the concentration of tracer in the oil phase with different mesh resolutions with $Sc_o = 10$; (b) Evolution of the Sherwood number in the oil with $Sc_o = 10$; (c) Evolution of the concentration of tracer in the oil phase with $Sc_o = 100$; (d) Evolution of the Sherwood number in the oil phase with $Sc_o = 100$; (e) Evolution of the concentration of tracer in the oil phase with different mesh resolutions with $Sc_o = 400$; (f) Evolution of the Sherwood number in the oil phase with $Sc_o = 400$.

8.2.2.1.2 $Q = 5.5l/min$ case

We will now look at the time evolution of the Sherwood number in water obtained for $Q = 5.5l/min$ in Figure 8.20-(a), (b), (c), (d). We can see here that for all the Schmidt numbers the Sherwood number shows some oscillations around an asymptotic value. We can also observe that the Sherwood number value present a gap when increasing the maximum mesh resolution in one direction from 2^{10} to 2^{11} and a smaller gap between 2^9 and 2^{10} . This could indicate that both maximum mesh resolutions of 2^9 and 2^{10} are too coarse to obtain converged results at this air flow rate. Or that we do not have simulated enough time to reach a pseudo-permanent regime at a maximum mesh resolution in one direction of 2^{11} cells. If we compare to the results of Figure 8.18-(b),(d),(f) obtained with $Q = 0.6l/min$ we can see that we obtain roughly a Sherwood number ten time larger than the results with $Q = 0.6l/min$.

At the same air flow rate, we look now at the Sherwood number in the oil phase in Figure 8.21-(a), (b), (c), (d). We can see here that the Sherwood number in the oil phase value present a gap when increasing the maximum mesh resolution only when $Sc_o \geq 100$ and that the results present fewer oscillations than in the water phase. If we look at Figure 8.21-(a) we can see that when $Q = 5.5l/min$ the Sherwood number seems to converge toward asymptotic value unlike the results obtained in Figure 8.19-(b) for $Q = 0.6l/min$. This means that at a constant $Sc_o = 10$, increasing the air flow rate by a factor of ten is sufficient to have a Reynold number high enough to have a high Péclet in the oil layer corresponding to our mass transfer model.

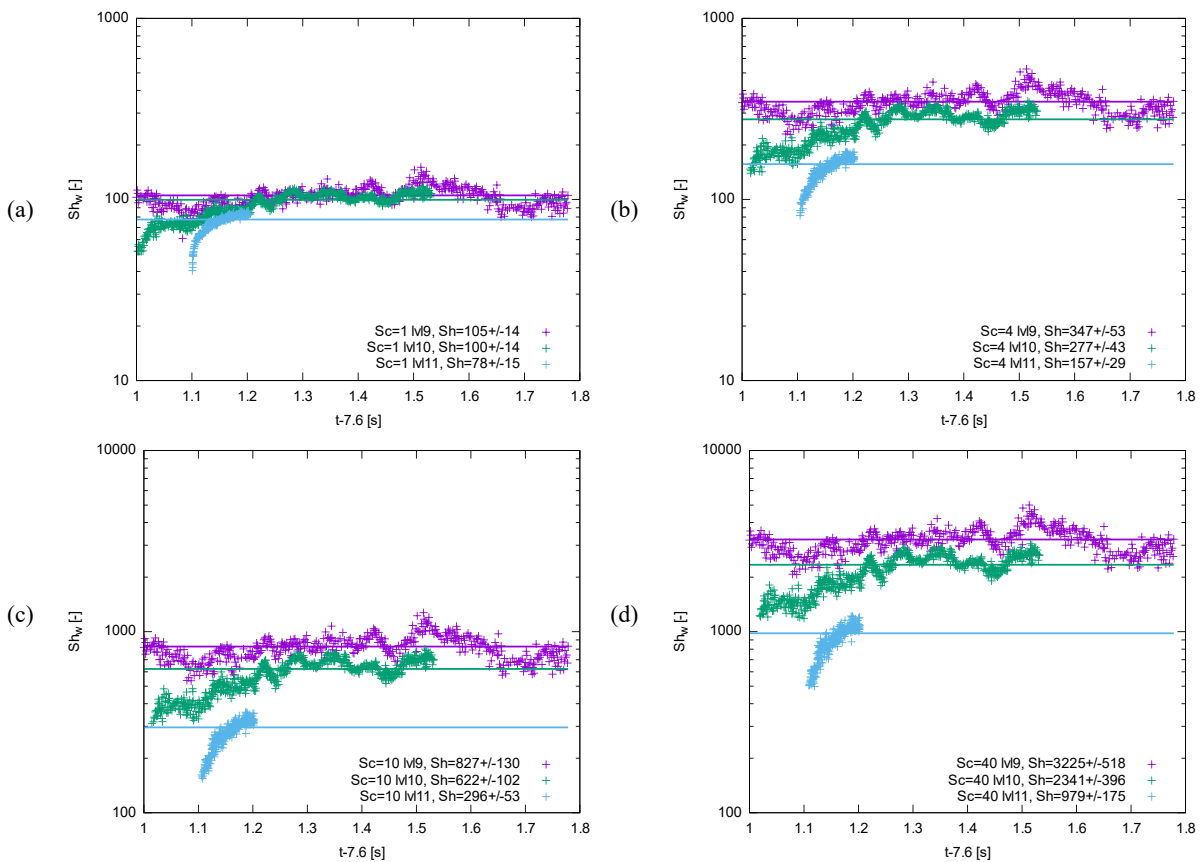


Figure 8.20: Evolution of the Sherwood number in the water phase with different mesh resolutions at a fixed air flow rate of $Q = 5.5l/min$. (a) $Sc_w = 1$; (b) $Sc_w = 4$; (c) $Sc_w = 10$; (d) $Sc_w = 40$.

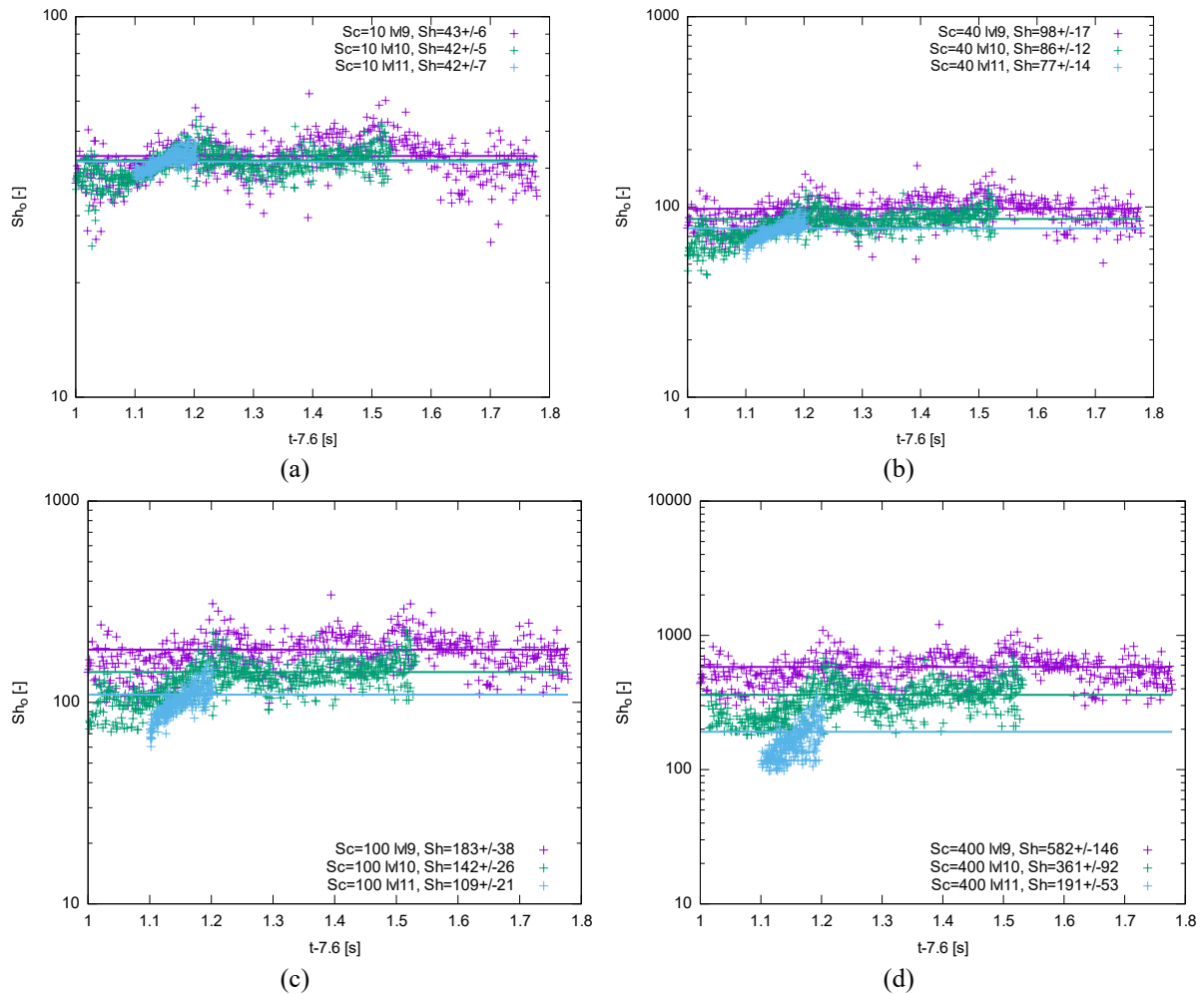


Figure 8.21: Evolution of the Sherwood number in the oil phase with different mesh resolutions at a fixed air flow rate of $Q = 5.5l/min$. (a) $Sc_o = 10$; (b) $Sc_o = 40$; (c) $Sc_o = 100$; (d) $Sc_o = 400$.

8.2.2.2 Time-averaged values

8.2.2.2.1 Sherwood number

In Figure 8.22 we plot the asymptotic value of the Sherwood number in the water phase with standard deviation identified in Figure 8.18 for all the Sc_w values at $Q = 0.6l/min$. We can see that the Sherwood number in water increases when the Schmidt number increases for all maximum mesh resolution and that the results follow the same trend. As we increase the mesh resolution the Sherwood number decreases but the difference between the results obtained with a maximum mesh resolution of 2^{10} and 2^{11} cells is smaller than between 2^9 and 2^{10} cells. Also, the standard deviation reduces as we increase the maximum mesh resolution, this indicates that the results show mesh convergence.

In Figure 8.23-(a) and (b) we still plot the Sherwood number in water but this time as a function of the modified Froude number with different Schmidt numbers and with respectively a constant maximum mesh resolution in one direction of 2^{10} and 2^{11} cells. This plot use the results of the Figure 8.18 to Figure 8.22 and the results of the plots in 11.2. We can clearly see that the Sherwood number value increases following the same trend when increasing the Schmidt number and the modified Froude

number. We can also note that the standard deviation of the Sherwood number increases with the Schmidt number. We can observe one gap in the Sherwood number value between the lowest modified Froude number point and the other points. Another gap between the highest modified Froude number point and data at lower modified Froude number can be observed. But we cannot make the distinction between several mass transfer regimes from the limited amount of points that we have. If we compare the two plots we can see that when we increase the maximum mesh resolution by a power of two in one direction from Figure 8.23-(a) to Figure 8.23-(b) the value of the Sherwood number and its associated standard deviation decrease for all modified Froude numbers.

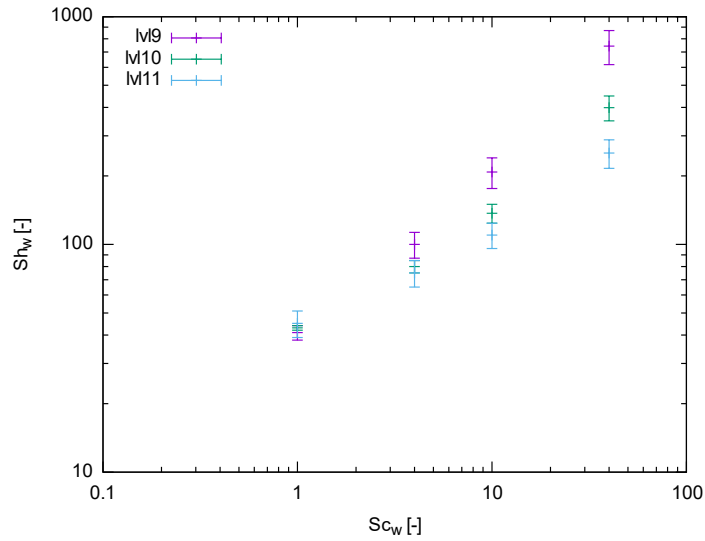


Figure 8.22: Comparison of the Sherwood number in water with standard deviation as a function of the Schmidt number in water with different maximum mesh resolutions at a fixed air flow rate of 0.6l/min.

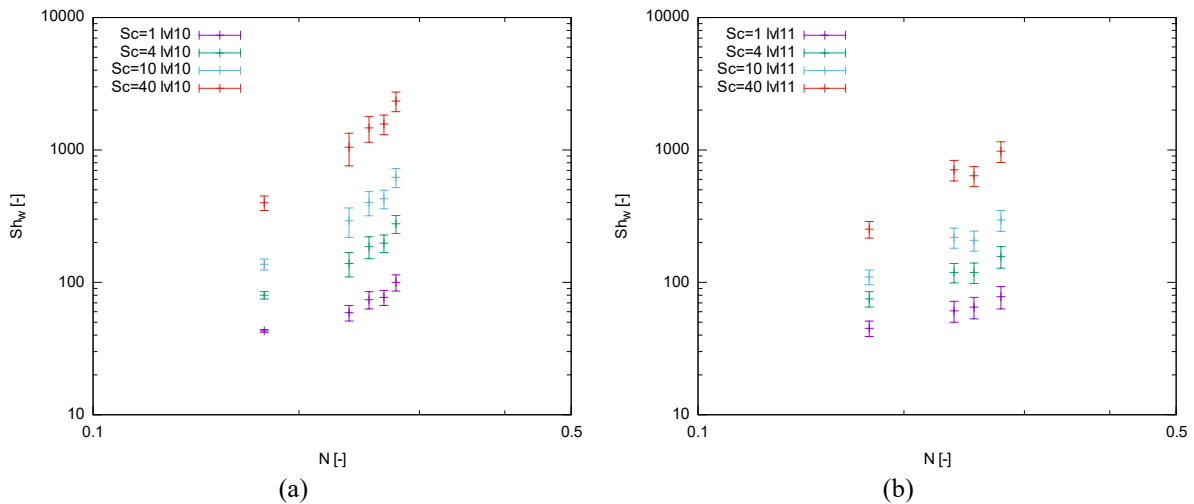


Figure 8.23: Comparison of the Sherwood number in water as a function of the modified Froude number with standard deviation. (a) results obtained with a fixed maximum number of cells in one direction of 2^{10} ; (b) results obtained with a fixed maximum number of cells in one direction of 2^{11} .

8.3 COMPARISON OF THE EXPERIMENTAL AND NUMERICAL RESULTS

We have to keep in mind that the numerical results are obtained for a maximum $Sc_w = 40$ which is thirty-seven times lower than the experimental value $Sc_w = 1.48 \cdot 10^3$ allowing to use reasonably small mesh resolution in order to save computational time. This means that we cannot directly compare the numerical results with the experimental one. Instead, we use the correlation (8.9) corresponding to a Nusselt profile in the oil layer which was used to predict the experimental results to fit the numerical results in Figure 8.24 and Figure 8.25. We start by looking at the results of Figure 8.24 obtained for $Q = 0.6$ l/min where we can see that as we increase the maximum mesh resolution in one direction from 2^9 to 2^{11} cells the fit gets closer to our experimental result. We can also remark that the fit of the Sherwood number follows a $Sc^{1/2}$ curve. The fit of the numerical results obtained for a maximum mesh resolution in one direction of 2^{11} cells is relatively close to our experimental measurement. So, we can reasonably fit our numerical results considering a maximum mesh resolution of 2^{11} and a Nusselt profile in the oil layer with the following correlation

$$Sh_{w,num1}^{NO} = 0.048 \left(\frac{h_o m Ar}{h_w 16} \right)^{1/2} Sc^{1/2} N + 0.021 \left(\frac{Ar}{16} \right)^{1/3} Sc^{1/3} N^{2/3} \quad (8.15)$$

We now consider in Figure 8.25 the maximum air flow rate simulated of $Q = 5.5$ l/min as we increase the maximum mesh resolution from 2^9 to 2^{11} there is almost no change in the estimated value of the Sherwood number given by the fit. But at this high air flow rate value, the standard deviation of the numerical Sherwood number is high, and we cannot say for sure that the results appear to show a mesh convergence. If we consider a maximum mesh resolution of 2^{11} and a Nusselt profile in the oil layer we can write the following correlation

$$Sh_{w,num2}^{NO} = 0.15 \left(\frac{h_o m Ar}{h_w 16} \right)^{1/2} Sc^{1/2} N + 1.91 \cdot 10^{-7} \left(\frac{Ar}{16} \right)^{1/3} Sc^{1/3} N^{2/3} \quad (8.16)$$

In Figure 8.26 we gather all the numerical results for each modified Froude number and Schmidt number and consider a constant maximum mesh resolution of 2^{10} cells. Then, we can do a two-dimensional fit of the numerical Sherwood number as a function of both the numerical Schmidt number in the water phase and the modified Froude number. From Figure 8.26 we can see that considering the small range of the modified Froude number, the estimated Sherwood number seems to be more dependent on the Schmidt number value than the modified Froude number. If we use the correlation (8.9) to predict the Sherwood number, we can write the following correlation from the results

$$Sh_{w,num3}^{NO} = 0.077 \left(\frac{h_o m Ar}{h_w 16} \right)^{1/2} Sc^{1/2} N + 1.79 \cdot 10^{-6} \left(\frac{Ar}{16} \right)^{1/3} Sc^{1/3} N^{2/3} \quad (8.17)$$

In Figure 8.27 we used the correlations (8.15), (8.16) and (8.17) corresponding to a Nusselt profile in the oil phase established from our numerical results at $Q = 0.6$ l/min, $Q = 5.5$ l/min and with the simultaneous fit of $Sh = (N, Sc)$ to compare with our experimental results. From Figure 8.27 we can see that there is a tendency for all the obtained fit from the numerical results to overestimate the experimental Sherwood number for the modified Froude number range considered. The fit with the correlation (8.15) obtained at $Q = 0.6$ l/min is the one giving the less overestimated results compared to the experimental results.

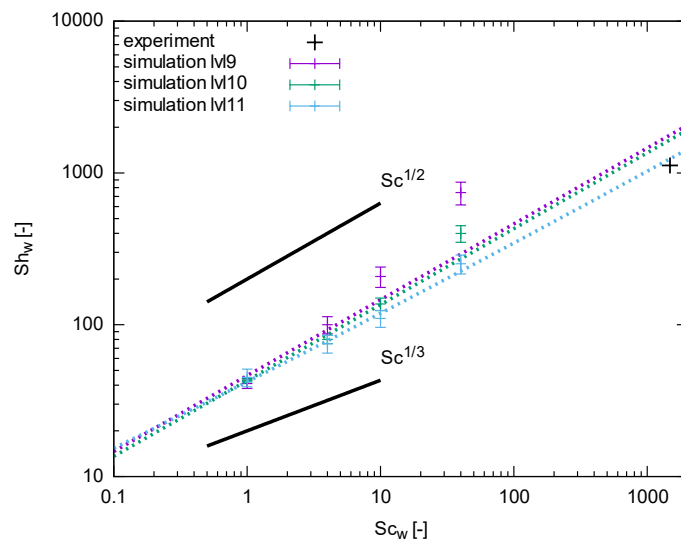


Figure 8.24: Fit of the numerical Sherwood number in water with standard deviation as a function of the Schmidt number at an air flow rate $Q = 0.6$ l/min and for different maximum numbers of cells in one direction. The black cross represents our experimental result.

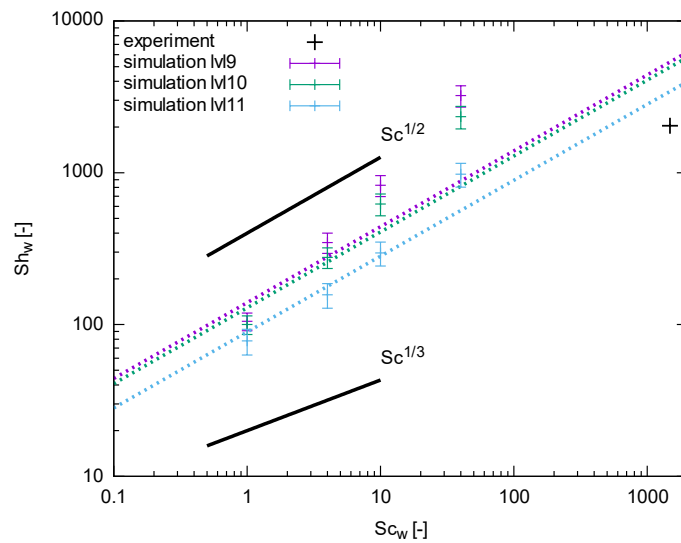


Figure 8.25: Fit of the numerical Sherwood number in water with standard deviation as a function of the Schmidt number at an air flow rate $Q = 5.5$ l/min and for different maximum numbers of cells in one direction. The black cross represents our experimental result.

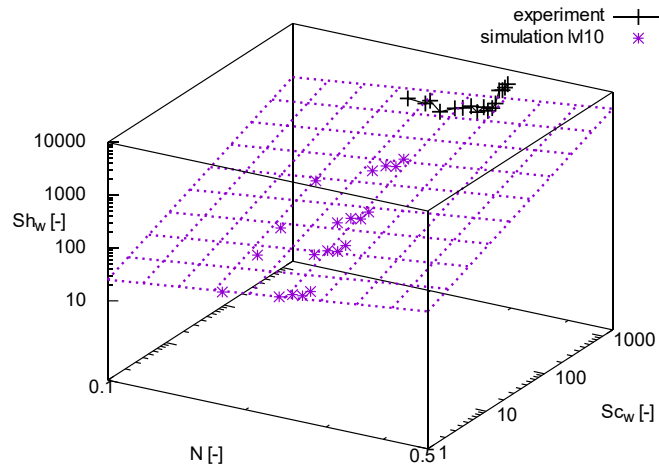


Figure 8.26: Fit of the numerical Sherwood number in water as a function of the Schmidt number and the modified Froude number. The black cross represents our experimental results.

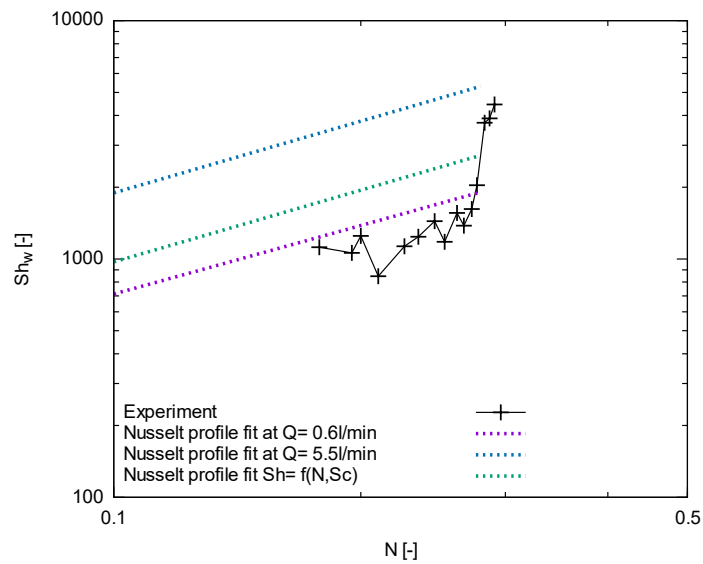


Figure 8.27: Fit of our experimental results of the Sherwood number in water as a function of the modified Froude number with the correlation applied to our numerical results.

8.4 SUMMARY

In this chapter, from the visualization we have seen that the continuous formation of oil droplets in the water phase is correlated to the change of mass transfer regime. Moreover, our experimental mass transfer results show a small influence of the injection diameter size on the mass transfer. Comparing our experimental results with the one of [32] showed that the change of mass transfer regime occur at similar critical air flow rate. On the other hand, the Sherwood number comparison reveals the importance of the size of the experimental ladle on the value of the Sherwood number.

Later, we tried to fit our experimental results and the one of [32] considering a Nusselt profile in the oil layer and using the corresponding correlation of the Sherwood number. It gave a reasonable fit of our experimental results but, it overestimates the results of [32] for the first mass transfer regime.

The numerical results showed a global good behaviour by reproducing the expected mass transfer configuration with a variation of the concentration essentially at the water-oil interface. For the small Schmidt numbers considered in the simulation the results showed that we could obtain mesh convergence on the Sherwood number for small air flow rate. Indeed, the results showed that the Sherwood number is more sensitive to the variation of the maximum mesh resolution at high Schmidt number than at low Schmidt number and at high air flow rate than at low air flow rate.

However, with the limited amount of data that we obtained we have not been able to reproduce different mass transfer regime with our numerical simulations as observed in our experimental results.

Then considering a Nusselt profile in the oil layer we have used the same correlation as previously to predict our experimental results, from the obtained numerical results. Unfortunately, this leads to an overestimation of the experimental Sherwood number. A first explanation is that the assumption that we have made are not sufficiently representative of the real mass transfer of the water experiment. Another explanation could be that we do not have a sufficient mesh resolution to resolve the concentration boundary layer at a high air flow rate, leading to an overestimation of the mass transfer.

9 TOWARD INDUSTRIAL APPLICATION- MASS TRANSFER CHARACTERIZATION

In the following, we will compare the experimental results obtained with water experiments first to liquid metals study in the literature then with an industrial ladle configuration study. The goal is to be able to predict the mass transfer in an industrial configuration from the results obtained with the water experiment. In order to simplify the model, we will not consider temperature variation in the experiments and so we consider constant physical properties and neglect the possible phase change by considering the steel and slag phase always at liquid states. Since we will compare experiments with different fluids, we will denote the physical properties of the steel and slag equivalent phase for both water and metal models with the respective indices m and s .

9.1 MASS TRANSFER MEASUREMENT

9.1.1 Liquid metal experiments in the literature

We want to compare the water experiment results on the characterization of the mass transfer with results from the literature obtained with liquid metals and various sizes of the ladle. To do so, we selected experiments representative of the desulfurization process where the chemical reaction rate is governed by the transport of chemical species. . Nevertheless, we faced an important difficulty that there are relatively few accessible studies of mass transfer characterization made with liquid metals with complete data in the literature. This is due to the inherent difficulty of doing experimental measurements at high temperature with liquid metals, and to the fact that some studies are not easily accessible in numerical version. This is particularly the case for experiment with liquid steel in an industrial ladle configuration. So here we restrained our self to analyze studies that are in majority accessible online.

In addition to our water experiment and the one of Kim & Fruehan [32] first, we consider the experiment of the desulphurization of liquid steel with slag in a 185-ton industrial ladle of Lachmund *et al.* [8] where we have relatively complete data that can be found in Table 9.1. As no diffusion coefficient value is given in this study, we take the value from Gaye [103]. Then we consider the study of Ishida *et al.* [9] obtained also for the reaction of the desulphurization of liquid steel with slag at 1600°C but with a 2.5-ton ladle. Only a few data about the experiment are available for this study and so we choose to adapt some of the data from [8] to this smaller ladle. Finally, we consider the results of Hirasawa *et al.* [99] obtained with the desiliconization of liquid copper with slag in a 0.4kg ladle at a temperature of 1250°C. In this study the slag physical properties are missing so we will again use the one from [8]. The diffusion coefficient of Si in the liquid copper is computed with the Stokes-Einstein relation. All the important quantities of the reduce scale experiments can be found in Table 9.1.

If we look now at Table 9.2, we can see that in the experiments considered the ratio of the Schmidt number in the steel and the slag equivalent phase $Sc_r = Sc_m/Sc_s$ shows a lower value in the water experiments than in the liquid metal. This is because of a higher Schmidt number in the slag and the steel equivalent phase for the water experiments than for the liquid metal experiments. Furthermore, as no measurement of the partition coefficient of chemical species for the liquid metal experiments has been done, we use a constant value corresponding to the partition coefficient of thymol between water and oil for all the experiments. We can also note that because of the size of the ladle a higher value of the ratio β is observed for the industrial ladle than for the reduced scale experiments.

	T (°C)	ρ_m (kgm^{-3})	ρ_s (kgm^{-3})	μ_m (Pa.s)	μ_s (Pa.s)	σ_{ms} (N/m)	D_m ($m.s^{-2}$)	D_s ($m.s^{-2}$)	L_x (m)	h_m (m)	h_s (m)
Our experiment	20	998	920	10^{-3}	0.079	0.0255	$6.8 \cdot 10^{-10}$	$6.8 \cdot 10^{-12}$	0.27	0.20	0.007
Kim et al. [32]	20	998	886	10^{-3}	0.033	0.0181	$6.8 \cdot 10^{-10}$	$6.8 \cdot 10^{-12}$	0.46	0.445	0.015
Ishida et al. [9]	1600	6800	2800	$5.4 \cdot 10^{-3}$	0.1	1.2	$4.4 \cdot 10^{-9}$	$2.8 \cdot 10^{-10}$	0.804	0.724	0.018
Hirasawa et al. [99]	1250	7800	2800	$3.1 \cdot 10^{-3}$	0.1	1.2	$2 \cdot 10^{-9}$	$2.8 \cdot 10^{-10}$	0.04	0.036	0.016
Lachmund et al. [8]	1600	6800	2800	$5.4 \cdot 10^{-3}$	0.1	1.2	$4.4 \cdot 10^{-9}$	$2.8 \cdot 10^{-10}$	3.3	3.2	0.08

Table 9.1: Main physical properties and quantities of the steel equivalent phase and the slag equivalent phase for our experiment and the experiments of [8, 9, 32, 99].

	m	r	Sc_m	Sc_s	Sc_r	P	β	h_m / L_x	h_s / L_x
Our experiment	$1.27 \cdot 10^{-2}$	1.08	$1.48 \cdot 10^3$	$1.26 \cdot 10^7$	$1.17 \cdot 10^{-4}$	350	$9.00 \cdot 10^{-2}$	0.74	0.035
Kim et al. [32]	$2.99 \cdot 10^{-2}$	1.13	$1.48 \cdot 10^3$	$2.36 \cdot 10^6$	$6.25 \cdot 10^{-4}$	350	$9.00 \cdot 10^{-2}$	0.98	0.034
Ishida et al. [9]	$5.4 \cdot 10^{-3}$	2.43	$1.82 \cdot 10^2$	$1.28 \cdot 10^5$	$1.38 \cdot 10^{-3}$	350	$1.2 \cdot 10^{-1}$	0.9	0.025
Hirasawa et al. [99]	$3.1 \cdot 10^{-3}$	2.79	$2.00 \cdot 10^2$	$1.28 \cdot 10^5$	$1.56 \cdot 10^{-3}$	350	$2.00 \cdot 10^{-2}$	0.9	0.44
Lachmund et al. [8]	$5.4 \cdot 10^{-3}$	2.43	$1.82 \cdot 10^2$	$1.28 \cdot 10^5$	$1.38 \cdot 10^{-3}$	350	4.57	0.94	0.026

Table 9.2: Main dimensionless physical properties of the steel equivalent phase and the slag equivalent phase for our experiment and the experiments of [8, 9, 32, 99].

9.1.2 Comparison of the results

9.1.2.1 Mass transfer

To avoid a too important dispersion of the results between the experiments we consider the gas flow rate per unit of mass of the steel equivalent phase considered. Otherwise, the effect of a large difference of ladle sizes between the experiments as can be seen in Table 9.1 would lead to a high value of the gas flow rate for the liquid metal experiments. Figure 9.1 shows a comparison of the capacity coefficient as a function of the gas flow rate at the operating condition per unit of mass of steel equivalent phase. In Figure 9.1 first, we observe for each experiment at least two different mass transfer regimes when the gas flow rate is increased. The results of [9] show higher values of the capacity coefficient that the one obtained with water experiments but similar evolution in the same range of gas flow rate per mass unit of steel equivalent phase. The results of [8] show similar values of the capacity coefficient but have a smaller slope for the second mass transfer regime than the results of [9]. Now if we look at the results obtained by [99] first we can observe that they show three different mass transfer regimes with a small change of the slope between each mass transfer regime. The first mass transfer regime and the third mass transfer regime have a similar slope. While for the second

mass transfer regime the capacity coefficient is almost constant. The value of the capacity coefficient of [99] is a hundred times higher than our results and with significantly higher maximum gas flow rate per mass unit of steel equivalent phase than for the other experiments. Something that could explain the different behaviour of the experiment of [99] is the high value of the ratio $h_s/h_m \sim 0.5$ when for the other experiments $h_s/h_m < 0.05$. It means that the experiment of [99] corresponds to a thick slag layer case with a possible different behavior of the slag layer than for the other experiments corresponding to a thin slag layer case. In addition to that, it used the reaction of desiliconization of liquid copper with slag which is different than the desulphurization of liquid steel. These two differences and really small size of the ladle could explain the deviation between their results and the results of the other experiments.

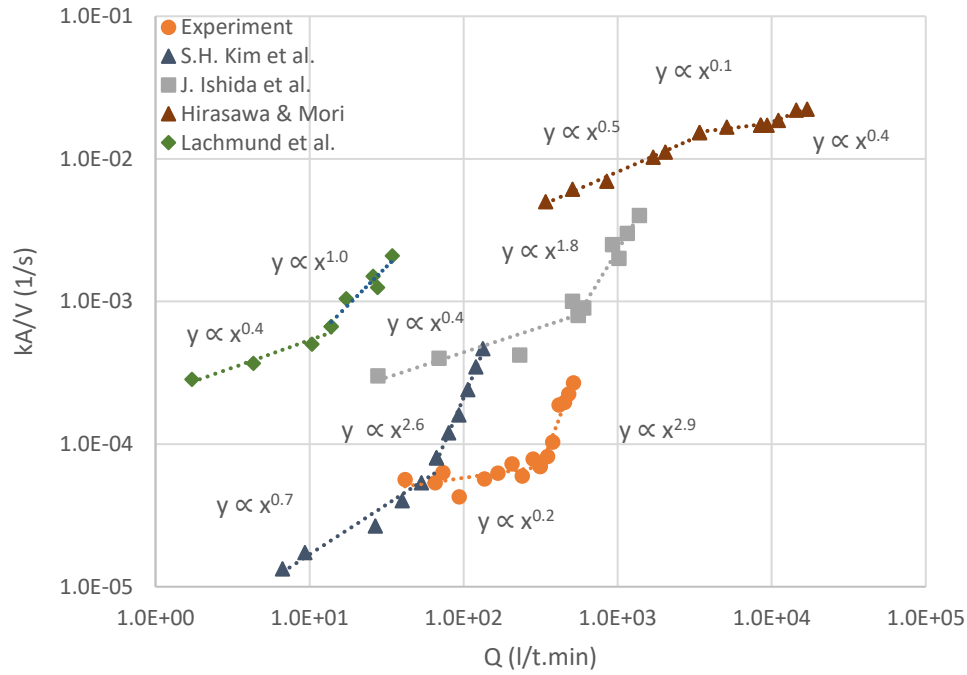


Figure 9.1: Comparison of the capacity coefficient in the steel equivalent phase as a function of the air flow rate at operating condition per mass unit of the steel equivalent phase for our experiment and the experiment of Kim & Fruehan [32], Lachmund et al. [8], Ishida et al. [9], Hirasawa et al. [99].

Now, if we consider the slag phase area without air injection as a reference area and the specific volume of steel equivalent phase in each experiment, we can compute the global Sherwood number for the steel equivalent phase from the results of Figure 9.1 with

$$Sh_m = \frac{K_m L_x}{4D_m} \quad (9.1)$$

We use the bubble column velocity formulation established in 2.3.2 , to compute the vertical buoyancy velocity

$$U = (g^2 Q)^{1/5}, \quad (9.2)$$

then from the gas flow rate at the operating conditions, we can compute the modified Froude number with

$$N = \left(\frac{Q}{g^{1/2} h_m^{5/2}} \right)^{1/5} \quad (9.3)$$

In Figure 9.2 we replot the data of Figure 9.1 using the Sherwood number in the steel equivalent phase as a function of the modified Froude number at the experimental operating conditions. From the results of Figure 9.2, the evolution of the Sherwood number of each experiment follows the same behaviour but with a different exponent for the slope than the results of Figure 9.1. The results of [8] show a higher value of the Sherwood number than the other experiments with a difference of a factor ten with the results of [9]. Then there is almost a factor ten of difference between the results of [9] and the results of [99]. This is interesting to note from the Schmidt number values in Table 9.2 that these three experiments are done with similar Schmidt number in the steel equivalent phase. But there is a maximum difference of a factor thousands of the Sherwood number between them. If we look back at Figure 9.1 we see that there is a small difference in the value of the capacity coefficient between the results of [8] and [9]. If we assume that these two experiments follow exactly the same chemical reaction between steel and slag, it means that the observed difference between these two experiments in Figure 9.2 is mainly due to the difference in the size of the ladle.

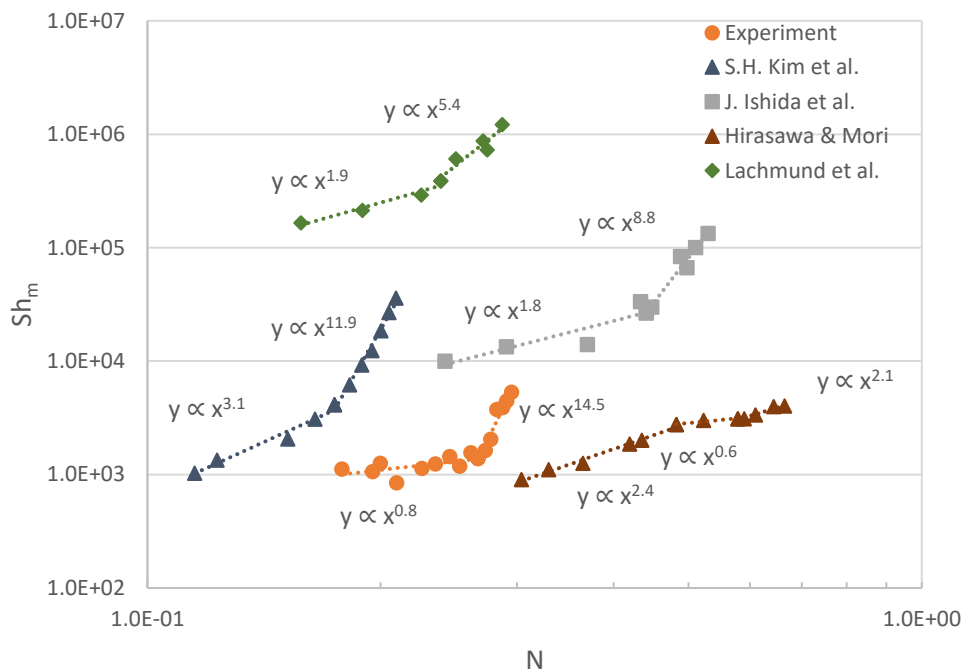


Figure 9.2: Comparison of the Sherwood number in the steel equivalent phase as a function of the modified Froude number for our experiment and the experiment of Kim & Fruehan [32], Lachmund et al. [8], Ishida et al. [9], Hirasawa et al. [99].

9.1.2.2 Critical modified Froude number

We will try now to characterize the critical modified Froude number N_{crit} at which the transition of the mass transfer regime changed is observed. We have seen from our water experiment results in 8.1 that the change of mass transfer regime is correlated with the fragmentation of the slag layer into droplets. So, in the following, we will consider that the critical modified Froude number N_{crit} indicating the transition of the mass transfer regime corresponds to the critical modified Froude number when slag fragmentation is expected. Two correlations to predict N_{crit} will be compared. The first one is established by Kim *et al.* [40] where the authors made a dimensional analysis from their water experiments using different combination of fluids to find the critical gas flow rate for the entrainment

of the slag layer. From their analysis, the authors obtained a relation for the critical modified Froude number following this expression

$$N_{crit} = a \left(\frac{\sigma_{ms} \Delta\rho}{\rho_s g h_m^2 \rho_s} \right)^b, \quad (9.4)$$

where a, b are numerical constants determined from the experiments. The second correlation comes from the chapter 2 section 2.3.4 of this dissertation where we have established that the apparition of slag droplets detachment should occur for the following critical modified Froude number

$$N_{crit} = c \left(Bo_{ms} \frac{\rho_m}{(\rho_m - \rho_s)} \frac{h_s}{h_m} \right)^{-1/10\alpha}, \quad (9.5)$$

where c is a numerical constant determined from the experiments, $\alpha = 1/3$ in the case of a bubble plume $\alpha = 1/5$ in the case of a bubble column and, Bo_{ms} is the Bond number at the slag/steel interface and is given by

$$Bo_{ms} = \frac{(\rho_m - \rho_s) g h_m^2}{\sigma_{ms}}. \quad (9.6)$$

In Figure 9.3 where we plot the critical modified Froude number N_{crit} as a function the right hand side of equation (9.4) for water and liquid metal experiments. We can see almost a factor ten of difference between the water and liquid metal experiments for the value of N_{crit} . Also, the liquid metal experiments present a high dispersion along the x-axis. Then, we fit the critical modified Froude number N_{crit} using (9.4) to obtain the following expressions for the water (9.7) and liquid metal (9.8) experiments

$$N_c = 0.6 \left(\frac{\sigma_{wo} \Delta\rho}{\rho_o g h_w^2 \rho_o} \right)^{0.1}, \quad (9.7)$$

$$N_c = 8.6 \left(\frac{\sigma_{ms} \Delta\rho}{\rho_s g h_m^2 \rho_s} \right)^{0.1}, \quad (9.8)$$

where the indices w and o are used to denote parameters respectively for the water and oil phase. From the correlation (9.7) and (9.8) we can see that there is more than a factor ten of difference for the value of a and that the value of b is the same between the water and liquid metal experiments.

Now we look at Figure 9.4 showing the critical modified Froude number N_{crit} as a function the right-hand side of the equation (9.5). Within this formulation, we can observe less horizontal dispersion of the results than previously. We can also note that now we consider the height of the slag layer unlike previously. If we fit the experimental results with the correlation (9.5) we obtain the following expressions

$$N_{crit} = 0.9 \left(Bo_{wo} \frac{\rho_w}{(\rho_w - \rho_o)} \frac{h_o}{h_w} \right)^{-0.2}, \quad (9.9)$$

$$N_{crit} = 10.5 \left(Bo_{ms} \frac{\rho_m}{(\rho_m - \rho_s)} \frac{h_s}{h_m} \right)^{-0.1}. \quad (9.10)$$

We can see from (9.9) and (9.10) that again there is a difference of factor ten in the value of α but a similar value of $1/\beta$ between the water and the liquid metal experiments.

From this attempt to establish a correlation to predict N_{crit} corresponding to the gas flow rate of the transition of the mass transfer regime we have seen that using equation (9.4) we can almost superpose the results of the water and liquid metal experiments unlike the results using equation (9.5).

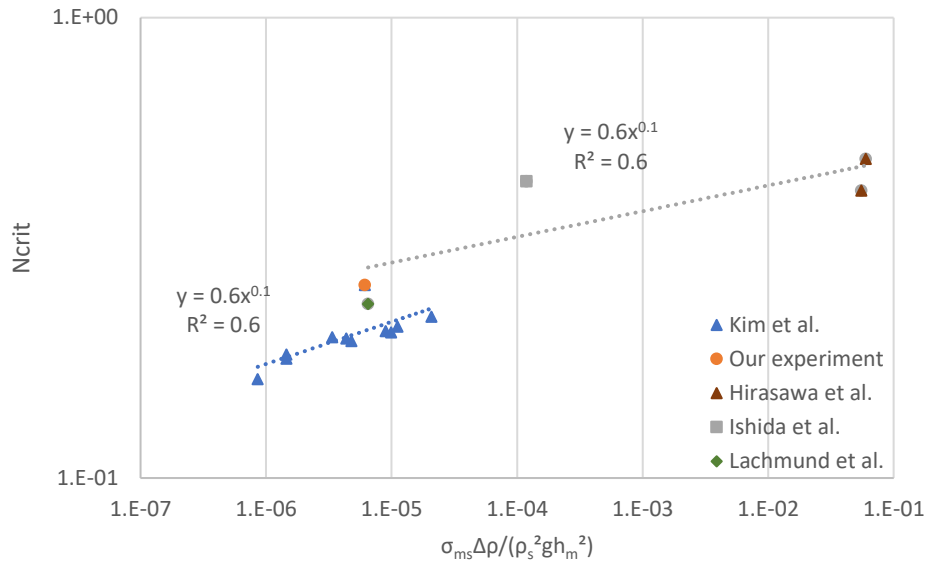


Figure 9.3: Fit of the critical modified Froude number with the correlation (9.4) for our experiment and the experiment of Kim et al. [40], Lachmund et al. [8], Ishida et al. [9], Hirasawa et al. [99].

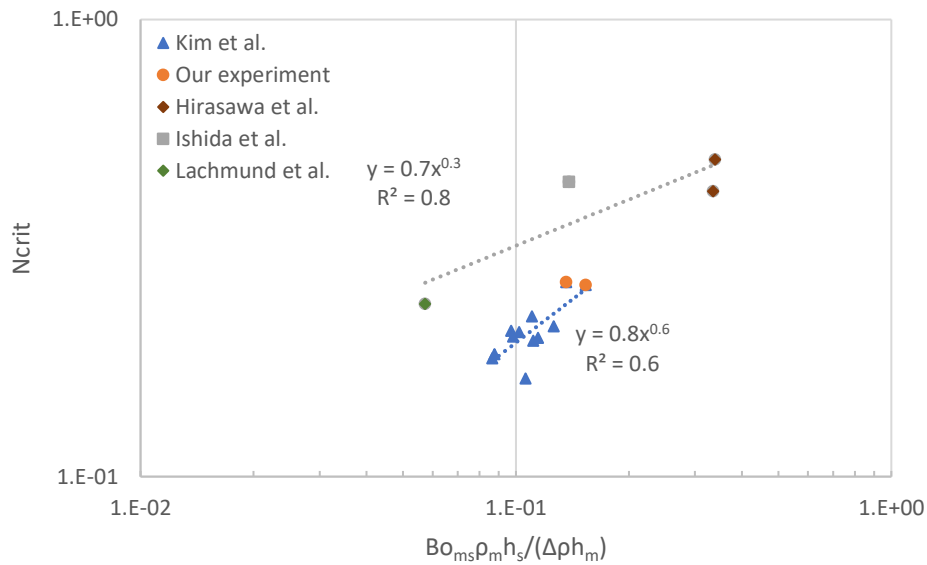


Figure 9.4: Fit of the critical modified Froude number with the correlation (9.4) (9.5) for our experiment and the experiment of Kim et al. [40], Lachmund et al. [8], Ishida et al. [9], Hirasawa et al. [99].

9.2 PREDICTION OF THE SHERWOOD NUMBER

9.2.1 Liquid metal experiments

Now, we will try to fit the first mass transfer regime of the liquid metal results of [9] and [99] with the correlations of the Sherwood number assuming a Nusselt profile in the slag layer already used with water experiments in 8.1.2. Depending on the choice of the formulation two correlations can be established to determine the Sherwood number as a function of the Schmidt and the modified Froude number

$$Sh_m^{NO} = a_2 \left(\frac{h_s m Ar}{h_m 16} \right)^{1/2} Sc_m^{1/2} N + b_2 \left(\frac{Ar}{16} \right)^{1/3} Sc_m^{1/3} N^{2/3}, \quad (9.11)$$

$$Sh_m^{NO-KY} = a_3 \left(\frac{h_s m Ar}{h_m 16} \right)^{1/2} Sc_m^{1/2} N + b_3 \left(\frac{Ar}{16} \right)^{1/2} Sc_m^{1/3} N, \quad (9.12)$$

where a_2 , b_2 , a_3 and b_3 are numerical constants determined from the experiments. From Figure 9.5, we can see that the results of [9] are better fitted with the correlations (9.11) and (9.12) corresponding to a Nusselt profile in the slag phase respectively without and with a turbulent boundary layer following Kader & Yaglom [94]. Following the correlation (9.11) corresponding to a Nusselt profile in the slag layer we fit the results of [9] to obtain the following correlation

$$Sh_{m,exp3}^{NO} = 0.18 \left(\frac{h_s m Ar}{h_m 16} \right)^{1/2} Sc_m^{1/2} N + 4.7 \cdot 10^{-6} \left(\frac{Ar}{16} \right)^{1/3} Sc_m^{1/3} N^{2/3} \quad (9.13)$$

Now, from Figure 9.6, we can see that the results of [99] do not present real abrupt increase in the Sherwood number in the steel equivalent phase between the different mass transfer regimes. We can also note that the correlations (9.11) and (9.12) overestimate the results of [99]. Following the correlation corresponding to a Nusselt profile in the slag phase, we fit the results of [99] to obtain the following correlation

$$Sh_{m,exp4}^{NO} = 0.21 \left(\frac{h_s m Ar}{h_m 16} \right)^{1/2} Sc_m^{1/2} N + 4.6 \cdot 10^{-6} \left(\frac{Ar}{16} \right)^{1/3} Sc_m^{1/3} N^{2/3} \quad (9.14)$$

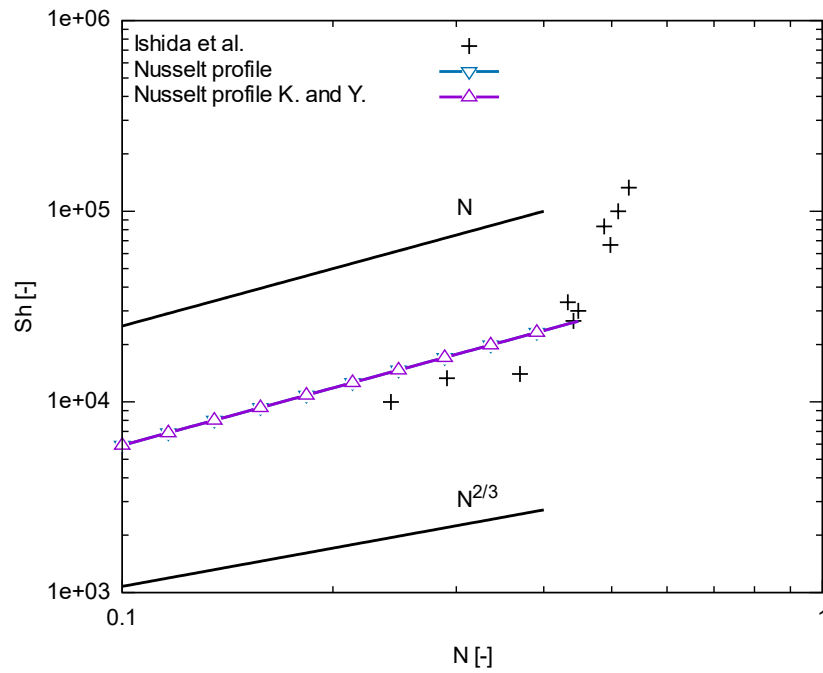


Figure 9.5: Sherwood number in the steel equivalent phase as a function of the modified Froude number for the results of Ishida et al. [9] fitted with correlations (9.11) and (9.12).

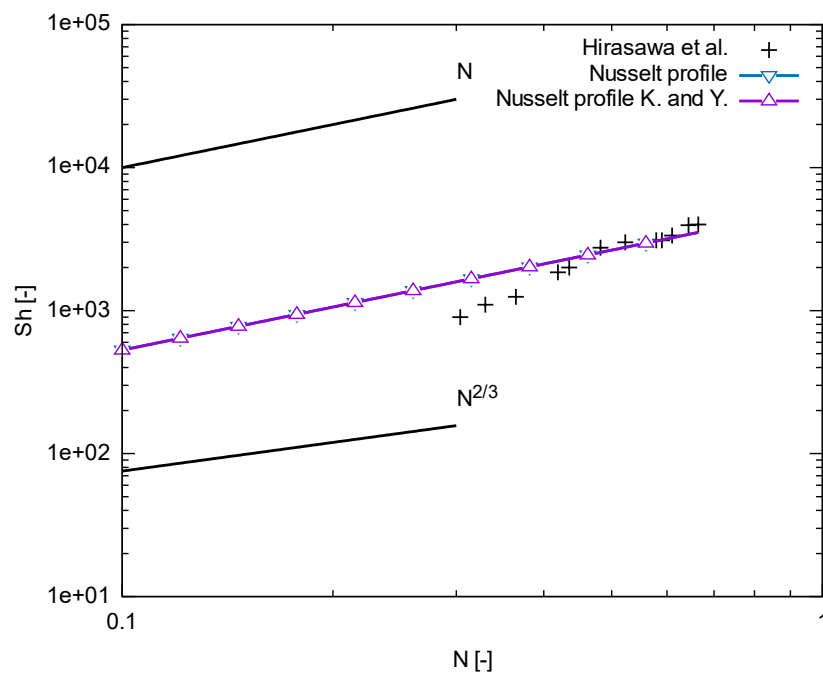


Figure 9.6: Sherwood number in the steel equivalent phase as a function of the modified Froude number for the results of Hirasawa et al. [99] fitted with correlations (9.11) and (9.12).

We will try now to use the following correlation (9.15) which was established in 8.1.2 from a fit of our water experimental results to predict the results of [9] and [99].

$$Sh_{m,exp1}^{NO} = 6.8 \cdot 10^{-2} \left(\frac{h_s m Ar}{h_m 16} \right)^{1/2} Sc_m^{1/2} N + 7.1 \cdot 10^{-3} \left(\frac{Ar}{16} \right)^{1/3} Sc_m^{1/3} N^{2/3} \quad (9.15)$$

From the results of Figure 9.7, we can see that the fit with the correlation (9.15) corresponding to the correlation of a Nusselt profile in the oil phase established from our results gives underestimated prediction of the Sherwood number compared to the results of [9]. We can note that because of the expression of the fit we are not able to reproduce the mass transfer regime change.

Now, in Figure 9.8 we try to fit the results of [99] with the correlation (9.15) and we can see that it gives also underestimated prediction of the Sherwood number compare to the results of [99]. As the results of [99] do not present an abrupt increase of the Sherwood number, the fit with the correlation (9.15) gives a relatively good prediction throughout the entire modified Froude range.

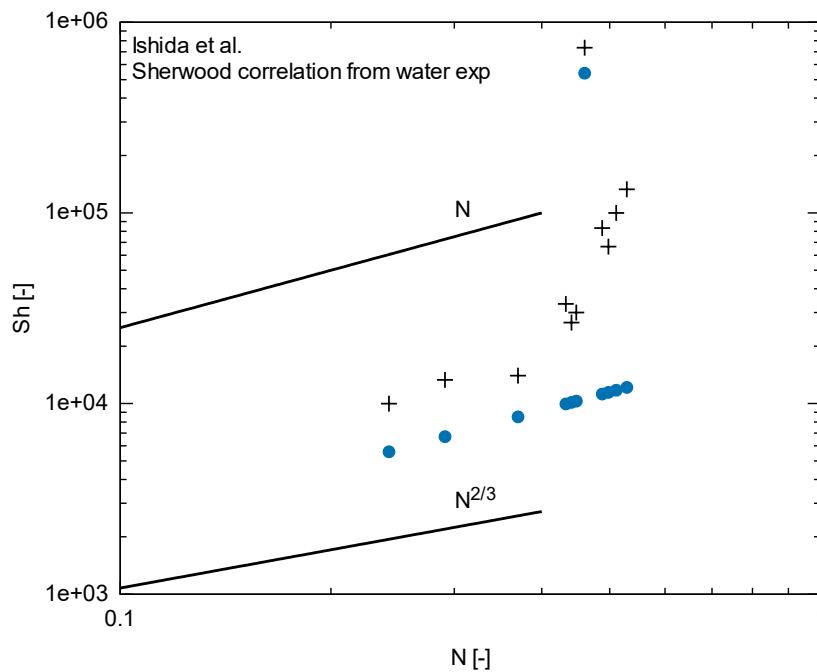


Figure 9.7: Sherwood number in the steel equivalent phase as a function of the modified Froude number for the results of Ishida et al. [9] fitted with correlation (9.15) corresponding to a Nusselt profile in the slag phase established from our water experiment.

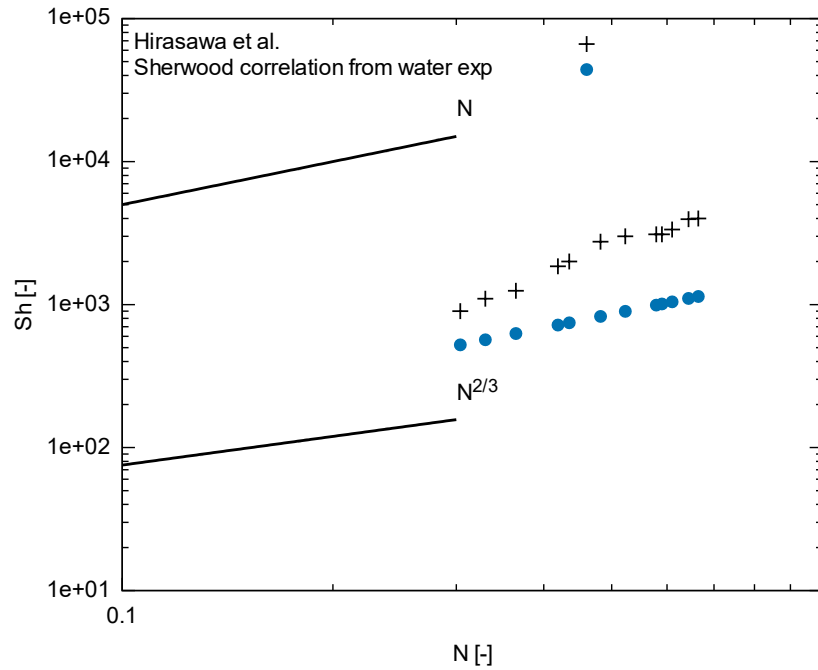


Figure 9.8: Sherwood number in the steel equivalent phase as a function of the modified Froude number for the results of Hirasawa et al. [99] fitted with correlation (9.15) corresponding to a Nusselt profile in the slag phase established from our water experiment.

9.2.2 Industrial ladle experiment

We will now proceed in a similar way than previously but this time with the results of [8] obtained with an industrial ladle. The main characteristics of the ladle can be found in Table 9.1. We first try to fit the Sherwood number in the steel phase of [8] assuming a Nusselt profile in the slag layer with the correlations (9.11) and (9.12) in Figure 9.9. We observe similar behaviour of the results than the one of [9] and so the correlation (9.11) and (9.12) give similar predictions of the results of [8]. Fitting the results of [8] with the correlation (9.11) considering a Nusselt profile in the slag layer, the following correlation can be established:

$$Sh_{m,il}^{NO} = 0.41 \left(\frac{h_s m Ar}{h_m 16} \right)^{1/2} Sc_m^{1/2} N + 4.6 \cdot 10^{-6} \left(\frac{Ar}{16} \right)^{1/3} Sc_m^{1/3} N^{2/3} \quad (9.16)$$

Now we use the correlation (9.15) which was established in 8.1.2 from a fit of our water experimental results to predict the results of [8] in Figure 9.10. From the results of Figure 9.10, we can see that the fit with the correlation (9.15) gives once again underestimated prediction of the Sherwood number compared to the results of [8].

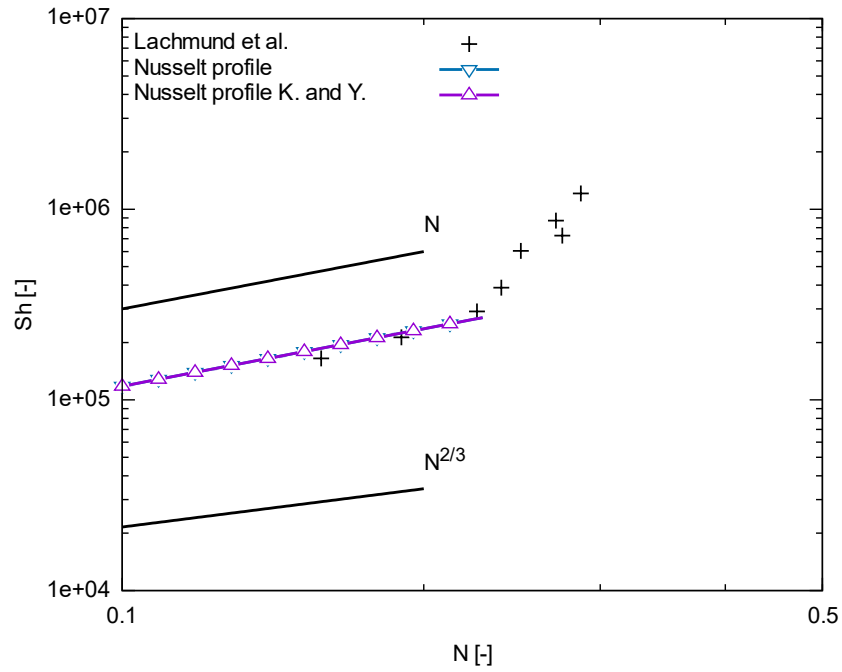


Figure 9.9: Sherwood number in the steel phase as a function of the modified Froude number for the results of Lachmund et al. [8] fitted with correlations (9.11) and (9.12).

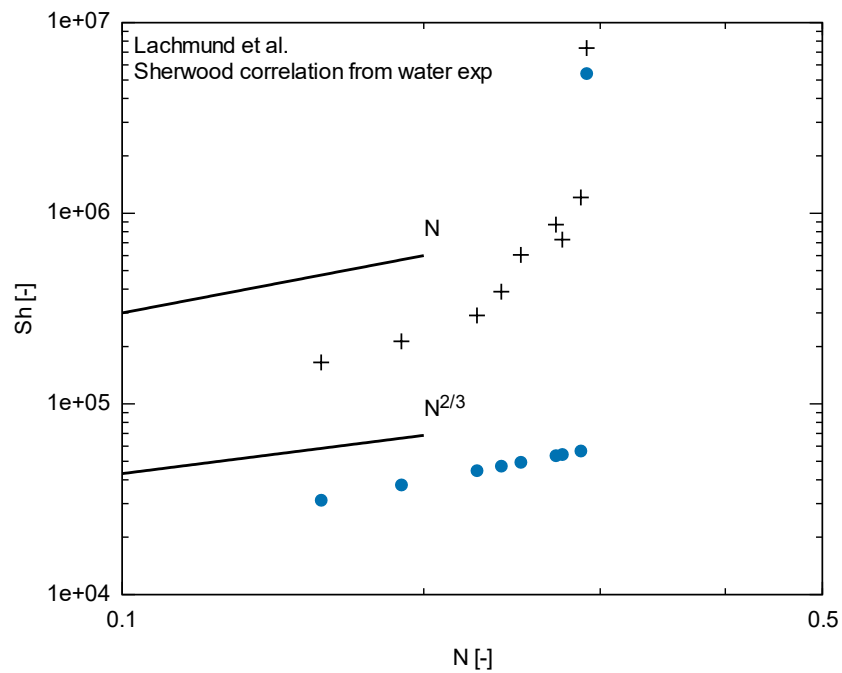


Figure 9.10: Sherwood number in the steel phase as a function of the modified Froude number for the results of Lachmund et al. [8] fitted with correlation (9.15) corresponding to a Nusselt profile in the slag phase established from our water experiment.

9.3 SUMMARY

In this chapter, we have seen that for both the water and liquid metal experiments different mass transfer regimes could be observed. From the results, we observed an important dispersion of the Sherwood number as a function of the modified Froude number between all the experiments. As we have seen the size of the ladle of the experiment is an important parameter to determine the value of the Sherwood number.

Then assuming that the critical modified Froude number at which the transition of the mass transfer regime corresponds to the start of the fragmentation of the slag layer into slag droplets we have seen that the correlation (9.4) could be used to almost superpose the results for both water and liquid metal experiments.

Finally, we have roughly predicted the Sherwood number for the first mass transfer regime using the correlations (9.11) and (9.12). Then, we have tried to use the correlation (9.15) established from a fit of our water experimental results. It gives a rough estimation of the Sherwood number in the steel equivalent phase but has a tendency to underestimate the experimental results of the liquid metal experiments especially for the industrial ladle case. More mass transfer measurement together with visual observations with water and liquid metal experiments should be done in order to increase the precision of the correlation and the range of application of both the critical modified Froude number and the correlation of the Sherwood number.

10 CONCLUSION AND PERSPECTIVES

In order to obtain a more precise description of the different phenomena involved in the mass transfer between steel and slag in an industrial gas stirred ladle, we have established in this dissertation a reduced scale water experiment together with its DNS. In addition, correlations have been established from phenomenological analysis to predict both the open eye and the fragmentation of the slag layer and also to estimate the mass transfer coefficient. Both the hydrodynamic and the mass transfer characterization have been done using experimental and numerical methods. To verify the validity of the obtained results in the case of an industrial ladle, we compared our results with water and liquid metal experiments available in the literature.

The first part of this dissertation is devoted to the hydrodynamic characterization of a water scaled model based on the study of Kim & Fruehan [32] using air, water and oil to reproduce the behaviour of an industrial ladle. From the face view of the experiment, we have observed that more oil droplets can be identified in the water phase when the air flow rate is increased and also that at a constant air flow rate more oil droplets were formed when the oil volume is increased. In addition to the normal oil droplets, we have also observed water encapsulated in oil films with a bubble-like shape and an oil layer at their top that we called anti-bubbles. The formation of these anti-bubbles seems to precede the formation of the regular oil droplets. At high gas flow rate, a water-oil emulsion was formed on almost the entire width of the ladle. Then from the top view of the experiment, we have seen that the open-eye area increases with the air flow rate while at a constant air flow rate an increase in the oil volume leads to a smaller open-eye area. On the other hand, the variation in the size of the injection diameter has only a small influence on the open-eye area and also on the critical gas flow rate at which occur the fragmentation of the oil layer. Furthermore, it seems that the open eye area for each class of experiments could be relatively well predicted with the correlation of Krishnapisharody & Irons [22] and the correlation established in this study in chapter 2. Nevertheless, the slope of the open eye area as a function of the gas flow rate is higher for the water experiments than for liquid metal experiments.

Besides, a three-phase numerical simulation was built with the Basilisk Free Software library to simulate the three-phase flow configuration of the water experiment. To respect the fact that the sum of all the fluid fractions should be between zero and one we normalized each fluid fractions by the sum of the fluid fractions. We also used a decomposition of the physical surface tension or interfacial tension into phase-specific surface or interfacial tension. The validity of the three-phase implementation was tested with the simulation of the spreading of an oil lens at an air-water interface. Two cases were successfully simulated the partial equilibrium of an oil lens and the total spreading of an oil lens. By comparing the results of the simulation at different air flow rates we have seen that much more oil droplets and a bigger open eye could be observed at a high air flow rate than at a low air flow rate. Furthermore, similar values of the critical air flow rate for the fragmentation of the oil layer were observed in the simulation and the experiment. From the results of the top view, we have seen that the open eye area has more fluctuations at a high air flow rate than at a low air flow rate. We have seen that the transient breaking of the oil layer at an early time of the simulation is responsible for most of the large oil droplets observed in our simulations. Looking at the time-averaged results we could observe that the vertical velocity follows a Gaussian function with a maximum above the centre of the injection orifice. As we get closer to the oil layer the vertical velocity decreases. On the border of the open eye, negative values of vertical velocity indicate the presence of a recirculation loop.

Finally, the comparison of the average experimental and numerical open eye area has shown that there is a tendency of the numerical results to overestimates the experimental open eye area, especially at a low air flow rate.

In the second part of this dissertation, we have detailed our experimental procedure based on the study of [32] to measure the mass transfer of thymol from the water to the oil phase. We considered for the mass transfer regime a free surface or a rigid surface case depending on the magnitude of the interfacial velocity U_I compared to the shear rate ω_p . Then, by an interpolation of these two limiting cases, we established correlations of the Sherwood number as a function of the modified Froude number and Schmidt number depending on the flow regime considered in the oil layer. Three flow regimes can be considered in the oil layer a laminar boundary layer, a parabolic profile and a turbulent regime. In this dissertation, only the Nusselt or parabolic profile in the oil phase has been considered. In this case, the following correlation of the Sherwood number in the steel equivalent phase has been established

$$Sh_m^{NO} = am^{1/2}Sc_m^{1/2}Re_m(h_s/h_m)^{1/2} + bSc_m^{1/3}Re_m^c, \quad (10.1)$$

where a and b are numerical constants determined from the experiments, $m = \mu_m/\mu_s$ is the viscosity ratio and m and s are the indices for respectively the steel and the slag equivalent phase, h_s and h_m are the height of respectively the slag end steel equivalent phase, the Reynolds number is expressed with $Re_m = UL_x/4v_m$ with L_x the horizontal size of the ladle, the Schmidt number is $Sc_m = v_m/D_m$ and $c = 2/3$ or $c = 1$ depending on whether we consider or not the turbulent boundary layer formulation of Kader & Yaglom [94] in the water phase. The difficulty to use the correlation (10.1) is to determine the characteristic velocity U . In this dissertation we used a scaling of the velocity to have an estimation directly from the injected gas flow rate value with $U = g^{2/5}Q^{1/5}$. Considering the Archimedes number given by $Ar = gL_x^3\rho_m(\rho_m - \rho_g)/\mu_m^2$ and that $L_x \sim h_m$ and neglecting the gas density ρ_g compared to the liquid steel one $\rho_g \ll \rho_m$ we could rewrite the Reynolds number to obtain $Re = (Ar/16)^{1/2}N$ where the modified Froude number is given by $N = [Q/(g^{1/2}h_m^{5/2})]^{1/5}$. This allowed us to rewrite (10.1) to obtain

$$Sh_w^{NO} = a\left(\frac{h_s m Ar}{h_m 16}\right)^{1/2} Sc_m^{1/2} N + b_2 \left(\frac{Ar}{16}\right)^{1/3} Sc_m^{1/3} N^c \quad (10.2)$$

From our experimental measurements, we have seen that the continuous formation of oil droplets in the water phase could be correlated with the different mass transfer regimes observed experimentally. Furthermore, our experimental mass transfer results show a small influence of the injection diameter size on the different mass transfer regimes. Considering a Nusselt profile in the oil layer, the correlation (6.79) predicts with a reasonable agreement our experimental results for the first mass transfer regime. In most of the mass transfer experiments in the literature, a new mass transfer regime occurs when the gas flow rate increases over a critical value. We have seen that the volume of the steel equivalent phase and the corresponding gas flow rate necessary to stir the ladle have an important effect on the Sherwood number leading to larger Sherwood numbers for the experiments with large ladle size. Before the critical gas flow rate, the Sherwood number of almost all the liquid metal experiments could be roughly predicted using the correlation (6.79). Nevertheless, we have seen that using the correlation (6.79) to fit our water experimental results and then try to predict the Sherwood number for the liquid metal experiments gives an underestimated prediction of the Sherwood number. It could be an interesting perspective to compare the results obtained with the correlations considered in this study with correlations established for a turbulent flow regime in the slag layer.

Later on, we have added a layer to our numerical simulation to be able to advect and diffuse chemical species in a multiphase flow context using the VOF method. The advection of the chemical species is done using the VOF scheme, and the diffusion is done only between the water and oil phase neglecting the influence of the air phase. Moreover, to reproduce a similar concentration jump at the interface than in the experiment, we imposed a Dirichlet condition on the interface. From the numerical results obtained at a much lower Schmidt number than in the experiment, we reproduced the global mass transfer configuration of the water experiment where the variation of the concentration of tracer was observed essentially on the concentration boundary layer at the water-oil interface. We could obtain mesh convergence at the low Schmidt number values for an air flow rate $Q = 0.6l/min$. Indeed, the results showed that for a Schmidt number value $Sc_m = 40$ the mesh resolutions considered in this study might be still too coarse to resolve sufficiently the concentration boundary layer, especially for the high air flow rate simulation. Furthermore, considering the limited amount of numerical simulations that we did we were not able to clearly reproduce abrupt increase of the Sherwood number as observed experimentally. Then the extrapolation of the Sherwood number as a function of the modified Froude number obtained from our numerical results gave an overestimated prediction of our experimental results but with nearly the same slope. This is especially true for the highest value of the air flow rate simulated $Q = 5.5l/min$ where we observed a factor ten of difference between the extrapolation of the numerical results and the experimental results. While we observed only a factor three of difference between the numerical and experimental results for the lowest air flow rate simulated $Q = 0.6l/min$.

To improve the knowledge obtained from this dissertation and considering the recent development of the Particle Image Velocimetry combined with shadowgraphy methods in bubbly flow (Sathe *et al.* [112], Hessenkemper & Ziegenhein [113]) possible characterization of the velocity in the water phase could further improve the validation of our numerical model. It might also be used to characterize the oil layer velocity, the velocity and size distribution of the oil droplets.

A good step toward the understanding of the behaviour of the flow and the mass transfer in the industrial ladle case would be to simultaneously measure the mass transfer and record visual observation with liquid metals experiments. The experiment should respect as closely as possible the same density and viscosity ratio and the same aspect ratio of the height of the bath of steel and slag equivalent phase than in the industrial configuration. Furthermore, visual observations with X-ray (Liu *et al.* [114]) of liquid metal experiments could give a deeper knowledge of the fragmentation phenomena. In addition, open eye area measurement in the case of liquid metal experiments would allow enriching the available data and further test improve the correlation used in this study. Moreover, the comparison with water experiments results could confirm that the phenomena resulting in the fragmentation of the slag layer into slag droplets are occurring in the same manner with water and liquid metal experiments. Also, the numerical model established in this dissertation could be used to simulate this liquid metal experiment allowing to validate further our numerical model. If an agreement for the main hydrodynamic characteristics between the experimental and numerical results can be found it would open the way for the simulation of a full industrial ladle configuration.

Concerning our numerical model, the three-phase implementation could be further tested and improved especially by introducing a more careful treatment of the cells containing three VOF tracers. For the mass transfer, a good first step has been done in this study using several assumptions the mass transfer configuration of the water experiment has been roughly reproduced. But as we have seen it cannot be realistically used at the high Schmidt number corresponding to the experimental condition. Indeed, it would require an extremely important computational resource to resolve sufficiently the concentration boundary layer in this case. To circumvent this major issue the use of a subgrid-scale model (Weiner & Bothe [110], Koynov *et al.* [105]) to resolve the concentration boundary layer has a high potential to satisfactorily simulate the mass transfer together with the hydrodynamic in the water experiment configuration with reasonable mesh resolution.

11 APPENDICES

11.1 ASSUMPTIONS NOT CONSIDERED IN THE PHENOMENOLOGICAL ANALYSIS

11.1.1 Water laminar boundary layer

A laminar boundary layer theory for the water gives

$$\delta_{m,w} \sim (\nu_w d / U_0)^{1/2}, \quad (11.1)$$

where $\omega_w = U_0 / \delta_w$ we get

$$\omega_w \sim U_0^{3/2} / (\nu_w d)^{1/2}. \quad (11.2)$$

We can then obtain

$$u_l = m^{1/3} n^{1/3} U_0, \quad (11.3)$$

and get

$$\frac{K_{w,l}}{U_0} = (m r)^{1/6} Sc^{-1/2} Re^{-1/2}, \quad (11.4)$$

where $Re = U_0 d / \nu_w$ for the free surface case. We get for the rigid surface case

$$\frac{K_{w,\omega}}{U_0} = Sc^{-2/3} Re^{-1/2}. \quad (11.5)$$

Another way to express this result is with the Sherwood number for thymol in water

$$Sh := \frac{dK_w}{D} \sim cSc^{1/3} Re^{1/2} \quad (11.6)$$

We find this result in Weiner et al. [115] equation (2) apparently due to Frössling.

11.1.2 Laminar Couette profile in the water

We can do simpler or more inertial

$$\omega_w = \frac{U_{0,w}}{d}, \quad (11.7)$$

if $d = L_z$ it is only a laminar Couette flow in the water. From (6.60) we get

$$K_{w,\omega} = Sc^{-2/3} Re^{-2/3} U_{0,w}. \quad (11.8)$$

This is highly improbable since the Reynold number in the water is too high.

11.1.3 Highly unstationary interface case

In the following, we are omitting the w indices. The boundary layer profile can be built as diffusion time

$$\tau_\delta \sim \delta_m^2/D \quad (11.9)$$

If we can show that this diffusion time is small compared to other characteristic time it is justified to neglect the temporal derivative in (6.35). Moreover, we have $K = D/\delta$ so, $\delta = D/K$ and so in the free surface case we have

$$\tau_\delta \sim D/K_{w,l}^2, \quad (11.10)$$

$$\tau_\delta \sim (D/U_0^2)(m r)^{-1/6} Sc^{1/2} Re^{1/2}. \quad (11.11)$$

In the rigid surface case, we have

$$\tau_\delta \sim D/K_{w,\omega}^2, \quad (11.12)$$

$$\tau_\delta \sim (D/U_0^2) Sc^{2/3} Re^{1/2}, \quad (11.13)$$

For a highly capillary oscillating interface of period $\omega_c \sim (\sigma k^3/\rho)^{1/2}$ we have

$$\begin{aligned} \tau_\delta \omega_c &\sim (D^2 \sigma / (\lambda^3 \rho U_0^4))^{1/2} Sc^{2/3} Re^{1/2} \sim (D / (\lambda U_0)) (\sigma / (\lambda \rho U_0^2))^{1/2} Sc^{2/3} Re^{1/2} \\ &\sim Pe^{-1} We^{-1/2} Pe^{1/2} Sc^{1/6}, \end{aligned} \quad (11.14)$$

and so, we can write

$$\tau_\delta \omega_c \sim Sc^{-1/3} Re^{-1/2} We^{-1/2} \quad (11.15)$$

With $Sc \gg 1$, $Re, We > 1$, the capillary oscillations have longer period than the establishing time of the boundary layer, so the stationary boundary layer theory stays valid. The case $We < 1$ can occur when the capillary waves are forced by other waves, for example, the gravity waves. We should do a complete computation of all the instabilities Helmholtz instability and gravity waves.

11.2 NUMERICAL RESULTS- MASS TRANSFER CHARACTERIZATION

11.2.1 Time evolution of the Sherwood number

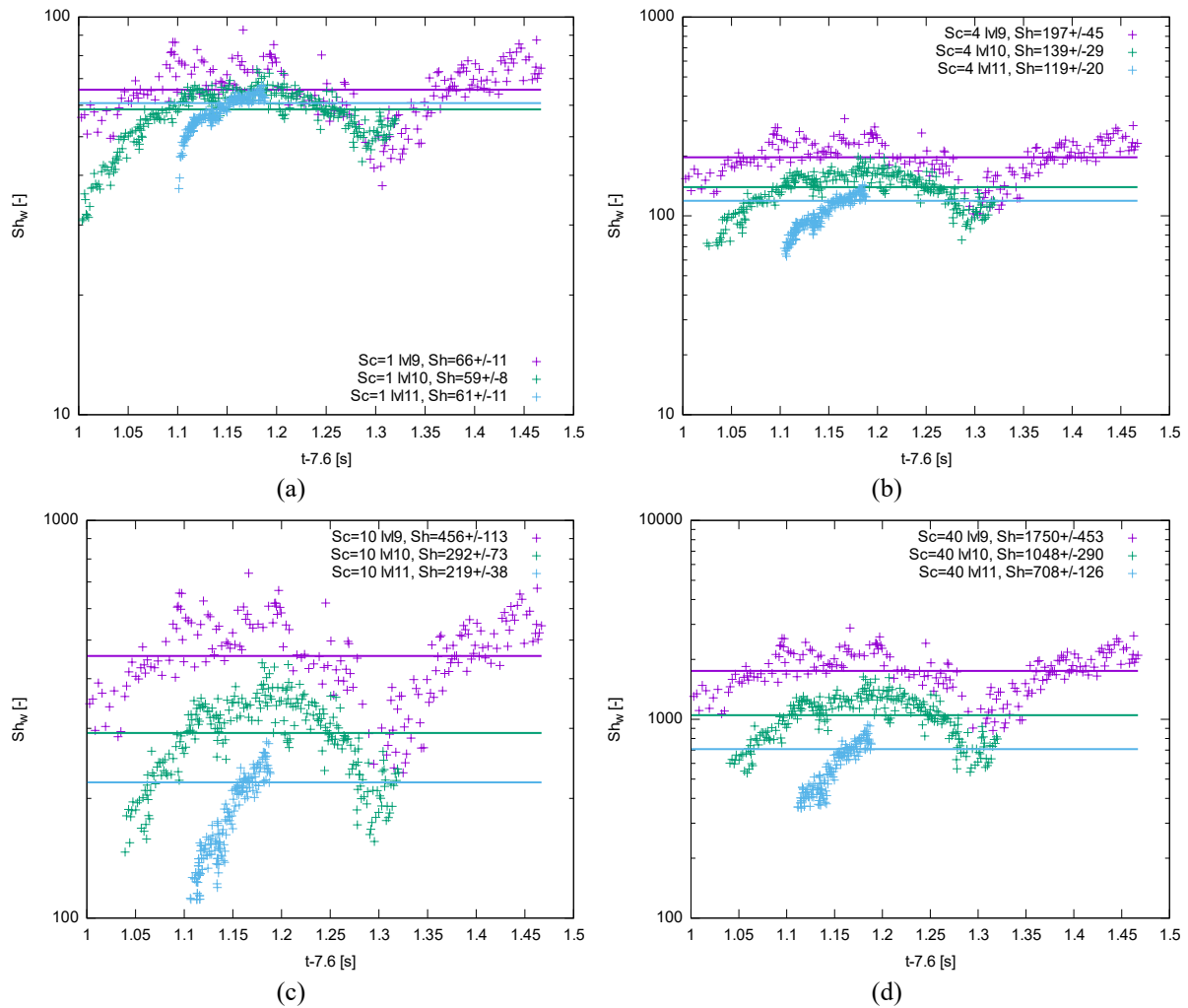


Figure 11.1: Time evolution of the Sherwood number in water with different mesh resolution at a fixed air flow rate of $Q = 2.5 \text{ l/min}$. (a) $Sc_w = 1$; (b) $Sc_w = 4$; (c) $Sc_w = 10$; (d) $Sc_w = 40$.

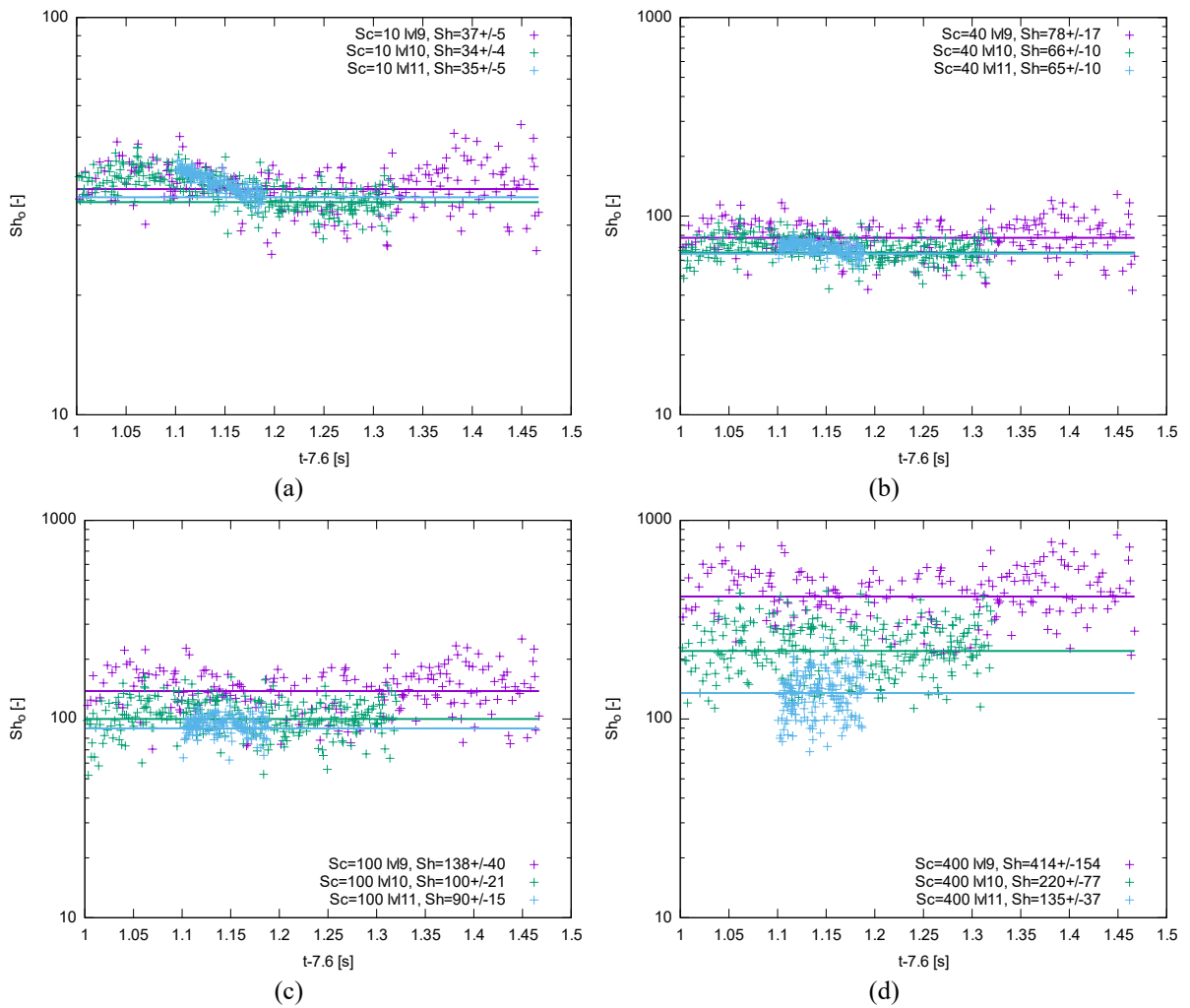


Figure 11.2: Time evolution of the Sherwood number in oil with different mesh resolution at a fixed air flow rate of $Q = 2.5\text{l/min}$. (a) $Sc_o = 10$; (b) $Sc_o = 40$; (c) $Sc_o = 100$; (d) $Sc_o = 400$.

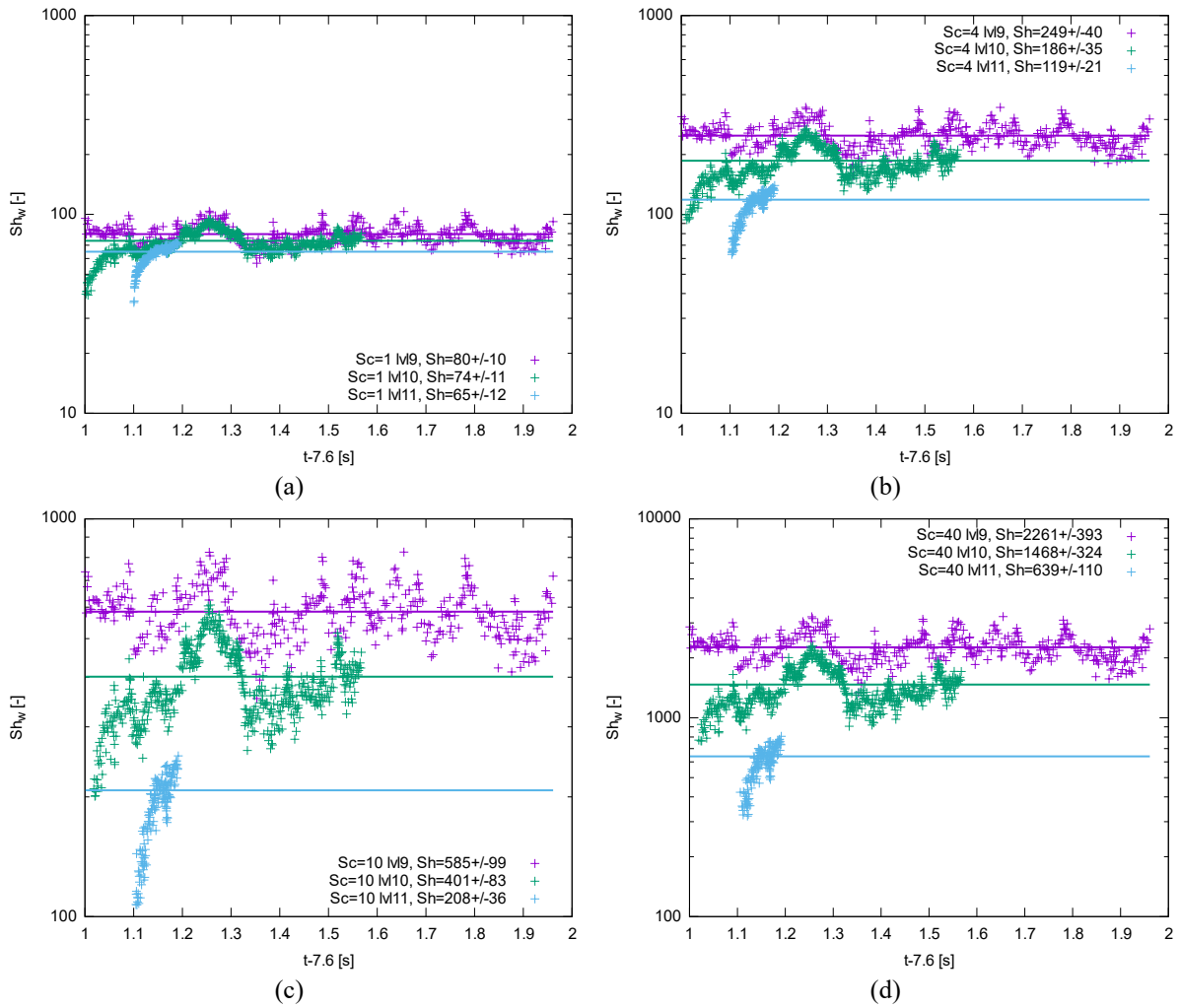


Figure 11.3: Time evolution of the Sherwood number in water with different mesh resolution at a fixed air flow rate of $Q = 3.5\text{l/min}$. (a) $Sc_w = 1$; (b) $Sc_w = 4$; (c) $Sc_w = 10$; (d) $Sc_w = 40$.

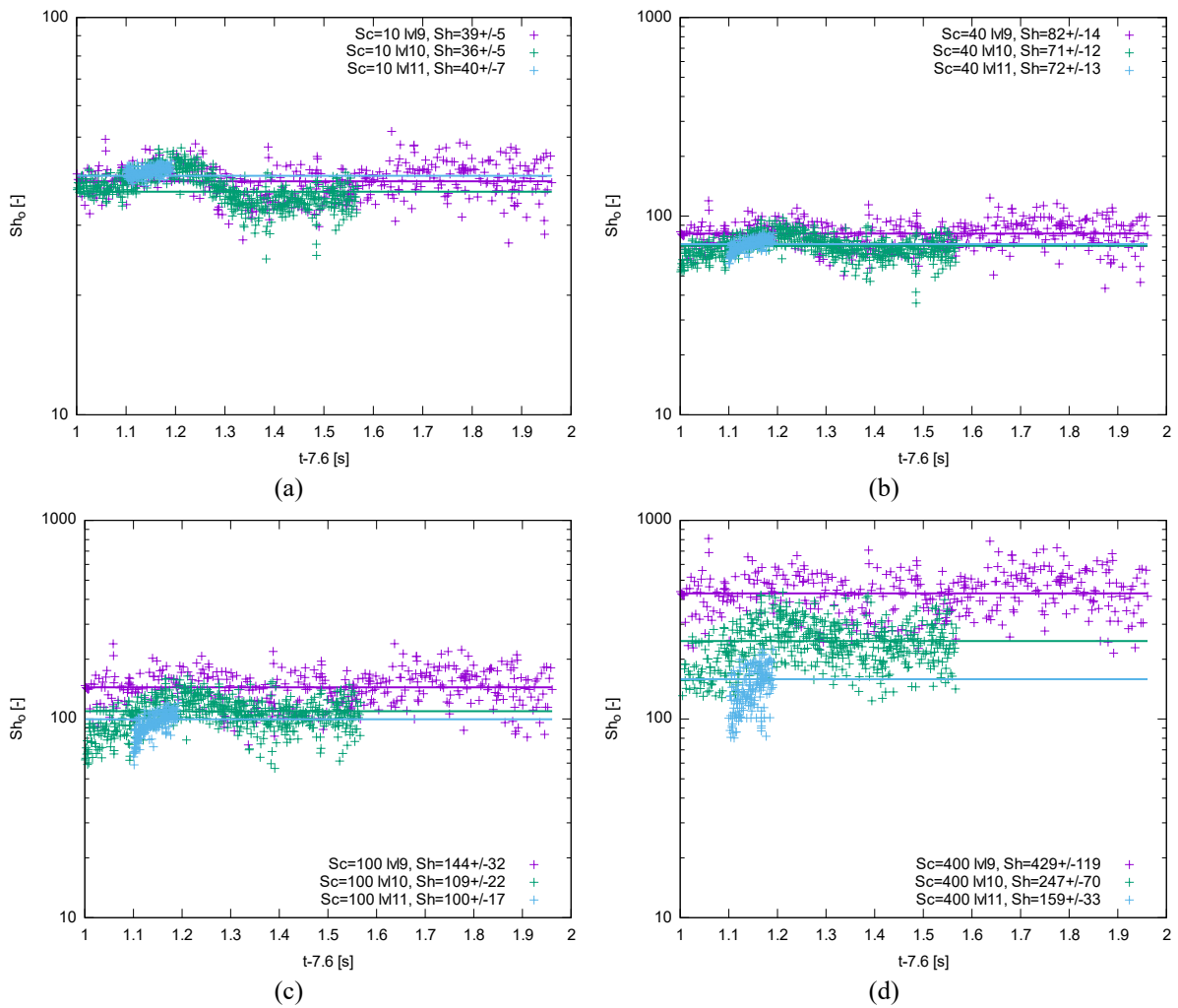


Figure 11.4: Time evolution of the Sherwood number in oil with different mesh resolution at a fixed air flow rate of $Q = 3.5\text{l/min}$. (a) $Sc_o = 10$; (b) $Sc_o = 40$; (c) $Sc_o = 100$; (d) $Sc_o = 400$.

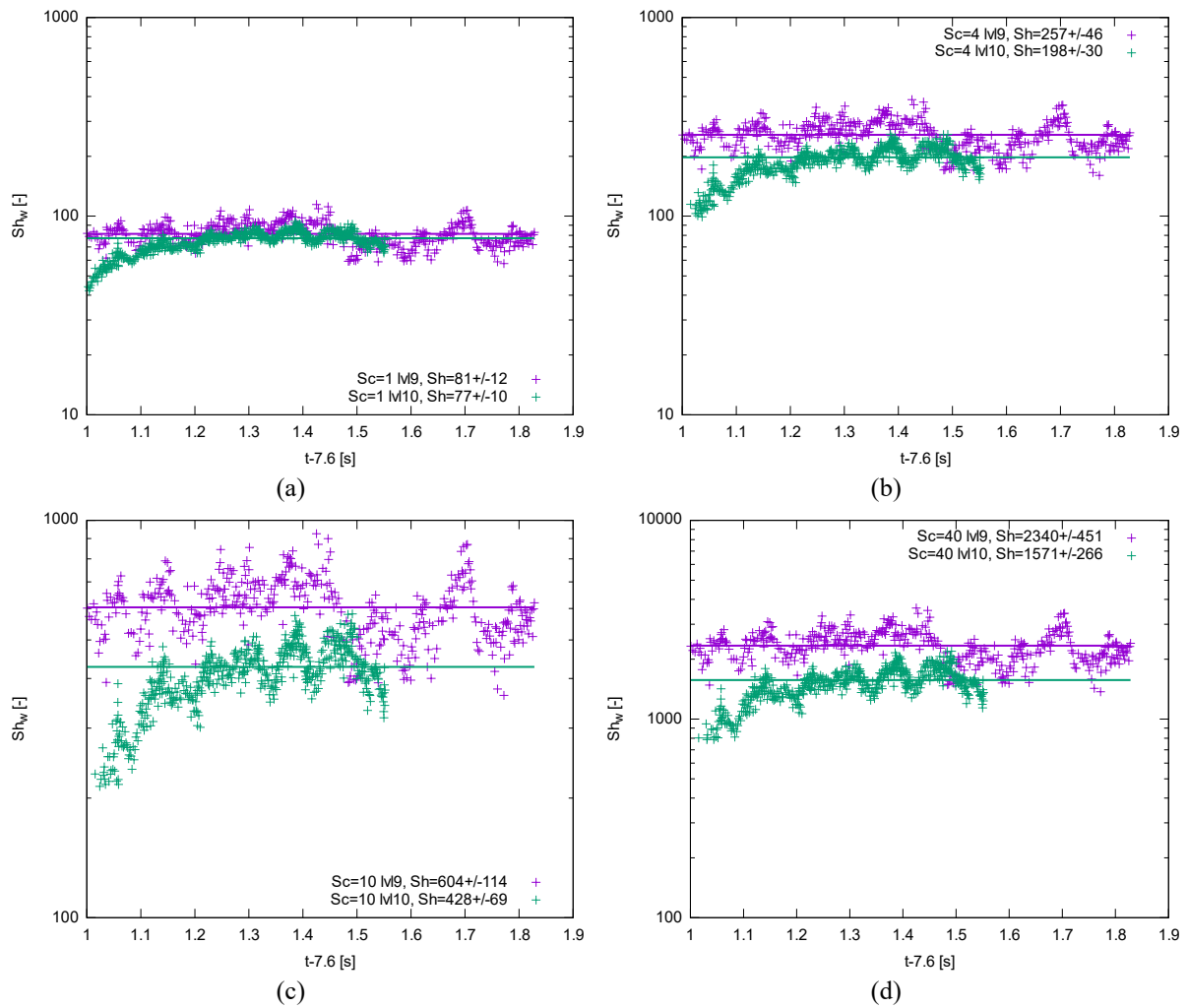


Figure 11.5: Time evolution of the Sherwood number in water with different mesh resolution at a fixed air flow rate of $Q = 4.5\text{ l/min}$. (a) $Sc_w = 1$; (b) $Sc_w = 4$; (c) $Sc_w = 10$; (d) $Sc_w = 40$.

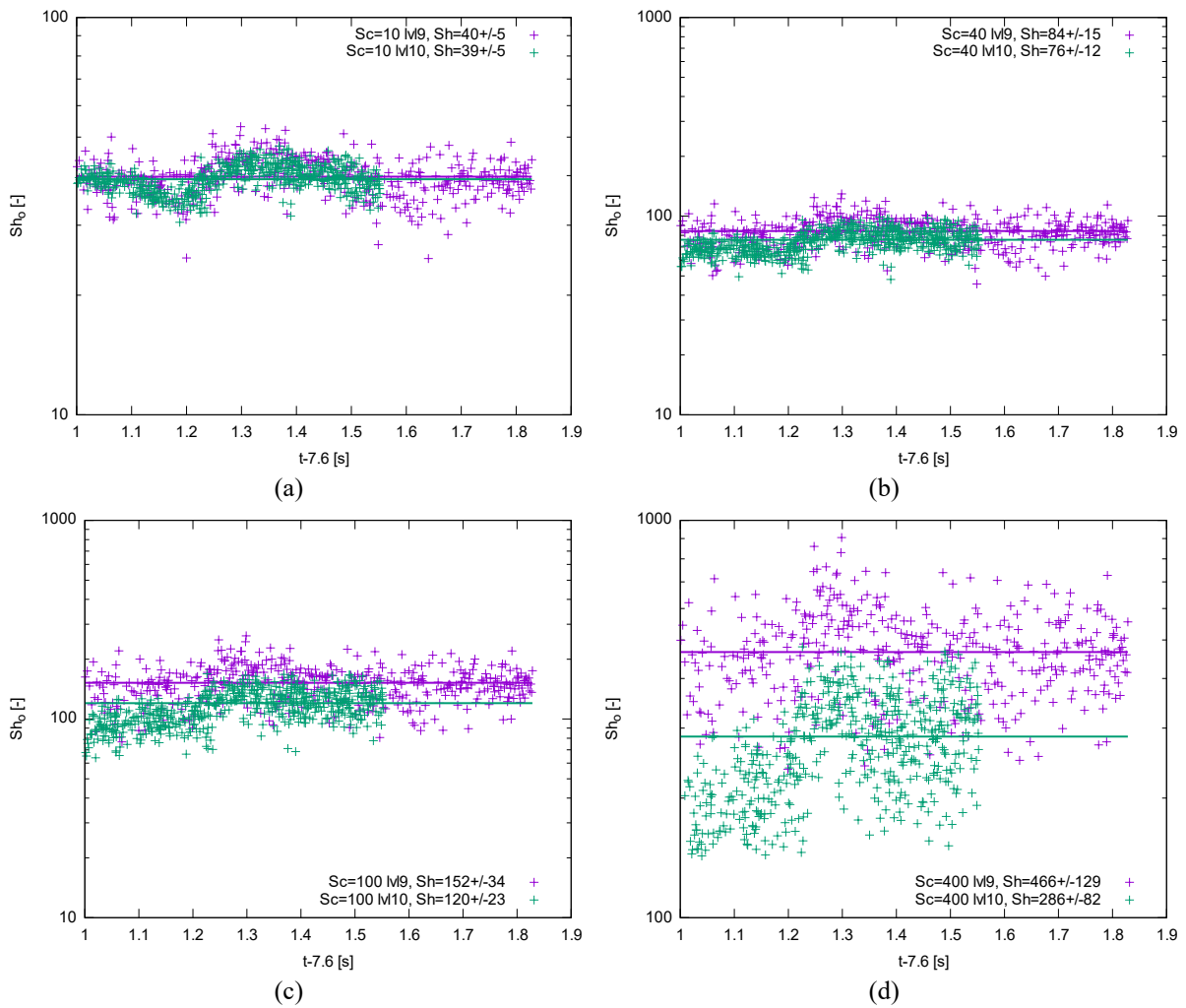


Figure 11.6: Time evolution of the Sherwood number in oil with different mesh resolution at a fixed air flow rate of $Q = 4.5\text{ l/min}$. (a) $Sc_o = 10$; (b) $Sc_o = 40$; (c) $Sc_o = 100$; (d) $Sc_o = 400$.

11.2.2 Time average Sherwood number

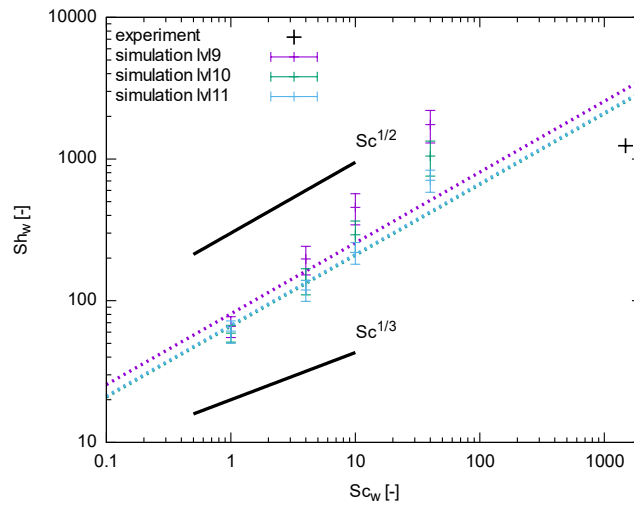


Figure 11.7: Fit of the numerical Sherwood number in water with standard deviation in function of the Schmidt number at an air flow rate $Q = 2.5$ l/min and for different maximum number of cells in one direction. The black cross represents our experimental result.

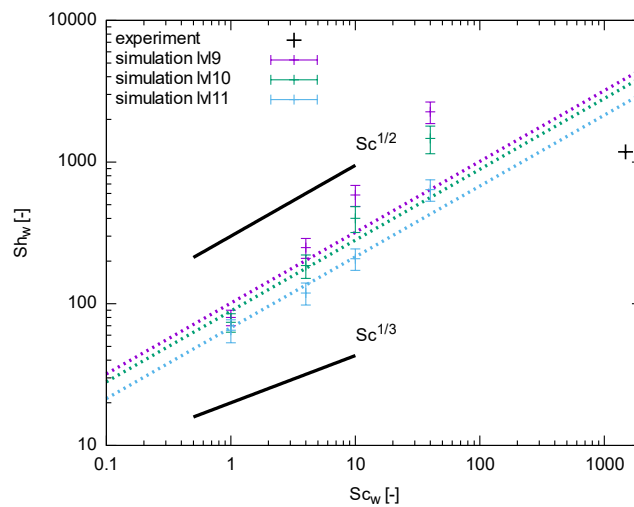


Figure 11.8: Fit of the numerical Sherwood number in water with standard deviation in function of the Schmidt number at an air flow rate $Q = 3.5$ l/min and for different maximum number of cells in one direction. The black cross represents our experimental result.

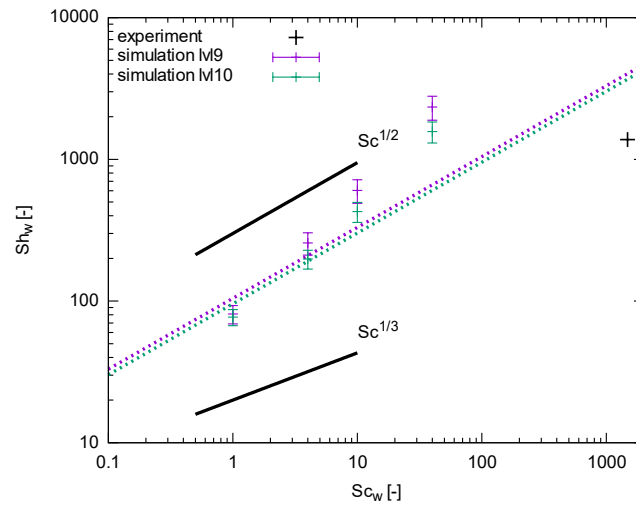


Figure 11.9: Fit of the numerical Sherwood number in water with standard deviation in function of the Schmidt number at an air flow rate $Q = 4.5$ l/min and for different maximum number of cells in one direction. The black cross represents our experimental result.

12 BIBLIOGRAPHY

- [1] R. I. Guthrie, "Fluid flows in metallurgy - friend or foe?" *Metallurgical and Materials Transactions B*, vol. 35, no. 3, pp. 417–437, 2004.
- [2] U. Siegenthaler and J. L. Sarmiento, "Atmospheric carbon dioxide and the ocean," *Nature*, vol. 365, no. 6442, pp. 119–125, 1993.
- [3] L. Deike, L. Lenain, and W. K. Melville, "Air entrainment by breaking waves," *Geophysical Research Letters*, vol. 44, no. 8, pp. 3779–3787, 2017.
- [4] J. Szekely, G. Carlsson, and L. Helle, *Ladle metallurgy*. Springer Science & Business Media, 2012.
- [5] Blisscommunication.com, "Overview of the steelmaking process," <https://www.worldsteel.org/about-steel.html>, 2016.
- [6] F. Richardson, "Drops and bubbles in extractive metallurgy," *Metallurgical Transactions*, vol. 2, no. 10, pp. 2747–2756, 1971.
- [7] P. Riboud and R. Vasse, "Désulfuration de l'acier en poche: synthèse des résultats théoriques et industriels," *Revue de métallurgie (Paris)*, vol. 82, no. 11, pp. 801–810, 1985.
- [8] H. Lachmund, Y. Xie, T. Buhles, and W. Pluschkell, "Slag emulsification during liquid steel desulphurisation by gas injection into the ladle," *steel research international*, vol. 74, no. 2, pp. 77–85, 2003.
- [9] J. Ishida, "Effects of stirring by argon gas injection on metallurgical reactions in secondary steelmaking," *Denki-Seiko (Electr. Furn. Steel)*, vol. 52, no. 1, pp. 2–8, 1981.
- [10] G. Tryggvason, R. Scardovelli, and S. Zaleski, *Direct numerical simulations of gas-liquid multiphase flows*. Cambridge University Press, 2011.
- [11] D. Deising, H. Marschall, and D. Bothe, "A unified single-field model framework for volume-of-fluid simulations of interfacial species transfer applied to bubbly flows," *Chemical Engineering Science*, vol. 139, pp. 173–195, 2016.
- [12] F. Gibou, R. Fedkiw, and S. Osher, "A review of level-set methods and some recent applications," *Journal of Computational Physics*, vol. 353, pp. 82–109, 2018.
- [13] I. V. Karlin, A. Ferrante, and H. C. Öttinger, "Perfect entropy functions of the lattice boltzmann method," *EPL (Europhysics Letters)*, vol. 47, no. 2, p. 182, 1999.
- [14] R. Van der Sman and S. Van der Graaf, "Diffuse interface model of surfactant adsorption onto flat and droplet interfaces," *Rheologica acta*, vol. 46, no. 1, pp. 3–11, 2006.
- [15] S. Popinet, "Gerris: a tree-based adaptive solver for the incompressible euler equations in complex geometries," *Journal of Computational Physics*, vol. 190, no. 2, pp. 572 – 600, 2003.
- [16] S. Popinet, "An accurate adaptive solver for surface-tension-driven interfacial flows," *Journal of Computational Physics*, vol. 228, no. 16, pp. 5838 – 5866, 2009.

- [17] K. Yonezawa and K. Schwerdtfeger, "Spout eyes formed by an emerging gas plume at the surface of a slag-covered metal melt," *Metallurgical and Materials Transactions B*, vol. 30, no. 3, pp. 411–418, 1999.
- [18] P. Valentin, C. Bruch, Y. Kyrlyenko, H. Köchner, and C. Dannert, "Influence of the stirring gas in a 170-t ladle on mixing phenomena—formation and on-line control of open-eye at an industrial steel plant," *steel research international*, vol. 80, no. 8, pp. 552–558, 2009.
- [19] L. Wu, P. Valentin, and D. Sichen, "Study of open eye formation in an argon stirred ladle," *steel research international*, vol. 81, no. 7, pp. 508–515, 2010.
- [20] B. Subagyo, G. A. I. GA *et al.*, "Spout eyes area correlation in ladle metallurgy," *ISIJ international*, vol. 43, no. 2, pp. 262–263, 2003.
- [21] M. Iguchi, K.-i. Miyamoto, S. Yamashita, D. Iguchi, and M. Zeze, "Spout eye area in ladle refining process," *ISIJ international*, vol. 44, no. 3, pp. 636–638, 2004.
- [22] K. Krishnapisharody and G. A. Irons, "Modeling of slag eye formation over a metal bath due to gas bubbling," *Metallurgical and Materials Transactions B*, vol. 37, no. 5, pp. 763–772, 2006.
- [23] K. Krishnapisharody and G. Irons, "A model for slag eyes in steel refining ladles covered with thick slag," *Metallurgical and Materials Transactions B*, vol. 46, no. 1, pp. 191–198, 2015.
- [24] M. A. Castello-Branco and K. Schwerdtfeger, "Large-scale measurements of the physical characteristics of round vertical bubble plumes in liquids," *Metallurgical and materials transactions B*, vol. 25, no. 3, pp. 359–371, 1994.
- [25] M. Peranandhanthan and D. Mazumdar, "Modeling of slag eye area in argon stirred ladles," *ISIJ international*, vol. 50, no. 11, pp. 1622–1631, 2010.
- [26] Z. Liu, L. Li, and B. Li, "Modeling of gas-steel-slag three-phase flow in ladle metallurgy: Part i. physical modeling," *ISIJ International*, vol. 57, no. 11, pp. 1971–1979, 2017.
- [27] Z. Lin and R. Guthrie, "Modeling of metallurgical emulsions," *Metallurgical and Materials Transactions B*, vol. 25, no. 6, pp. 855–864, 1994.
- [28] S. L. Feldbauer and A. Cramb, "Slag entrainment in the mold of a continuous caster," Ph.D. dissertation, thesis 1995, Carnegie Mellon University, Pittsburgh, 1995.
- [29] R. Hagemann, H. Heller, S. Lachmann, S. Seetharaman, and P. Scheller, "Slag entrainment in continuous casting and effect of interfacial tension," *Ironmaking & Steelmaking*, vol. 39, no. 7, pp. 508–513, 2012.
- [30] R. Hagemann, R. Schwarze, H. P. Heller, and P. R. Scheller, "Model investigations on the stability of the steel-slag interface in continuous-casting process," *Metallurgical and materials transactions B*, vol. 44, no. 1, pp. 80–90, 2013.
- [31] J. Savolainen, T. Fabritius, and O. Mattila, "Effect of fluid physical properties on the emulsification," *ISIJ international*, vol. 49, no. 1, pp. 29–36, 2009.
- [32] S.-H. Kim and R. J. Fruehan, "Physical modeling of liquid/liquid mass transfer in gas stirred ladles," *Metallurgical Transactions B*, vol. 18, no. 2, pp. 381–390, Jun 1987.

- [33] Z. Xiao, Y. Peng, and C. Liu, "Modelling study of the entrapment phenomena at the slag-metal interface in the gas-stirred ladle," *Chinese Journal of Metal Science and Technology*, vol. 3, no. 4, pp. 187–193, 1987.
- [34] J. Mietz, S. Schneider, and F. Oeters, "Emulsification and mass transfer in ladle metallurgy," *Steel Research*, vol. 62, no. 1, pp. 10–15, jan 1991.
- [35] T. Wei and F. Oeters, "A model test for emulsion in gas–stirred ladles," *Steel research*, vol. 63, no. 2, pp. 60–68, 1992.
- [36] M. Iguchi, Y. Sumida, R. Okada, and Z.-i. Morita, "Evaluation of critical gas flow rate for the entrapment of slag using a water model," *ISIJ international*, vol. 34, no. 2, pp. 164–170, 1994.
- [37] R. V. Calabrese, T. Chang, and P. Dang, "Drop breakup in turbulent stirred-tank contactors. part i: Effect of dispersed-phase viscosity," *AIChE Journal*, vol. 32, no. 4, pp. 657–666, 1986.
- [38] R. Calabrese, C. Wang, and N. Bryner, "Drop breakup in turbulent stirred-tank contactors. part iii: Correlations for mean size and drop size distribution," *AIChE journal*, vol. 32, no. 4, pp. 677–681, 1986.
- [39] C. Wang and R. V. Calabrese, "Drop breakup in turbulent stirred-tank contactors. part ii: Relative influence of viscosity and interfacial tension," *AIChE journal*, vol. 32, no. 4, pp. 667–676, 1986.
- [40] S.-H. Kim, R. Fruehan, and R. Guthrie, "Physical model studies of two phase mass transfer in gas-stirred ladles," in *Steelmaking Conference Proceedings, Iron and Steel Society*, vol. 70, 1987, pp. 107–117.
- [41] L. d. De Oliveira Campos, "Mass transfer coefficients across dynamic liquid steel/slag interface," Theses, Université de Bordeaux, Mar. 2017.
- [42] D. J. Tritton, *Physical fluid dynamics*. Springer Science & Business Media, 2012.
- [43] A. Monin and A. M. Yaglom, "Statistical fluid mechanics, vols. 1 and 2," *MIT Press, Cambridge, MA*, vol. 1975, p. 11, 1971.
- [44] H. Schlichting, *Boundary-layer theory*. McGraw-Hill, 1979.
- [45] A. Ezzamel, P. Salizzoni, and G. R. Hunt, "Dynamical variability of axisymmetric buoyant plumes," *J. Fluid Mech*, vol. 765, pp. 576–611, 2015.
- [46] P. Sulasalmi, V.-V. Visuri, A. Kärnä, and T. Fabritius, "Simulation of the effect of steel flow velocity on slag droplet distribution and interfacial area between steel and slag," *steel research international*, vol. 86, no. 3, pp. 212–222, 2015.
- [47] E. K. Ramasetti, V.-V. Visuri, P. Sulasalmi, R. Mattila, and T. Fabritius, "Modeling of the effect of the gas flow rate on the fluid flow and open-eye formation in a water model of a steelmaking ladle," *steel research international*, vol. 90, no. 2, p. 1800365, 2019.
- [48] A. Senguttuvan and G. A. Irons, "Modeling of slag entrainment and interfacial mass transfer in gas stirred ladles," *ISIJ International*, vol. 57, no. 11, pp. 1962–1970, 2017.
- [49] S. Vincent, J. Larocque, D. Lacanette, A. Toutant, P. Lubin, and P. Sagaut, "Numerical simulation of phase separation and a priori two-phase LES filtering," *Computers & Fluids*, vol. 37, no. 7, pp. 898–906, aug 2008.

- [50] J. Delteil, S. Vincent, A. Erriguible, and P. Subra-Paternault, "Numerical investigations in rayleigh breakup of round liquid jets with VOF methods," *Computers & Fluids*, vol. 50, no. 1, pp. 10–23, nov 2011.
- [51] A. Huang, H. Gu, M. Zhang, N. Wang, T. Wang, and Y. Zou, "Mathematical modeling on erosion characteristics of refining ladle lining with application of purging plug," *Metallurgical and Materials Transactions B*, vol. 44, no. 3, pp. 744–749, 2013.
- [52] W. Lou and M. Zhu, "Numerical simulations of inclusion behavior in gas-stirred ladles," *Metallurgical and Materials Transactions B*, vol. 44, no. 3, pp. 762–782, 2013.
- [53] W. Lou and M. Zhu, "Numerical simulation of desulfurization behavior in gas-stirred systems based on computation fluid dynamics–simultaneous reaction model (cfd–srm) coupled model," *Metallurgical and Materials Transactions B*, vol. 45, no. 5, pp. 1706–1722, Oct 2014.
- [54] W. Lou and M. Zhu, "Numerical simulation of slag-metal reactions and desulfurization efficiency in gas-stirred ladles with different thermodynamics and kinetics," *ISIJ International*, vol. 55, no. 5, pp. 961–969, 2015.
- [55] Q. Cao and L. Nastac, "Mathematical investigation of fluid flow, mass transfer, and slag-steel interfacial behavior in gas-stirred ladles," *Metallurgical and Materials Transactions B*, vol. 49, no. 3, pp. 1388–1404, 2018.
- [56] L. Li, Z. Liu, B. Li, H. Matsuura, and F. Tsukihashi, "Water model and cfd-pbm coupled model of gas-liquid-slag three-phase flow in ladle metallurgy," *ISIJ International*, vol. 55, no. 7, pp. 1337–1346, 2015.
- [57] L. Li, Z. Liu, M. Cao, and B. Li, "Large eddy simulation of bubbly flow and slag layer behavior in ladle with discrete phase model (dpm)–volume of fluid (vof) coupled model," *JOM*, vol. 67, no. 7, pp. 1459–1467, 2015.
- [58] L. Li, B. Li, and Z. Liu, "Modeling of gas-steel-slag three-phase flow in ladle metallurgy: Part ii. multi-scale mathematical model," *ISIJ International*, pp. ISIJINT–2017, 2017.
- [59] W. Liu, H. Tang, S. Yang, M. Wang, J. Li, Q. Liu, and J. Liu, "Numerical simulation of slag eye formation and slag entrapment in a bottom-blown argon-stirred ladle," *Metallurgical and Materials Transactions B*, vol. 49, no. 5, pp. 2681–2691, 2018.
- [60] H. Liu, Z. Qi, and M. Xu, "Numerical simulation of fluid flow and interfacial behavior in three-phase argon-stirred ladles with one plug and dual plugs," *steel research international*, vol. 82, no. 4, pp. 440–458, 2011.
- [61] D. Fuster, J.-P. Matas, S. Marty, S. Popinet, J. Hoepffner, A. Cartellier, and S. Zaleski, "Instability regimes in the primary breakup region of planar coflowing sheets," *Journal of Fluid Mechanics*, vol. 736, pp. 150–176, 2013.
- [62] Y. Ling, D. Fuster, S. Zaleski, and G. Tryggvason, "Spray formation in a quasiplanar gas-liquid mixing layer at moderate density ratios: A numerical closeup," *Phys. Rev. Fluids*, vol. 2, p. 014005, Jan 2017.
- [63] W. Aniszewski, Y. Saade, S. Zaleski, and S. Popinet, "Planar jet stripping of liquid coatings: Numerical studies," *International Journal of Multiphase Flow*, vol. 132, p. 103399, nov 2020.
- [64] S. Popinet and collaborators, "Basilisk," <http://basilisk.fr>, 2013–2020.

- [65] S. Popinet, "Incompressible navier-stokes solver (centered formulation)," <http://basilisk.fr/src/navier-stokes/centered.h>, 2020.
- [66] P.-Y. Lagrée, L. Staron, and S. Popinet, "The granular column collapse as a continuum: validity of a two-dimensional navier-stokes model with a $[\mu](i)$ -rheology," *Journal of Fluid Mechanics*, vol. 686, p. 378, 2011.
- [67] J. U. Brackbill, D. B. Kothe, and C. Zemach, "A continuum method for modeling surface tension," *Journal of computational physics*, vol. 100, no. 2, pp. 335–354, 1992.
- [68] S. Popinet, "Numerical models of surface tension," *Annual Review of Fluid Mechanics*, vol. 50, no. 1, pp. 49–75, jan 2018.
- [69] J. A. van Hooft, S. Popinet, C. C. van Heerwaarden, S. J. A. van der Linden, S. R. de Roode, and B. J. H. van de Wiel, "Towards adaptive grids for atmospheric boundary-layer simulations," *Boundary-Layer Meteorology*, vol. 167, no. 3, pp. 421–443, feb 2018.
- [70] D. C. Kurt A. Smith, Francisco J. Solis, "A projection method for motion of triple junctions by level sets," *Interfaces and Free Boundaries*, 2002.
- [71] X. Chen, Y. Sun, C. Xue, Y. Yu, and G. Hu, "Tunable structures of compound droplets formed by collision of immiscible microdroplets," *Microfluidics and Nanofluidics*, vol. 21, no. 6, p. 109, Jun 2017.
- [72] B. Wallmeyer, S. Trinschek, S. Yigit, U. Thiele, and T. Betz, "Collective cell migration in embryogenesis follows the laws of wetting," *Biophysical Journal*, vol. 114, no. 1, pp. 213 – 222, 2018.
- [73] A. Esmaeeli and G. Tryggvason, "Direct numerical simulations of bubbly flows. part 1. low reynolds number arrays," *Journal of Fluid Mechanics*, vol. 377, pp. 313–345, 1998.
- [74] J. C. Cano-Lozano, C. Martinez-Bazan, J. Magnaudet, and J. Tchoufag, "Paths and wakes of deformable nearly spheroidal rising bubbles close to the transition to path instability," *Physical Review Fluids*, vol. 1, no. 5, p. 053604, 2016.
- [75] S. B. Pope, *Turbulent flows*. IOP Publishing, 2001.
- [76] J. Schindelin, I. Arganda-Carreras, E. Frise, V. Kaynig, M. Longair, T. Pietzsch, S. Preibisch, C. Rueden, S. Saalfeld, B. Schmid *et al.*, "Fiji: an open-source platform for biological-image analysis," *Nature methods*, vol. 9, no. 7, pp. 676–682, 2012.
- [77] C. A. Schneider, W. S. Rasband, and K. W. Eliceiri, "NIH image to ImageJ: 25 years of image analysis," *Nature Methods*, vol. 9, no. 7, pp. 671–675, jun 2012.
- [78] M. Thunman, S. Eckert, O. Hennig, J. Björkvall, and D. Sichen, "Study on the formation of open-eye and slag entrainment in gas stirred ladle," *steel research international*, vol. 78, no. 12, pp. 849–856, 2007.
- [79] W. K. Lewis and W. G. Whitman, "Principles of gas absorption." *Industrial & Engineering Chemistry*, vol. 16, no. 12, pp. 1215–1220, 1924.
- [80] R. Higbie, "The rate of absorption of a pure gas into a still liquid during short periods of exposure," *Trans. AIChE*, vol. 31, pp. 365–389, 1935.
- [81] P. Danckwerts, "Significance of liquid-film coefficients in gas absorption," *Industrial & Engineering Chemistry*, vol. 43, no. 6, pp. 1460–1467, 1951.

- [82] G. Fortescue and J. Pearson, "On gas absorption into a turbulent liquid," *Chemical Engineering Science*, vol. 22, no. 9, pp. 1163–1176, 1967.
- [83] S. Banerjee, D. Scott, and E. Rhodes, "Mass transfer to falling wavy liquid films in turbulent flow," *Industrial & Engineering Chemistry Fundamentals*, vol. 7, no. 1, pp. 22–27, 1968.
- [84] J. C. Lamont and D. Scott, "An eddy cell model of mass transfer into the surface of a turbulent liquid," *AIChE Journal*, vol. 16, no. 4, pp. 513–519, 1970.
- [85] G. K. Batchelor, *The theory of homogeneous turbulence*. Cambridge university press, 1953.
- [86] T. Theofanous, R. Houze, and L. Brumfield, "Turbulent mass transfer at free, gas-liquid interfaces, with applications to open-channel, bubble and jet flows," *International Journal of Heat and Mass Transfer*, vol. 19, no. 6, pp. 613–624, 1976.
- [87] M. McCreedy, E. Vassiliadou, and T. Hanratty, "Computer simulation of turbulent mass transfer at a mobile interface," *AIChE Journal*, vol. 32, no. 7, pp. 1108–1115, 1986.
- [88] W. Chan and L. Scriven, "Absorption into irrotational stagnation flow. a case study in convective diffusion theory," *Industrial & Engineering Chemistry Fundamentals*, vol. 9, no. 1, pp. 114–120, 1970.
- [89] S. Banerjee and S. MacIntyre, "The air-water interface: Turbulence and scalar exchange," in *PIV and Water Waves*. World Scientific, 2004, pp. 181–237.
- [90] S. McKenna and W. McGillis, "The role of free-surface turbulence and surfactants in air–water gas transfer," *International Journal of Heat and Mass Transfer*, vol. 47, no. 3, pp. 539–553, 2004.
- [91] J. Magnaudet and I. Calmet, "Turbulent mass transfer through a flat shear-free surface," *Journal of Fluid Mechanics*, vol. 553, p. 155, 2006.
- [92] G. H. Jirka *et al.*, "Experiments on gas transfer at the air-water interface induced by oscillating grid turbulence," *Journal of Fluid Mechanics*, vol. 594, p. 183, 2008.
- [93] D. E. Turney and S. Banerjee, "Air–water gas transfer and near-surface motions," *Journal of Fluid Mechanics*, vol. 733, pp. 588–624, 2013.
- [94] B. Kader and A. Yaglom, "Heat and mass transfer laws for fully turbulent wall flows," *International Journal of Heat and Mass Transfer*, vol. 15, no. 12, pp. 2329–2351, 1972.
- [95] I. Calmet and J. Magnaudet, "Large-eddy simulation of high-schmidt number mass transfer in a turbulent channel flow," *Physics of Fluids*, vol. 9, no. 2, pp. 438–455, 1997.
- [96] D. A. Shaw and T. J. Hanratty, "Turbulent mass transfer rates to a wall for large schmidt numbers," *AIChE Journal*, vol. 23, no. 1, pp. 28–37, 1977.
- [97] J. Mietz, S. Schneider, and F. Oeters, "Model experiments on mass transfer in ladle metallurgy," *Steel research*, vol. 62, no. 1, pp. 1–9, 1991.
- [98] I. M. S. Asai, M. Kawachi, "Mass transfer rate in ladle refining processes," in *Proc. Scaninject III*, 1983.
- [99] M. Hirasawa, K. Mori, M. Sano, A. Hatanaka, Y. Shimatani, and Y. Okazaki, "Rate of mass transfer between molten slag and metal under gas injection stirring," *Transactions of the Iron and Steel Institute of Japan*, vol. 27, no. 4, pp. 277–282, 1987.

- [100] L. S. Karaffa, *The Merck index: an encyclopedia of chemicals, drugs, and biologicals*. RSC Publishing, 2013.
- [101] W. M. Haynes, *CRC handbook of chemistry and physics*. CRC press, 2014.
- [102] R. C. Reid, J. M. Prausnitz, and B. E. Poling, *The properties of gases and liquids*. McGraw Hill Book Co., New York, NY, 1987.
- [103] H. Gaye, "Lois du transport de matiere par diffusion dans les gaz et dans les phases condensees," 1976.
- [104] M. R. Davidson and M. Rudman, "Volume-of-fluid calculation of heat or mass transfer across deforming interfaces in two-fluid flow," *Numerical Heat Transfer: Part B: Fundamentals*, vol. 41, no. 3-4, pp. 291–308, 2002.
- [105] A. Koynov, J. G. Khinast, and G. Tryggvason, "Mass transfer and chemical reactions in bubble swarms with dynamic interfaces," *AIChE Journal*, vol. 51, no. 10, pp. 2786–2800, 2005.
- [106] A. Onea, M. Wörner, and D. G. Cacuci, "A qualitative computational study of mass transfer in upward bubble train flow through square and rectangular mini-channels," *Chemical Engineering Science*, vol. 64, no. 7, pp. 1416–1435, 2009.
- [107] H. Marschall, K. Hinterberger, C. Schüler, F. Habla, and O. Hinrichsen, "Numerical simulation of species transfer across fluid interfaces in free-surface flows using openfoam," *Chemical engineering science*, vol. 78, pp. 111–127, 2012.
- [108] S. Fleckenstein and D. Bothe, "A volume-of-fluid-based numerical method for multi-component mass transfer with local volume changes," *Journal of Computational Physics*, vol. 301, pp. 35–58, 2015.
- [109] J. López-Herrera, A. Ganan-Calvo, S. Popinet, and M. Herrada, "Electrokinetic effects in the breakup of electrified jets: A volume-of-fluid numerical study," *International Journal of Multiphase Flow*, vol. 71, pp. 14–22, 2015.
- [110] A. Weiner and D. Bothe, "Advanced subgrid-scale modeling for convection-dominated species transport at fluid interfaces with application to mass transfer from rising bubbles," *Journal of Computational Physics*, vol. 347, pp. 261–289, 2017.
- [111] N. Balcázar-Arciniega, O. Antepará, J. Rigola, and A. Oliva, "A level-set model for mass transfer in bubbly flows," *International Journal of Heat and Mass Transfer*, vol. 138, pp. 335–356, 2019.
- [112] M. J. Sathe, I. H. Thaker, T. E. Strand, and J. B. Joshi, "Advanced piv/lif and shadowgraphy system to visualize flow structure in two-phase bubbly flows," *Chemical Engineering Science*, vol. 65, no. 8, pp. 2431–2442, 2010.
- [113] H. Hessenkemper and T. Ziegenhein, "Particle shadow velocimetry (psv) in bubbly flows," *International Journal of Multiphase Flow*, vol. 106, pp. 268–279, 2018.
- [114] L. Liu, O. Keplinger, T. Ziegenhein, N. Shevchenko, S. Eckert, H. Yan, and D. Lucas, "Euler–euler modeling and x-ray measurement of oscillating bubble chain in liquid metals," *International Journal of Multiphase Flow*, vol. 110, pp. 218–237, 2019.
- [115] A. Weiner, J. Timmermann, C. Pesci, J. Grewe, M. Hoffmann, M. Schlüter, and D. Bothe, "Experimental and numerical investigation of reactive species transport around a small rising bubble," *Chemical Engineering Science: X*, vol. 1, p. 100007, 2019.